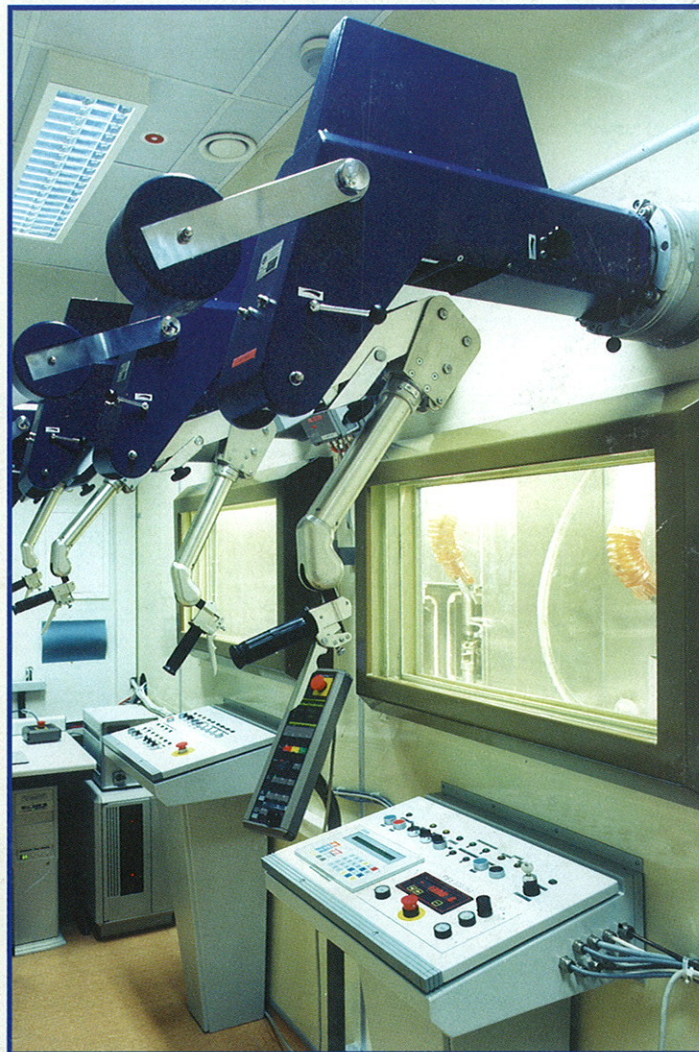FZR-238

Institute of Safety Research

Annual Report 1997

BRD

Cover photograph:
The mechanical testing laboratory for radioactive materials. View on the working front of the hot cell. The laboratory allows to test specimens with a maximum activity of 5×10^{19} Bq ^{60}Co and is equipped with an instrumented impact tester, a servo-hydraulic testing system and a video-measuring microscope (see also p. 80).

Annual Report 1997

Institute of Safety Research

Editors: Prof. Dr. F.-P. Weiß
PD Dr. U. Rindelhardt

CONTENTS

Preface

Selected Reports

Preface

Preface

The Institute of Safety Research is one of the five scientific instituts of Forschungszentrum Rossendorf e. V. The Forschungszentrum Rossendorf is a member of the „Wissenschaftsgemeinschaft Gottfried Wilhelm Leibniz" and is funded by the Federal Ministry of Education and Research and by the Saxon Ministry of Science and Arts with 50% each.

The research work of the institute aims at the assessment and increase of the safety of technical facilities. Subject of the investigation are equally nuclear plants and installations of process industries.

To analyse thermo-fluiddynamic phenomena of accident scenarios physical models and computer codes are developed as well for multi-phase and multi-component flows as for the time and space dependent power release (neutron kinetics in light water reactors, reaction kinetics of exothermic chemical reactions). Emphasis is put on the description of spatial flows and the transient evolution of flow patterns.

To improve the base for theoretical work extended experimental research is indispensable. Therefore, the institute plans a large scaled thermal hydraulic facility for the investigation of basic transient phenomena in two-phase flows. It is aimed to perform investigations of basic problems in thermo-fluiddynamics and of phenomena related to process industries. To better characterize the pulse, mass, and energy transfer between the phases and components sophisticated two phase measuring equipment is developed.

The efforts in materials safety are mainly devoted to the behaviour of materials under neutron and gamma irradiation. The susceptibility to embrittlement and the sustainability of annealing are studied by means of fracture mechanical testing of irradiated and thermally annealed specimens. The micro-structural mechanisms of irradiation embrittlement and of materials damaging at all shall be revealed by high resolution structural analytics as e. g. small angle x-ray scattering. To provide highly accurate values of the received radiation fluences that are required for the embrittlement studies Monte Carlo calculation methods are applied, further developed, and validated against experimental data.

Starting from the determined accident loads (pressure, temperature) and from the fracture mechanical properties of the safety relevant components the integrity of plants and components can be assessed by structure-dynamic calculations. This assessment must consider thermal and mechanical interactions between the components and the fluids.

Recent initiatives of the institute are directed to modelling the transport of pollutants in the hydro- and geosphere. The focus is put on the development of

codes for the simulation of physical and chemical phenomena during the transport of natural radionuclides in soils that are not saturated with water.

The non-nuclear activities are complemented by the work on magneto-fluiddynamics. It is not the intention to develop MHD generators but to study the basic interactions of electromagnetic fields and conducting fluids. One of the main topics in that context is the self-excitation of magnetic fields in liquid metal flows to explain the source of the magnetic field of the earth. Another promising subject is the influence of external electromagnetic fields upon the flow of conducting fluids to promote mixing or to reduce the drag of bodies in a flow.

In the nuclear field, the institute together with the Technische Universität Dresden (TUD) and with the Hochschule für Technik, Wirtschaft und Sozialwesen (HTWS) Zittau/Görlitz as a regional association takes care to maintain the nuclear competence in Germany. For that this regional centre of competence closely works together with the institutes of the Helmholtz-Gesellschaft and with Gesellschaft für Anlagen- und Reaktorsicherheit.

The following graphs give an overview about the sources and the deployment of funding amongst the different research tasks. In 1997 41% of the total budget came from external sources with 31% from public research grants (24% from Federal Ministries and from the Saxonian Ministry of Science and Arts, 7% from Deutsche Forschungsgemeinschaft) and with 10% from research orders.

In 1997 the institute took part in several concerted actions of the EU (e. g. concerted action of the EU on Future Boiling Water Reactors and concerted action on the Reconstitution of Materials Specimens) and as the leader of a Western consortium launched a safety related research TACIS project on the „Improvement of the Validation of Coupled Thermalhydraulics, Neutron-Kinetics Codes". Moreover, the institute is member of a Western consortium accomplishing the TACIS research project „Development of Advanced Methods for the Evaluation of Irradiation Embrittlement of VVER-1000 Reactore Pressure Vessels".

The institute made particular efforts to extend its engagement in the process industries. Among others, these efforts lead to research contracts with Krupp/UHDE about the behaviour of chlorine-alkaline membrane electrolysis cells and with Arzneimittelwerk Dresden (AWD) on the kinetics of exothermic reactions. Part of the work will be accomplished in the new laboratory for process chemistry, that was constructed in 1997.

Distribution of funding sources 1997

basic budget
59%

research orders (industry,
public offices)
10%

public research grants/ DFG
7%

public research grants/ BMBF,
SMWK, ...
24%
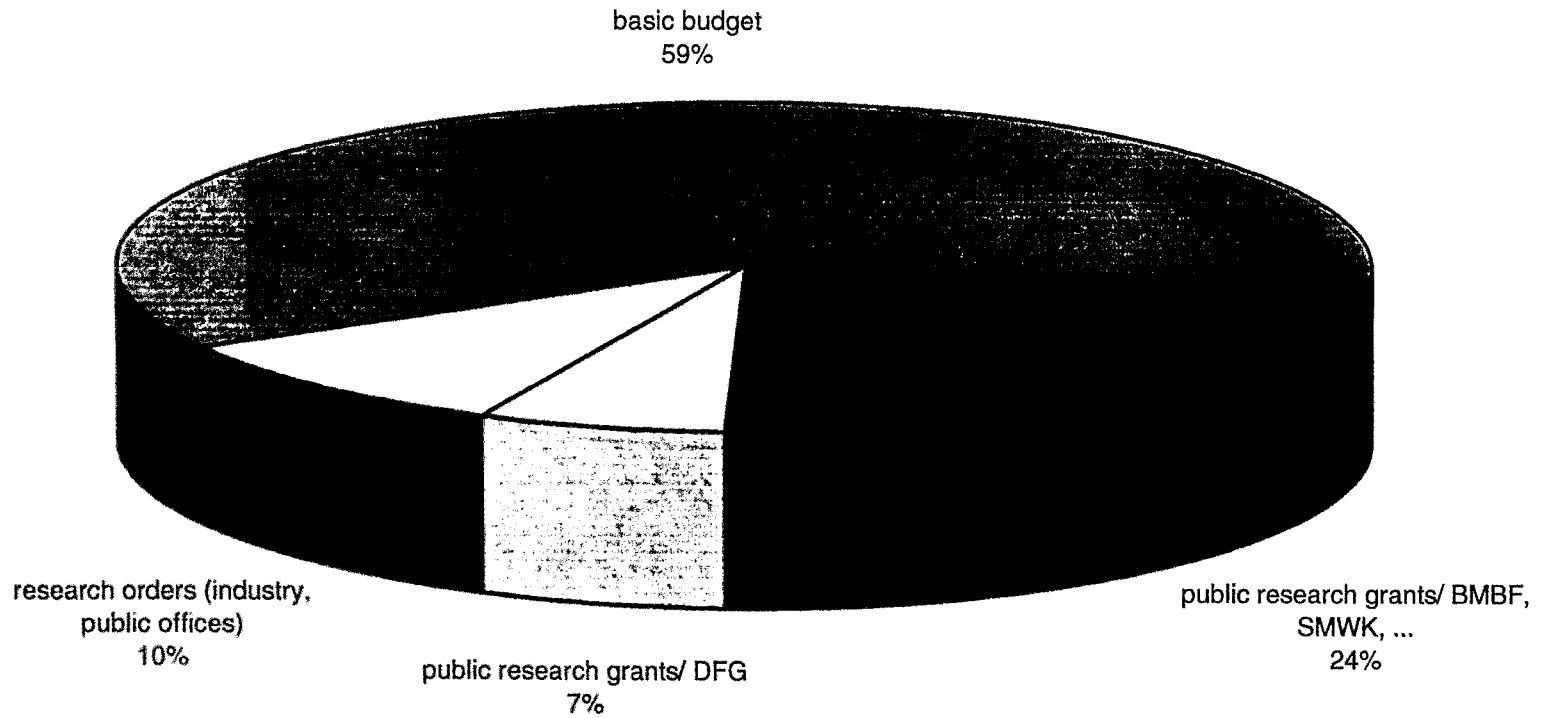
Deployment of funding on the various tasks/projects 1997

thermo-fluiddynamic single effects
22%

magneto-hydrodynamics of
conductive fluids
24%

thermal hydraulics and neutron
kinetics for accident analysis
17%

hazard ranking and risk
management of waste deposits
3%

mechanical behaviour of LWR-
components under conditions of
accident
9%

simulation of radiation and particle
transport
8%

materials safety
17%
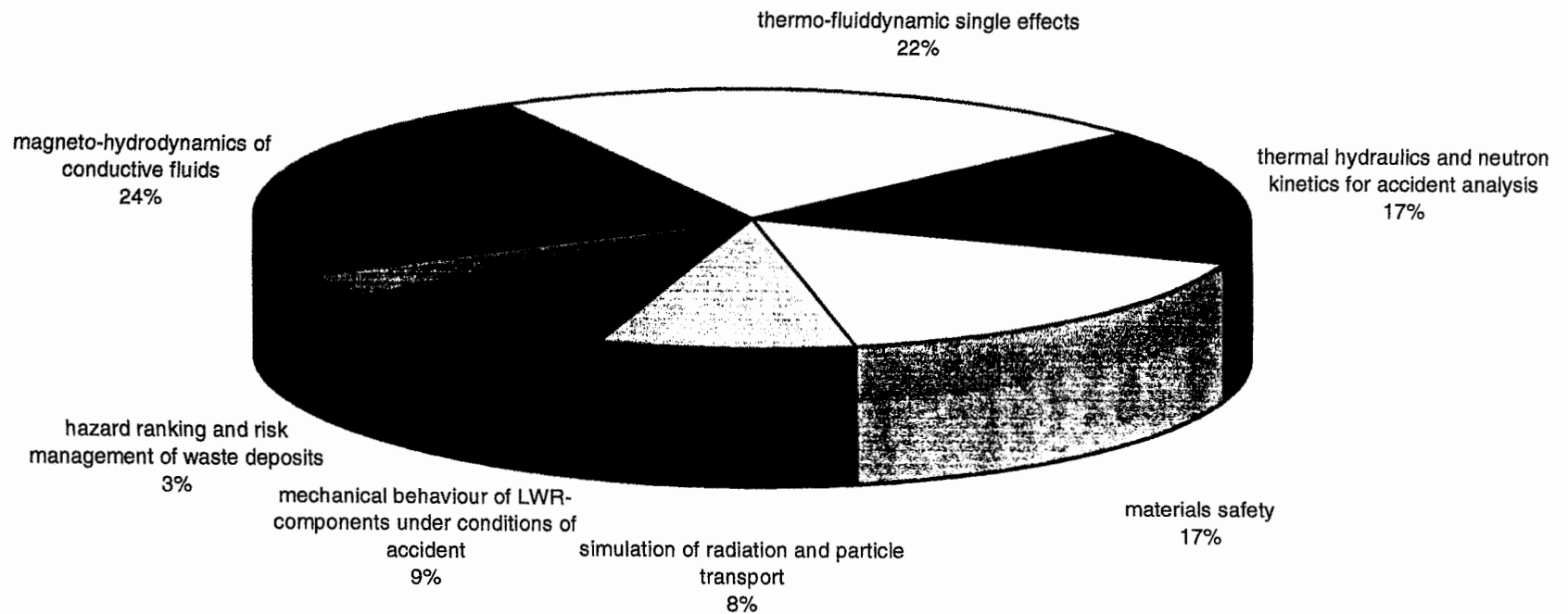
Selected Reports

COOLANT MIXING IN PRESSURIZED WATER REACTORS

T. Höhne, G. Grunwald

1. Introduction

The behavior of PWRs during cold water or boron dilution transients is strongly influenced by the distribution of coolant temperature and boron concentration at the core inlet. This distribution is the needed input to 3-dimensional neutron kinetics to calculate the power distribution in the core. It mainly depends on how the plugs of cold or unborated water formed in a single loop are mixed in the downcomer and in the lower plenum.

To simulate such mixture phenomena requires the application of 3-dimensional CFD (computational fluid dynamics) codes. The results of the simulation have to be validated against mixture experiments at scaled facilities.

Therefore, in the framework of a research project funded by BMBF, the institute creates a 1:5 mixture facility representing first the geometry of a German pressurized water reactor and later the European Pressurized Water Reactor (EPR) geometry. The calculations are based on the CFD Code CFX-4.

2. Scenarios leading to cold water transients or boron dilution

Inherent boron dilution can occur when the decay heat is removed from the core by phase-separating natural circulation. That is, whenever it is removed by reflux condensation, in the case of vertical U-tube steam generators.

These conditions lead to boron dilution because

- Boric acid is not dissolved in the steam
- Boron-free condensate can accumulate in a subspace of the primary loop (for example in the loop seal)

If one-phase natural circulation restarts or a reactor coolant pump starts, the diluted slugs can enter the reactor vessel and proceed through the downcomer and the lower plenum. Depending on the coolant velocity, the slug is more or less mixed with the ambient fluid. In general, low velocities lead to sufficient mixing, high velocities might be connected with weak mixing. Weak mixing can result in recriticality and possibly in significant power release.

Cold water transients can occur at a main steam line break scenario (pressure drop). The result can be overcriticality and power excursion of the reactor.

3. Calculation of mixing processes with a CFD code

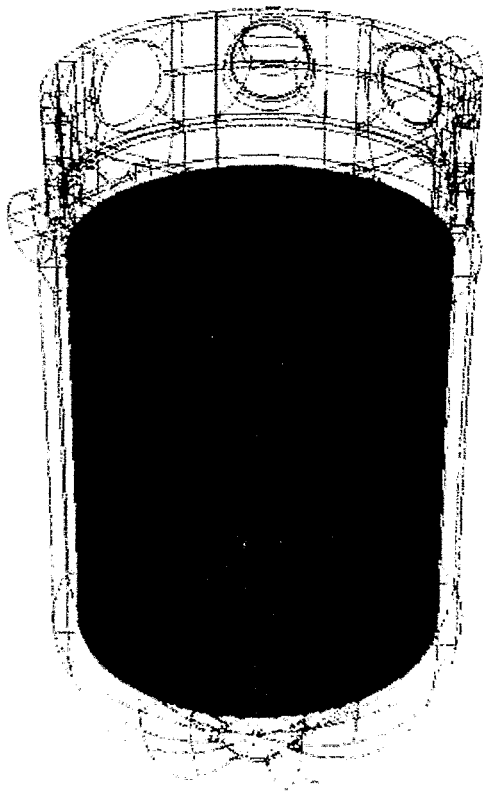## 3.1 Model assumptions, geometry preparation and grid generation

Fig. 1: Computational grid (Konvoi)

An incompressible fluid was assumed for the coolant flow in pressurized water reactors. The turbulence was modeled using the Standard k-ε approximation. The inlet boundary conditions (velocity, temperature, boron concentration etc.) were set at the inlet nozzles. The outlet boundary conditions were pressure controlled. Applying passive scalar fields is the best option to describe the boron dilution processes. The calculations were done on a SGI Origin 200 (1 GB RAM, 4x R 10000 180 Mhz, 64 Bit CPU) workstation platform.

The nodalization (grid generation) was carried out step by step. This allowed to analyze the influence of geometric details on the flow. The following important factors were identified: Exact representation of the inlet region (bend radii etc.), extension of the downcomer below the inlet region and obstruction of the flow by the outlet nozzles cut through the downcomer (Figure 1).

3.2 Results of steady state calculations of the PWR Konvoi and the VVER-440

Two types of pressurized water reactors (PWR) were used to analyze the flow field and mixing processes. The PWR Konvoi (1300 MW) is a common reactor type in Germany, the VVER-440 (440 MW) is a standard Russian reactor operating in several east European countries. The first step for analyzing the boron and temperature transients are steady state calculations. CFD-calculations were made at nominal conditions i.e. all main coolant pumps were operating. To describe the mixing of the coolant one loop was running with colder temperature.

The flow fields in the downcomers of the PWR's Konvoi and VVER-440 is represented in Figure 2 at steady state conditions. To visualize the flow in Figure 2 the downcomers are represented in one plane, all pumps were running.

2

The velocity field of the PWR Konvoi calculated for the case of operation of all four main circulation pumps show a good agreement with experimental results (air operated model of Ulrych and Weber [1]). The calculations especially confirm the back flow areas below the inlet nozzles. A maximum velocity exists at azimutal positions between the inlet and outlet nozzles. To simulate the mixing of the coolant one loop was assumed to introduce coolant with lower temperature than the other 3 loops. The coolant mixing in the downcomer at nominal condition is weak (Figure 3). A sector of low temperature coolant is still existing at the inlet of the core.

The downcomer flow of the Russian VVER-440 has smaller recirculation areas than at PWR Konvoi. The calculations of the downcomer and lower plenum confirmed the analytical mixing model of Dräger [2,3,4] (applicability of potential flow approximation). A maximum velocity exists also at azimutal positions between the inlet nozzles.
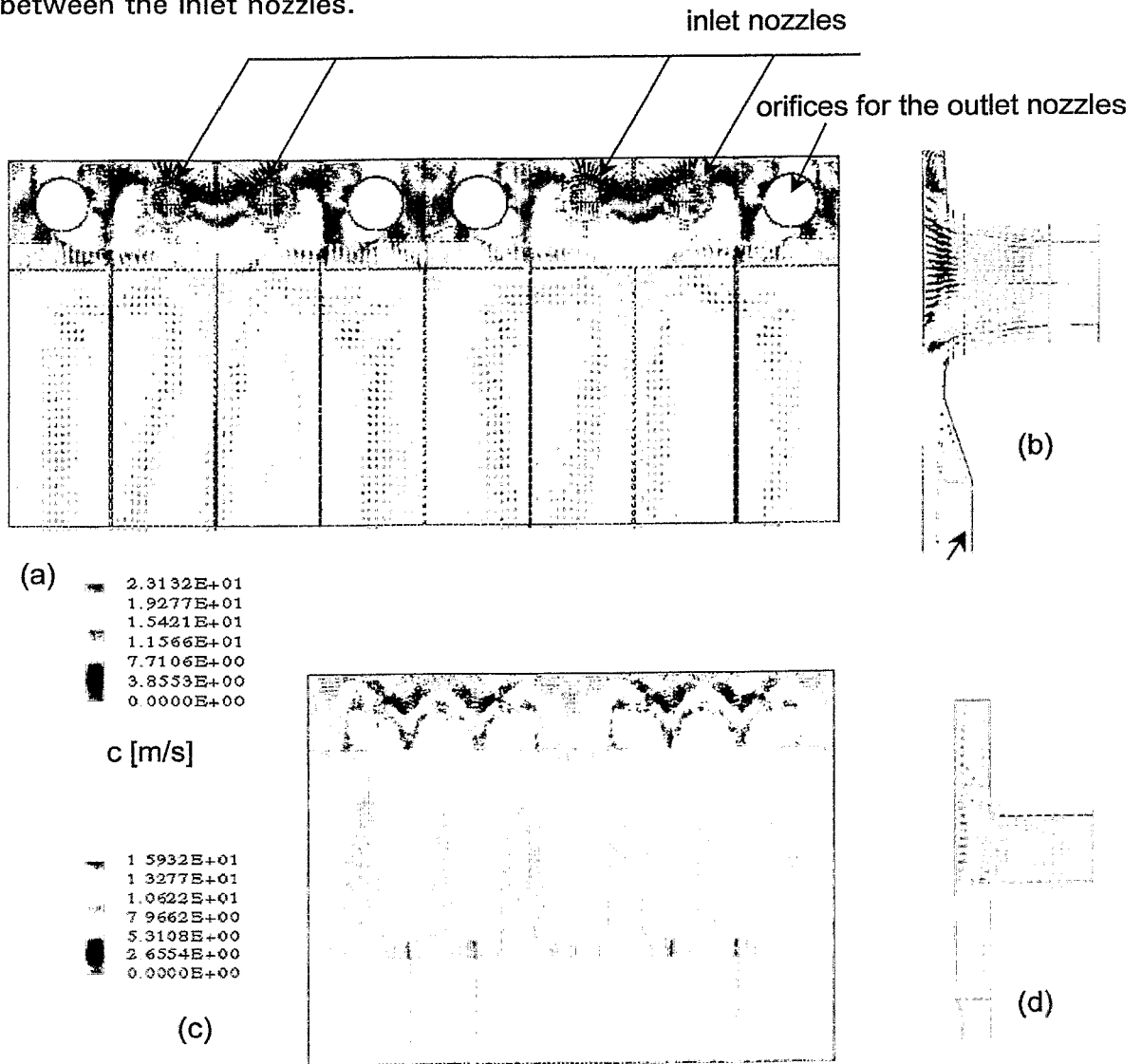
Fig. 2: Flow fields in the downcomer (a) and the inlet nozzle (b) of the PWR Konvoi, the downcomer (c) and the inlet nozzle (d) of VVER-440

3
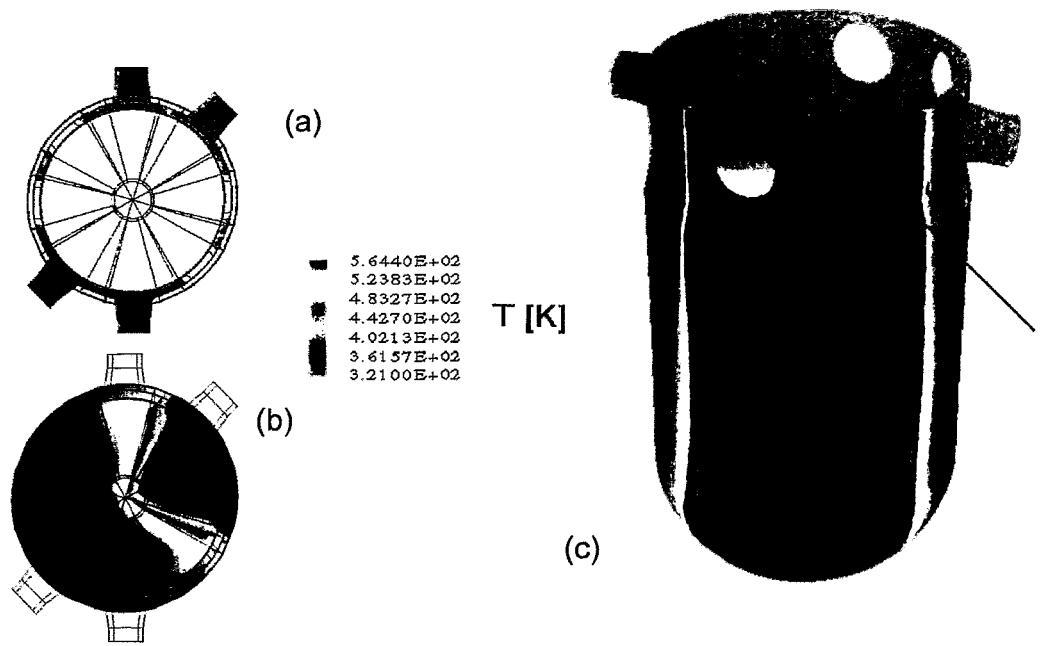
Fig. 3: Temperature mixing in the nozzle area (a), core inlet (b) and near the outer wall (c) of the PWR Konvoi at nominal conditions (steady state, one loop runs with colder temperature)

4. Scaling of the mixing test facility
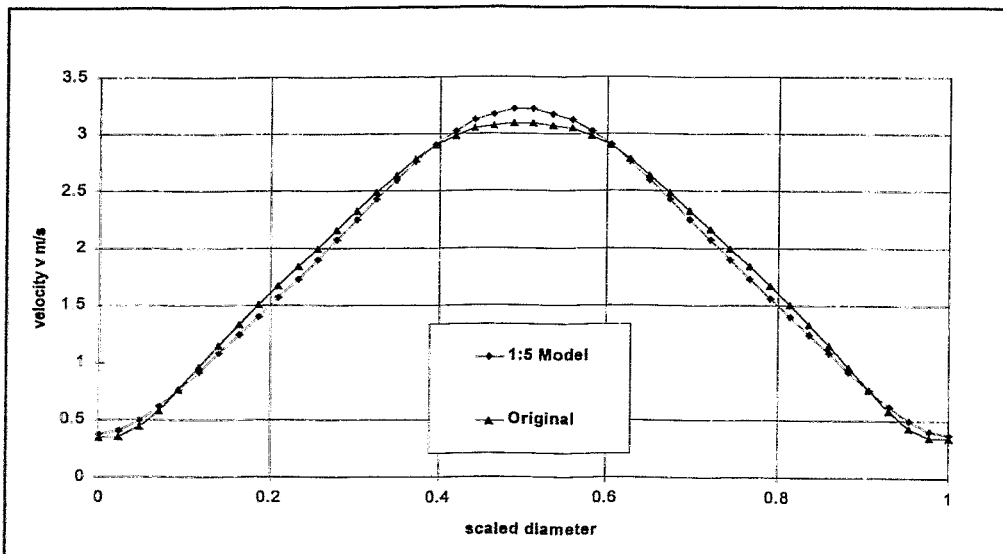
Fig. 4: Velocity along the diameter at the core inlet of the PWR Konvoi

The validation of the theoretical models, especially with respect to the choice of an appropriate turbulence model or the dispersion coefficients in the analytical solutions respectively, require experiments at a test facility, which is reproducing the flow phenomena of the original reactor as well as possible. For Konvoi type reactors such a test facility did not exist. CFD-calculations were

4

performed to analyze scaling factors. The velocities along the diameter of the core inlet cross section are shown in Figure 4. Almost no differences are to be seen between the velocities in the model and the original reactor. It turned out that the 1:5 scaling meets economic and physical demands optimally.

The requirements concerning quality of the experimental results need a non-pressurized test rig operated with water (room temperature). It has to dispose of separately controllable main coolant pumps in each loop (Figure 5). The measurement instrumentation has to be designed for the necessary spatial and time resolution.
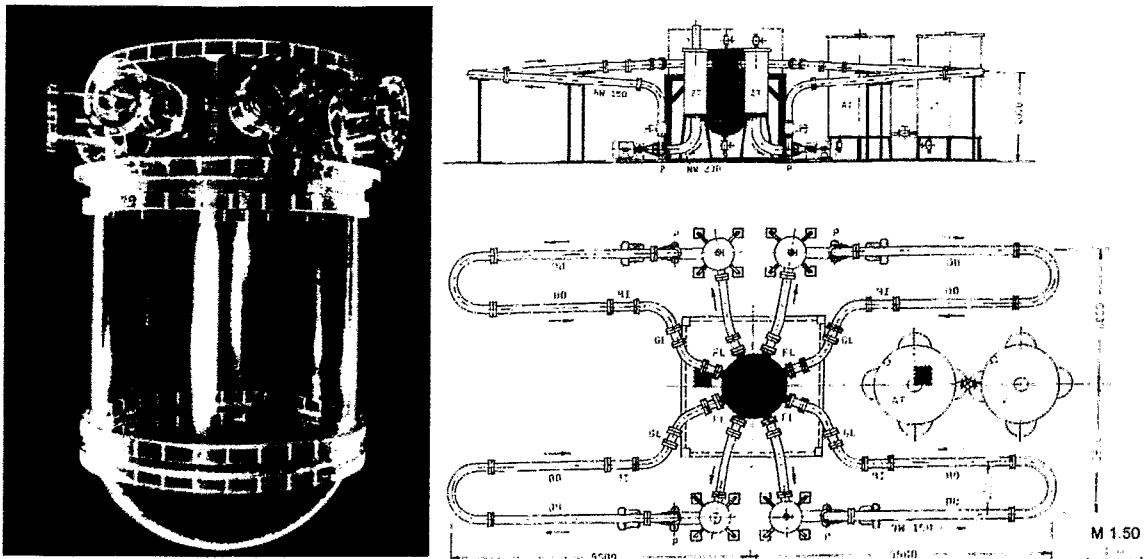
Fig. 5: 1:5 scaled plexiglas model of the PWR Konvoi

5. Fluiddynamic model of the coolant flow in the downcomer

A simplified description of the flow distribution in the downcomer of a Konvoi type PWR based on potential theory was set up. Macroscopic vortices were approximated by introducing local sources of vorticity. The analytical model describes the experimental findings in the downcomer at steady state conditions with acceptable accuracy.

6. Future Programme

Transient CFD-calculations with changing inlet boundary conditions are necessary to simulate real scenarios. For validation of the CFX-4 code it is necessary to compare the results with experiments of our own scaled model.

To analyze the dependencies of the temperature and/or boron distribution on the

power output of the reactor an interface to the neutron kinetic code DYN3D has to be set up at the core inlet region. To avoid extensive flow calculations it is necessary to develop an analytical model using transfer functions between inlet nozzles and core inlet of the reactor. This model can describe the coolant mixing after validation against measurements or CFD-calculations. In a next step the mixing shall be analyzed generically for the EPR. These investigations are in agreement with national and international actions such as the Concerted Action on Boron Dilution Experiments and with other European partners.

Literature

[1]   G. Ulrych und E. Weber (1983), *Neuere Ergebnisse zur Kühlmittel-strömung in Druckwasserreaktoren*, Atomkernenergie-Kerntechnik, 424, 217

[2]   G. Ackermann und P. Dräger (1985), *Theoretische und experimentelle Ermittlung der Temperaturverteilung am Eintritt in die Spaltzone des WWER-440*, Kernenergie, 28, 293

[3]   P. Dräger (1987), *Makroskopische Kühlmittelvermischung in Druck-wasserreaktoren*, TH Zittau

[4]   G. Ackermann und M. Sonnenkalb (1986), *Näherungsweise Berechnung des Kühlmittel-Strömungsfeldes in Druckwasserreaktoren oberhalb des Reaktorkernes*, Kernenergie, 29, 419

POST TEST CALCULATIONS OF THE
NOKO BUNDLE EXPERIMENTS

A. Schaffrath

1. Introduction

In 1997 a *BWR Physics and Thermohydraulic Complementary Action (BWR-CA)* was established to further assist and broaden the objectives of the *"European BWR R&D Cluster for Innovative Passive Safety Systems"* [1]. The partners are: CEA (Commissariat a l'Energie Atomique, France), CIEMAT (Centro de Investigaciones Energeticas, Medioambientables Tecnologicas, Spain), ENEA (Ente per le Nuove Tecnologie l'Energia e'Ambiente, ITALY), FZR (Forschungszentrum Rossendorf, Germany), Siemens AG (Germany) and TU Delft (Netherlands). The activities are divided into 4 work packages (WP). The work presented in this paper is performed in WP2: Passive decay heat removal from the core region, where two different decay heat removal systems were investigated. These are isolation condensers (e.g. as operated in Gundremmingen A, Dodewaard or in the PANDA facility) or emergency condensers (e.g. as envisaged for the SWR1000 and tested in the NOKO facility).

Within the BWR Cluster the Forschungszentrum Jülich had performed 10 NOKO test series. Six of these test series were carried out with a four tube bundle, four test series with a single tube. Several post test calculations and an additional blind calculation of NOKO tests were performed in the BWR-CA by FZR with an improved version of ATHLET Mod. 1.1 Cycle C. The tests were selected by Forschungszentrum Jülich (FZJ) [2]. The results of these calculations are presented here and compared with the experimental data.

2. NOKO Test Facility

The general design of the NOKO test facility is shown in Fig. 1. Main components of the facility are the pressure vessel (height 12.6 m, diameter 0.448 m) simulating the reactor pressure vessel of the SWR1000 and the laterally connected emergency condenser bundle. In NOKO, the steam (maximum mass flow 2.5 kg/s) is produced by an electrical heater with a maximum power of 4 MW [3].

3. Initial and boundary conditions of the tests

Table 1 gives an overview on the tests which were calculated with ATHLET. All experiments were performed with a test bundle consisting of four tubes. The NOKO tests are so called steady-state tests. The experiments can be divided

into three time periods. In the first phase the initial and boundary conditions (e.g. pressure and water level in the pressure vessel and the condensation tank) were adjusted. For that, the valve in the outlet line of the emergency condenser (see Fig. 1) was closed. By opening this valve the experiment was initiated. After reaching steady-state conditions the data acquisition was started and runs approximately 20 minutes. Then the next water level in the pressure vessel is adjusted and the procedure is repeated [4]. The tests were to assess the emergency condenser capacity (removable power) as a function of the parameters given in table 1. The capacity is independently determined by three different energy balances. The first one is the balance of the emergency condenser bundle ($L_{NOKO,1}$), the second for the condenser ($L_{NOKO,2}$) and the third for the whole primary circuit containing the electrical heater loop, the pressure vessel and the emergency condenser system ($L_{NOKO,3}$).
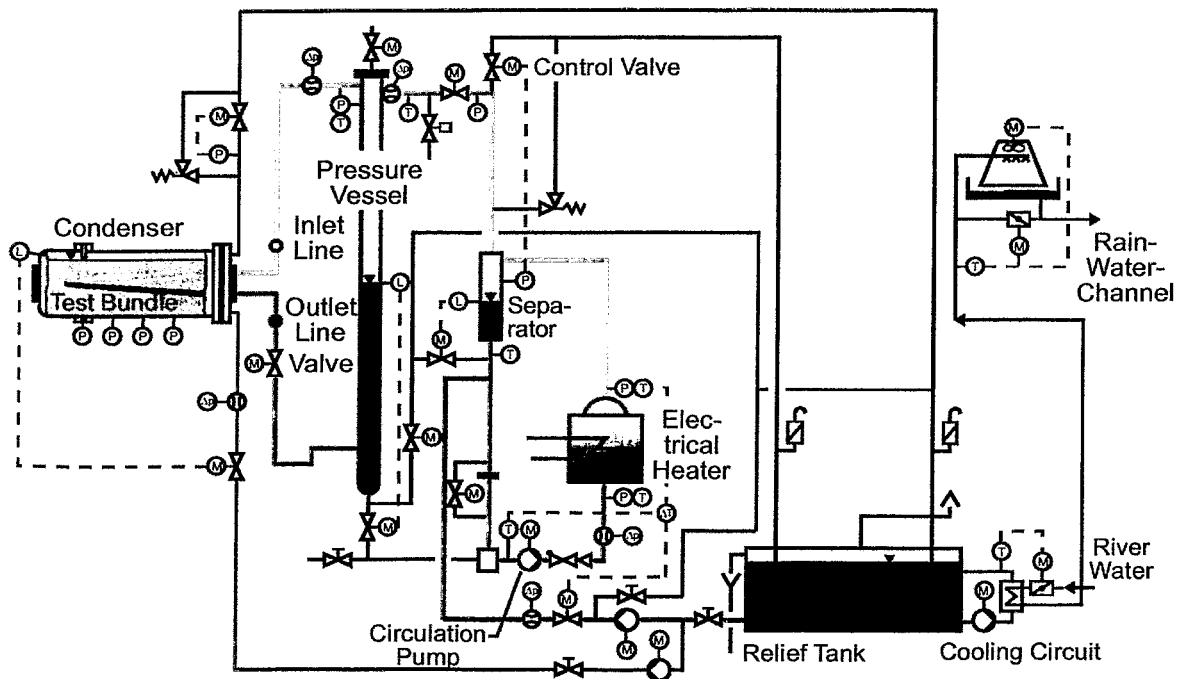
Fig. 1: NOKO test facility [3].

4. Nodalization of the NOKO facility

The nodalization scheme used for the calculations with ATHLET is shown in Fig. 2. The ATHLET model consists of the emergency condenser system (that means in- and outlet line, in- and outlet header and a bundle of 4 tubes). In the ATHLET input deck the bundle is modeled by 4 tubes, each with an individual length and geodetic height. In Fig. 2 only two tubes are shown. Additionally, the ATHLET input deck includes the pressure vessel and the condenser. Therefore, pressure and water level in the pressure vessel and the pressure in

the condenser have to be controlled. The control actions are modeled with the general control simulation module (GCSM) of ATHLET.

Table 1: Initial and boundary conditions for the NOKO post test calculations [2].

Test	Primary Conditions			Secondary Conditions		
	pressure [MPa]	water level [m]	mass flow [kg/s]	water level [m]	tempera-ture [°C]	pressure [MPa]
EU1-3	0.98	3.66	0.42	1.33	66.1	0.11
EU1-4	1.00	2.49	0.50	1.33	88.0	0.11
EU3-2	3.02	4.83	0.69	1.40	63.2	0.11
EU3-3	3.01	3.64	1.01	1.43	101.7	0.11
EU3-4	3.01	2.47	1.17	1.37	111.0	0.14
EU4-1	3.01	4.85	0.65	1.41	105.1	0.12
EU5-2	7.07	5.89	0.78	1.37	44.6	0.11
EU5-4	7.07	3.58	1.60	1.39	111.0	0.14
EU5-6	7.06	1.29	2.08	1.34	117.0	0.17
EU6-2	7.07	4.42	1.19	1.38	113.5	0.15
Blind	0.95	2.5	0.31	1.58	132.5	0.29

Fig. 2: ATHLET nodalization scheme.

5. Condensation model

As shown in [3] an improvement of the ATHLET condensation model for NOKO calculations is necessary. In Fig. 3 the different options for the calculation of heat transfer coefficients (HTC) inside tubes of the original and the improved version of ATHLET are compared. The condensation model of ATHLET (see left side of Fig. 3) was developed for the calculation of HTC in vertical tubes. The condensation process is characterized by symmetrica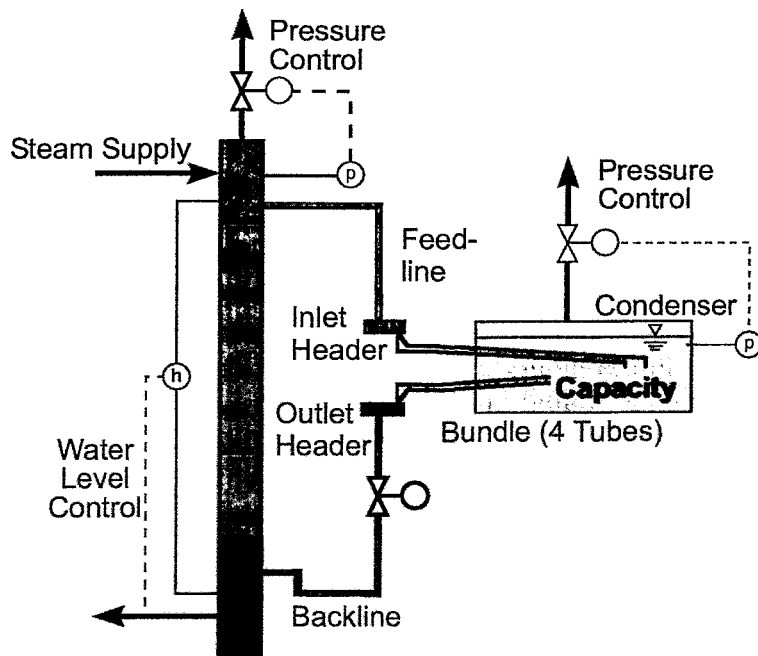l condensate films with the equal layer thickness over the cross section area. The HTC are calculated using the correlations of Chen [5], Nusselt [6] and Carpenter-Colburn [7]. In the calculations, the maximum of these values is used, which has to exceed the value of 20 W/(m²K).

The condensation process in horizontal tubes is much more complicated than in vertical tubes. Over the tube length the flow regimes (e.g. spray, plug, slug, bubble and stratified flow) are changing (see right side of Fig. 3). For the calculation of HTC it is necessary to identify the flow regimes in the concerning cross section area. For the improved description of condensation the model KONWAR (Kondensation in waagerechten Rohren) [8] uses the flow map of TANDON [9]. Here the dimensionless steam velocity of Wallis j_D^* is plotted versus the ratio of the condensate and void fraction $(1-\varepsilon)/\varepsilon$. According to Palen [10] a transition regime between annular and stratified flow has to be considered in the flow map. The HTC are calculated by the correlations of Soliman (spray flow) [11], Nusselt (laminar annular flow) [6], Kosky and Staub (turbulent annular flow) [12], Rufer and Kezios (stratified flow) [13] and Breber (bubble, slug and plug flow) [14].

6. Computational results and comparison with the experimental data

The measured values in the emergency condenser system are the mass flow, the temperature at the outlet, the pressure losses over the in- and outlet headers and the capacity of the emergency condenser. These values are compared with the computational data (characterized by the abbreviation ATH) in Table 2. The scattering of the measured values should be low per definition. For steady state these scatterings are documented in Table 2, too.

6.1 Post test calculations

In Tab. 2 an excellent agreement for the mass flows, the temperatures in the outlet line and the capacities could be obtained. Additionally in Fig. 4 the bundle capacity is plotted versus water level for the primary side pressures of 1, 3 and 7 MPa. The comparison of the measured and the calculated temperatures shows good agreement in cases of high and medium pressures, and an acceptable agreement in cases of low pressure. Due to the effectiveness of condensa-

tion is much higher than the effectiveness of convective heat transfer the sub-cooling of the condensate has a negligible influence on the emergency condenser capacity. Because of missing instrumentation inside the tubes a deeper analysis of the condensation phenomena is not possible.

ATHLET MOD1.1 - Cycle C
Original: Vertical Tube

ATHLET MOD1.1 - Cycle C + KONWAR
Improvement for Condensation in Horizontal Tubes
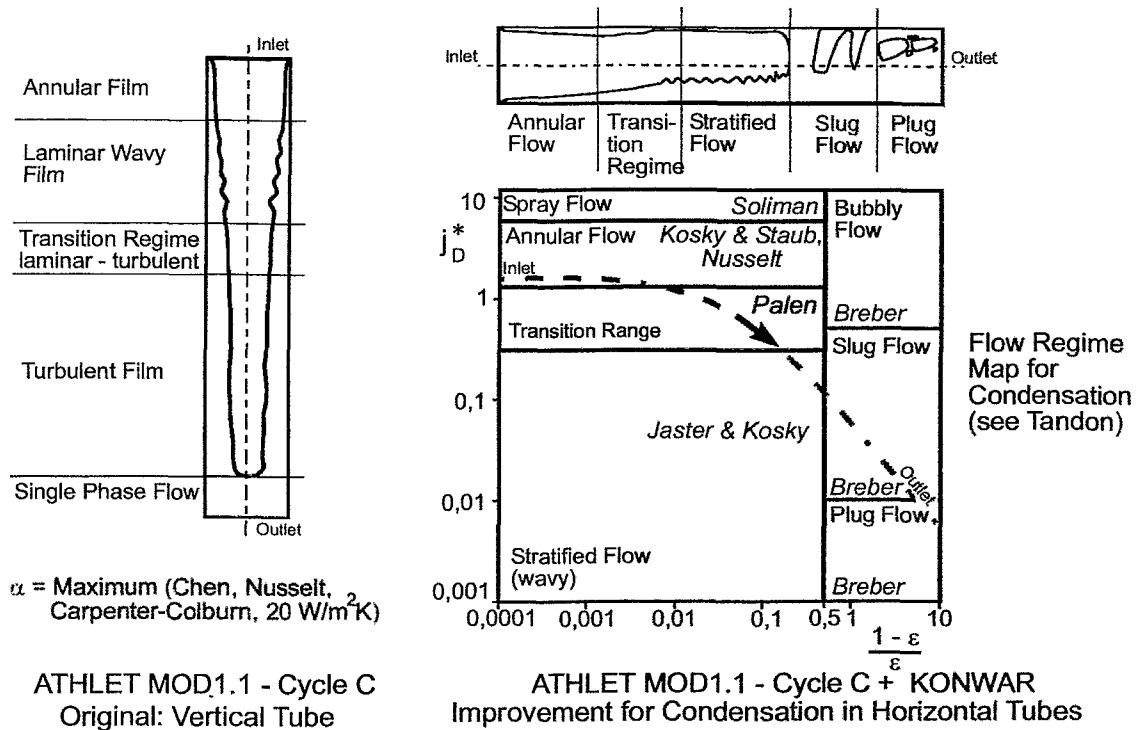
Fig. 3: Calculation of heat transfer coefficients for condensation with the original and with the KONWAR version of ATHLET [8].

6.2 Blind calculation

In Table 3 the results of the blind calculation are compared with the experimental data. The initial and boundary conditions are given in Table 1. Again, the calculation shows a good agreement for all considered values. The deviations are of the same magnitude as the scatterings of the measurements. From Table 3 it can be seen that the fluctuations of the capacities range up to 0.1 MW, which is nearly 15% of the measured value. Moreover, there were problems with the water level for the second balance, which is used for the determination of the inventory in the condenser. Therefore, only the time period between 100 and 600 seconds is taken into account for the comparison.

Table 2: Comparison of experimental and computational NOKO data.

Test	Mass Flow [kg/s]		Outlet Line Temperature [°C]		Capacity [MW]		Pressure Drop [kPa]	
	measured	ATH	measured	ATH	measured	ATH	measured	ATH
EU1-3	0.36 - 0.46	0.57	118 - 130	170	0.73 - 1.05	1.17	1.75 -1.8	2.7
EU1-4	0.44 - 0.57	0.61	156 - 161	178	0.88 - 1.21	1.19	2.8 -3.1	3.1
EU3-2	0.66 - 0.72	0.66	141 - 148	157	1.46 - 1.64	1.38	1.5 - 1.8	0.7
EU3-3	0.98 - 1.04	1.02	185 - 192	203	1.56 - 2.20	1.99	3.2 - 3.6	2.5
EU3-4	1.14 - 1.21	1.21	224 - 228	229	1.64 - 2.30	2.21	4.5 - 4.8	3.9
EU4-1	0.63 - 0.68	0.59	151 - 155	178	1.20 - 1.47	1.18	-6.8 - -6.2	-6.5
EU5-2	0.73 - 0.83	0.75	141 - 146	164	1.60 - 1.82	1.55	-9.5 - -9.0	-1.03
EU5-4	1.57 - 1.67	1.56	227 - 235	245	2.75 - 2.92	2.68	-2.4 - -1.8	-3.1
EU5-6	2.05 - 2.16	2.11	277 - 282	276	2.72 - 3.30	3.29	5.0 - 6.0	3.1
EU6-2	1.16 - 1.26	1.24	198 - 203	219	2.21 - 2.42	2.27	-5.5 - -5.8	-5.7

7. Conclusions and outlook

The blind NOKO calculation - as well as the other NOKO post test calculations - prove, that the modified version of ATHLET (ATHLET with the extension KON-WAR) is capable of predicting the global parameters in the range of the scatterings of the measured values. In the next EU complementary action it is planned to perform additional post test calculations of the single tube experiments, experiments with steam/non-condensable mixtures and pre test calculations of a second optimized emergency condenser test bundle. The optimization proposal is to increase the heat transfer, which allows to decrease the number of heat exchanger tubes and the emergency condenser dimensions. This is desirable because it reduces the surface of the pressurized BWR circuit and the probability of leakages, which is a safety relevant task.
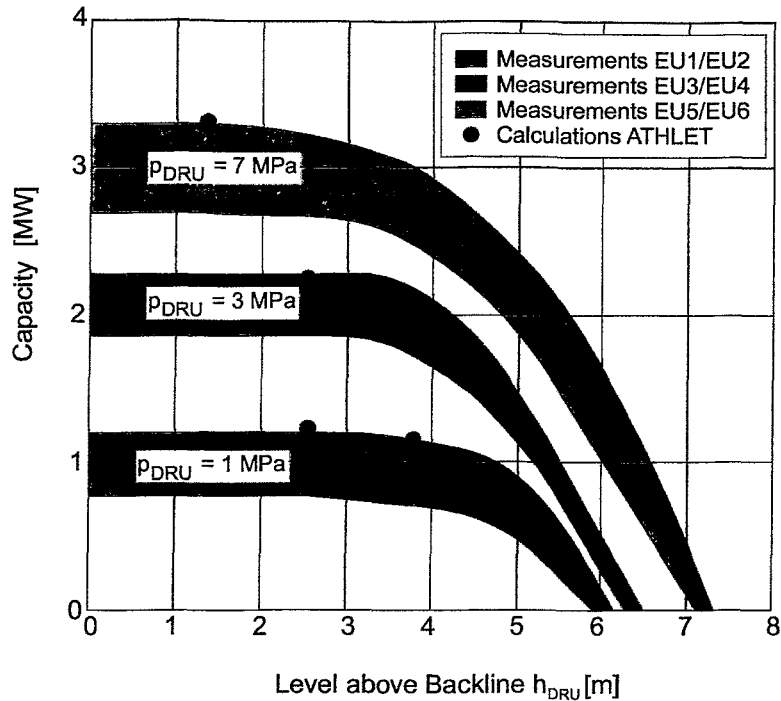
Fig. 4: Comparison of the experimental and computational values of the emergency condenser capacity.

Table 3: Comparison of experimental and computational data for the blind test.

Blind Calculation	Mass Flow [kg/s]	Outlet Temperature [°C]	Pressure difference [kPa]	Capacity [MW]
Experiment	0.31	175.5	0.98	0.55 - 0.65
Calculation	0.31	177	0.76	0.61

References

[1]   E. F. Hicken and W. von Lensa (1996), Innovative BWR R&D Cluster for Innovative Passive Safety Systems, *Proceedings of the Jahrestagung Kerntechnik*, (pp. 298-301), Mannheim, Inforum Verlag

[2]   H. Jaegers (1997), *European BWR R&D Cluster for Innovative Passive Safety Systems - WP2: NOKO Experiments for Code Calculations and Blind Calculation*, Jülich, INNO-IPPS(907)-D-0

[3]   A. Schaffrath (1997), Experimentelle und analytische Untersuchungen zur Wirksamkeit des Notkondensators des SWR600/1000, *Report of the Forschungszentrum Jülich*, Jül. 3326

[4]   A. Schaffrath, H.-M. Prasser, E. F. Hicken and H. Jaegers (1997), Test and Calculation of the Emergency Condenser of the SWR1000, *Proceedings of the Post SMiRT 14 International Seminar 18 "Passive Safety Systems in Nuclear Installations"*, Pisa

[5]   J. C. Chen (1966), Correlation for Boiling Heat Transfer to Satured Fluids in Convective Flow, *1-EC Process Design and Developement*, 5, 322

[6]   W. Nusselt (1916), Oberflächenkondensation des Wasserdampfes, *Zeitschrift des Vereins Deutscher Ingenieure*, 27, 541 and 569

[7]   E. F. Carpenter and A. P. Colburn (1951), *The Effect of Vapor Velocity on Condensation Inside Tubes*, General Discussion of Heat Transfer, Inst. Mech. Eng.

[8]   A. Schaffrath (1997), KONWAR - eine Erweiterung von ATHLET zur Berechnung der Kondensation in waagerechten Rohren, *Report of the Forschungszentrum Jülich*, Jül. 3343

[9]   T. N. Tandon, H. K. Varma and C. P. Gupta (1982), A New Flow Regimes Map for Condensation Inside horizontal Tubes, *Journal of Heat Transfer* 104, 763

[10]   J. W. Palen, G. Breber and J. Taborek (1979), Prediction of flow Regimes in Horizontal Tube-side Condensation, *Heat Transfer Eng.*, 1, 47-57

[11]   H. M. Soliman (1986), The Mist - Annular Transition During Condensation and its Influence on the Heat Transfer Mechanism, *Int. J. Multiphase Flow*, 12, 277

[12]   P. G. Kosky and W. F. Staub (1971), Local Condensing Heat Transfer Coefficients in the Annular Flow Regime, *AIChE Journal*, 17, 1037

[13]   C. E. Rufer and S. P Kezios (1966), Analysis of Two-Phase, One-Component Stratified Flow with Condensation, *Trans. Am. Soc. Mech. Eng. Journal Heat Transfer*, 88, 265

[14]   G. Breber, J. W. Palen and J. Taborek (1979), Prediction of horizontal tube-wise condensation of pure components using flow regime criteria, *Advances in Enhanced Heat Transfer ASME, Proceedings of the 18th National Heat Transfer Conference*, (pp. 1-8), San Diego California

CALCULATION OF AN ACCIDENT WITH DELAYED SCRAM AT NPP GREIFSWALD USING THE COUPLED CODE DYN3D/ATHLET

S. Kliem

1. Introduction

Complex computer codes modeling the whole reactor system including 3D neutron kinetics in combination with advanced thermohydraulic plant models become more and more important for the safety assessment of nuclear reactors. Such codes only are capable of estimating the feedback effects in a realistic way, for instance in reactivity initiated accidents with strongly asymmetric neutron flux distribution in the core caused by a perturbation in one of the primary circuit loops. At Forschungszentrum Rossendorf, Institut für Sicherheitsforschung, both the hexagonal and the Cartesian version of the 3-D neutron kinetic code DYN3D were coupled with the advanced thermalhydraulic system code ATHLET. The different ways of coupling and several plausibility test calculations for the hexagonal version including comparisons with the ATHLET point kinetic model are described in [1].

Transients or experiments with both neutron kinetic and thermalhydraulic data are needed for the validation of such coupled codes like DYN3D/ATHLET. First of all measured results from nuclear power plant (NPP) transients should be used, because the experimental thermalhydraulic facilities do not offer the possibility to model space-dependent neutron kinetic effects and research reactors with reliably measured 3D neutron kinetic data do not allow to study thermalhydraulic feedback effects.

In this paper, an accident with delayed scram which occurred in 1989 at the NPP Greifswald is analyzed. Calculations of this accident were carried out with the goal to validate the coupled code DYN3D/ATHLET.

2. Background and Scenario

The unit 5 of the NPP Greifswald (VVER-440) was in the commissioning phase. According to the commissioning instructions several commissioning experiments were conducted at the reactor. On November 24th, 1989 the power limitation device (ROM) was tested. The ROM response to a core mass flow rate perturbation was tested. The reactor operated at a
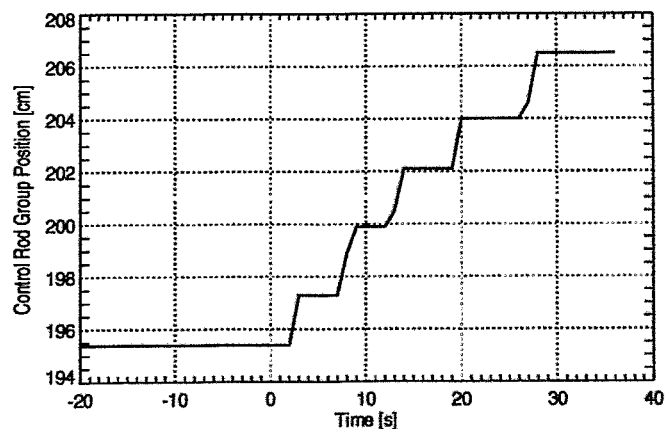

Fig. 1: Measured position of control rod group K6

15

power level of about 50%. All main coolant pumps (MCP) were running. The power control system (ARM) worked in the automatic regime: 'keep the neutron power constant'. The core mass flow rate was reduced by switching-off the MCP's in the loops 2, 4 and 6 with stabilization times between the actions. The power was stabilized by ARM very well. At the end of the test the reactor power was 52.7%. The test was successfully finished.

Later on, due to a false steamgenerator level limit one more MCP was switched-off. Switching-off the fourth from six MCP should activate the reactor scram. This scram was not initiated because the corresponding signal was not transmitted to the reactor protection system. The power control system which had been tested before continued to stabilize the power. The expected power decrease caused by the further reduction of the core mass flow rate was compensated by withdrawing the control rod group K6. The group K6 was activated five times (Fig. 1). The reactor scram was initiated by the operator 36s after the switch-off of the MCP [2].

3. Calculation of the Accident

A part of the recorded measured data has a low time resolution. Further, the cold leg temperatures show an asymmetry after the coastdown of the third MCP (at the beginning of the accident, Fig. 2). All six reactor loops should be represented in the calculation including non-homogeneous coolant mixing in the upper and in the lower plenum. This cannot be accomplished, because coolant mixing models considering loops with forward and loops with backward flow at the same time do not exist.

These two shortcomings make the data less suitable for code validation. Despite these disadvantages calculations of the accident were carried out, because the reported abnormal event offers the possibility to make calculations, where interaction between the thermohydraulics and the neutron kinetics can be compared with reported data. Therefore, the calculation of this accident will contribute to the validation of the coupled code DYN3D/ATHLET significantly.

Fig. 2: Cold leg arrangement on the reactor pressure vessel with coolant flow direction and temperature in the initial state

According to the limitation mentioned above the six loops were modeled by a 3-fold (passive), a 2-fold (active) and a single loop (with the MCP to be switched-off at the beginning of the transient). The selected representation suppresses the asymmetry of the cold leg temperatures revealed in the evaluation of the data. The
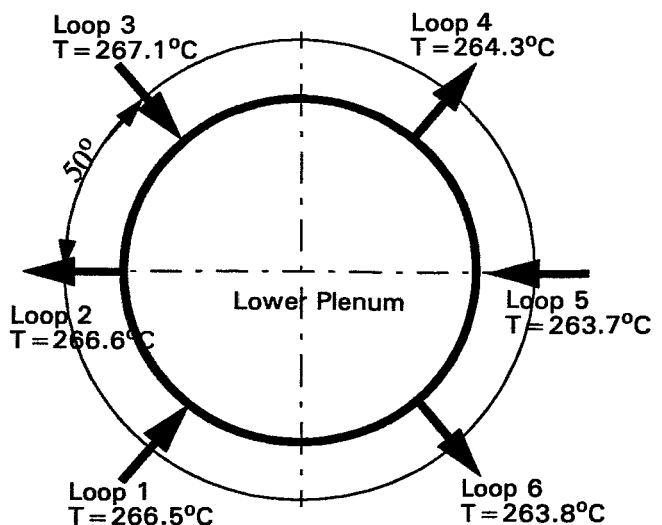
data measured in the loops represented by one loop in the calculation can be averaged to obtain data that can be compared with theory. It should be noticed that the possible deviations can partly be caused by this averaging.

The accident was modeled based on the following scenario:

t = 0s   Switching-off the fourth MCP

t = 2 - 36s   Moving of the control rod group K6 according to the measured data (Fig. 1)

t = 36s   Activation of the scram

t = 36.5s   Insertion of all control rods

t = 49s   The rods reach the lower core boundary

Pressure drop curve over the switched-off MCP

The pressure difference over the switched-off MCP is shown in Fig. 3. The calculated pressure difference is very close to the measured one within the first ten seconds. The new quasi-stationary pressure drop after the full coastdown of the MCP is remarkably smaller than the measured value. This effect corresponds to the deviations between the measured and calculated initial pressure drops over the MCP's in the passive loops.
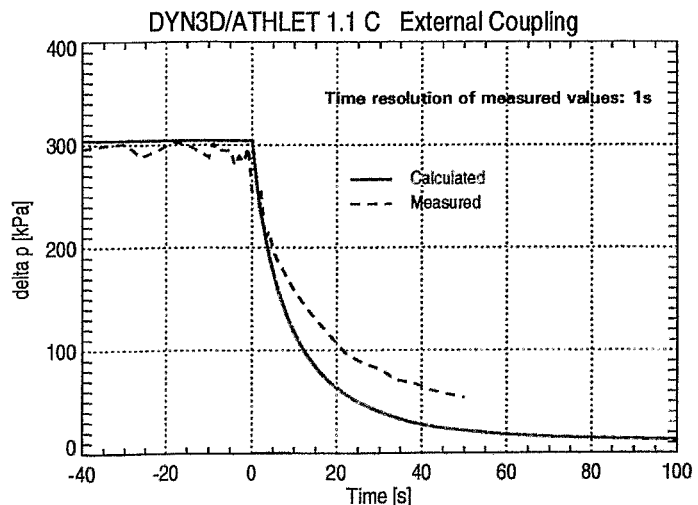
Fig. 3: Pressure drop over the switched-off MCP

Temperatures in the coasting down loop

Switching-off of the MCP-3 causes a coolant mass flow decrease through the corresponding loop and through the core. The decreasing core mass flow causes an increase of the hot leg temperature (not only in the loop with the switched-off MCP, but also in the remaining active loops). The reduced hot leg mass flow leads to an overcooling in the SG and decreasing cold leg temperature. After the reactor scram and reduction of power to the decay heat level the hot leg temperature decreases. As shown in Fig. 4, the calculated temperature in both legs is very close to the measured data until t = 80s after the MCP switch-off. Then the agreement between calculation and measurement is worse. The deviation may be caused by difficulties in predicting the phenomenon of coolant flow reversal after pump stop.

17

The flow reversal is indicated by the minimum of the cold leg temperature. This temperature minimum is obtained at t = 110s in the calculation while it is around t = 51-91s in the measurement. That means, in the calculation the flow reversal is predicted by about 30s to late. This observed time delay is also the reason for the remarkable difference in the second maximum of the hot leg temperature between measurement and calculation. After the reactor scram, the reactor outlet temperature and the hot leg temperature of the working loops (with the corresponding time delay) decrease very fast. For this reason the temperature difference between the entrance into the hot leg (where the measuring point is located) and the SG inlet collector is greater than it would be in a later phase of the transient. The flow reversal in the transient occurred closer to the reactor scram. Therefore, the hot water coming back from the SG inlet collector after this flow reversal caused a remarkable maximum. 30 seconds later, when the flow reversal occurs in the calculation, the temperature difference between the hot leg entrance and the SG inlet collector is smaller caused by the smaller time gradient of the reactor outlet temperature. Therefore, the second maximum of the hot leg temperature in the calculation is smaller, too.
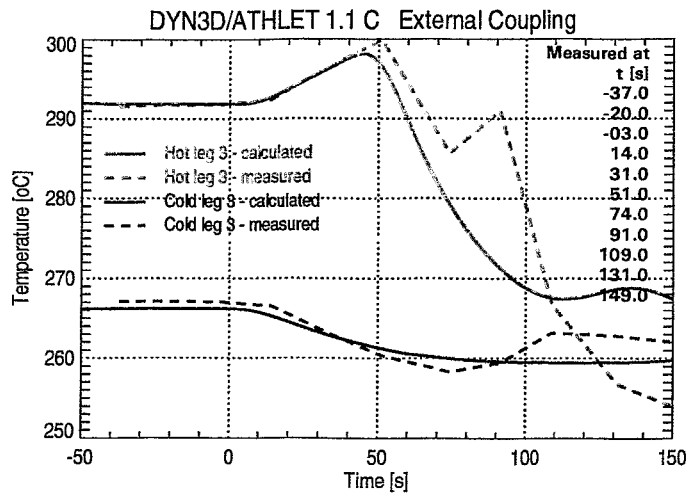
Fig. 4: Temperatures in the loop with the switched-off MCP

Nuclear Power

In Fig. 5 the nuclear power until the reactor scram is shown. As mentioned earlier, the control rod group was moved in the calculation according to the measured values. The changes of the power due to the five control rod displacements can be seen clearly. The power decrease between these activations caused by the moderator temperature feedback effect can be seen in the calculation as well as in the measured values. When MCP coastdown starts, a small, but continu-
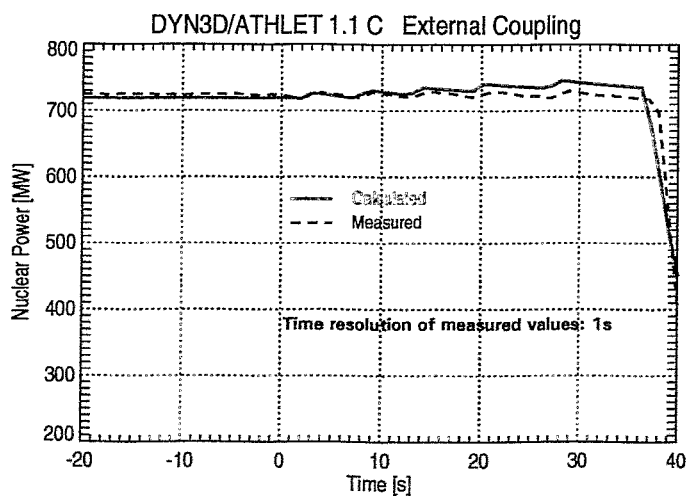
Fig. 5: Nuclear power (prescribed control rod group motion)

18

ous global power increase is observed in the calculation during the whole transient while the measured power is remaining almost constant. In the following section a possible explanation will be given for the difference between the measured and calculated power.

4. Sensitivity Study

While in the basic calculation the control rod positions were changed according to the measured values, now the ARM was modeled according to the behaviour of the real plant to carry out a variation calculation. The setpoints for the activation of the ARM were adopted to the real plant values. As it can be seen in Fig. 6 the control rod group was activated only four times in this calculation, contrary to five registered during the transient. The reason for this discrepancy could be either an

Fig. 6: Nuclear power (with ARM working in the automatic regime)

overpredicted control rod efficiency or an underpredicted feedback due to the moderator temperature/density effect. The time intervals between the activation points of the control rod group are determined by the moderator feedback effect. The extension of these time intervals supports the second hypothesis. Further, it should be realized that the isothermal moderator temperature coefficient (IMTC) describing the moderator feedback effect is very small, only a few pcm, at the beginning of the fuel cycle. Then, small uncertainties in the group data library can lead to great relative deviations in the results. Post-test calculations of critical start up experiments at NPP Dukovany-4 (VVER-440) showed deviations between the measured and calculated IMTC [3]. Changes in the library were necessary to fit the data.

Therefore, a series of calculations were carried out where the IMTC was varied. The IMTC without any corrections was determined with

$$\alpha_{IMTC} = -5.47 \text{pcm/K}.$$

Fig. 6 also shows the nuclear power with a corrected IMTC. The used value is

$$\alpha_{IMTCcor} = -8.54 \text{pcm/K}.$$

The calculation with this value shows a very good agreement of the nuclear power with the measured curve. The integral displacement of the control rod group agrees with the measured one, too. It is important to note, that the correction of the IMTC did not exceed the recommendations on accuracy of the IMTC as presented in [4].

19

References

[1] U. Grundmann, D. Lucas, S. Mittag und U. Rohde (1995), *Weiterentwicklung und Verifikation eines dreidimensionalen Kernmodells für Reaktoren vom Typ WWER und seine Ankopplung an den Störfallcode ATHLET*, Rossendorf, Report FZR-84

[2] H. Rebohm, B. Mängel (1990), *Der ATWS-Störfall vom 24.11.1989 am Block 5 KKW Nord III - Zeitablauf und Meßdatensammlung,* KAB Berlin, Interner Bericht

[3] I. Tinka (1993), "Critical Start-up Parameters of the WWER-440 core", in *Proceedings of the third Symposium of AER* (pp. 105 - 116), Budapest, KFKI

[4] J. Svarny (1993), "Information on Working Group A Activities", in *Proceedings of the third Symposium of AER* (pp. 9- 13), Budapest, KFKI

POST-TEST ANALYSIS OF THE EXPERIMENT 5.2C - TOTAL LOSS OF FEED WATER AT THE BETHSY TEST FACILITY

E. Krepper, F. Schäfer

1. Introduction

In the framework of the external validation of the thermohydraulic code ATHLET, which was developed by the „Gesellschaft für Reaktorsicherheit", post test analyses of tests at the integral test facility BETHSY were performed in the Research Center Rossendorf. The presented report refers to the results of the BETHSY test 5.2c, during which several accident management procedures were investigated.

The BETHSY-test facility is a 1:100 scaled thermohydraulic model of a 900 MW(el) pressurized water reactor (FRAMATOME). The test facility is mainly designed to investigate various accident scenarios and to provide an experimental data base for code validation and for the verification of accident management measures. In the test facilitiy, the three identical loops of the primary circuit are modelled with a volume scaling ratio of 1:100 with retaining the original heights, [1],[2]. Each primary loop is equipped with a vertical steamgenerator. The

Fig 1: Sketch of the BETHSY Test Facility (single loop and reactor model)

maximum pressure on the primary side is 17.2 MPa and on the secondary 8.0 MPa. The BETHSY experiment 5.2c investigates accident management procedures in case of a total loss of feedwater at the steam generator secondary side (T. Chataing and P. Clement [3]). In such an accident the emergency cooling of the reactor core by primary bleed and feed, the behaviour of the steam generators in case of dry out, and the long time behaviour of the test facility are of particular
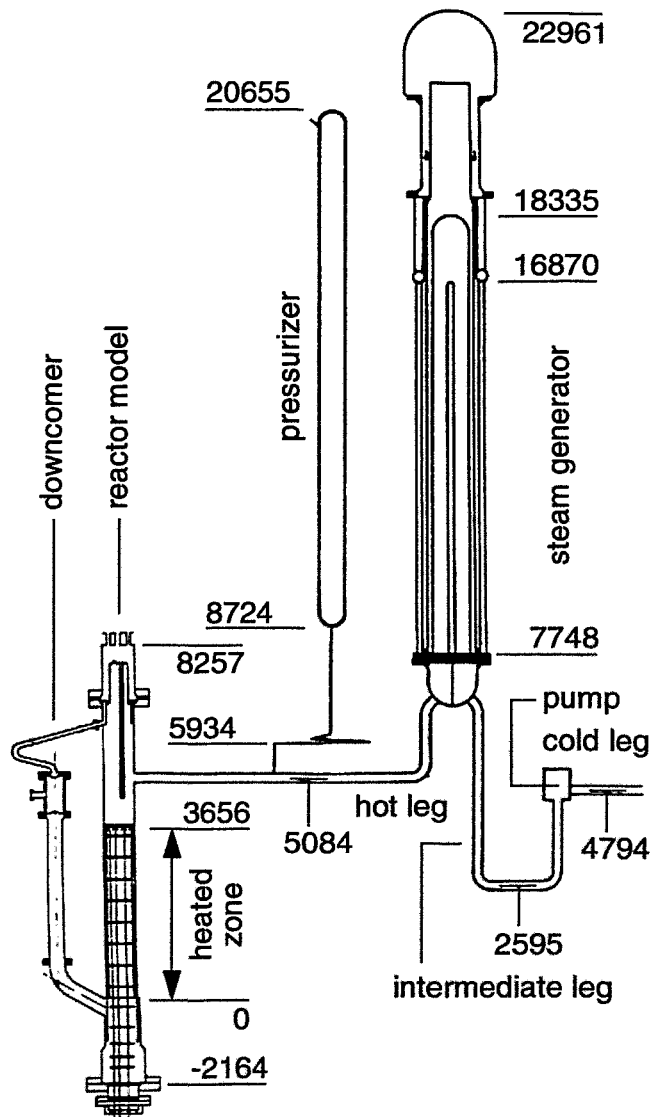
interest. During the experiment, the high pressure injection system (HPSI), the hydroaccumulators and the low pressure injection system (LPSI) were available. These emergency cooling systems feed into the cold legs of the primary circuit. Fig. 1 illustrates the structure of the primary circuit with the reactor model, the hot and cold leg, the pressurizer and the steam generator. The indicated levels are related to the lower part of the heater rods in the reactor core.

2. Thermohydraulic model

The presented post-test calculations were performed with the thermohydraulic computer code ATHLET Mod 1.1 Cycle D. The input deck models the three loops of the test facility in detail and consists of 87 thermofluid objects with a total amount of 504 control volumes. In all control volumes the five-equation model with separate conservation equations for liquid and vapour mass and energy and a mixture momentum equation was applied. The one-dimensional critical discharge model (CDR1D) was used to model the depressurization of the primary circuit via the pressurizer relief valve. For the calculation of the mass flows at the steam generator secondary side the homogeneous isentropic equilibrium model (Moody-model) was applied. At the BETHSY test facility the maximal core power is limited to 10 % of the nominal power. Therefore, the experiment starts with already reduced mass inventory at the secondary side. The steam generator levels were adjusted in a steady state calculation from the nominal value of 12.7 m to the initial value of 5.76 m for the transient.

Table 1 gives a comparison of measured and calculated times of the main events in the transient. In the ATHLET calculation, the various hardware actions are modelled with special GCSM signals (General Control and Simulation Module) depending on the system pressure, the filling levels and the problem time. With the initiation of the transient at $t = 0$ s the reactor power was reduced and the secondary pressure was controlled at 7.03 MPa (turbine bypass mode). The safety injection (SI) signal is triggered when two steam generator levels drop below 3 m. Simultaneously, the pump coast down and the HPSI were initiated. The feed and spill mode starts when the primary pressure reaches the setpoint of 16.3 MPa. In this mode the primary pressure remains constant by a controlled depressurization via the pressurizer relief valve. The steam lines at the steam generator secondary side were isolated 300 s after the SI-signal and the secondary pressure was controlled at a constant value of 7.17 MPa. 1800 s after the SI-signal the feed and bleed mode was initiated by fully opening the pressurizer relief valve. The injection from the hydroaccumulators was started at a primary pressure of 4.2 MPa and the injection was stopped at 1.5 MPa. At the end of the transient the LPSI starts at a setpoint pressure of 1.0 MPa. For the calculation of the injected mass flows the pressure dependence of the mass flows of the HPSI and LPSI was considered.

3. Results of the ATHLET calculation

The first stage of the transient is mainly characterized by the processes at the steam generator secondary side. Due to the total loss of feedwater the secondary coolant will be vaporized and the steam generators levels decrease very fast

(Fig. 3). At t = 752 s (788 s in the experiment) the steam generators levels drop below the setpoint of the SI-signal (3 m). At the same time the pump coast down and the HPSI are initiated (Fig 2 and Fig. 6). The rapid decrease of the steamgenerator levels leads to a reduced heat transfer from the primary to the secondary side and the primary pressure increases up to the setpoint of 16.3 MPa (Fig. 2). In this way the primary pressure regulation via the pressurizer relief valve is initiated at t = 956 s (1033 s in the experiment).

Table 1: Measured and calculated course of the transient

Phenomena	Experiment	Calculation
Start of Experiment:		
Total loss of feedwater	0 s	0 s
Reactor SCRAM	0 s	0 s
Turbine bypass mode (7.03 MPa controled)	0 s	0 s
2 Steam generator levels < 3m:		
SI Signal	788 s	752 s
Start of pump coast down	793 s	760 s
Start of HPSI	799 s	760 s
Primary pressure = 16.3 MPa:		
Regulation of primary pressure	1033 s	956 s
300 s after Safety Injection Signal:		
Isolation of SG steam lines and regulation of secondary pressure (7.17 MPa)	1095 s	1088 s
1800 s after Safety Injection Signal:		
Full opening of pressurizer relief valve	2593 s	2588 s
Primary pressure = 4.2 MPa:		
Start of accumulator injection	4450 s	4393 s
Primary pressure = 1.5 MPa:		
End of accumulator injection	8278 s	8735 s
Primary pressure = 1.0 MPa:		
Start of LPSI	8815 s	8975 s
End of transient	10025 s	10050 s

The depressurization of the primary system starts 1800 s after the safety injection signal by fully opening the pressurizer relief valve. Immediately after the full opening, the primary pressure decreases very fast from 16.3 MPa to approximately
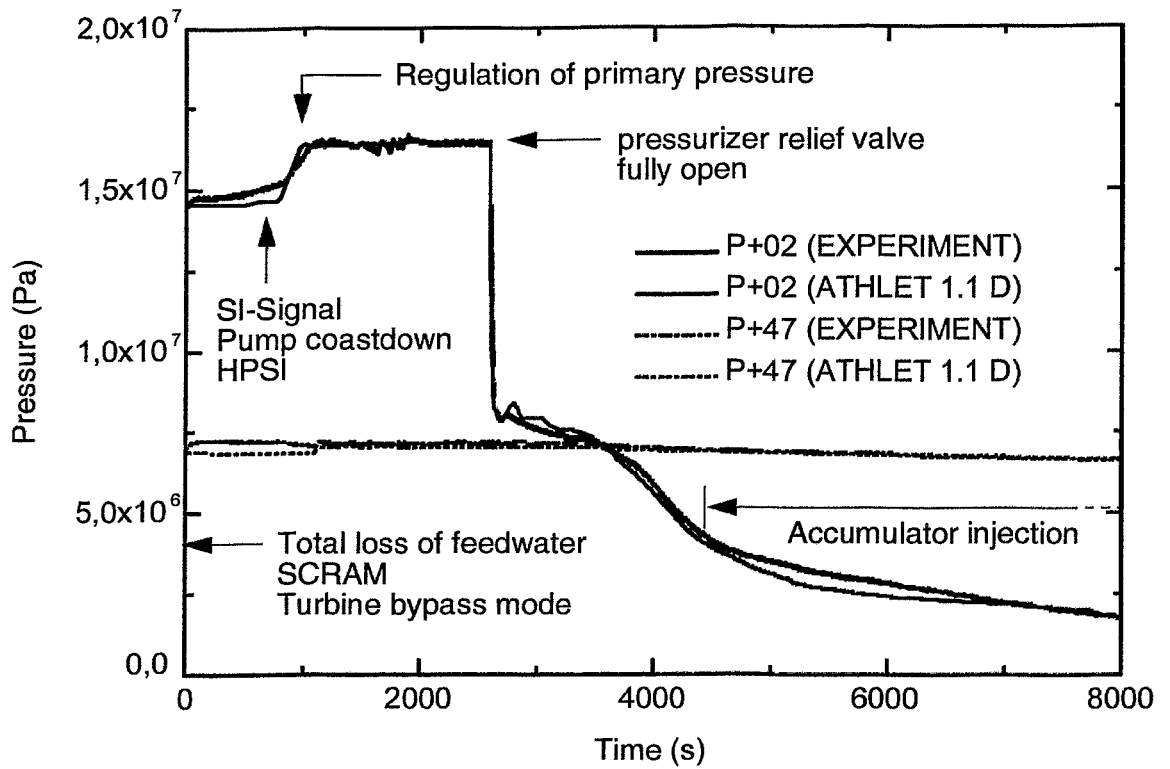
Fig. 2: Primary pressure (P+02) and secondary pressure (P+47)
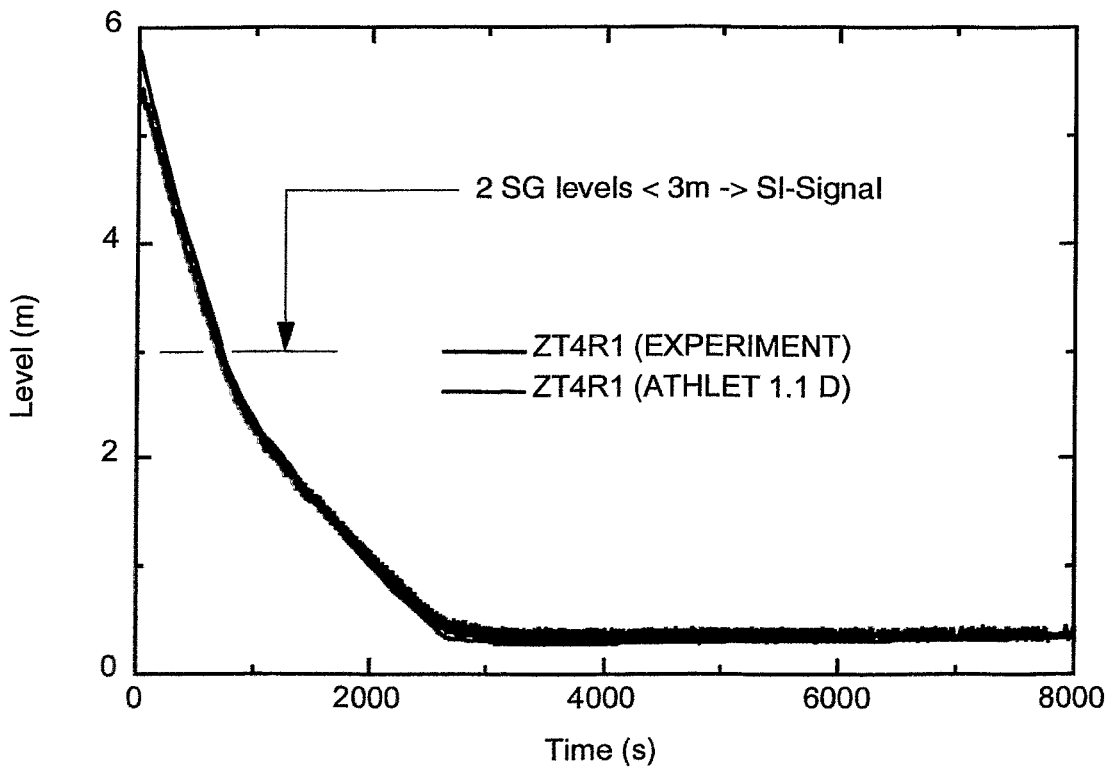

Fig. 3: Comparison of measured and calculated level in steam generator 1

24
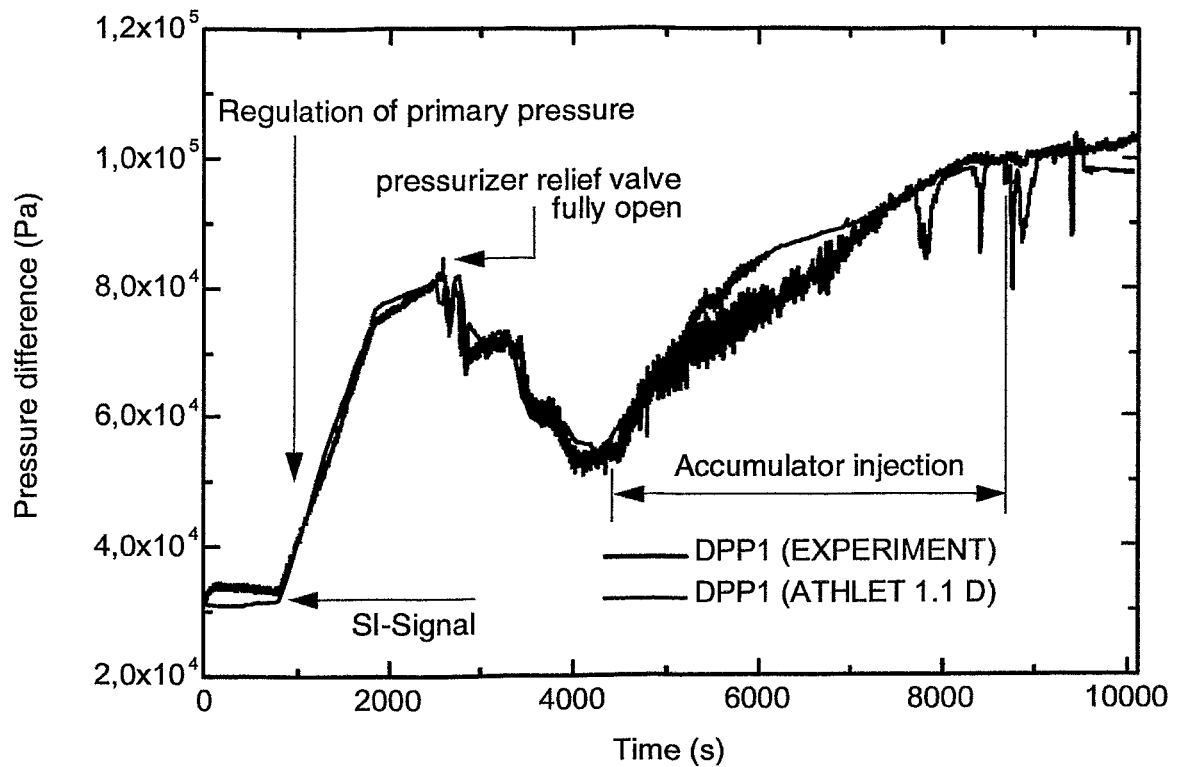
Fig. 4: Pressure difference in the pressurizer in experiment and calculation
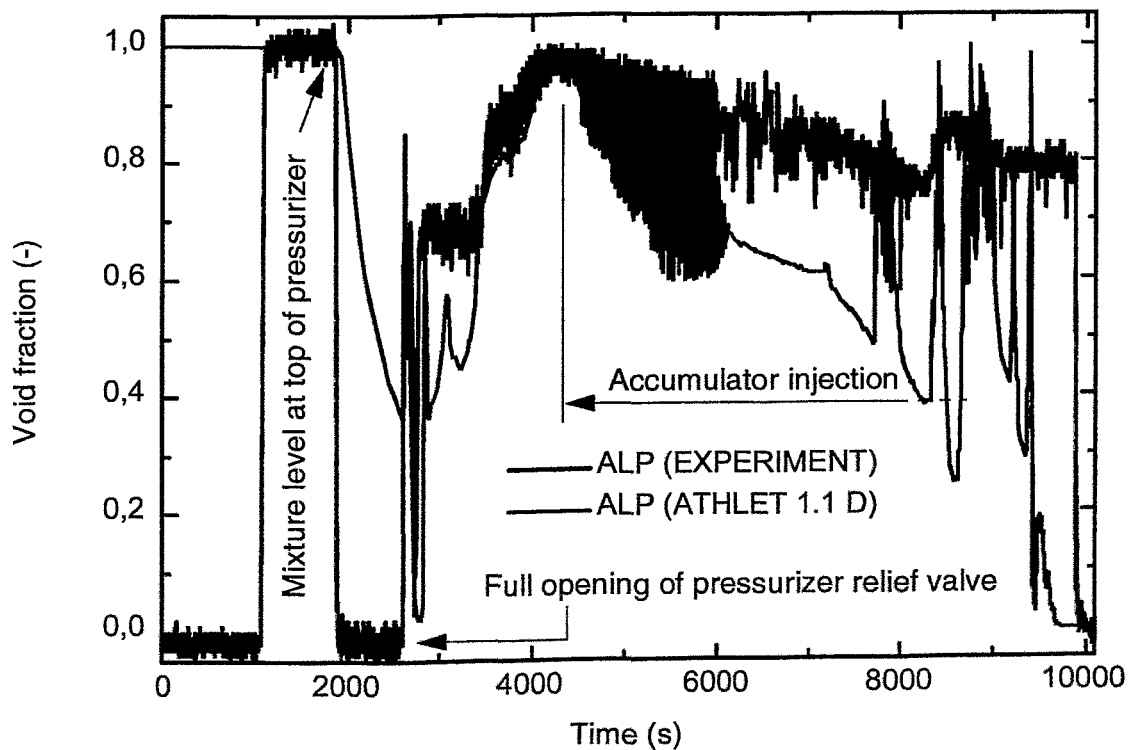
Fig. 5: Void fraction upstream from the pressurizer relief valve

8 MPa. Due to this pressure decrease the mass flow from the HPSI is increased by a factor of about 2.7 (Fig. 6). At the same time vaporization can be observed in the hot and also in the cold leg. Up to about 2590 s the pressurizer is continuously filled with water. When depressurization starts the level decreases again (Fig. 4). The mass flow and void fraction in the pressurizer vent line and the general behaviour of the pressurizer level are calculated very well by the ATHLET code. Most of the hardware actions in the calculation are initiated by the primary pressure and the problem time. Due to the good agreement between the measured and calculated pressure the general course of the calculated transient shows no significant deviations. Approximately 2000 s after primary depressurization the
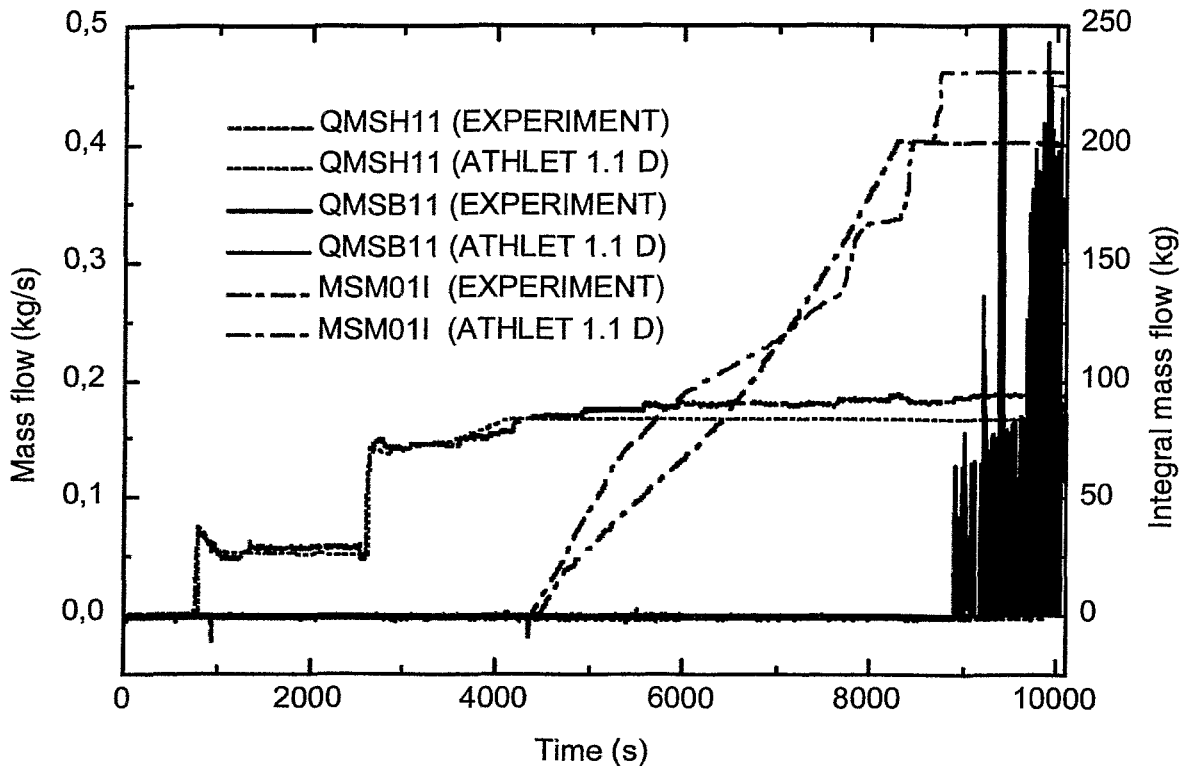
Fig. 6: Integral mass injected from the accumulator 1 (MSM01I) and mass flows from HPSI (QMSH11) and LPSI (QMSB11); injection into loop 1

mass flow and void fraction in the pressurizer vent line oscillate very strongly. These oscillations are a consequence of a feedback between the mass flow in the vent line and the pressure gradient in the pressurizer. The nature of these oscillations was investigated by D. Lucas and H.-M. Prasser [4]. The period of the oscillations is determined by the length of the vent line. This effect is also calculated very well by ATHLET (Fig 5).

The primary pressure reaches the setpoint for the accumulator injection at $t = 4393$ s (4450 s in the experiment). The calculated mass flow is at first overestimated. Therefore, the calculated primary pressure deviates from the experiment (Fig. 2). In the further course of the transient the injected mass flow decreases slightly but the integral injected mass is higher than in the experiment (Fig. 6). The

hydroaccumulator injection leads to an increase in the reactor and pressurizer coolant levels from 4500 s up to 8735 s (8278 s in the experiment). The calculated primary pressure at the end of the accumulator injection is a little higher than in the experiment. For this reason the start of the LPSI is calculated with a 160 s delay. In contrast to the experiment the calculated mass flow shows unrealisticly strong oscillations, which result in a significant extension of CPU time.

The evaluation of the calculated results shows that all main phenomena can be calculated in agreement with the experiment. Resulting from various calculations it should be noticed that the quality of the results strongly depends on the heat losses of the facility, which were partly compensated by the trace heating. This trace heating was changed several times in the experiment to compensate the changing heat losses. The exact modelling of the resulting heat losses strongly influences the course of the whole transient. In this test, the unsufficient modelling of the resulting heat losses may be the reason for deviations of the calculated transient from the observed transient.

References

[1]   P. Bazin (1988), *BETHSY: Data Base*, Departement des Reacteurs a Eau, Service d' Etudes Thermohydrauliques, Centre d' Etudes Nucleaires de Grenoble

[2]   E. Ercolani, Ph. Gully (1995), *BETHSY - Measurement System, Update of the initial Report and of its Addendum*, Departement de Thermohydraulique et de Physique Service de Thermohydraulique des Reacteurs

[3]   T. Chataing, P. Clement (1990), *BETHSY Test 5.2c.2, Total Loss of Feedwater, Data Report*, Departement de Thermohydraulique et de Physique Service d' Etudes Thermohydrauliques, Centre d' Etudes Nucleaires de Grenoble

[4]   D. Lucas, H.-M. Prasser (1997), "Oscillations of the Mass Flow Rate at Pressure Relief Systems", in F.P. Weiß and U. Rindelhardt (Ed.), *Annual Report 1996* (pp. 18-21), Rossendorf, FZR-190

[5]   E. Krepper, F.Schäfer (1998), *Verifikation des ATHLET-Rechenprogramms im Rahmen der externen Verifikationsgruppe ATHLET, BETHSY Test 5.2c Totalverlust des Speisewassers*, Rossendorf, FZR-231

CALCULATIONS TO AN IAHR-BENCHMARK TEST
USING THE CFD-CODE CFX-4

E. Krepper

1. Introduction

The calculation concerns a test, which was defined as a benchmark for 3-D codes by the working group of advanced nuclear reactor types of IAHR (International Association of Hydraulic Research). The test is well documented and detailed measuring results are available [1].

The test aims at the investigation of phenomena, which are important for heat removal at natural circulation conditions in a nuclear reactor. The task for the calculation was the modelling of the forced flow field of a single phase incompressible fluid with consideration of heat transfer and influence of gravity. These phenomena are typical also for other industrial processes. The importance of correct modelling of these phenomena also for other applications is a motivation for performing these calculations.

2. The test

The test arrangement consisted of a flat tank (see Figure 1). The flow field was predominated by 2-D effects. Therefore the test was modelled by a 2-D simulation. The arrangement consisted of a long inlet channel from below, a test volume with a cooled wall section and an outlet channel to the top. The upper wall was sloped. The vertical profiles of the flow field and the temperature distribution in the test volume were measured at four positions (see Figure 2, P1 to P4). Moreover the flow profile in the inlet channel before the entrance into the test volume was measured.

Four tests were documented, which mainly are distinguished by the velocity at the
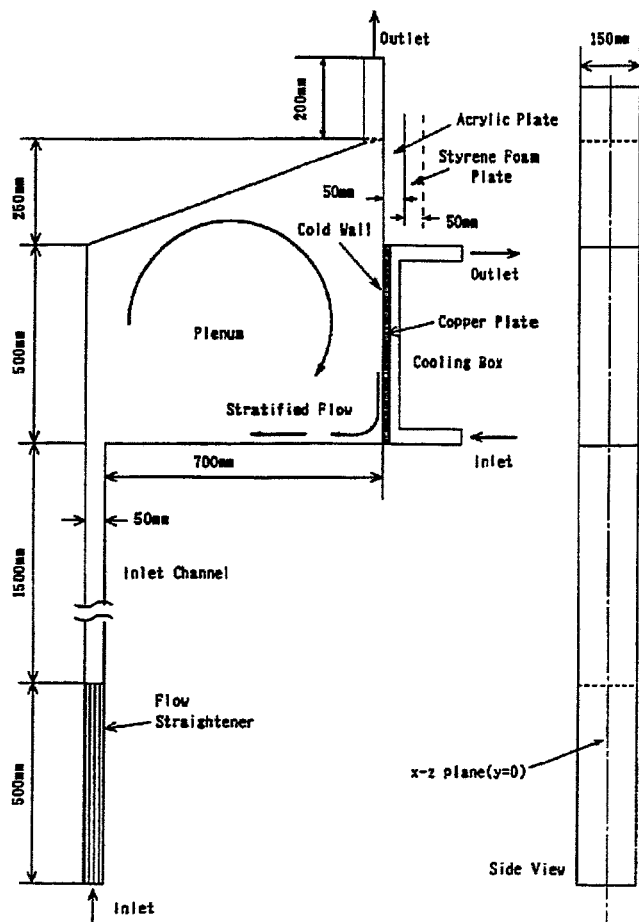
Fig. 1: Test arrangement

28

bottom of the inlet channel (see Table 1). The velocity was varied between $5.0 \cdot 10^{-2}$ m/s and $10.0 \cdot 10^{-2}$ m/s. The inlet temperature ranged about 50 °C. The coolant temperature at the cooling wall was about 15 °C. The corresponding heat flux was given by the authors to be in the region of -2.1 to $2.4 \cdot 10^{+4}$ W/m^2.

3. The CFX-Grid

The test was modelled as a 2-dimensional Cartesian problem. Figure 3 shows the block structure and the co-ordinate system. The boundary conditions are described by an INLET-patch IN, a patch with PRESSURE boundary condition OUT and a wall CLB with defined heat flux. The grid subdivisions were unequally distributed, so that the divisions were finer near the cooled wall and at the walls of the inlet channel.
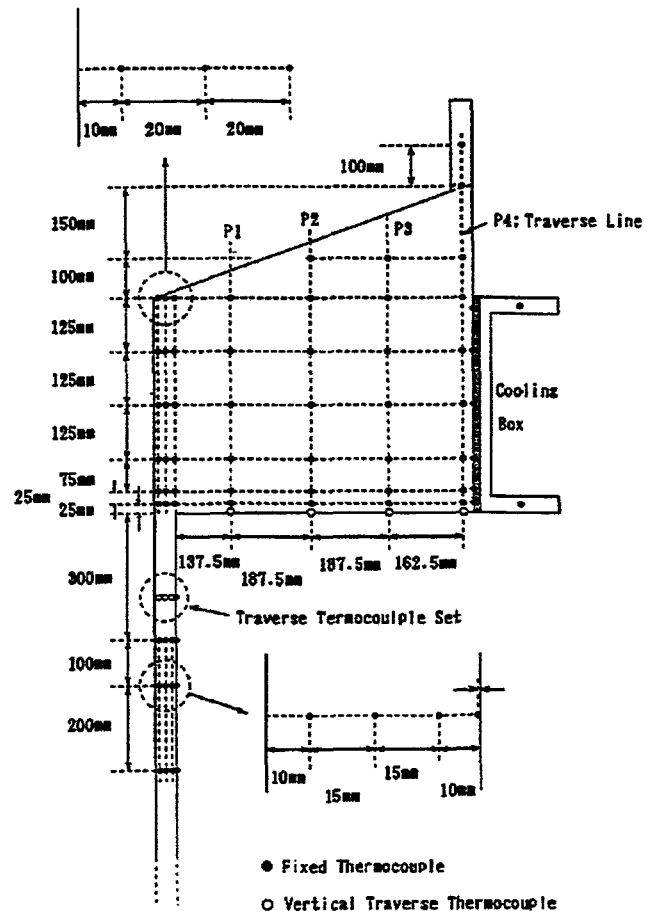
Fig. 2: Measuring system

Tab. 1: Parameters of the reported tests

Test No.		1	2	3	4
Inlet temperature	[°C]	48.9	49.0	49.1	49.1
	[K]	322.05	322.15	322.25	322.25
av. inlet velocity	[m/s]	4.15e-2	5.16e-2	6.34e-2	11.4e-2
Temperature at the cold wall	[°C]	14.8	14.4	14.5	15.4
	[K]	287.95	287.55	287.65	288.55
Heat flux at the cold wall	[W/m^2]	-2.13e+4	-2.24e+4	-2.34e+4	-2.40e+4
Temperature at the bottom of P4	[°C]	37.0	36.7	36.4	38.5
	[K]	310.05	309.85	309.55	311.65

29

4. Results

Different turbulence models were tested. Using the „Standard Reynolds K-Epsilon-Model" the vortex in the centre of the test chamber was overestimated. All presented result plots are related to calculations, which used the „Low Reynolds Number K-Epsilon-Model". The test is a steady state problem. Therefore, the first calculations were performed using the steady state option (see Figures 4 to 6, 9). The example was calculated using 4000 iteration steps. The figures show, that the modelling of a transient problem with constant boundary conditions yields much better results. Using a fixed time step of 0.5 sec and 50 iterations per step, the calculation after 200 steps results in excellent agreement with the experiments. The integral number of iteration steps was the same like at the transient case. Also in the other tests calculations using these boundary conditions yielded a good agreement with the experiment. Figures 11 to 14 show the case of test 4.

5. Conclusions

The application of the „Low Reynolds Number K-Epsilon-Model" has proven to be most convenient for such type of problems. The treatment as transient problem with constant boundary conditions yielded a much better agreement to the measured values than the calculation using the steady state option even with the same number of iteration steps.
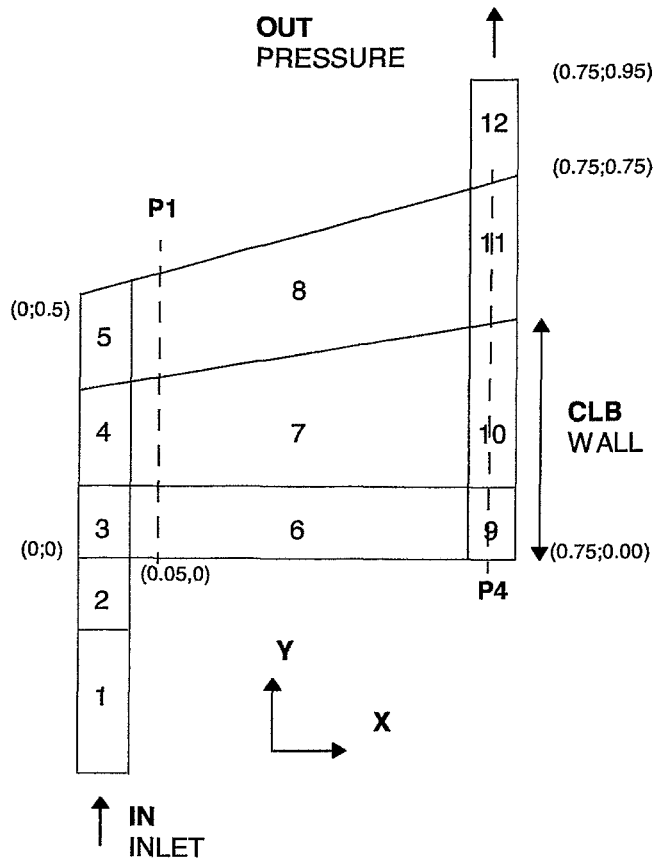
Fig. 3: Block structure and boundary conditions of the CFX-grid
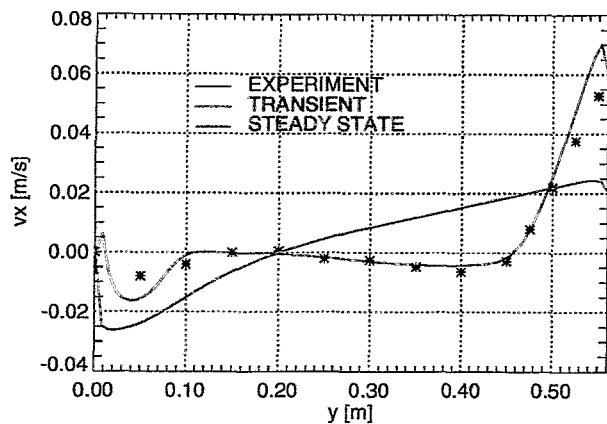
Fig. 4: Horizontal velocity at the line P1 (x = 0.1875 m) (see Fig. 1-2)

30
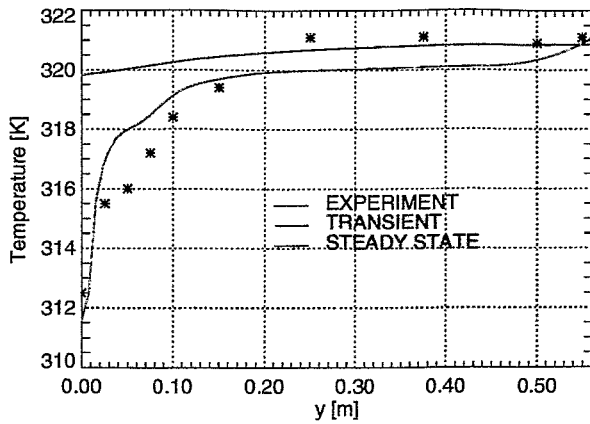
Fig. 5: Test1: Temperature at the line
P1 (x=0.1875m) (see Fig. 2)
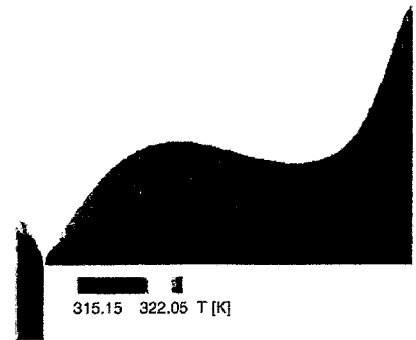
Fig. 6: Test1: Temperature
Steady state calculation
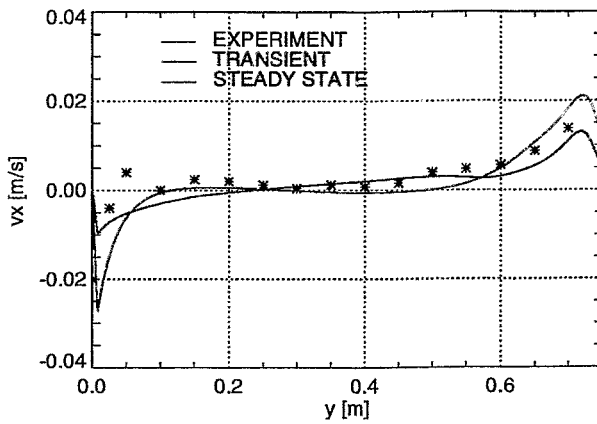
Fig. 7: Test1: Velocity at the line
P4 (x = 0.725 m) (see Fig. 2)
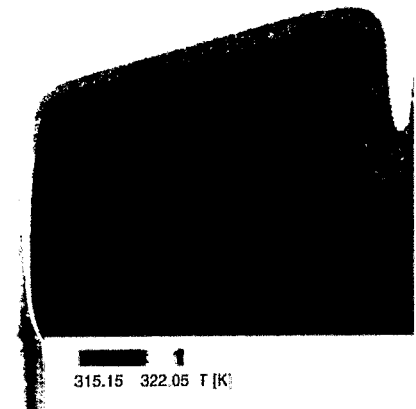
Fig. 8: Test1: Temperature
Transient calculation
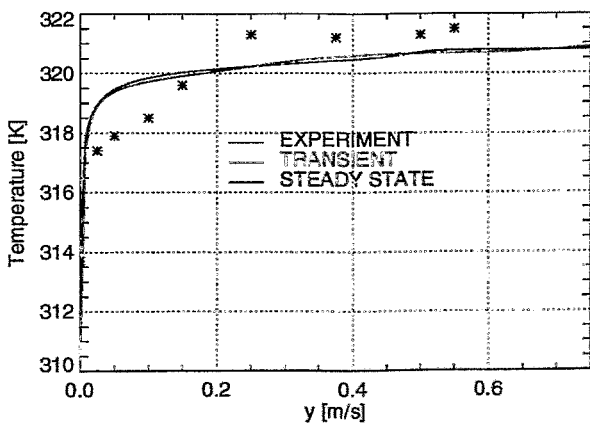
Fig. 9: Temperature at the line
P4 (x = 0.725 m) (see Fig. 2)
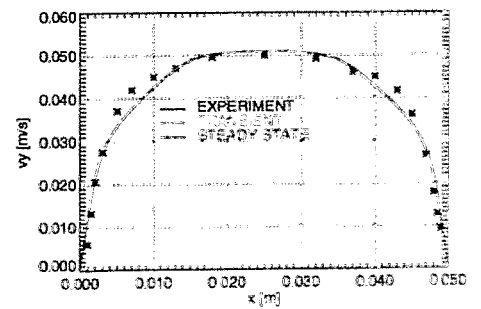
Fig. 10: Velocity profile at inlet

31
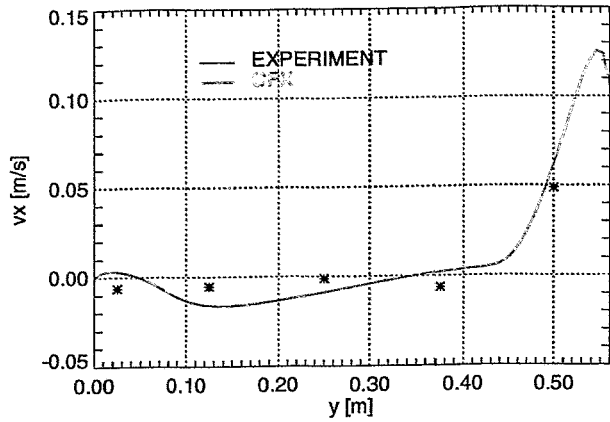
Fig. 11: Test4: Horizontal velocity at the
line P1 (x = 0.1875 m) (see Fig. 2)
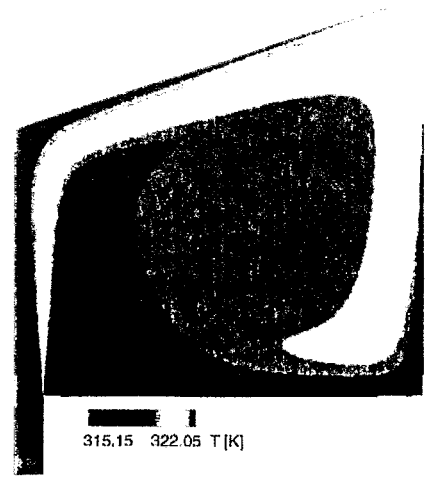
Fig. 12: Test 4: Temperature
Transient calculation
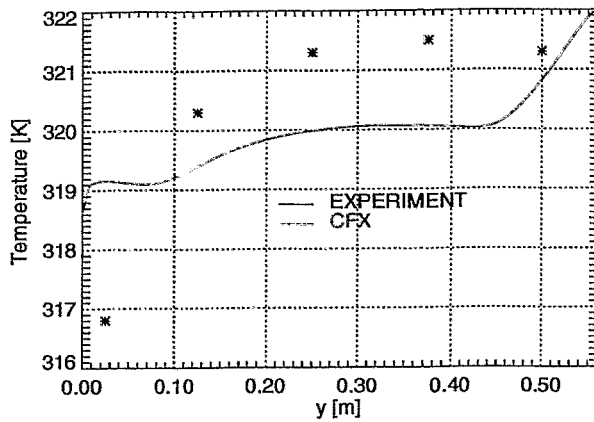
Fig. 13: Test4: Temperature at the
line P1 (x = 0.1875 m) (see Fig. 2)
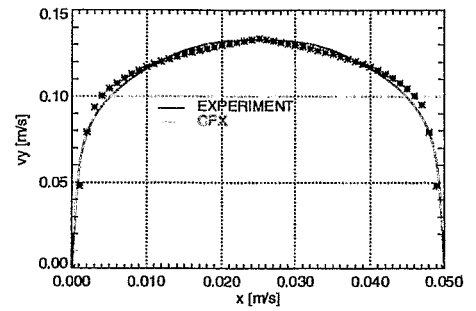
Fig. 14:
Test 4: Velocity profile at inlet

6. References

[1]   Kamide, H., Ieda. Y and Ninokatá, H.(1991),*Benchmark Problem Description prepared for the 7th Meeting of the IAHR Working Group on Advanced Nuclear Reactors Thermal Hydraulics to be held in Kernforschungszentrum Karlsruhe GmbH*, August 1991

[2]   W. Baumann (1992)*Contibution to the 7th IAHR Benchmark Using the Thermal-Hydraulics Code COMMIX-2(V)*,KfK, Interner Bericht INR 1802, PSF-Ber. 3104, Sept. 1992

[3]   W. Baumann (1993),*7th IAHR Benchmark: Recalculation of Case 4 using FLUTAN Code with LECUSSO Scheme*,KfK, Interner Bericht INR 1834, PSF-Ber. 3128, März 1993

[4]   W. Baumann, Y. Kimhi, G. Grötzbach (1995),Turbulente Naturkonvektion in einem Plenum simuliert mit Differenzenverfahren erster und zweiter Ordnung, *Proceedings der Jahrestagung Kerntechnik* Nürnberg *1995*, INFORUM GmbH, ISSN 0720-9207, S. 100

[5]   Y. Kimhi, W. Baumann, G. Grötzbach (1996), *Simulation of convection in upper reactor plenum using first- and second order differencing schemes*, KfK, Interner Bericht IRS 2/96, PSF-Nr. 3246, Feb. 1996

POST-TEST ANALYSIS OF THE BETHSY 9.3 EXPERIMENT - STEAM GENERATOR TUBE RUPTURE WITH FAILURE OF BOTH THE HIGH PRESSURE SAFETY INJECTION AND AUXILIARY FEEDWATER SYSTEMS

E. Krepper, F. Schäfer

1. Introduction

In the framework of the external validation of the thermohydraulic code ATHLET, which was developed by the „Gesellschaft für Reaktorsicherheit" (see Wolfert et al [1]), post test analyses of tests at the integral test facility BETHSY (see [3]) were performed in the Research Center Rossendorf. The presented report refers to the results of the BETHSY test 9.3, during which several accident management procedures were investigated.

2. The BETHSY-test facility

The BETHSY-test facility is a 1:100 scaled thermohydraulic model of a 900 MW(el) pressurized water reactor (FRAMATOME). The test facility is mainly designed to investigate various accident scenarios and to provide an experimental data base for code validation and for the verification of accident management measures. The three identical loops enable the simulation of asymmetric loop behavior. In the test facility, the primary circuit is modeled with a volume scaling ratio of 1:100 retaining the original heights, [3, 4]. Each primary loop is equipped with a vertical steam generator. The maximum pressure on the primary side is 17.2 MPa and on the secondary 8.0 MPa.
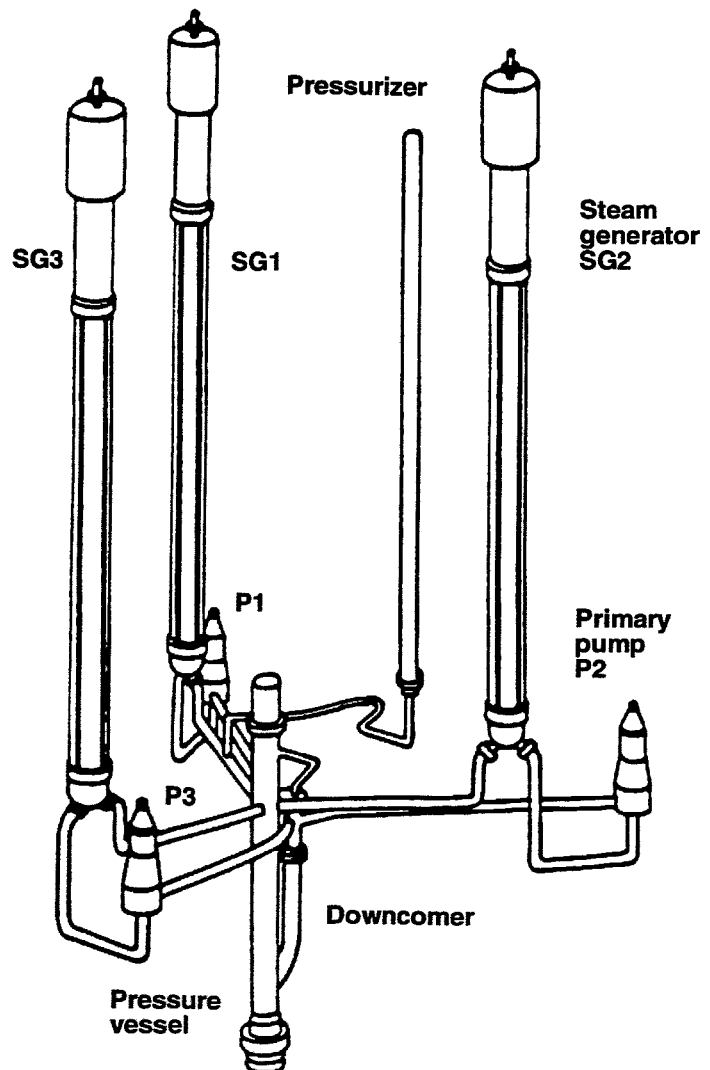
Fig 1: BETHSY Test Facility

Table 1: Scenario and observed thermohydraulic events during the test 9.3

Action	Condition	Time [s]	Thermohydraulic event
U-tube rupture		0	Fast decrease of $P + P^*$
SCRAM SG Isolation	$P + P^* < 12.9$ MPa	273	Increase of secondary pressure until safety valves opens
Safety injection signal = t_{SI}	$P + P^* < 11.9$ MPa	309	Stop of feedwater supply
Pump coast down	core outlet saturation margin < 10 K	391	steam in hot legs and upper pleum $P + P^*$ increasing Natural circulation
Atmospheric steam dump of the intact SG2 & SG3	$t_{SI} + 1200$ s	1509	Decrease of primary pressure to the level of secondary pressure
		1659	Interruption of mass flow in SG1 heat removal only via SG2 & SG3
		1810	Break flow cancellation
		1860	recovery of core outlet saturation margin
Atmospheric steam dump of the damaged SG1	LE SG2** < 2 m LE SG3** < 2 m	2728	primary heat removal via SG1
Accumulator injection	$P + P^* < 4.28$ MPa	3058	
		3260	Boiling in primary circuit --> stabilization of $P + P^*$ at 3.2 MPa stagnation of accumulator injection
Depressurization of the pressurizer	LE SG1** < 2 m	8065	Fast decrease of $P + P^*$ enhanced accumulator injection
		10600	Accumulator empty
Low pressure injection	$P + P^* < 1.75$ MPa	11720	
		17700	stable heat removal conditions

* P+P   Primary Pressure

** LE SG$_i$ Collapsed level in steam generator i

3. The Test 9.3

Steam generator tube ruptures are small break Loss of Coolant Accidents which allow a primary to secondary system flow and may result in a release of radioactive products to the atmosphere. The measures during such an accident situation are therefore first the isolation of the damaged steam generator, then the mass flow cancellation through the break by balancing the primary and damaged steam generator pressure while cooling the primary side with the atmospheric steam dumps of the intact steam generators. Finally the primary mass inventory can be controlled by the safety injection system (high pressure injection, accumulators and low pressure injection) and the reactor state will be shifted to stable residual heat removal conditions.

The simultaneous failure of the high pressure safety injection and auxiliary feedwater systems is a Beyond Design Basis Accident, which leads to core heat up, if no additional measures are taken. During the test 9.3 the efficiency of both the steam generator atmospheric steam dump and the depressurization of the primary circuit via the pressurizer relief valve is investigated. In Table 1 the test scenario is described and the observed thermohydraulic phenomena are listed.

During the test the following phenomena are observed, which have to be modeled by the code simulation (see [2]):

- natural circulation
- asymmetric loop behaviour concerning the heat removal from the primary circuit
- break flow
- mixture level and entrainment of the steam generator secondary side

Fig. 2: Primary pressure

36
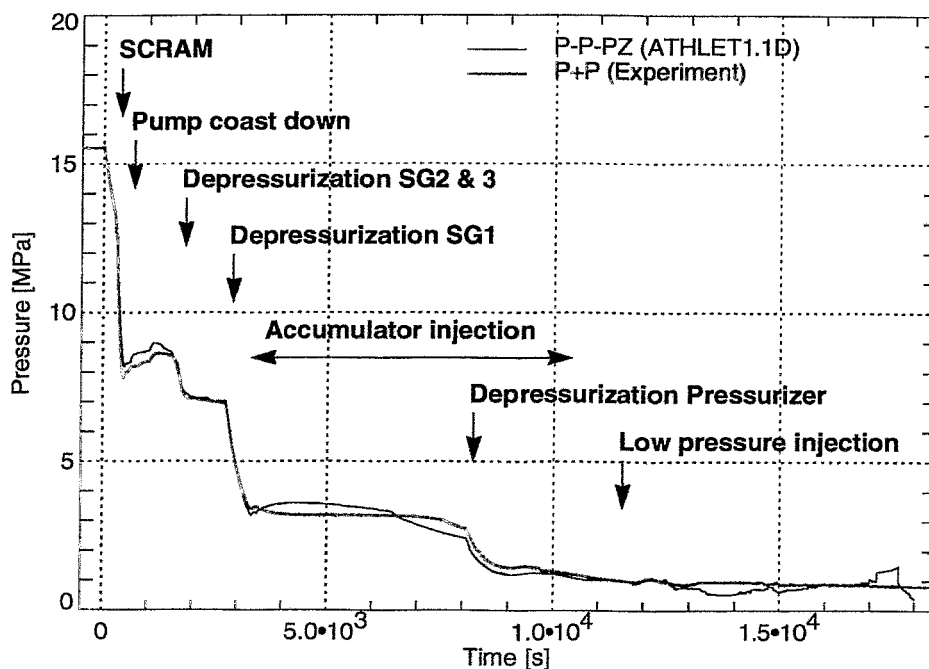
- emergency core cooling: mixing and condensation
- heat transfer in the covered core
- heat transfer at steam generator primary and secondary side
- surgeline and pressurizer thermohydraulics
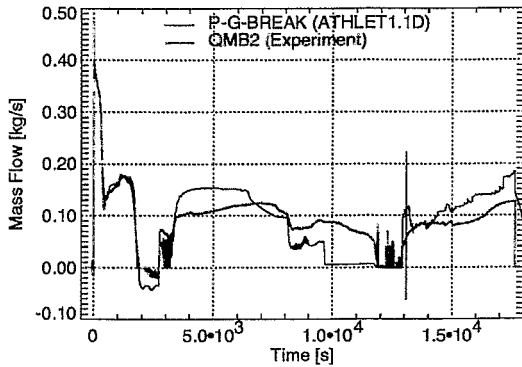
Fig. 3: Break mass flow
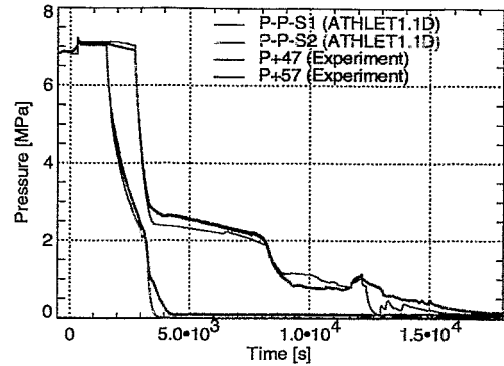
Fig. 4: Secondary pressure in SG1 (damaged) and SG2 (intact, identical to SG3)

4. The ATHLET-calculations

The presented post-test calculations were performed with the thermohydraulic computer code ATHLET Mod 1.1 Cycle D. The input deck models the three loops of the test facility in detail and consists of 87 thermofluid objects with a total amount of 504 control volumes. In all control volumes the five-equation model was applied with separate conservation equations for liquid and vapor mass and energy and a mixture momentum equation. The one-dimensional critical discharge model (CDR1D) was used to model the depressurization of the primary circuit via the pressurizer relief valve. For the calculation of the mass flows at the steam generator secondary side the homogeneous isentropic equilibrium model (Moody-model) was applied. Since no critical mass flow occurred at the break, this model was also used to model the break mass flow.

Most of the hardware actions in the test scenario are controlled by the primary pressure. Figure 2 shows the calculated and the measured primary pressure and
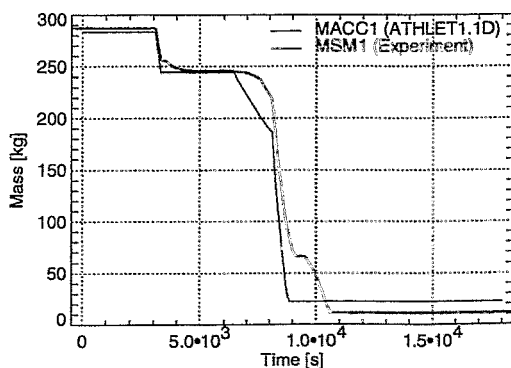
Fig. 5: Accumulator inventory
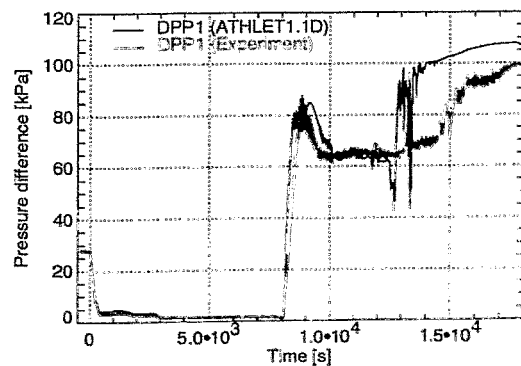
Fig. 6: Difference pressure in the pressurizer

37
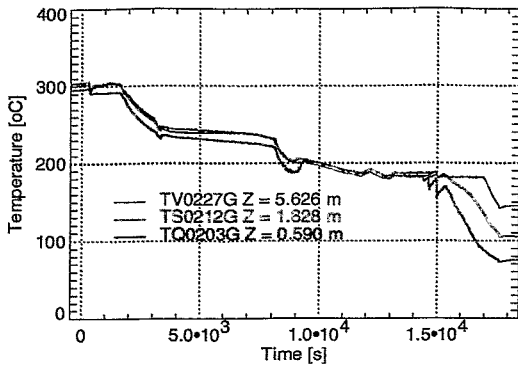
Fig. 7: Measured rod cladding tempe-
rature in different heights
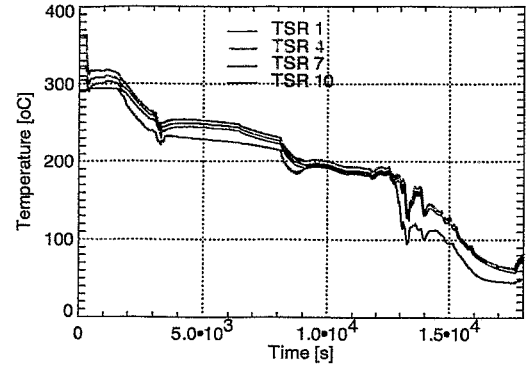
Fig. 8: Calculated rod cladding tempe-
rature in different heights

the times of the main safety related actions. First a fast decrease of the primary pressure is observed. Steam occurs in the primary circuit when the pumps are switched off. The primary pressure increases slightly at a level of 8 to 9 MPa. The safety injection signal at 11.9 MPa automatically shuts down the steam generator main feedwater systems (see Tab. 1). 1200 seconds after the failure of the high pressure injection, the depressurization of the secondary sides of the two intact steam generators was started. The primary pressure decreases slightly below the secondary pressure of the damaged steam generator. Consequently an inversion of the break mass flow was observed. For a short time the saturation margin of the core outlet was recovered.

When the collapsed levels of the secondary sides of the intact steam generators dropped below the 2 m limit, the damaged steam generator was depressurized too. Then all residual heat of the primary circuit was removed only via the dam- aged steam generator. The break flow is again directed from the primary to the secondary side. The primary pressure decreased below the setpoint of the accu- mulator injection. Figure 5 shows, that the process of the accumulator injection was modeled with good agreement to the experiment.
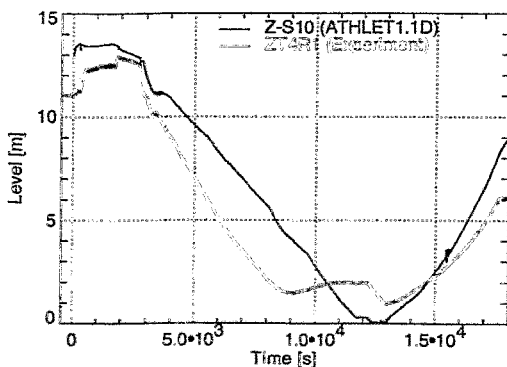
Fig. 9: Collapsed level of the damaged
steam generator secondary side
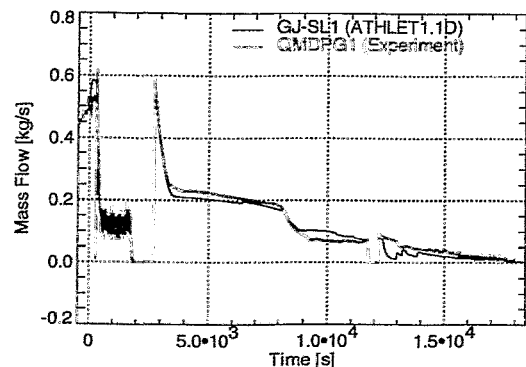
Fig. 10: Steam mass flow from the da-
maged steam generator

Figure 9 shows deviations between the measured and the calculated secondary collapsed level for the damaged steam generator. During this scenario the secondary side is simultaneously filled through the break and depleted by the steam dump. The atmospheric dump mass flow was calculated in good agreement to the experiment (see Fig. 10) whereas the calculated break flow is too high (see Fig. 3). The calculated break mass flow is not only influenced by the leak model, but also by the thermohydraulic conditions near the break during this period.

After 8065 seconds even the collapsed level of the damaged steam generator dropped below 2 m. Efforts for residual heat removal had to be made quickly to reach the threshold of low pressure injection. Therefore the pressurizer valve was opened, which lead to a further drop of the primary pressure (see Fig. 2) and an increased accumulator injection (see Fig. 5). Figure 11 shows the void fractions at this time in the primary and secondary components of the damaged steam generator. The secondary side will be depleted by the depressurization. At a certain level the heat sink of the first steam generator gets low. Steam occur in the primary U-tubes and the natural circulation will be interrupted.

Also the increasing pressure difference in the pressurizer, which is a measure for the pressurizer collapsed level, was modeled with good accordance to the experiment (see Fig. 6). Finally at 11720 seconds the setpoint for the low pressure injection was arrived and stable heat removal conditions were established. Neither in the test nor in the calculation no heating up of the rod cladding temperatures were observed (see Fig. 7 and 8).
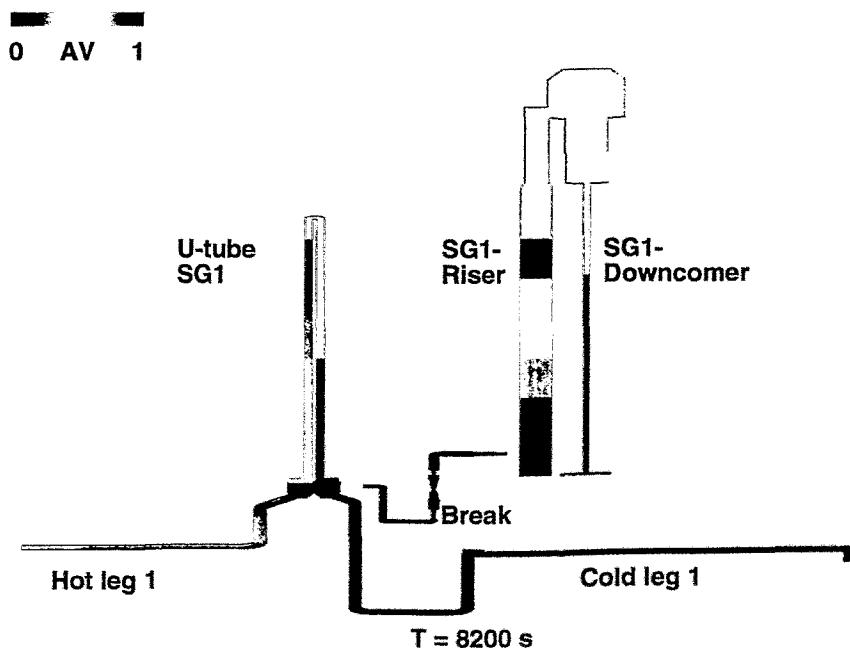
Fig. 11: Void fractions at the primary and secondary side of the damaged steam generator
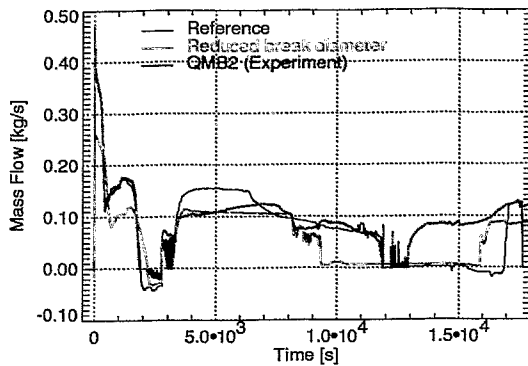
Fig. 12: Break mass flow with reduced break diameter
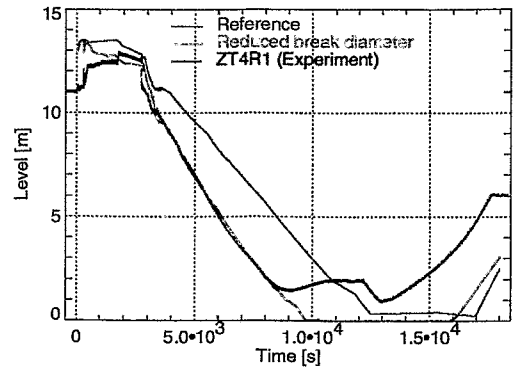
Fig. 13: Collapsed level in SG1 with reduced break diameter

5. Variations of the scenario

To get a deeper insight into the processes during the transient, calculations with slightly reduced break diameter were performed. Whereas the break mass flow during the first 3000 seconds is too low in the calculation, the values between 3500 and 8000 seconds fit very well the measured mass flow (see Fig. 12). Even the collapsed level of the damaged steam generator is modeled with good agreement to the experiment (see Fig. 13). But the lower the secondary coolant inventory of the damaged steam generator, the lower is the cooling capacity during the depressurization period. Therefore in the calculations with reduced break diameter at the end of the steam dump phase a short heating up of the rod cladding temperature was observed (see Fig. 14). But these temperatures are still far below the permitted value of 1200 °C.
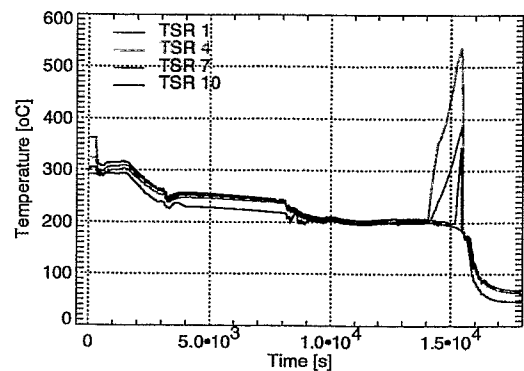
Fig. 14: Rod cladding temperature with reduced break diameter

6. Conclusions

Most of the thermohydraulic phenomena could be modeled with good agreement to the experimental results. Difficulties arose to model the processes near the break, when at the same time the secondary relief valve opens.

From the safety point of view the main statement of the test could be confirmed by the calculations. At a failure of both the high pressure injection and the auxiliary feedwater system the atmospheric steam dump first of the intact, then of the damaged steam generators and finally the depressurization of the primary circuit via the pressurizer valve, can avoid any heat up of the rod cladding temperatures.

40

References

[1]   K. Wolfert, V. Teschendorff, G. Lerchl et. al.(1989), The thermalhydraulic code ATHLET for analysis of PWR and BWR systems, *NURETH-4 Karlsruhe 1989*, Proc. Vol. II pp. 1234-1239

[2]   CSNI integral test facility validation matrix for the assessment of thermal-hydraulic codes for LWR LOCA and transients (1996), NEA/CSNI/R(96)17

[3]   BETHSY General Description, SETh/LES/90-97, April 1990

[4]   Ph. Gully, R. Deruaz, BETHSY Measurement System, SETh/LES/87-27, October 1987

[5]   J.C. Barbier, P.C. Clement (1993): *BETHSY Test 9.3: Steam Generator Tube Rupture with Failure of both the High Pressure Safety Injection and Auxiliary Feedwater Systems*, Quick Look Report, STR/LES/92-107, December 1992

[6]   J.C. Barbier, P.C. Clement (1993): *BETHSY Test 9.3: Steam Generator Tube Rupture with Failure of both the High Pressure Safety Injection and Auxiliary Feedwater Systems*, Data Report, STR/LES/93-134, August 1993

[7]   J.C. Barbier, P. CLement, R. Deruaz (1994): A single steam generator tube rupture with unavailability of both the high pressure safety injection system and the steam generator auxiliary feedwater system on BETHSY integral test facility. *Int. Conf. on „New Trends in Nuclear System Thermalhydraulics"*, Pisa, Proc. Vol. 1 pp. 533-538

[8]   E. Krepper, F. Schäfer (1998): *Verifikation des ATHLET-Rechenprogramms im Rahmen der externen Verifikationsgruppe: BETHSY Test 9.3 - Heizrohrbruch mit Versagen der Hochdruck-Noteinspeisung*, FZR-Bericht, FZR-232 August 1998

FLUID MECHANICS OF ELECTROLYTIC CELLS

C. Schneider

1. Introduction

In membrane cells, the fluid sometimes tends to foaming because of the high concentration of electrolytes. For example, in the alkaline clorine electrolysis (Fig. 1) the sodium chloride concentration in the anolyte is well above the critical value for coalescence inhibition. Another example is the anodic oxygen generation in the alkaline water electrolysis process. In the result, with increasing current density the anolyte chamber is more and more filled with foam and the working fluid is expelled. This has several negative effects on the cell performance: (1) reduction of the anolyte density, and, as a consequence, local undersupply of the anode and the membrane, causing a decrease of the life time of the membrane and

Cl$_2$ and NaCl-brine (200 g/l)   H$_2$ and 33% NaOH

Foam

NaCl-brine (300 g/l)   30% NaOH
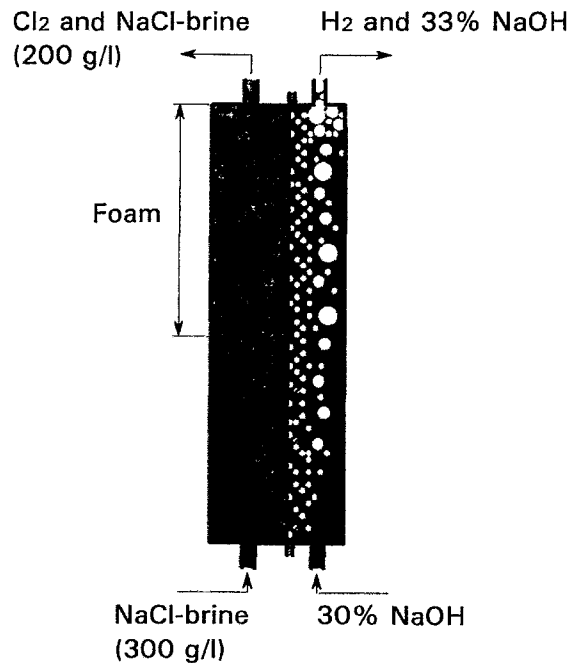
Fig. 1: Two-phase flow in membrane cells for alkaline chloride electrolysis

a growth of the cell voltage, (2) stagnation of natural circulation of the fluid inside the anode space, leading to a bad mixing of the fresh sodium chloride solution and (3) bad transient behaviour during load changes. The latter can increase the probability of membrane failures.

The present work was carried out in the frame of a research contract with KRUPP UHDE, a major design and construction company of electrolysis

Fig. 2: Cell room at General Electric Plastics B.V., Netherlands, equipped with KRUPP UHDE membrane cells

42

plants throughout the world (Fig. 2). Main attention was paid to the clarification of the foam effects and the search for methods for foam destruction or for the prevention of foaming.

2. Model of the anode reaction

The first step was the search for a model reaction, which is easily to handle. It is the idea to have an experimental mock-up that allows to carry out tests of modified cell designs quickly and without the necessity to handle chlorine and the other dangerous products of a real electrolysis cell. Gas injection through perforated or porous plates and membranes did not provide the small bubble size characteristic for the chlorine generation. Catalytic decomposition of hydrogen peroxide on a platinum surface was found to be an ideal substitute for the original chlorine generation process because of the low size of the oxygen bubbles. The products of the reaction are easily to handle, the raw material, a 35% hydrogen peroxide solution in water, does not cause considerable handling problems, as well. The size of the primary bubbles generated at the surface of the anode and at the platinum catalyst were measured under approximately the same conditions by a video system. The comparison has shown that the size of the primary oxygen and chlorine bubbles are of the same order of magnitude. Further, both systems are coalescence inhibited. In fact, the oxygen bubbles are smaller by a factor of 2 (O_2 in 35% H_2O_2 solution: 97 μm, Cl_2 in anolyte: 191 μm). It was therefore expected that the gas fraction at the same superficial gas velocity is higher in the model reaction because of a smaller rise velocity of the oxygen bubbles. The foaming behaviour is also more unfavourable than that of the anolyte in the electrolysis cell. This is a good prerequisite for studying the effectiveness of foam destruction and prevention measures.

3. Foam stability comparison

In order to verify the applicability of the model reaction, foam stability tests were performed. For this purpose, a cylindrical reaction column was built (Fig. 3). In the centre of the column a cylindrical catalyst tube was placed. It was made of titanium, covered with a 1 μm layer of platinum. The mock-up has the same height and an identical ratio of the gas producing surface to the fluid volume as the original electrolysis cell.

Hydrogen peroxide decomposition is an exothermic process. That means that the catalyst has to be cooled for keeping the reaction rate constant. The catalyst tube was connected to a water cooling circuit. The circuit was equipped with a thermostat to control the catalyst temperature. By these means the reaction rate can be controlled, which was measured by a flow meter for the oxygen output.

The foam stability was studied by so-called shut-down experiments carried out at both an electrolysis cell and the hydrogen peroxide mock-up. For the first, a
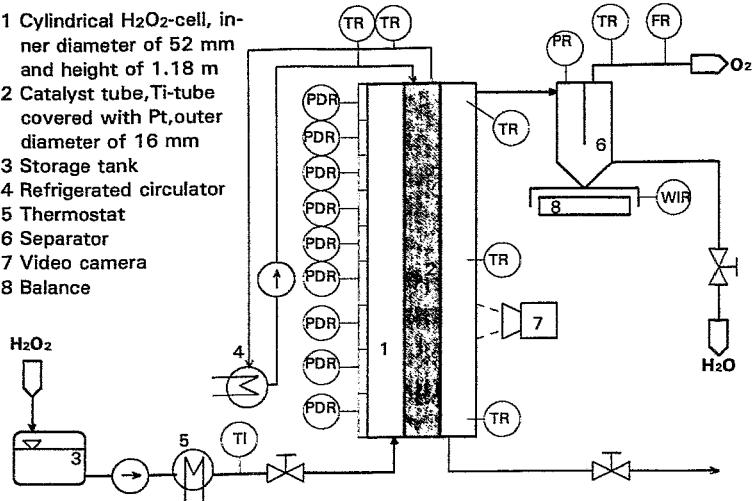
Fig. 3: Process flow scheme of the hydrogen peroxide facility

0.16 m^2 test cell was used. After the cell had been operated for a certain period on a given current density, the current was suddenly switched off and the decay of the gas-liquid dispersion was recorded with a video camera. The gas disengagement takes approximately 20 seconds to reach the clear liquid level. This points to the presence of wet, instable foam that does not form stable lamellae. In case of the hydrogen peroxide mock-up, it is not possible to stop the decomposition reaction at the catalyst surface by any means. Here, the dispersion decay after a quick withdraw of the catalyst rod was studied. Decay times of about 40 seconds were measured. The different decay behaviour can be explained by the smaller diameter of the oxygen bubbles.

The experiments also allowed to compare the average gas fraction in the anode chamber with the hydrogen peroxide mock-up. For this purpose, the oxygen production in the H$_2$O$_2$-cell is transformed into a fictive current density, at which the electrolysis cell produces the same volume flow of gas related to the electrode and catalyst surface, respectively. In the cylindrical H$_2$O$_2$-cell the same gas fractions as in the anode chamber were found at a much lower specific gas production per unit an-
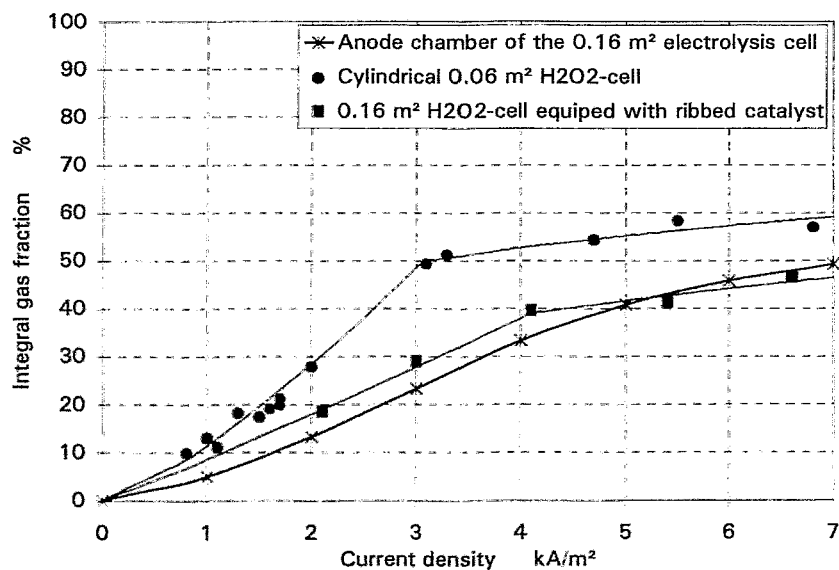
Fig. 4: Integral gas fraction in the cylindrical 0.06 m^2 and in the 0.16 m^2 H$_2$O$_2$-cell in comparison with that in the anode chamber of the 0.16 m^2 membrane cell

44

ode (respectively catalyst) surface (Fig. 4). In a wide range, similar gas fractions are observed, when the specific oxygen production in the model system corresponds to a 1.5 times larger value of the specific chlorine production. A good agreement between electrolysis and hydrogen peroxide decomposition was achieved with a 0.16 m² H₂O₂-cell equipped with a ribbed catalyst like a jalousie.

4. The 0.16 m² hydrogen peroxide cell

This test facility was built to further improve the similarity between the original electrolysis cell and the hydrogen peroxide model. It is a rectangular column (Fig. 5) with the same dimensions as the anode chamber of the 0.16 m² electrolysis cell. The catalyst was as much as possible approximated to the electrode design of the original anode (Fig. 6). This was achieved by using a grid of flattened copper tubes imitating the anode ribs. One has to keep in mind that the catalyst must be cooled. For this purpose hollow ribs were manufactured. Each of them is connected to the cooling loop by two collectors at both sides. The surface was covered by a 2.5 μm platinum layer.

The 0.16 m² hydrogen peroxide cell is equipped with the following standard instrumentation:

- chain of 9 differential pressure transducers for the axial gas fraction distribution
- flow meters for O₂ output and a metering pump for H₂O₂ feed flow
- balance for liquid discharge with the gas flow
- thermocouples and Pt resistance thermometers for H₂O₂ and cooling water temperatures
- pressure transducer for pressure in the separator.
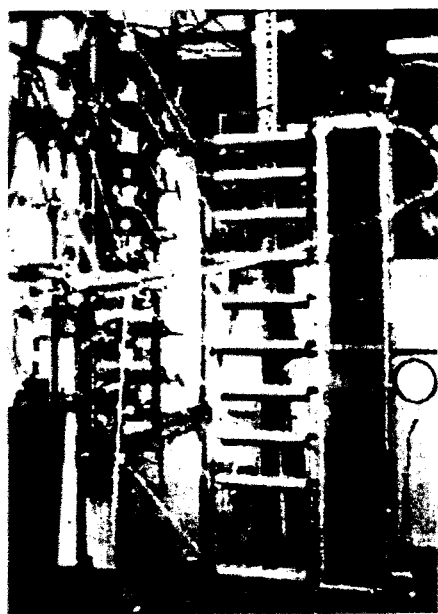
Fig. 5: The 0.16 m² H₂O₂-cell
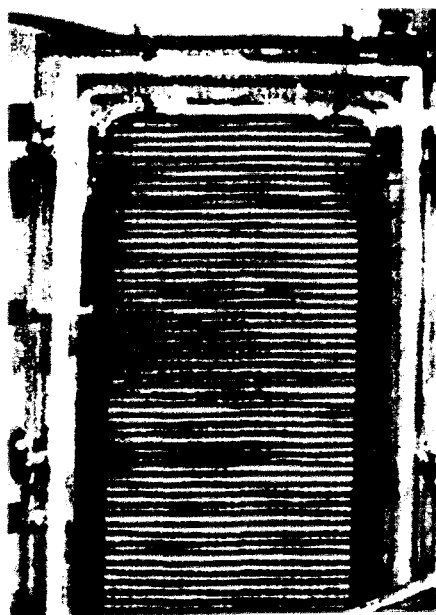
Fig. 6: The ribbed catalyst

During the experiments samples were taken to determine the H_2O_2 concentration. Temporarily the column was equipped with a gamma densitometer to verify the gas fractions measured by the differential pressure method. The gamma densitometer was also used to measure the gas fraction profile perpendicular to the catalyst. The bubble size distribution was determined by means of a Phase Doppler Particle Analyser (PDPA) and a CCD camera with digital image processing software. The circulation inside the model chamber was measured by a Laser Doppler Anemometer (LDA). These special measurements were performed to collect data for the development of a theoretical model. The test facility was successively used to check several ideas to improve the hydrodynamic behaviour of the cell. A large number of different cell configurations was investigated.

5. Main results

The anode chamber behaves much different than a bubble column with the gas supply at the bottom. The superficial gas velocity is increasing from the bottom to the top due to the side supply of gas from the electrode. The axial gas fraction profiles in the anode chamber is divided into three characteristic areas: (1) the bubble flow region in the bottom part, (2) the area of spherical foam of a nearly constant gas fraction of 60-70% and (3) a region of transition from spherical to cell foam at the top (Fig. 7) with gas fractions higher than 70%. As already mentioned, the foam is comparatively wet and unstable. This foam is nevertheless responsible for the losses of liquid, when the cell performance is increased. The resulting low collapsed level in the anode chamber leads soon to a bad supply of the upper parts of the anode and the membrane with anolyte.

Attempts to theoretical modelling have shown that the bubble flow in region 1 is mainly dominated by a circulation of the liquid driven by the asymmetric gas supply from the side of the electrode (respectively catalyst). In region 2, the increase of superficial gas velocity does not cause a significant gas fraction increase. In this area, the increase of the gas flow rate is in balance with the increase of the bubble rise velocity, caused by bubble growth due to coalescence.

Fig. 7: Axial gas fraction profiles as a function of the cell power in the 0.16 m² H_2O_2-cell

46

In the result of the different studies a configuration was found that was capable of reducing the gas fraction significantly. The integral gas fraction in the hydrogen peroxide cell was reduced from 40% down to 5% at a specific gas production corresponding to 4 kA/m² in the electrolysis cell (Fig. 8).

6. Process improvements

The optimal configuration found in the test series at the hydrogen peroxide cell was transferred to the 0.16 m² electrolysis cell. Shut-down experiments have confirmed the results of the drastic gas fraction reduction in the anolyte chamber.

This means that the cell performance can be increased significantly without the danger of expelling the anolyte. Another positive effect is, that the cell voltage at 6 kA/m² was by approximately 60 mV lower than in the reference cell configuration. Taking into account that a decrease of 10 mV results in a gain of 7 kWh/t_{NaOH}, the improved cell design scaled to a reference plant of 100.000 t/a allows to save about $4.2 \cdot 10^6$ kWh/a. For the clarification of the effects on the membrane and the anode long term tests are necessary, which are planned for the near future.

Fig. 8: Reduction of gas content in the 0.16 m² H₂O₂-cell at 4 kA/m²

7. Conclusion

The optimisation of the two-phase flow characteristics of electrolysis plants can have a strong effect on the economy of the process. The present work demonstrated that fluid dynamic improvements in the anolyte chamber of a membrane cell for alkaline chlorine electrolysis allow to save electric energy as well as other resources in a considerable degree. This has positive economic, environmental and safety impacts.

47

MEASUREMENT AND SIMULATION OF THE TURBULENT DISPERSION OF A RADIOACTIVE TRACER IN A TWO-PHASE FLOW SYSTEM

F. Hensel, U. Rohde

1. Introduction

The turbulent dispersion of a radiotracer in an experimental setup with a natural convection liquid–gaseous flow was investigated. A liquid–gaseous bubbly flow was generated in a narrow tank by injection of pressurized air into water or by catalytic disintegration of H_2O_2. The Positron Emission Tomography (PET) technique was used to observe the spreading of a radiotracer liquid in the bubbly flow. The dispersion coefficient D describing the spreading of the tracer in the flow was calculated from the experimental data. For selected experiments, the behavior of the tracer in the two–phase flow was also calculated using the computational fluid dynamics code CFX–4. Here, the Euler–Euler continuum approach including a homogeneous low Reynolds number K,ε –model was applied. Turbulent Prandtl numbers for gas and tracer dispersion were varied. In the case of higher gas superficial velocities ($j_{gas} \approx 5\text{-}15\,mm/s$), a reasonable agreement was achieved between calculated and measured tracer transport velocity and dispersion coefficient values. A nearly linear correlation between j_{gas} and D was found in agreement with other authors. The calculation results contribute to a better understanding of the phenomena and interpretation of the measurement results as well as to the validation of the CFD code for turbulent two-phase flow applications. Further investigations are necessary to improve the agreement in the cases of H_2O_2 disintegration and low gas superficial velocities.

2. Positron Emission Tomography

Positron Emission Tomography is an imaging technique originating from nuclear medicine. It is mainly applied as an in vivo non invasive tool by which metabolic activities can be investigated. Typical PET positron emitters like ^{11}C, ^{13}N, ^{15}O and ^{18}F can substitute naturally occurring isotopes in a wide range of organic compounds. From the annihilation of the positrons originate two γ-quanta providing the event line information which is necessary for the calculation of the tracer activity in the investigated object. Besides medical imaging, industrial and engineering applications are known, including the investigation of chemical processes like catalysis (Jonkers et al., [1]) and flow monitoring in an oil reservoir rock (van den Bergen et al. [2]). Using this technique, the spreading of a tracer in a bubbly flow in a tank was monitored. The objective of these investigations was to study the turbulent mixing in chlorine electrolysis cells, particularly the estimation of turbulent dispersion coefficients.

3. Description of the Measurements

The transport of a tracer in a turbulent bubbly flow was studied in a series of experiments using a narrow tank (Fig. 1) [3]. Gas bubbles are generated at the bottom of the tank. In the case of the injection of pressurized air the bubbles are created at nozzles on top of the gas injection rod. Using a decomposition reaction, the gas and the bubbles are generated at the whole surface of the injection rod covered with the catalyst. In some experiments, the tank was subdivided in a riser part and a downcomer part to enhance the fluid circulation rate.

In the experiments with air bubbles distilled water was used as liquid phase with additives of isopropanol and NaCl. NaF (^{18}F) was selected as tracer because of its half-life of 1.83 h and a low maximum positron energy (0.63 MeV) causing a small positron range. Further, NaF behaves very similar to NaCl and is therefore suited to study the spreading of the NaCl in this bubbly flow. In the case of H_2O_2-decomposition, the liquid phase in the tank consists of a 35 Vol% H_2O_2 solution. The same tracer was applied. The reaction speed was modified by the variation of the temperature of the catalyst rod. The tracer injector allows a low momentum injection of about 0.8 ml of the tracer liquid. Using this transparent tank, preliminary tests with ink injection tests were also carried out.
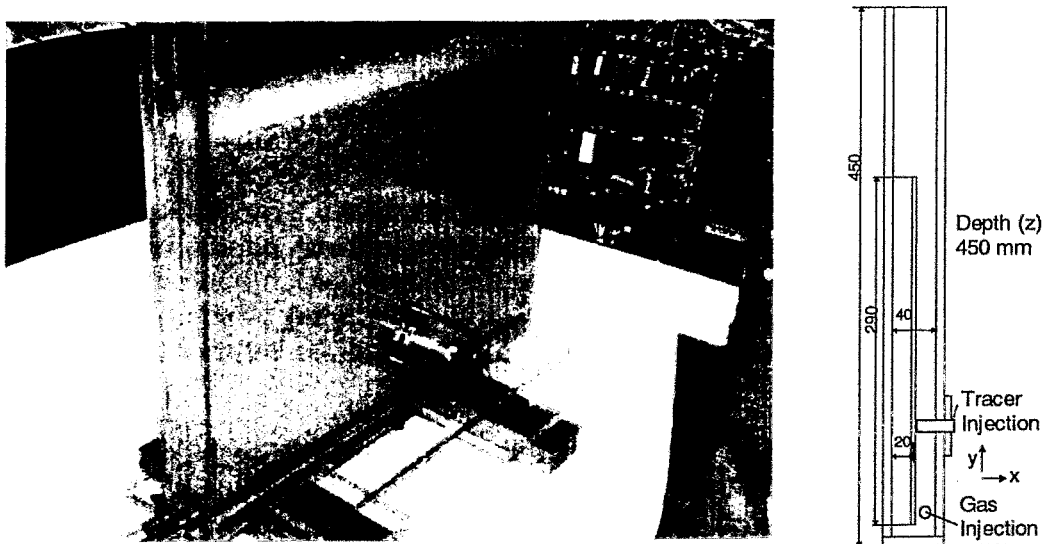
Fig. 1: Experimental setup for the PET measurements

The spreading of the tracer was monitored using a double head PET scanner described by Pawelke in [4]. The measured positron annihilation rate is proportional to the tracer concentration. The tank is centered between the heads of the PET scanner. Then an area of about 20×40 cm can be monitored. Each registered annihilation event is stored separately, together with so-called time events. Thus, midplane intensity distributions for any time slices can be calculated by a backprojection. Due to the tank geometry, the midplane backprojection was considered to be the best fitting method for the evaluation of the experimental data. Applying corrections for the geometry of the scanner, the

49

two-dimensional midplane intensity values are proportional to the tracer concentration in the tank. The concentration profile in the 3rd dimension (x-axis, Fig. 1) cannot be resolved.

Fig. 2 shows typical normalized tracer concentration distributions. In each of the 500 ms time intervals about 50.000 events have been processed. The resulting distributions prove that even activities of only about 5 MBq can supply quantitative insight into the spreading process.
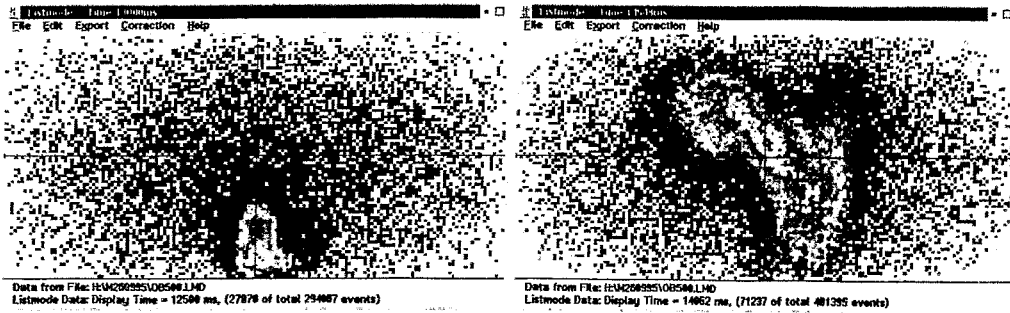
Fig. 2: Midplane concentrations of the tracer (0.5s and 2s after injection)

The dispersion coefficient D for the tracer liquid in the bubbly flow was calculated from the experimental data assuming an isotropic spreading of the concentration profile within a diffusion approximation

$$\frac{\partial c}{\partial t} = D \cdot \nabla c .\tag{1}$$

Thus, D was estimated by fitting the midplane activity distributions to the solution of the two-dimensional diffusion equation in polar coordinates, which is given by

$$c(r, t) = \frac{C_0}{4\pi Dt} \cdot \exp\left(\frac{-r^2}{4Dt}\right) .\tag{2}$$

This procedure was carried out after the separation of the convective displacement of the tracer distribution from the experimental data. In (2), C_0 is the total tracer amount. For a given distribution, a concentration c_m smaller than the maximum concentration c_{max} corresponds to a certain radius r_m (distance from center). If the parameters of equation (2) are known, the radius r_m of this concentration can be calculated. The area $A = \pi r_m^2$ within the radius r_m then corresponds to a tracer amount C located inside the area A:

$$C = 2\pi \int_0^{r_m} c(r, t)r dr = C_0 - 4\pi Dt \cdot c_m\tag{3}$$

Thus, c_m can be substituted using (2) and (3), with

$$r_m = \sqrt{4Dt \cdot \ln\frac{C_0}{4\pi Dt \cdot c_m}} \quad \text{the expression } A = \pi \cdot r_m^2 = 4\pi Dt \cdot \ln\left(\frac{C_0}{C_0 - C}\right)\tag{4}$$

can be obtained. Assuming the measured activities I are proportional to the local amount of tracer, all quantities can be determined from the experimental data. Furthermore, equation (4) is assumed to be valid also for the case of not exact symmetric shapes of the tracer distribution. Thus, the dispersion coefficient D is determined from the ratio of sum intensity I inside an area A to the measured total intensity I_0. From the experimental data the quantities A and C (i.e. I) were determined for each time step t with several thresholds I_m lower than the maximum midplane intensity. This increases the accuracy and averages effects resulting from the choice of I_m: Near to the intensity maximum of the distribution the error of the area determination is quite high due to a small number of pixels the midplane is divided into. At a lower intensity threshold the intensity values are more affected by the scattered coincidences leading to an overestimation of the area A. The dispersion coefficient D was determined by means of the least squares fit method according to

$$\frac{A}{\ln K} = 4\pi D(t+t_0) \text{ with } K = \frac{C_0}{C_0 - C} = \frac{I_0}{I_0 - I}. \tag{5}$$

The resulting values for D are shown in Fig. 3. They show a good agreement to values published by Ohki and Inoue in [5] and by Millies [6]. The solid line in the Figure 3 was calculated according to an empirical equation by Ohki and Inoue [5]:

$$D = 0,30 \cdot \left(\frac{s^{0.2}}{cm^{1.2}}\right) \cdot d_s^2 \cdot j_{gas}^{1.2} + 170 \frac{cm}{s} \cdot d_L \tag{6}$$

This equation is valid for bubble columns with gas injection through a bottom sieve plate which can be compared with the apparatus used here. d_S denotes the column diameter, d_L the diameter of the holes in the sieve plate and j_{gas} the gas superficial velocity. The diameter here corresponds to the width of the tank (4 cm), a characteristic parameter of the flow. In an earlier publication [7] the diameter of a cylindrical column with the same cross-section area was used for
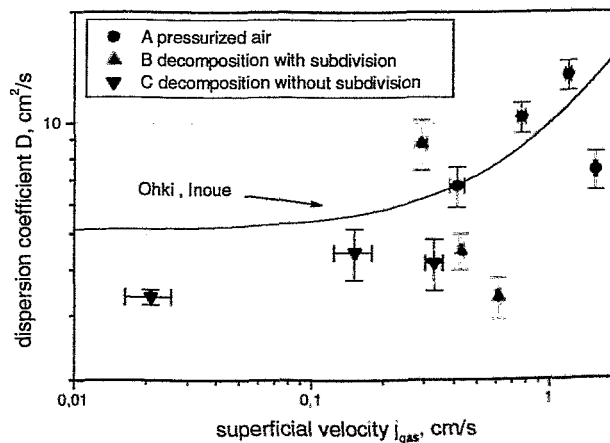
Fig. 3: Dispersion coefficients for several experiments (cf. Table 1)

this parameter. Therefore, the coefficients calculated according to (6) were determined too high. In contrast to the experiments of Ohki and Inoue here the gas was injected through 23 holes of 0.3 mm diameter in a metal rod or along a platinum covered rod, respectively. Equation (6) is valid for the injection of air into water. The big influence of d_L in (6) is possibly overestimated. It expresses the influence of the bubble diameters on the dispersion. This influence has to be corrected for low gas superficial velocities below the range investigated by Ohki and Inoue [5]. For the decomposition experiments, this parameter has no physical meaning at all, and (6) can not be applied.

4. Models and Assumptions for CFD Simulation

Calculations of the two–phase flow with a spreading tracer were carried out for selected experiments using the computational fluid dynamics code CFX–4 [8]. To limit computing time, most of the calculations are carried out in 2D geometry assuming an infinite length of the measurement cell in z-direction and using about 7500 mesh cells. Some calculations are performed in 3D simulation to study the real geometry, where at least 40.000 cells are required. The Euler–Euler continuum model was applied for the two–phase flow. The flow is assumed to be a disperse bubbly flow with bubbles of constant diameter. The gas is injected using a volume source near the gas injection tube. The separation of the gas at the fluid surface is performed assuming a wall with free slip conditions for the liquid and arbitrary velocity conditions for the gas phase.

While the mass and momentum conservation are considered for both phases separately, a homogeneous low Reynolds number K,ε - model was used considering balance equations for the turbulent energy and its dissipation rate only for a homogeneous phase mixture. This assumption was made due to the lack of generalized models for source terms and phase exchange rates of K and ε of the phases. The turbulent dispersion of a scalar quantity Φ within one of the phases is modeled using the eddy diffusivity hypothesis

$$\frac{\partial}{\partial t}(\alpha\rho\Phi) + \nabla(\alpha(\rho\Phi\overline{U} - \Gamma\nabla\Phi)) = S \tag{7}$$

where α is the volumetric phase fraction, ρ the density of the corresponding phase, $\overline{U}$ the phase velocity and S a source term, while $\Gamma = \mu_{turb}/\sigma_{turb}$ is the turbulent diffussivity. The relation between turbulent viscosity μ_{turb} and Γ is given by the turbulent Prandtl number σ_{turb}. The value $\sigma_{turb} = 0.1$ was used for the description of the turbulent dispersion of the gas phase. In this case, the scalar Φ in equation (7) is unity.

Because the radioactive tracer was assumed not to affect the velocity field, it is possible to describe it as a scalar connected with the liquid phase. The balance of this scalar is also given by equation (7), then the scalar Φ represents the tracer concentration. First, the two-phase flow was calculated without tracer until achieving a steady-state solution. Then the tracer was injected by switching on a source in a small volume at the injection position for a short time (0.1 s). After that, the dispersion of the tracer was observed during an instationary calculation over the measurement time interval. The value of the

turbulent Prandtl number for the tracer diffusion was varied. The best results were achieved using a value of $\sigma_{turb} = 0.45$.

The effective turbulent dispersion coefficient D of the tracer was obtained from the calculated tracer concentration distribution backprojected to the midplane of the tank after separation of the convective tracer motion in the analogous manner like from the measured tracer distributions, i.e. from equation (5) with three different threshold values.

5. Results of CFD Simulation

With the code CFX-4, the following selected experiments have been simulated:

- injection of pressurized air into water, tank without subdivision (A1 - A4),
- catalytic disintegration of H_2O_2, tank with subdivision (B1 - B3),
- catalytic disintegration of H_2O_2, tank without subdivision (C1 - C3).

In Table 1, the values of the effective linear tracer motion velocity v_{trac} and the dispersion coefficient D obtained from the calculations are compared with measured values. For some experiments, particularly of group A, the error of the calculated dispersion coefficient value is rather high. In these experiments with relatively high superficial gas velocities and without subdivision of the tank, a part of the tracer is spread to the downcoming stream. This part moves downwards, while the other part of the tracer moves upwards. In the calculation we can observe the development of two maxima in the backprojected tracer concentration distribution (see Fig. 4), causing a fictional broadening of the tracer distribution used for the determination of the dispersion coefficient. This leads to an overestimation of the coefficient D. Using different threshold values, equation (5) gives very different values for the dispersion coefficient, because

Table 1: Comparison between measured and calculated parameters

Experiment	Measured values			Calculated values	
	j_{gas} in cm/s	v_{trac} in cm/s	D in cm²/s	v_{trac} in cm/s	D in cm²/s
A1	0.40	1.82	6.73 ± 0.85	2.32	5.24 ± 3.23
A2	0.767	3.47	10.3 ± 0.96	2.42	7.46 ± 2.48
A3	1.192	4.49	13.4 ± 1.23	1.98	14.8 ± 5.66
A4	1.543	2.99	7.41 ± 0.90	2.83	17.6 ± 6.8
B1	0.290	5.37	8.80 ± 1.37	8.75	2.66 ± 0.28
B2	0.423	3.67	4.49 ± 0.49	8.71	3.52 ± 0.33
B3	0.605	2.92	3.35 ± 0.43	8.64	4.2 ± 2.9
C1	0.022	0.62	3.37 ± 0.16	0.86	0.24 ± 0.06
C2	0.151	-0.67	4.45 ± 0.71	3.63	1.33 ± 0.34
C3	0.330	0.76	4.16 ± 0.66	3.31	9.50 ± 5.83

the backprojected tracer distribution deviates significantly from the homogeneous diffusion curve.
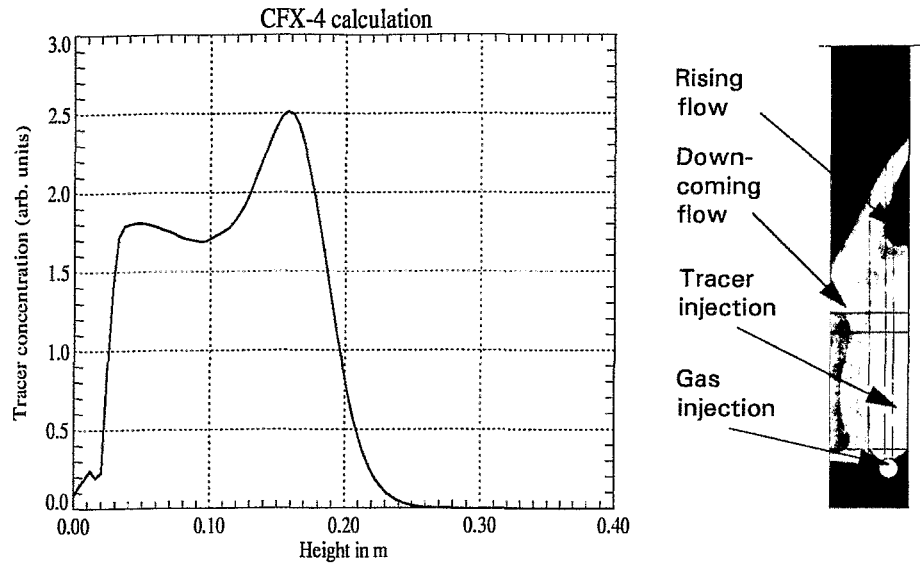
Fig. 4: Tracer distribution in the *x-y*-plane of the tank (right) and axial distribution projected to the tank midplane (left) for experiment A1

This effect could not be detected in the measurements, because the lower part of the tank could not be seen by the detector array (Fig. 1). A similar effect was found in the calculated results of experiment B3. Here the tracer cannot penetrate into the downcomer zone because of the subdivision of the tank, but it swaps over the top of the subdividing shield. Within the range of uncertainties caused by these effects, the calculated values of the dispersion coefficient for the experiments of group A are in good agreement with the experimental results and the results obtained by Ohki and Inoue [5] for bubble columns.
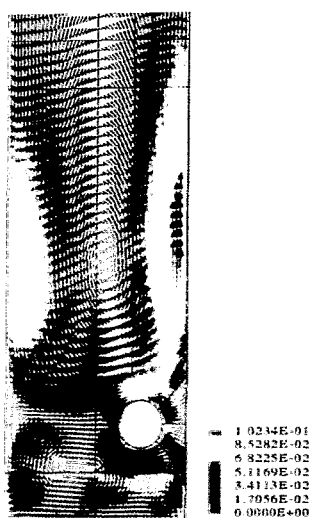
Fig. 5: Local distribution of the fluid velocity in the tank

In general, the experimental values of the turbulent dispersion coefficient and the tracer velocity depend rather sensitively on the local fluid velocity and the local turbulent viscosity. Fig. 5 shows the velocity field in the lower part of the tank for the experiment A1. From the comparison between measured and calculated turbulent flow parameters compiled in Table 1 the following conclusions can be drawn:

For the experiments of group A (air injection into water), the relation between measured and calculated values can be interpreted with a tracer penetration into the downcoming flow. This can also explain the stagnation or even reduction of the tracer movement with increasing gas flow in the experiments of groups A and C.

54

For low gas flow rates (j_{gas} < 0.4 cm/s), the measured values of the dispersion coefficient D are underestimated by the calculations, while the calculated tracer velocities are higher than the measured ones. This is probably caused by the underestimation of the turbulent dispersion due to the limited applicability of the turbulence model in the region of low Reynolds numbers.

For the experiments of group B (subdivision between rising and downcoming flow) tracer penetration into the downcomer part is not possible. The natural circulation rate is enhanced by the subdivision. Therefore, the measured and calculated tracer velocities are higher than in experiments without subdivision for the same superficial velocities of the gas. However, the calculated values overestimate the measured ones. This can possibly be explained by the fact, that in the experiments significant fluid velocity oscillations in z-direction were observed, which are increasing the effective measured dispersion coefficient and decreasing the transport velocity. Since this velocity component cannot be modeled in the 2D calculations, some 3D calculations were carried out. However, the experimentally observed oscillations could not be reproduced in these calculations, too.

In general, the agreement between calculated and measured results is much worse for H_2O_2 disintegration than for air injection into water. A possible reason for this fact is the different bubble size spectrum. While the uniform bubble diameter seems to be a good approximation for the air-water flow, we observe very small bubble sizes during H_2O_2 generation at the surface of the tube and their coalescence into larger bubbles during the fluid movement. This effect is not taken into account in the calculation model.
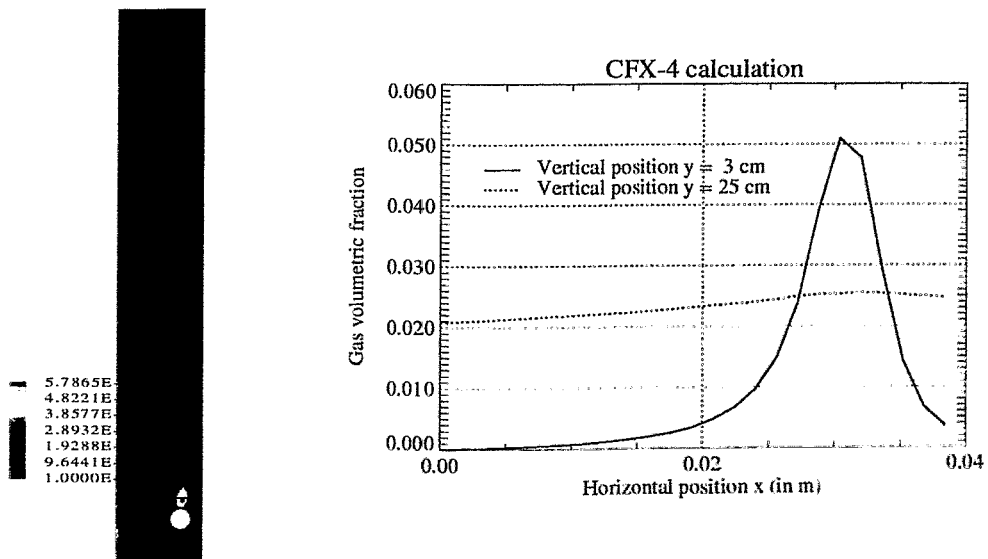
Fig. 6: Gas volumetric fraction distribution for experiment A1

Fig. 6 shows the void fraction distribution over the tank width for the same experiment at different heights and a global view of the void distribution. It can be seen, that it is rather uniform in the upper part of the tank in spite of the fact, that we have a rising fluid flow on the one side of the tank and a downcoming flow at the other side. The bubbles are spread in the fluid due to tur-

bulent dispersion. As the bubble drift velocity in the liquid is higher than the velocity of downcoming fluid, bubbles can rise also in the downcoming stream. This result is in agreement with observations in the experiment.

6. Conclusions

The feasibility of the estimation of turbulent dispersion coefficients in a natural circulation two-phase flow using a Positron Emission Tomography (PET) technique has been shown. Selected experiments were simulated by means of the Computational Fluid Dynamics code CFX-4. The measured average turbulent dispersion coefficient values are significantly affected by local fluid velocity and turbulent viscosity distributions. However, measured and calculated values of the turbulent dispersion coefficient are in good agreement with literature results for bubble columns in the case of air injection into water. In the case of catalytic decomposition of H_2O_2, discrepancies occur which are probably caused by the specific bubble size spectrum, what has to be clarified in further investigations.

However, it was necessary to take into account the significant deviation of the tracer distribution from the ideal diffusion equation solution in some cases, in particular if the tracer has been spread over upwards and downwards regions of the natural circulation velocity field.

References

[1]   Jonkers G. et al. (1992), Surface catalysis studied by in situ positron emission. *Nature* 63, 355

[2]   van den Bergen E.A. et al. (1989), Industrial Applications of positron emission computed tomography. *Nucl.Geophys.* 3, 407

[3]   Hensel F. (1996), "Studies of Liquid-Gaseous Two-Phase Systems by Positron Emitting Radiotracers", in Weiß F.-P., Rindelhardt U. (Ed.), *Institute for Safety Research. Annual Report 1995* (pp. 12-16) Schönfeld-Weißig, Forschungszentrum Rossendorf e.V.

[4]   Pawelke J., Byars L., Enghardt W. et al. (1996), The investigation of different cameras for in-beam PET imaging. *Phys. Med. Biol.* 41, 279

[5]   Ohki Y., Inoue H. (1970), Longitudinal mixing of the liquid phase in bubble columns. *Chem. Eng. Sci.* 25, 1

[6]   Millies M. (1993), *Fluiddynamik, Vermischung und Stoffübergang in Zirkulationszellen in Blasensäulen.* Fortschr.-Ber. VDI Reihe 3 Nr. 307, 100

[7]   Hensel, F. (1997), Studies of Liquid-Gaseous Two-Phase Systems by Positron Emitting Radiotracers. *Appl. Radiat. Isot.* 48, 1485

[8]   *CFX-4.1 Users Guide* (1996), AEA Technology, Computational Fluid Dynamics Division, Oxfordshire

VOID FRACTION MEASUREMENT IN FOAMING LIQUIDS USING NEEDLE SHAPED CONDUCTIVITY PROBES

T. Kern

1. Introduction

Gas-liquid dispersions are of great importance to the chemical and process industries. Absorption and distillation columns, flotation and bubble columns, sewage treatment and fermentation are just a few examples. During the process gas-liquid foam can occur which is not always desired. Whereas foam is used in flotation columns to fractionate mixtures, it has negative effects in many other applications.

The knowledge of the void fraction of gas-liquid dispersions is therefore a matter of interest for the process control and modelling. One technique to measure void fractions in gas-liquid dispersions are needle shaped conductivity probes. They have been applied successfully in bubbly flows [1,2,3,4]. However, they have not yet been tested in foam.

Until now it has not yet been achieved to describe and model foam satisfactorily. Former works of Mersmann [5] investigated only integral parameters such as foam heights. For a comprehensive modelling of foam it is therefore indispensable to measure the properties of foam precisely. That was the reason to improve needle shaped conductivity probes in order to measure vertical void fraction profiles in a foam zone above the bubbly flow.

2. Measuring Principle

The measuring principle is based on the different conductivity of gas (air) and liquid (water). If one puts a voltage onto the probe, a current between the probe tip and another electrode in the dispersion can be measured. The magnitude of the current depends on whether there is gas or liquid at the probe tip. This leads to a plot of the probe current versus the measurement time. Introducing a threshold level one gets the times when the probe tip was in contact with liquid and gas respectively. The overall gas contact time divided by the total measurement time results in the time averaged local void fraction:

$$\varepsilon = \frac{T_{GAS}}{T_{TOTAL}}$$

In addition the number of counted bubbles divided by the measurement time delivers the bubble frequency. The bubble frequency can be converted into a

bubble density or a mean bubble diameter. In addition the gas contact times measured yield a contact time distribution which can be transformed into a bubble size distribution assuming vertical upward bubble movement and spherical bubble shape.

In comparison to the bubbly flow the bubbles are densely packed in the foam zone. Therefore the recognition of foam bubbles is much more complicated than in the bubbly flow. Whereas one only records single bubbles in the bubbly flow, one now has to identify the thin lamellae and plateau borders between the bubbles (see Fig. 1).
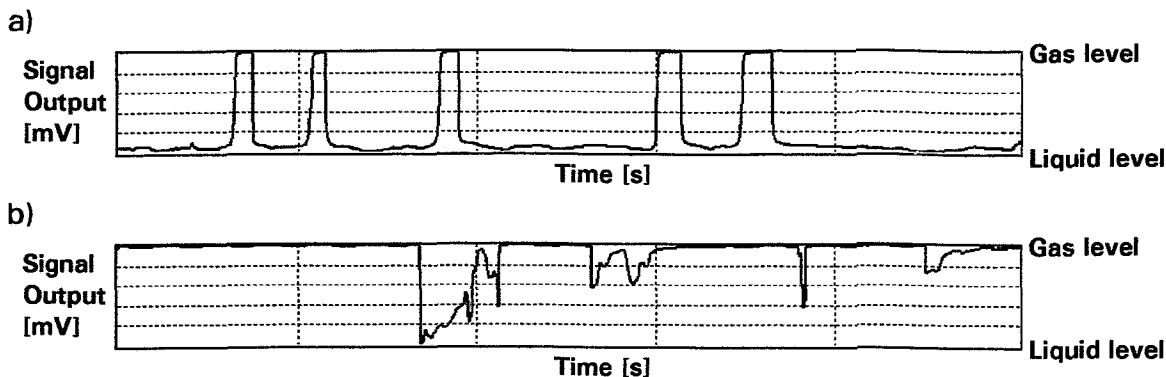
Fig. 1: Differences of the probe signal output
    a) Bubbly Flow: Recognition of single bubbles in liquid
    b) Foam: Recognition of thin liquid lamellae between the foam bubbles

Besides, the conductivity in the foam is reduced in comparison to the pure liquid. It depends on the local foam structure around the probe tip. In contrast to the bubbly flow it is much more difficult to determine the right threshold level which results in the correct void fraction. Another problem is that the probe material is mainly hydrophile and the probe itself can influence the hydrodynamics of the measuring system.

3. Experimental Setup

The probes were used to measure vertical void fraction profiles in a bubble column with a foam zone above the homogeneous bubbly flow. Fig. 2 shows the experimental setup. The bubble column consisted of perspex and had an inner diameter of 100 mm and a height of 1000 mm. The air was injected through the bottom of the column by 91 capillaries of 0.3 mm diameter. It was first cleaned and saturated with water by 4 gas washing bottles. The air flow rate could be adjusted by a pressure reducer and measured by a flow meter. The needle probes were attached to a traversing unit in order to shift them vertically through the dispersion. The probe module on the one hand controlled the needle probes and on the other hand transmitted the measured data to the PC.

In order to achieve a steady foam zone small amounts of alcohol were added to the liquid (water). The alcohols used were isobutylalcohol and amylalcohol. The foam generated was wet and dynamic, i.e. after switching off the gas supply the foam decayed very quickly within a few seconds.
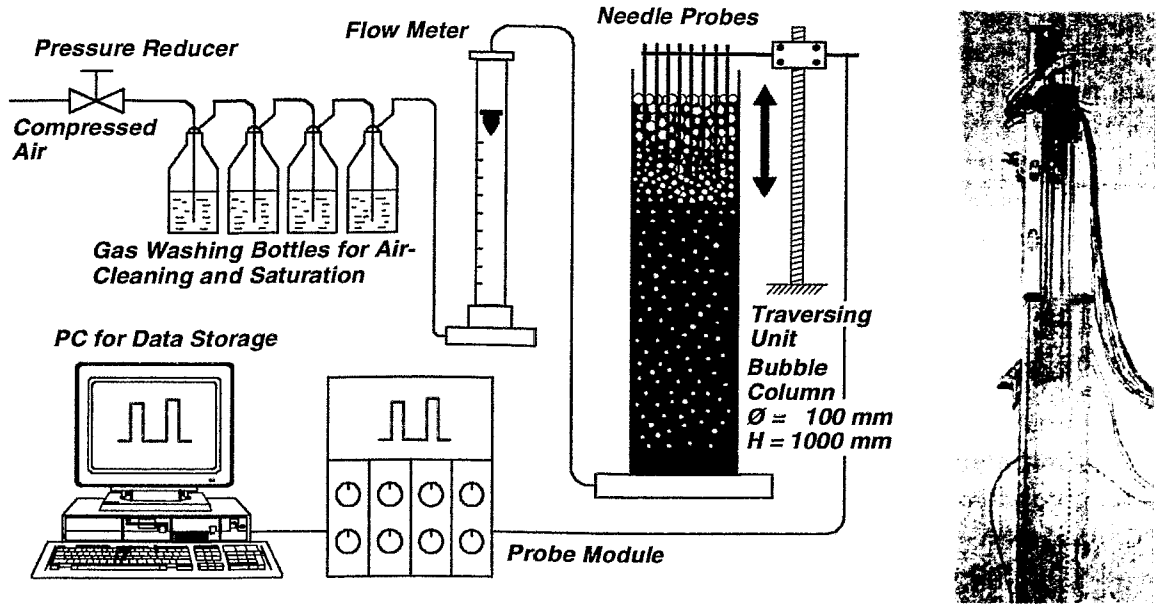
Fig. 2: Experimental Setup

4. Results

As it can be seen in Fig. 3, the void fraction is small and almost constant in the homogeneous bubbly flow regime. At the transition to the foam zone it rises steeply and then increases only slowly in the foam zone. The void fraction reaches its maximum at the coalescing interface. The bubble frequency decreases in the foam due to coalescence. Near the coalescing interface with the homophase the measured bubble frequency rises again which is in contradiction to the coalescence. On the one hand this might be caused by the increasing deformation of the bubbles. Another reason could be that when the bubbles coalesce with the homophase the foam height fluctuates and the foam structure rebuilds rapidly. Hence the same bubbles may be detected several times by a probe.
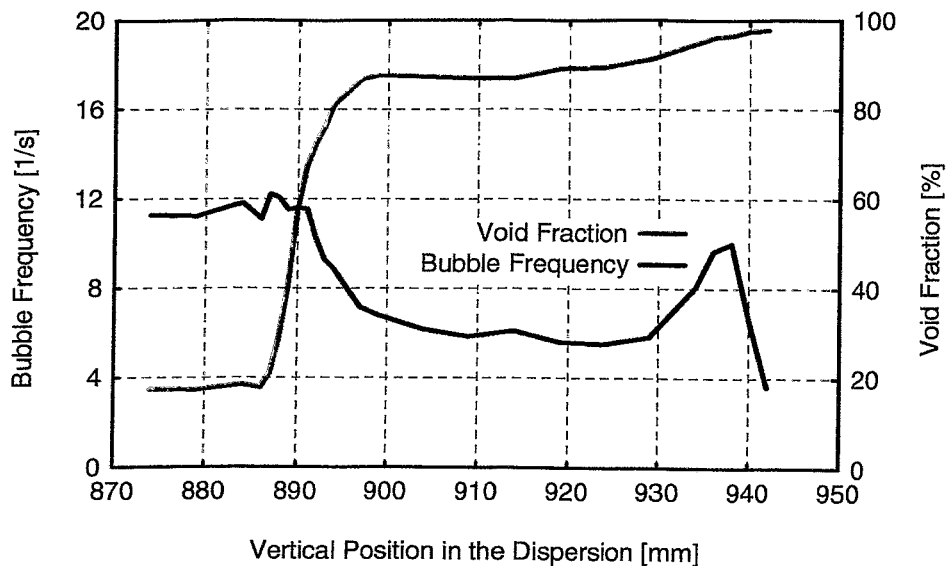
Fig. 3: Vertical Profiles of Void Fraction and Bubble Frequency in an Air/Water-Dispersion with 1 Vol-% Isobutylalcohol. The Superficial Gas Velocity was 2.83 cm/s.

Converting the bubble frequency to a bubble density one receives information on the mean bubble diameter and the coalescence behaviour of the dispersion. Fig. 4 shows an example. The bubble density first rises at the transition from the bubbly flow to the foam zone due to a bubble accumulation at this region. The coalescence in the foam decreases the bubble density, thus the mean bubble diameter increases steadily.
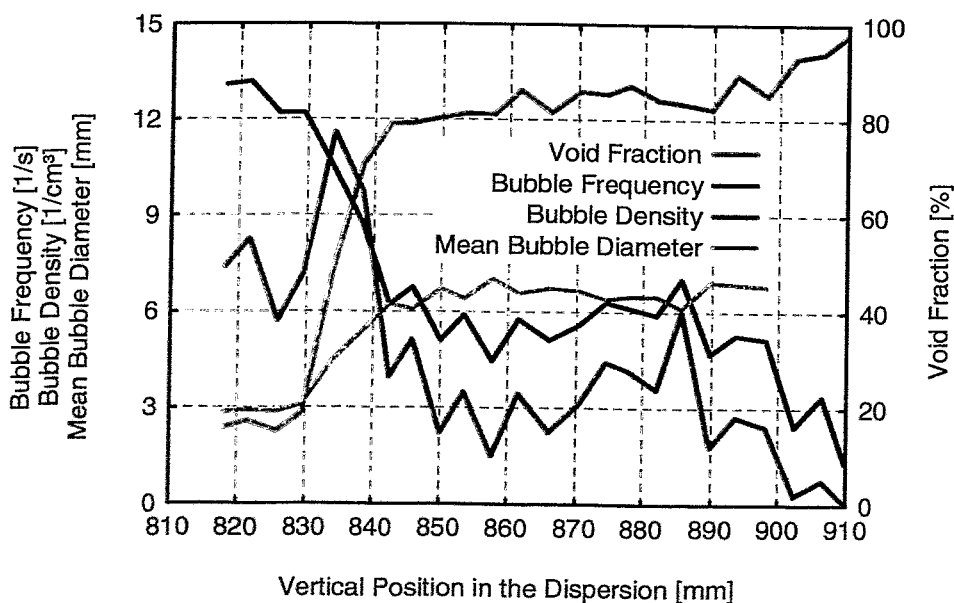
Fig. 4: Vertical Profiles of Void Fraction, Bubble Frequency, Bubble Density and Mean Bubble Diameter in an Air/Water-Dispersion with 1 Vol-% Amyl-alcohol. The Superficial Gas Velocity was 3.01 cm/s.

The vertical profile of the bubble density can be used to determine the coalescence rate in the foam. The coalescence times in the dispersions investigated were below 1 second.

5. Conclusions

Needle shaped conductivity probes are capable of measuring the local void fraction and bubble frequency in foams. The measured values for void fraction and bubble frequency meet the expectations. Only near the coalescing interface with the homophase the increase of the measured bubble frequency could not yet be fully explained. As a next step the comparison of the measured data with another measuring technique, such as γ-densitometry, is required for an accurate calibration of the probes.

References

[1]   H.-M. Prasser and C. Schlenkrich (1995), Void Fraction Measurement in Transient Bubble Columns by Needle Shaped Conductivity Probes, *Proceedings of the 33rd European Two Phase Flow Group Meeting, 30 May - 2 June 1995* (Paper F-2), 's Hertogenbosch, Netherlands

[2]   J. F. Lafferty and F. G. Hammitt (1967), A Conductivity Probe for Measuring Local Void Fractions in Two-Phase Flow, *Nuclear Appl.*, 3, 317

[3]   M. Castello-Branco (1988), *Beitrag zur Hydrodynamik der Gasinjektion in Metallschmelzen*, Dissertation TU Clausthal-Zellerfeld

[4]   K.-W. Linneweber (1981), *Örtliche Gehalte an Gas sowie Gas und Feststoff in Blasensäulen*, Dissertation TU München

[5]   A. Mersmann (1962), *Druckverlust und Schaumhöhen von gasdurchströmten Flüssigkeitsschichten auf Siebböden*, VDI-Forschungsheft 491, Ausgabe B, Band 28, VDI-Verlag Düsseldorf

COMPARING INVESTIGATIONS OF THE DETECTION OF DYNAMIC CRACK INITIATION BY ACOUSTIC EMISSION AND LASER LIGHT SCATTERING

H. Richter, J. Böhmert, M. Valo [1], H.-W. Viehrig

1. Introduction

There are many suggestions but no satisfied solution to determine stable crack initiation under dynamic loading by means of a single specimen method. Apart from methods, which recognise crack initiation from the sophisticated analysis as the load-displacement curve proceeds, the most methods suggested use an additional probe fixed at the specimen or the loading equipment. This probe measures a physical signal or a property which are related to crack initiation or crack growth.

For the instrumented charpy V-notch impact test three methods seem to be successful:

- crack opening displacement (COD)
- acoustic emission (AE)
- magnetic emission (ME).

The COD methods was developed by Rintamaa et al. [1]. The conception uses an inverted impact testing arrangement (rigid hammer with specimen, mobile support). This arrangement allows the measurement of the crack opening and reduces the load oscillations due to the impact impulse. Measurements of the acoustic emission during a Charpy impact test were already carried out by Engelhardt et al. [2,3] with a AE probe fixed at the specimen. In several papers Richter et al. [4-6] could show that an AE probe, which was installed within the hammer tup, records AE signals of different types. A signal type characterized by lower amplitude and longer duration appears in the time range of the crack initiation for the first time. Eventually, applications of ME for crack initiation detection was demonstrated by Winkler [7] and Lenkey et al. [8].

Till now, a convincing, physically based model, which describes the relation between material processes during crack initiation and the signal response of the above-mentioned methods, has not yet been existing. An evaluation of the methods can, therefore, only be performed on the base of an empirical comparison. For that the inverted pendulum equipment was additionally equipped with AE- and ME-probes. Thus, for the first time crack initiation could be

---

[1] VTT Manufacturing Technology Espoo (Finland)

determined at the same specimen by these three methods. The use of material of different strength-toughness-relations generalizes the comparison. Besides the crack initiation was determined by a multiple specimens method in order to support the verification of the single specimen methods. The paper reports about the results of this investigation.

2. Experimental

2.1 Material

The study uses the heat resistant 10CrMo9 10 steel according to DIN 17243 and the ASTM-related A533B1 pressure vessel steel. The chemical composition is given in table 1. The mechanical properties of the 10CrMo9 10 steel was varied by annealing. The survey of the mechanical properties, which the different steels or states respectively exhibit, is shown in table 2. Different values of the toughness was, furthermore, reached by different orientation of the specimen (L-T, T-L according to ASTM E 399).

Table 1: Chemical composition of the material (weight-%)

Material	Code	C	Si	Mn	P	S	Mo	Cr	Ni	Cu
10 CrMo 9 10	1	0.10	0.32	0.55	0.01	0.019	0.96	2.32	0.10	0.15
ASTM A533B1	JRQ	0.18	0.24	1.41	0.02	0.007	0.50	0.13	0.87	0.15

Table 2: Mechanical properties of the material

Abbr.: $R_{p0.2}$ - 0.2 % yield strength; R_m - tensile strength; A_g - uniform elongation, A_5 - total elangation related to measuring length $l = 15\ d_o$; Z - reduction of area; USE - upper shelf energy; $T_{68\ J}$ - transition temperature related to 68 J impact energy; R_{ed} - dynamic stress at general yield 7load; R_{md} - dynamic stress at maximum load

Material/ Specimens Code		$R_{p0.2}$ MPa	R_m MPa	A_g %	A_5 %	Z %	USE J	$T_{68\ J}$ °C	R_{ed} MPa	R_{md} MPa
ASTM A533B1										
JRQ (L-T)	55	477	630	-	26	76	212	-13	612	790
10 CrMo 9 10										
D (L-T)	24	740	825	7	22	73	191	-47	885	1119
D. (T-L)	24	-	-	-	-	-	55	-	870	995
E (L-T)	24	627	723	9	27	75	206	-99	776	973
F. (T-L)	24	-	-	-	-	-	100	-20	625	835
G (L-T)	24	392	512	25	50	81	>300	-105	550	783

Altogether, material with a yield stress range of 390 MPa to 740 MPa, an upper shelf energy of 55 J to > 300 J and a transition temperature of -105 °C to -13 °C was available.

2.2 Testing condition

The tests were carried out at the inverted and laser instrumented pendulum equipment of the VTT Espoo in Finland [1]. This arrangement measures COD by means of laser light scattering at the crack surfaces. The AE measurement was performed by an equipment developed by Institute for Safety Research of the Forschungszentrum Rossendorf. For adjustment of this equipment the inverted pendulum was modified. Additionally, a ME probe developed by Winkler was used for the a ME measurement.

The total measuring arrangement and the characteristic parameters of the measurement system are shown in Fig. 1.

① Moving hammer ③ Magnetic transducer
② Instrumented tup / ④ Specimen
  AE transducer

Fig. 1: Experimental arrangement for impact load testing at an inverted impact pendulum tester with simultaneous measurement of AE and ME.

The specimens used were ISO-V notch specimens, 20 % side grooved and fatigue cracked up to a crack length-to-width-ratio $a_o/W = 0.5$.

The specimens were impact-loaded by 3-point-bending. The characteristic loading parameters were: hammer mass $m_H = 41$ kg, deflection angle $\alpha_0 = 60°$, pendulum length $l_{red} = 804$ mm, impact velocity $v_0 = 2,8$ m s^{-1}, impact energy $E_0 = 161$ J. These conditions remained constant for all tests.

The specimens were tested in the temperature interval of -50 to +150 °C. The interval covers the lower transition range and reached the upper shelf energy range. After testing the specimens were microfractographically evaluated and both ductile crack growth and stretch zone length were measured.

3. Results

For the most part, characteristic signal phenomena could be recognized by the AE- and COD-method. Only in the lower transition range neither the COD method nor the AE method provide any evidence of crack initiation. This is not unexpected for the COD method because the evaluation procedure requires a sufficiently large stable crack growth. The AE-method, probably, fails as the crack initiation already starts before the AE impact signals are faded. These impact AE signals were not reduced by the inverted arrangement in contrast to the load oscillations. Apart from one material state, the ME method did not give information about crack initiation.

In Fig. 2 characteristic signal sequences are depicted and the detection points for crack initiation are marked.
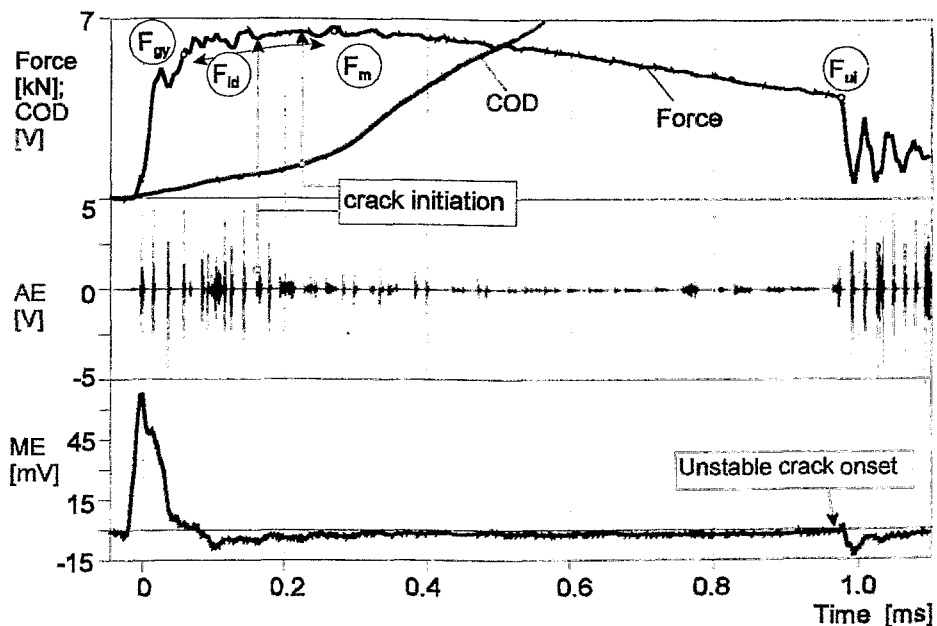
Fig. 2: Characteristic load-, COD-, AE-, and ME-curves in the ductile brittle transition range.

When perceptible, the crack initiation times were determined by the different methods. The corresponding load-displacement values were used to calculate the consumed deformation energy and the J-integral J_i on formally the same way as usual for static 3-point bending according to ESIS P2-92 [9]. This J-integral is

defined as dynamic crack initiation toughness J_{id}^{COD}, J_{id}^{AE} or J_{id}^{ME}. The upper index refers to the method used.

For the 10CrMo910 steel, heat treatment D the temperature dependence of the dynamic J-integrals is shown in Fig. 3 as an example. In addition to the crack initiation toughness, the J-integral for unstable crack growth $J_{d\Delta a}$ and the J-integral at the load maximum J_{dm} are also presented. Their course provides the typical temperature dependence of the toughness behaviour of ferritic steels.
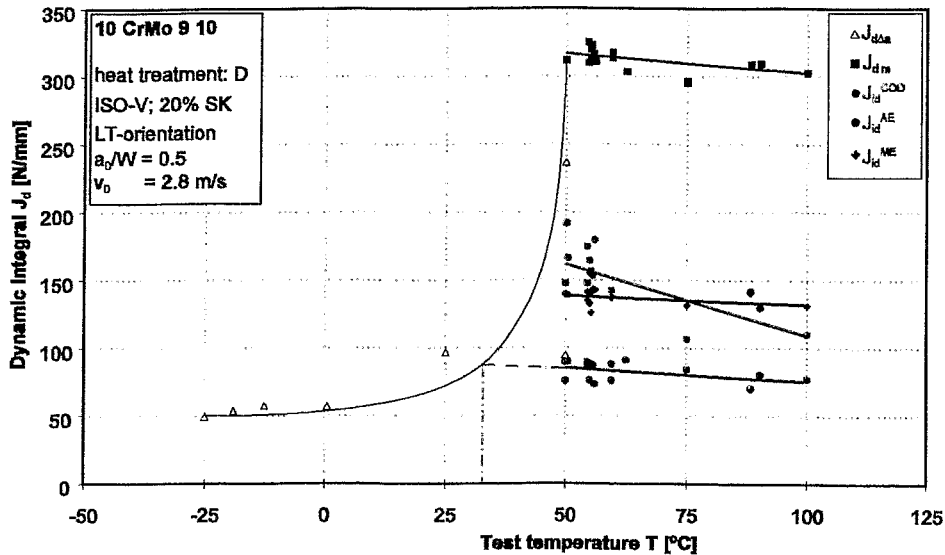
Fig. 3:   Dynamic J-integrals in dependence on the temperature for 10CrMo9 10 steel, state D.

Instable crack growth occurs at low temperatures and low J-integral values. In the transition temperature range instable crack growth appears after preceeding stable crack growth and, thus, with higher J-integral values. The crack initiation toughness J_{id}^{AE} determined by AE is only little higher than the instable crack initiation $J_{d\Delta a}$ and hardly depends on the temperature. The COD method indicates crack initiation clearly later what yields higher values J_{id}^{COD}. These values weakly decline with increasing temperature, similar to the temperature dependence of the J-integral at maximal load J_{dm}. The same tendencies are found for the other materials or material states. For further evaluation the weak temperature dependence was neglected and mean values were calculated from all results of one specimen set. These values are given in table 3 together with the crack initiation toughness J_{id}^{SZW} which was determined by the multiple specimen method. As an appropriate procedure the cleavage method according to Böhme [10] was selected. It uses the phenomenon that different contributions of stable crack growth can be realized by small temperature variation within the transition temperature range. The different values of the stable crack growth Δa are connected with the consumed deformation energy. In this way the crack resistance curve J-integral = f(Δa) can be calculated. Additionally, the stretch

66

zone width SZW is measured. Then the crack initiation toughness is equal to the J-integral at a crack growth Δa_i = SZW. A disadvantage of the method is that only few measuring points lie near crack initiation. Therefore, the curve has to be extrapolated from the range of higher crack growth and has a limited accuracy in the range of crack initiation.

Table 3: Crack initiation toughness J_{id} determined by single specimen method in comparison with the physical crack initiation toughness J_{id}^{SZW}

| Code | SZW [mm] $(SZW)_i = \Delta a_i$ | dynamic crack initiation toughness [N/mm] | | |
		$J_{id}^{SZW\,*)}$	J_{id}^{AE}	J_{id}^{COD}
JRQ	0.07	120 ± 16	102 ± 23	113 ± 22
D (L-T)	0.044	83 ± 5	83 ± 7	148 ± 27
D. (T-L)	0.024	41 ± 1	76 ± 4	109 ± 30
E (L-T)	0.042	79 ± 10	74 ± 24	144 ± 26
F. (T-L)	0.029	60 ± 2	73 ± 7	116 ± 20
G (L-T)	0.092	142 ± 16	62 ± 8	115 ± 21

*) curve fit according to power law: $J_d = A\,\Delta a^B$

Dynamic crack resistance curves determined this way are shown in Fig. 4 for two orientations of state D of 10CrMo910 steel. One can see the lower crack resistance and, thus, the lower toughness of the T-L orientation. Fig. 4 also shows the crack initiation toughness determined by the different methods. It is clearly visible that the COD method detects crack initiation not before larger stable crack growth occurs. The crack initiation points determined by COD correspond to the engineering approach of the crack initiation related to 0.2 mm crack extension [9]. AE shows crack initiation near the SZW multiple specimens method for this example. In other cases the J_{id}^{AE} values are clearly lower than J_{id}^{SZW}.
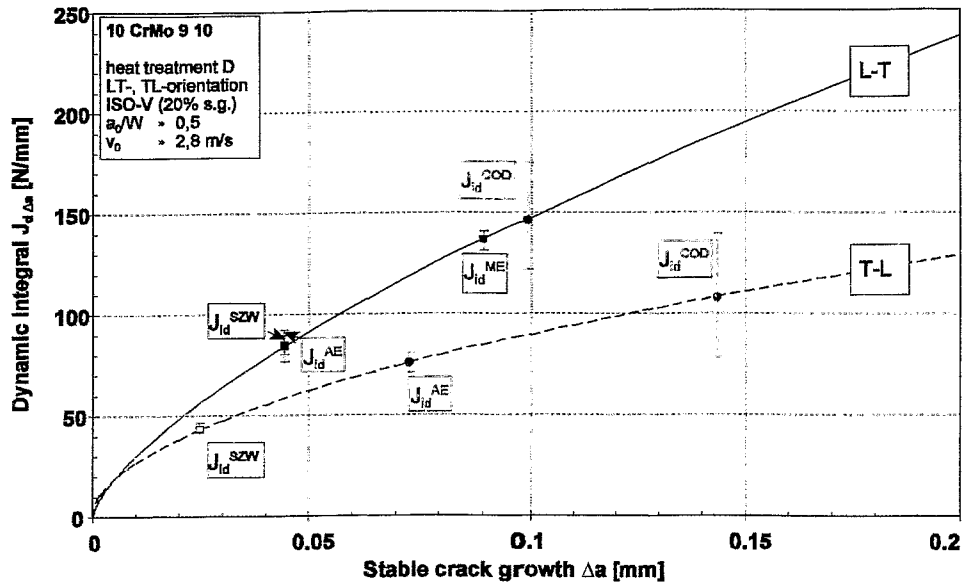
Fig. 4: Dynamic J_d-Δa-crack resistance curve with scatter band for ductile crack initiation obtained with different methods, material: 10CrMo 9 10, state D, orientation: L-T; T-L.

Assuming that the SZW multiple specimens method provides the correct (physical) crack initiation toughness values, Fig. 5. illustrates a summarizing evaluation.
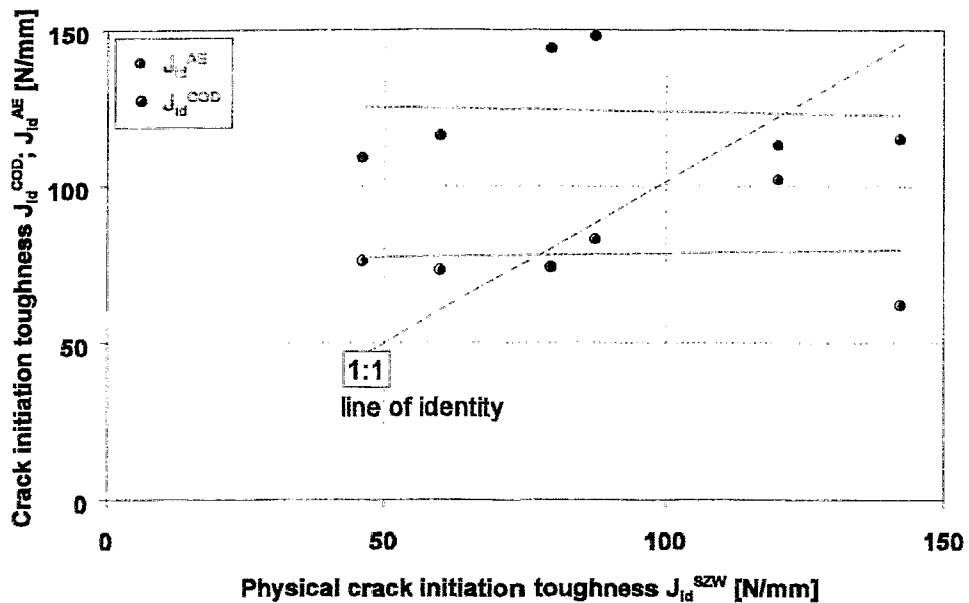
Fig. 5: Comparison of the crack initiation toughness determined by AE and COD with the physical crack initiation toughness J_{id}^{SZW}.

In Fig. 5 the crack initiation toughness defined by COD or AE is compared with the physical crack initiation J_{id}^{SZW}. By considering all results there is neither a correlation between COD-crack initiation toughness and J_{id}^{SZW} nor between AE crack initiation toughness and J_{id}^{SZW}. Especially the AE method provides values which only weakly depend on the material, orientation and heat treatment.

Richter [6,11] has, however, proven in previous studies that AE is produced near the crack tip and in the temporal vicinity of the physical crack initiation. From the point of view of the results of this paper one can conclude that AE is connected with material processes, which are certainly characteristic for the material response in the vicinity of crack initiation.

When the two measuring points of high toughness are neglected there is a 1:1 correlation between J_{id}^{COD} and J_{id}^{SZW} although shifted to higher J_{id}^{SZW} values. This stimulates two conclusions. First, the COD method responds to crack initiation with delay and is suitable to determine an engineering approach of the crack initiation toughness. Secondly, the COD method is not universally applicable. Strong deformation before crack initiation additionally influences the COD measurement and distorts the results.

4. Summary

For the first time, Charpy V-impact tests were performed using an integrated testing equipment which simultaneously records COD, AE, and ME. In this way crack initiation toughness was determined and compared with the physical crack initiation toughness. That was determined by a dynamic multiple specimens methods according to the ESIS P2-92 procedure for quasistatic 3 point bending. The comparison was carried out for several steels with widely modified strength and toughness levels.

Both COD- and AE-method but not the ME method are suitable to provide a fracture mechanical parameter for characterizing the onset of stable crack growth, at last if the ductile crack growth is more than about 0.1 mm. The use of these methods provides a better approximation of the critical load for crack initiation than the use of the maximum load point as often proposed. However, the methods do not detect the same material processes. The COD method only responds after sufficient stable crack growth and results in higher crack initiation toughness. AE is very sensitive against material processes in the vicinity of crack initiation but does not seem to directly indicate stable crack growth.

The crack initiation toughness hardly depends on the temperature and is only little higher than the J-integral for instable crack growth. This corresponds to the assumption of two competing mechanisms which need comparable energy in the ductile brittle transition range.

References

[1] R. Rintamaa, K. Rahka, K. Wallin, K. Ikonen, H. Talja, H. Kotilainen, E. Sirkkola (1994), *Instrumented impact testing machine with reduced specimen oscillation effects*, Espoo, Technical Research Centre of Finland, Research Reports 290

[2] A. H. Engelhardt, H.-D. Steffens, H.A. Crostack (1978), Anwendung der Schallemissionsanalyse beim instrumentierten Kerbschlagbiegeversuch, DVM, Deutscher Verband für Materialprüfung e.V., *10. Tagung des DVM-Arbeitskreises Bruchvorgänge*, Darmstadt, S. 95-106

[3] H.-A. Crostack, H.-D. Steffens, A.K. Engelhardt (1981), Measurement of Dynamic Fracture Toughness Applying Acoustic Emission Techniques, In: G.C. Sih, M. Mirabile (Eds.): *Analytical and Experimental Fracture Mechanics*, Proc. Of an Internat. Conf.; Alphen an den Rijn (Netherlands), pp. 507

[4] H. Richter, H.-W. Viehrig, S. Winkler (1994), Ermittlung dynamischer Rißeinleitungszähigkeiten mit dem instrumentierten Kerbschlagbiegeversuch bei elastisch-plastischem Werkstoffverhalten, *26. Vortragsveranstaltung des DVM-Arbeitskreises Bruchvorgänge*, Magdeburg, Vortragsband DVM, S. 373

[5] H. Richter, J. Böhmert, H.-W. Viehrig (1996), Determination of Crack Initiation Toughness by Impact and Dynamic Testing, *Proceedings of the 11th European Conference on Fracture - ECF 11*, Vol. III, Ed. J. Petit, Poitiers-Futuroscope, France, pp. 2001

[6] H. Richter (1997), Untersuchungen zum Rißeinleitungsverhalten von Stahl unter schlagartiger Belastung mittels Schallemission, Deutsche Gesellschaft für Zerstörungsfreie Prüfung e.V., *Statusberichte zur Entwicklung und Anwendung der Schallemissionsanalyse*, 11. Kolloquium Schallemission, Jena, DGZfP-Berichtsband 58, S. 77 ff.

[7] S. Winkler (1988), Magnetic Emision Detection of Crack Initiation, in: J.P. Gudas, J.A. Joyce, E.M. Machell (Eds.), *Fracture Mechanics: Twenty-First National Symposium*, ASTM STP 1074, Philadelphia, American Society for Testing and Materials (ASTM), pp. 178

[8] G. Lenkey, S. Winkler, Z. Major, I. Lévay (1996), Applicability of Magnetic and Electric Emission Techniques for Detecting Crack Initiation in Impact Tests, *Proceedings of the 11th European Conference on Fracture - ECF 11*, Poitiers-Futuroscope, France, pp. 1989

[9]   ESIS P2-92 (1992), *ESIS Procedure for Determining the Fracture Behaviour of Materials*, European Structural Integrity Society, Delft, The Netherlands, January 1992

[10] W. Böhme (1989), *Experimentelle Untersuchungen zum Elastisch-Plastischen Bruchverhalten eines Druckbehälterstahles unter dynamischer Beanspruchung*, Fraunhofer-Institut für Werkstoffmechanik, IWM-Bericht W3/89

[11] H. Richter, J. Böhmert, H.-W. Viehrig, The use of acoustic emission todetermine characteristic dynamic strength and toughness properties of steel, *Nucl. Eng. & Des.*, submitted for publication

EFFECTS OF IRRADIATION AT LOWER TEMPERATURE ON THE MICROSTRUCTURE OF Cr-Mo-V-ALLOYED REACTOR PRESSURE VESSEL STEEL

M. Grosse, J. Boehmert, R. Gilles[1]

1. Introduction

The microstructural damage process due to neutron irradiation [1] proceeds in two stages:

- formation of displacement cascades
- evolution of the microstructure by defect reactions.

In the first stage atoms are removed by multiple collision from their regular lattice positions, thereby creating vacancy-rich displacement cascade cores and a large number of interstitial defects (Frenkel pairs, isolated point defects) at their periphery. Additionally, precipitates can be dissolved partially or completely. These processes occur almost spontaneously and depend on the material parameter (crystal structure, chemical composition) and the irradiation condition (neutron energy, dose rate) but hardly on the temperature.

During the second stage the surviving point defects and super-small clusters can be rearranged. They can be annihilated by recombination, can escape from their native displacement cascade, can be trapped in sinks like grain boundaries, voids, interfaces or dislocations, or can form dislocation loops. Basically, the system will enter a permanent non-equilibrium state with high point defect supersaturation. This yields irradiation-enhanced or irradiation-induced precipitation and competes with the above-mentioned process of precipitation dissolution. The processes are strongly influenced by the temperature. The higher the irradiation temperature the lower is the concentration of the surviving point defects and the nearer is the state of the system to the equilibrium.

Continuing our systematic investigation about the microstructural changes of Russian reactor pressure vessel steel due to neutron irradiation the microstructure of two laboratory heats of the VVER 440-type reactor pressure vessel steel after irradiation at 60°C was studied by small angle neutron scattering (SANS). 60°C-irradiation differently changes the irradiation-induced microstructure in comparison with irradiation at reactor operation temperature and can, thus, provide new insights into the mechanisms of the irradiation damage.

---

[1] Hahn-Meitner-Institut Berlin

2. Experimental

The study used two laboratory heats (designation: ESW-A, ESW-C) of 15 CrMoV 2 steel (Russian code: 15kh2MFA), which meet the Russian regulation for the VVER 440-type vessel steel. The essential difference between the two heats is the copper content. The heats were produced as a 50-kg ingot, forged, rolled and hardened by a typical heat treatment for VVER440-type vessel steel. Details of the fabrication are given in [2]. The chemical compositions are listed in Table 1. Charpy V-standard specimens from these heats were irradiated at the Research Reactor Rossendorf (RFR) at about 60°C [2] according to the condition given in Table 2.

Table 1:   Chemical composition (in at-%) of the used materials (Fe: balance)

material code	C	N	Si	P	V	Cr	Mn	Ni	Cu	Mo
ESW-A	0,67	0,07	0,27	0,03	0,24	2,45	0,27	0,07	0,12	0,39
ESW-C	0,67	0,07	0,35	0,03	0,33	2,78	0,36	0,06	0,29	0,39

Table 2:   Irradiation conditions

Material	Reactor	Fluence [10^{18} cm^{-2}]	dpa [10^{-2}]	Temp. [°C]
ESW-A	RFR Rossendorf	23	3.1	60
ESW-C		11	1.5	

Samples of a thickness of 1 mm were cut from Charpy specimens and investigated in the unirradiated, in the irradiated and in a state made by subsequent annealing at 270°C/1h.

The SANS experiments were performed at the SANS-V4 facility at the BER-II research reactor of the Berlin Neutron Scattering Center BENSC [3]. In order to gain genuine size distribution of the scattering defects the experiment was focused on the measurement of the scattering vector over a wide range. This was realized by measuring with two different sample-detector distances. For the absolute calibration a water standard was used. The characteristic data of the SANS experiments are summarized in Table 3.

The calibration, the correction of the detector sensitivity and of the background, the radial averaging of the SANS intensity and the separation between magnetic and nuclear scattering were carried out by BENSC standard software. With the

differential scattering cross section calculated in this way, the size distribution function, defined as volume distribution $D_V(R)$, was calculated by the Glatter method [4] using Glatter`s ITP92 software.

Table 3:   Experimental data of the small angle scattering experiments

Neutron wavelength / nm	0.6
sample-detector-distance / m	1.09; 4.00
measuring range of the scattering vector/nm^{-1}	0.2 ... 3.0
magnetic field / T	1.4
detector	2-dimensional position sensitive cells: 64x64, cell size: 1 cm x 1 cm

3. Results

Fig. 1 shows the magnetic scattering of the three states of the material ESW-A. Similar figures are obtained for the nuclear scattering and for the other material. There are obvious differences between the three states, preferentially but not only at higher values of the scattering vector.
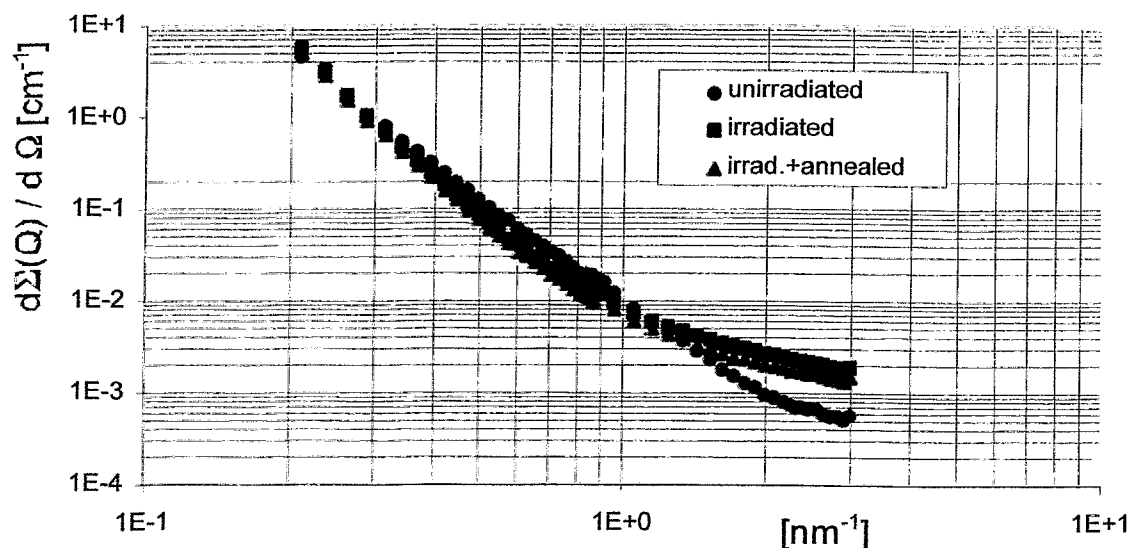
Fig. 1: Magnetic small angle neutron scattering of the unirradiated, the irradiated and the irradiated + annealed (270 °C) states of material ESW-A

In this range the differential scattering cross section seems to be only weakly dependent on the scattering vector. This points to the existence of a constant, that means scattering vector independent, contribution. Such constant contributions are caused by incoherent scattering, for example due to different iron isotopes, and by

74

the monotonic Laue scattering of point defects in the matrix. The constant contribution can be estimated from the measured scattering by assuming the validity of Porod´s law [5]. According to Porod the small angle scattering intensity decreases proportionally to the fourth power of the scattering vector. Fig. 2 shows a Porod plot of the measured magnetic scattering of ESW-A irradiated. The linear course proves the validity of the approximation; the slope of the line provides the constant scattering contribution. Analysing the measuring data in this way the results given in Table 4. are obtained. The constant scattering contribution has the lowest value in the unirradiated state, especially regarding the magnetic scattering. Irradiation enhances the constant scattering contribution, annealing slightly reduces it.
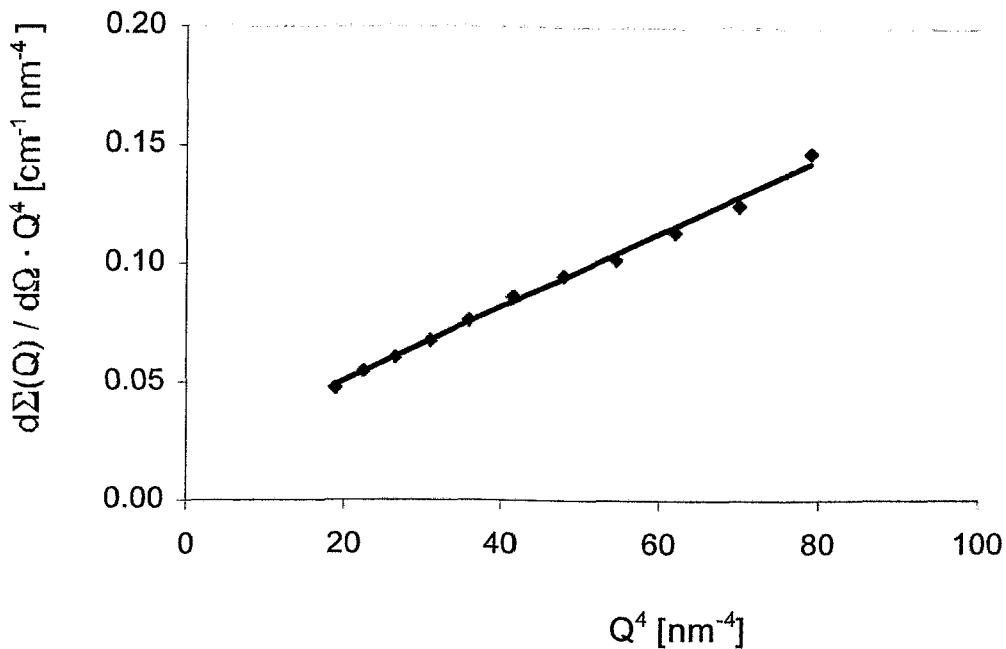
Fig. 2: Porod plot for the estimation of the constant scattering contribution: ESW-A, irradiated, magnetic scattering

Table 4: Constant scattering contribution of the investigated materials

$(d\Sigma/d\Omega)_c$ [cm^{-1}]	ESW-A			ESW-C		
	unirrad.	irrad.	irrad. + ann.	unirrad.	irrad.	irrad. + ann.
nuclear	0.002056	0.002728	0.002440	0.002184	0.002530	0.002338
magnetic	0.000430	0.001588	0.001245	0.000499	0.001518	0.001414

The differential scattering cross section after the correction is shown in Fig. 3. Figs. 4 and 5 depict the volume distribution functions, which were calculated on the base of the corrected curves.
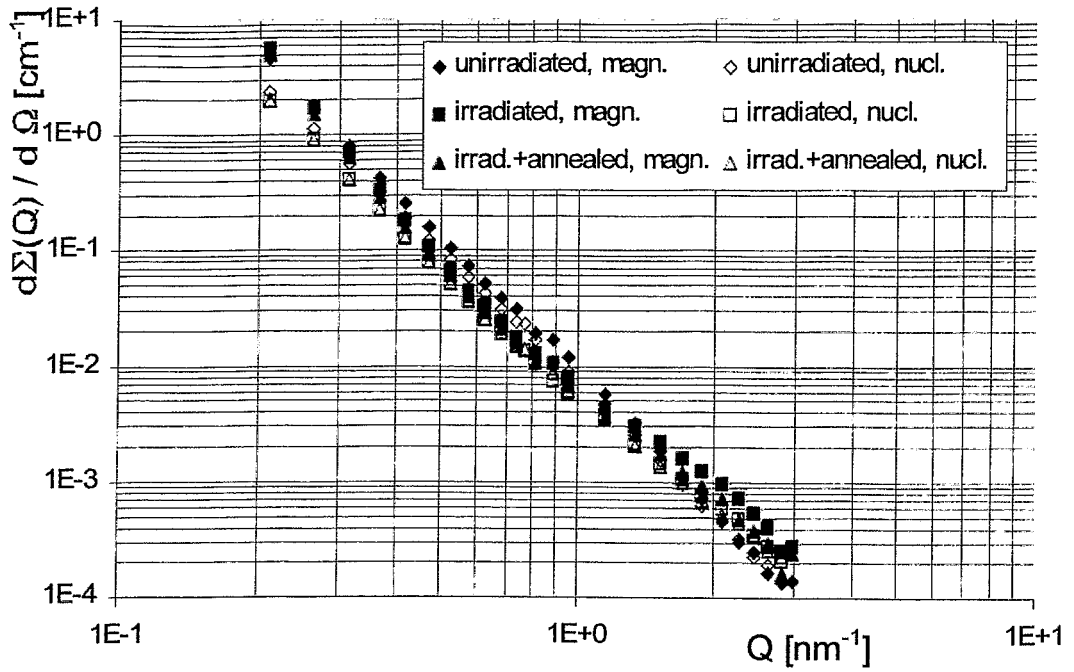
Fig. 3: Corrected magnetic and nuclear small angle neutron scattering of the different states of material ESW-A
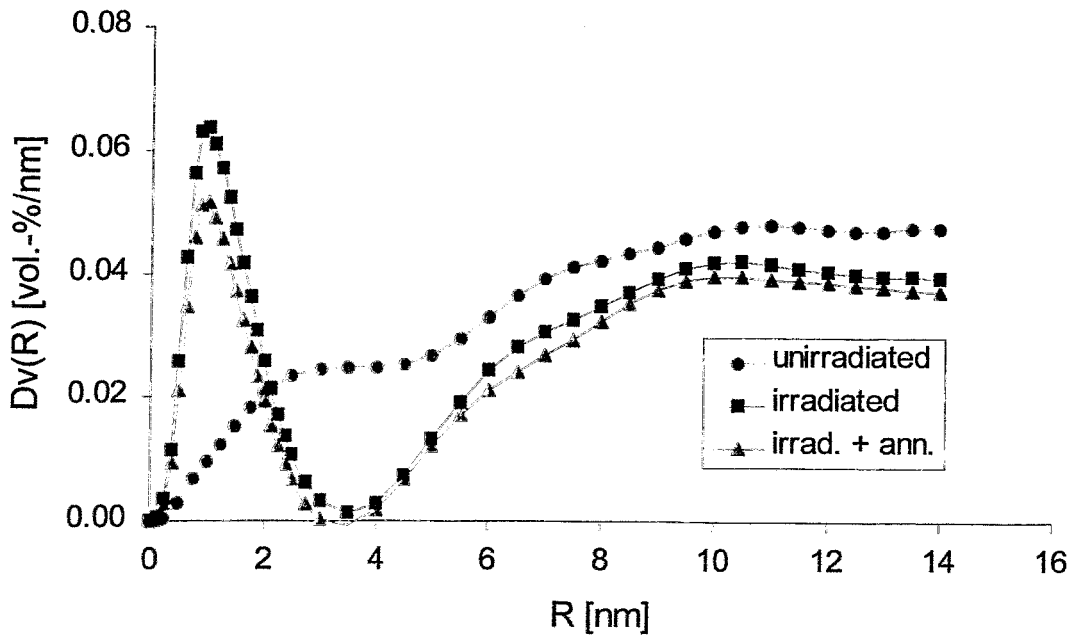
Fig. 4: Volume distribution function of the unirradiated, irradiated + annealed (at 270 °C) state of the material ESW-A, calculated from the magnetic
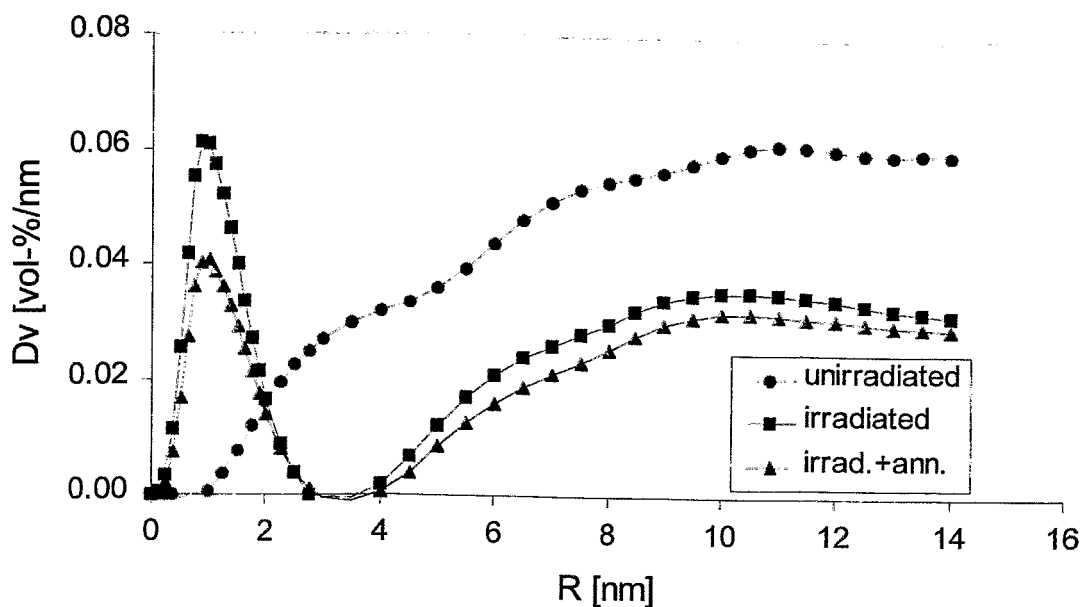
SANS

Fig. 5: Volume distribution function of the unirradiated, irradiated and irradiated + annealed (at 270 °C) state of the material ESW-C, calculated from the magnetic SANS

4. Discussion and conclusion

It is evident that irradiation causes a scattering intensity which does not depend on the scattering angle. This constant scattering contribution can be recognized by means of small angle scattering measurements. It influences the measuring results and can yield distorted results when not considered. Recently, it is not usual to analyse the measuring results in this way. After irradiation at reactor operation temperature the constant contribution is, however, less significant. In order to consider the constant contribution, the first condition is to measure over a sufficiently large range of the scattering vector.

In the unirradiated state the constant scattering contribution is mainly caused by the different scattering length of the iron isotopes. The different isotopes only cause nuclear scattering. Therefore, the contribution of the constant magnetic scattering is very low. As irradiation does not significantly change the isotope composition, the increased contribution after irradiation results from the production of additional point defects. The stronger increase of the magnetic scattering than of the nuclear scattering seems to be caused by formation of point defects which strongly differ from the iron atoms in the magnetic length than in the nuclear length. Such point defects could be, for instance, copper or nickel but

77

no vacancies. Annealing at 270°C diminishes only weakly the number of point defects.

The volume distribution curve shows a broad maximum for particles of a radius between 10 to 15 nm. Precipitates of this size can be seen by transmission electron microscopy. Irradiation results in a reduction of the content of such precipitates which are dissolved due to the knock-out-process by the neutrons. After irradiation at reactor operation temperature the dissolution of precipitates cannot or hardly be observed because, obviously, the re-precipitation covers the process of dissolution.

Without further investigation it cannot be understood why the process is more pronounced for the material ESW-C than for ESW-A although the material ESW-A was irradiated to higher fluence. Maybe, the higher content of carbide forming elements (Cr,V) in ESW-C results in a higher content of precipitates, already in the as-received state.

Finally, in accordance with the results after irradiation at elevated temperatures, irradiation produces a large number of defects with sizes between 0.3 and 3 nm and a maximum at about 1.0 nm. The irradiation-induced defects are decreased by 270°C annealing. The ratio between the magnetic and the nuclear small scattering, which provides information about the composition of the scattering defects, shows differences between the different states and the different size ranges. For the larger precipitates the ratio (A = 2.5) is in accordance with the expected value for vanadium carbide. The irradiation induced defects have higher values (A = 3.0 - 3.2) as expected for copper rich precipitates. The values are reduced by annealing (A = 2.0 - 2.2) what suggests that the composition of the defects is changed. Trapping of vacancies could explain the effect and would correspond with the simultaneous reduction of point defect concentration.

Comparing both alloys it can be stated that the volume fraction of nanoscale precipitates increases with the copper content whereas their thermal stability decreases. This confirms earlier investigations at VVER 440-type vessel steel irradiated at elevated temperatures [6,7].

The Laue scattering can be measured without genuine small angle scattering being superimposed as scattering background between the Bragg reflexes in the wide angle range. Such experiments are in preparation.

References

[1]   W. Schilling, H. Ullmaier (1994), Physics of Radiation Damage in Metals, in: *Materials science and Technology: A Comprehensive Treatment*/ed. by R.W. Cahn, P. Haasen, E.J. Kramer, Vol. 10, Nuclear Materials,vol.-ed.: Brian R.T. Frost, B. Part 2, Weinheim

[2]   K. Popp, H.-P. Schützler, H.-W. Viehrig (1989), *Bestrahlungsexperimente zur*

Untersuchung der Neutronenversprödung von Reaktordruckbehälterstählen, Report Zentralinstitut für Kernforschung, Rossendorf, ZfK-679

[3]   *Neutron-Scattering Instrumentation at the Research Reactor BER II*, Berlin Neutron Scattering Center - BENSC, May 1996

[4]   O. Glatter (1980), *J. Appl. Cryst.* 13, 7

[5]   O. Glatter, O. Kratky (1982), *Small Angle X-ray Scattering*, London, pp.17

[6]   M. Große, P. Nitzsche, J. Böhmert, G. Brauer (1996), Investigation of the Development of Irradiation - Induced Precipitates in VVER-440-Type Reactor Pressure Vessel Steels and Weld Metals During Irradiation Annealing, 18. Int. Symposium *"Effects of Radiation in Materials"* ASTM STP 1325

[7]   J. Böhmert, M. Große, P. Nitzsche (1997), SANS Investigations of the Irradiation-Caused Structural Damages in VVER 440-Type Reactor Pressure Vessel Steels, *Physica B 234-236*, 997

THE HOT CELL LABORATORIES FOR MATERIAL INVESTIGATIONS OF THE INSTITUTE FOR SAFETY RESEARCH

H.-W. Viehrig

1. Introduction

The investigation of aging phenomena of materials has been a subject of interest at the Institute for Safety Research of the Forschungszentrum Rossendorf e.V.. Within these research activities the irradiation-induced embrittlement of reactor pressure vessel (RPV) materials is investigated. It is the aim to determine the change of the mechanical properties due to fast neutron irradiation and to obtain information on the microstructural interactions.

Special facilities for handling and testing of irradiated specimens are necessary, to perform the investigation of activated material. The Institute for Safety Research has two hot cell laboratories:

- the preparation laboratory and
- the materials testing laboratory.

This report is intended to give a overview of the available facilities and developed techniques in the laboratories.

1. Preparation Laboratory

The preparation of special sheets from specimens and the microscopic investigation can be done in the preparation laboratory. The following facilities are installed within the four medium activity cells for post-irradiation preparation:

- a lead shielded storage for maximum activity of $5 \cdot 10^{12}$ Bq ^{60}Co,
- a rotating metall brush,
- an ultrasonic bath,
- a cutting machine with diamond abrasive blade,
- a metallographic grinding and polishing machine, and
- an optical microscope with a microhardness tester.

One hot cell is empty and available for special preparation and examination, for example inspection of damages. The maximum activity which can be handled in one hot cell is $2 \cdot 10^9$ Bq ^{60}Co.

The possible preparation techniques are:

- cleaning and storing of specimens,

- cutting of specimens or irradiation capsules,
- mechanical grinding and polishing,
- metallographic section preparation (etching and the like),
- metallographic optical microscopy and
- and micro hardness testing.

Outside of the hot cells a local lead shielded small-scale hardness tester and heat treating furnace are available. The furnace is used for annealing experiments. Furthermore there is a glove box with a metallographic grinding and polishing machine and special tools for repairing contaminated equipment. The metallographic grinding and polishing machine is used for finishing of thin samples for microstructural investigations after they were preprocessed in the hot cells.

2. Materials Testing Laboratory

Fig. 1 shows the overall view of the materials testing laboratory. The laboratory consists of two hot cells and a railway transport system for moving the lead container. The hot cell on the right side contains a lead shielded storage for about 1000 irradiated specimens of Charpy geometry with a maximum total activity of $5 \cdot 10^{12}$ Bq ^{60}Co. The other part of the hot cell on the left side is named "Shielded Containment" and consists of an outer lead shielding against nuclear radiation and an inner containment against the spreading of radioactive contamination. Here, it is possible to handle specimens with a maximum activity of $5 \cdot 10^{19}$ Bq ^{60}Co. Both hot cells are conceded with railways for moving the lead container with the irradiated specimens.
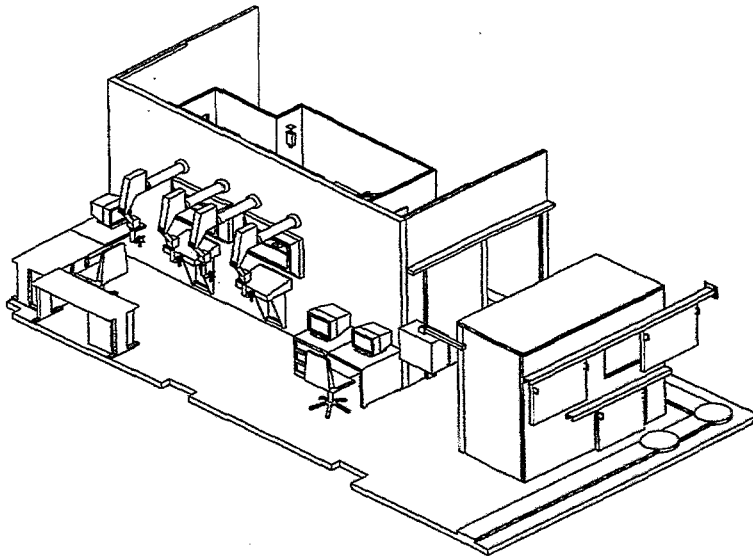
Fig. 1:   Diagrammatic overall view of the mechanical testing laboratory

Fig. 2 shows the working front of the "Shielded Containment". There are an instrumented impact tester, a servo-hydraulic testing system, a video-measuring microscope and an additional lead shielded storage (maximum total activity $2 \cdot 10^{12}$ Bq ^{60}Co) within the "Shielded Containment". All drive units, electronics, hydraulic components and light sources are situated outside the inner containment. Hence, they will not be contaminated. The construction of this hot cell allows to enter the shielded area outside the inner containment for transporting the container and maintaining the equipment. The following experiments can be carried out:

— notched bar impact tests,
— tensile tests,
— quasistatic and dynamic fracture mechanics tests, and
— fatigue tests.
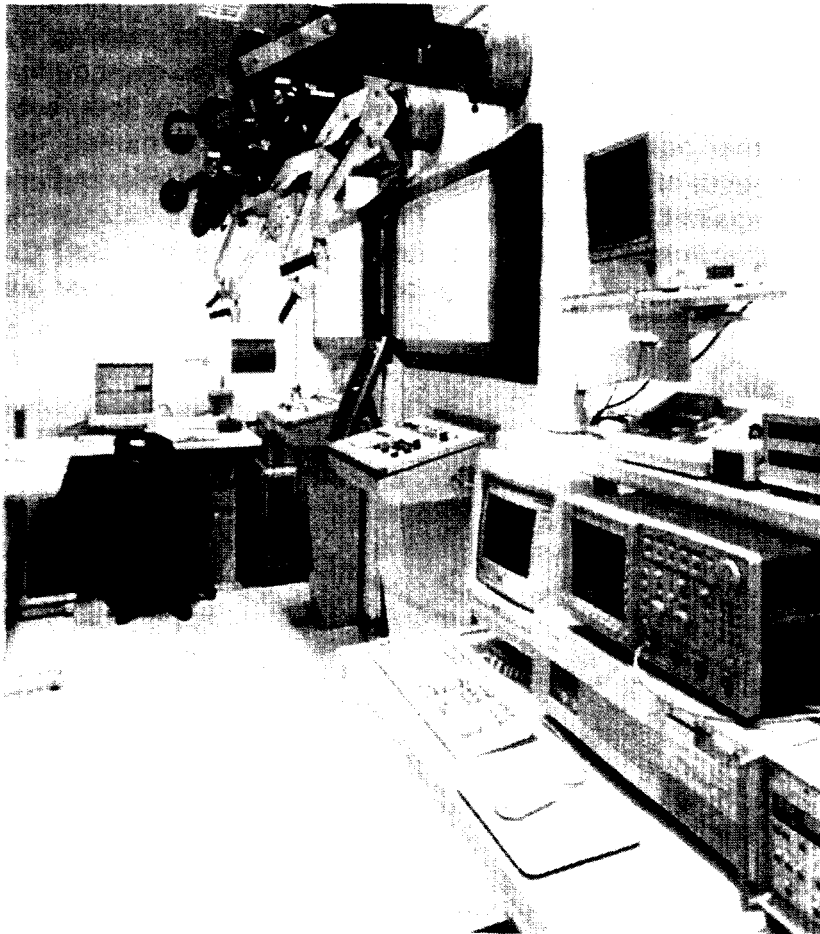
Fig. 2:   Working front of the „Shielded Containment"
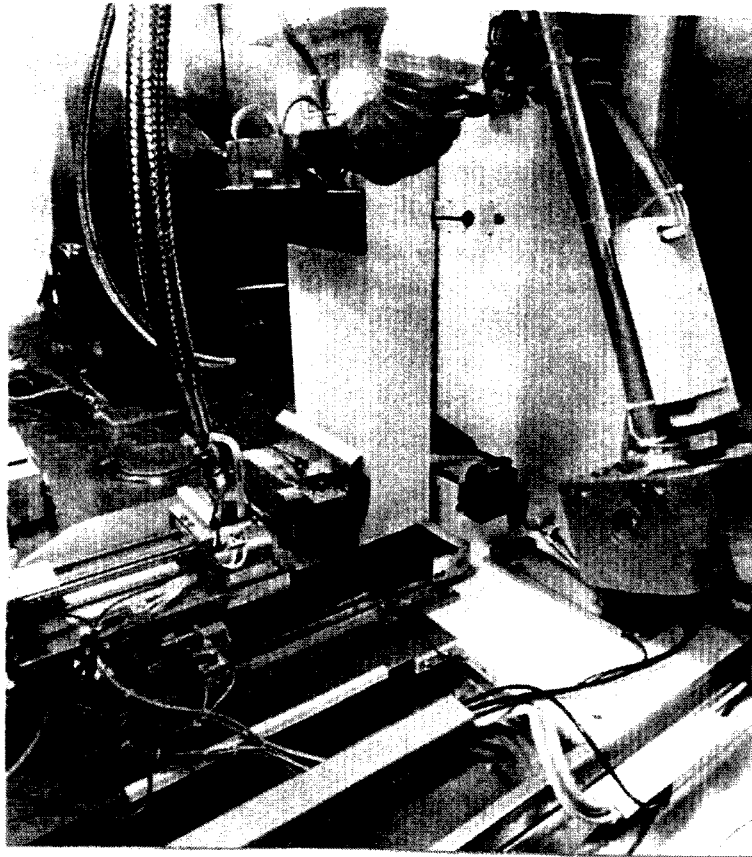
Fig. 3: Instrumented impact tester with the specimen tempering and positioning device

The impact tester (Fig. 3) is instrumented to measure the impact force and equipped with a special specimen tempering and positioning device. Impact tests can be performed under the following testing conditions:

–	impact energy:	up to 300 J
–	impact velocity:	up to 5.5 m/s
–	temperature range:	-150 to +300°C
–	geometrical dimension of the specimens:	10 mm·10 mm·55 mm.

The instrumented Charpy-V impact and dynamic fracture mechanics tests are performed according to the DIN 50115 standard "Testing of Metallic Materials-Notched Bar Impact Test", the ISO/DIS 14556 "Steel-Charpy V-Notch Pendulum Impact Test-Instrumented Test Method" and the ESIS draft "Combined K_{1d}, J_{1d} and CTOD Test Methods" for instrumented pre-cracked Charpy impact testing.

For tensile and quasistatic fracture mechanics tests the servo-hydraulic testing system is used. The tests can be performed in the temperature range of -150 to +300°C within a tempering chamber. The servo-hydraulic testing system, having

83

a static load capacity up to ± 50 kN, is provided with a computer system and a digital controller, which allow fully digital control of the system and data acquisition. There are different loading arrangements for compact tension (CT), single-edge notched bend (SENB) and tensile specimens of various geometrical dimensions. Fig. 4 shows the loading arrangement for three point bend testing of Charpy size SENB specimens (geometrical dimension 10 mm·10 mm·55 mm) installed within the tempering chamber.
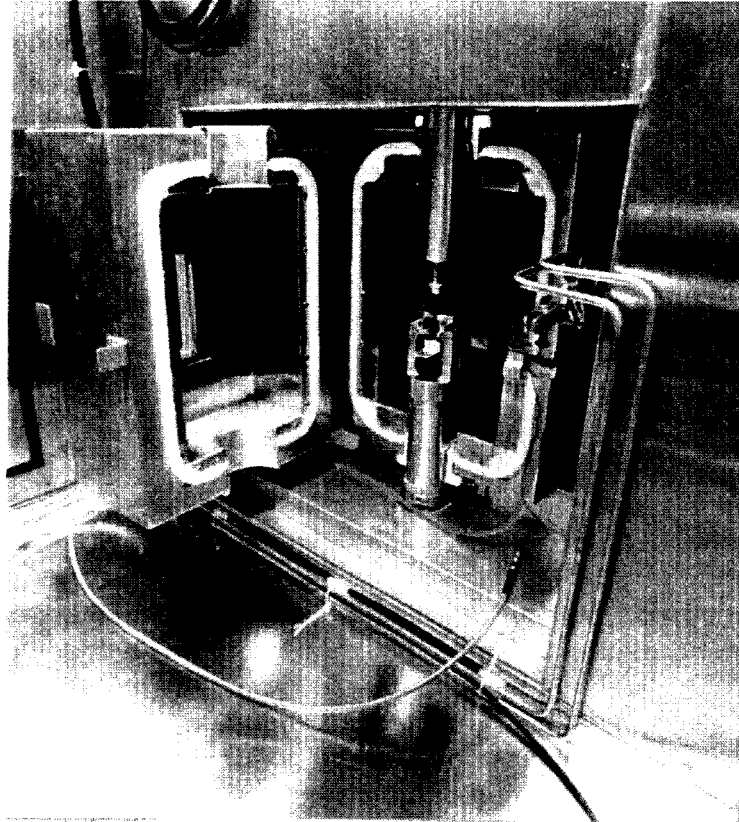
Fig. 4:   Loading arrangement for three point bend testing of Charpy size SENB specimens installed within the tempering chamber

Fracture mechanics experiments include the determination of stress intensity factors (K_{1c}), elasto-plastic parameters (J_{1c}) and crack growth resistance parameters $(J_R$-curves). Measurements of crack propagation during J_R-curve testing is done using the partial unloading compliance technique. All these experiments are performed and evaluated according to EN, ISO, ESIS DIN and ASTM standards.

The video-measuring microscope is primarily designed to measure the geometrical dimensions, the fracture surface and the lateral extension of irradiated specimens prior and after testing. The fracture appearance of Charpy V-notch specimens as

well as the initial crack length and stable crack extension of Charpy size SENB specimens are measured on the fracture surface after testing.

4. Summary and Concluding Remarks

Hot cell laboratories are available in the Institute for Safety Research of the Forschungszentrum Rossendorf e.V.. The facilities for preparation and mechanical testing installed within the hot cells allow to investigate contaminated and activated specimens of structural materials. This is the basis for contribution to basic materials research programmes within the framework of IAEA, AMES and regulatory authorities. The main research field is the neutron embrittlement of reactor pressure vessel steels. The hot cell laboratories are, however can able of carriing out further tasks like failure analysis and mechanical testing programmes for national and foreign customers.

FINITE ELEMENT BASED STRESS ANALYSIS OF BWR INTERNALS EXPOSED TO ACCIDENT LOADS

E. Altstadt, F.-P. Weiss, M. Werner, H.-G. Willschuetz

1. Introduction

During a hypothetical accident the reactor pressure vessel internals of boiling water reactors can be exposed to considerable loads resulting from temperature gradients and pressure waves. Three dimensional FE models were developed for the core shroud, the upper and the lower core supporting structure, the steam separator pipes and the feed water distributor. The models of core shroud, upper core structure and lower core structure were coupled by means of the substructure technique. All FE models can be used for thermal and for structural mechanical analyses. As an example the FE analysis for the case of a station black-out scenario (loss of power supply for the main circulating pumps) with subsequent emergency core cooling is demonstrated. The transient temperature distributions within the core shroud and within the steam dryer pipes as well were calculated based on the fluid temperatures and the heat transfer coefficients provided by thermo-hydraulic codes. At the maximum temperature gradients in the core shroud, the mechanical stress distribution was computed in a static analysis with the actual temperature field being the load. It could be shown that the maximum resulting material stresses do not exceed the permissible thresholds determined in the appropriate regulations. Another scenario which was investigated is the break of a feed water line leading to a non-symmetric subpressure wave within the reactor pressure vessel. The dynamic structural response of the core shroud was assessed in a tranisient analysis. Even for this load case the maximum resulting stresses remain within the allowed limits at any time.

2. Finite Element Models

Based on the finite element code ANSYS®, models were developed for the core shroud, the upper and the lower core supporting structure, the steam separator pipes and the feed water distributor of a German boiling water reactor.

The model of the core shroud was assembled from 8 node brick elements. The 3 dimensional modeling is especially required for load cases with transient temperature loads leading to a non-linear temperature distribution over the wall thickness. Four element layers were used for the shroud wall. The whole core shroud model consists of about 13,000 elements. In case of meshing with thermal elements it has about 17,000 degrees of freedom (one temperature per node), and in case of structural elements it has 104,000 degrees of freedom (three displacements and three rotations per node). At load symmetry a 180° half model with only 6,500 elements can be used. The models for the lower and the upper

core structure consist of shell and beam elements. The beam elements are used to model the reinforcements at the crosspiece sheets. The whole upper core structure model consists of about 33,000 elements and the lower core structure model of 43,500 elements. Especially for temperature loads the models of the upper and the lower core structures must be coupled to the core shroud model to be able to realistically compute the stress due to temperature non-homogenities. The substructure technique is an efficient tool for the coupling.

The models for the upper and the lower core structure are reduced by means of static condensation to some few degrees of freedom (DOF). The remaining DOF (master DOF) are connected with the appropriate DOF of the full core shroud model. The steam separator pipes which are welded with the core shroud head are also modeled with 8 node brick elements. Because of the curvature of the core shroud head the steam separator pipes are of different lengths. In average one pipe consists of about 4,000 elements with 4 layers over the wall thickness. The material properties elasticity modulus, thermal expansion coefficient and heat conductivity are temperture dependent, whereas density and heat capacity are constant.

3. Load Case: Station Blackout

The station black-out scenario begins with a natural convection followed by the start of the high pressure emergency core cooling system. During the natural convection phase a steady state temperature profile in the core shroud wall develops having low gradients. After the start of the emergency cooling system cold water is injected into the downcomer through one nozzle only. This leads to a transient non-axisymmetric decrease of the fluid temperatures at the outside of the core shroud. Due to forced convection the heat transfer coefficient immediately increases by a factor of more than 10.

First, the time dependent temperature distribution in the core shroud is calculated in a transient thermal analysis. The heat fluxes result from the fluid temperatures and the heat transfer coefficients which were available from thermohydraulic investigations. The calculation was performed for a total time interval of 900 seconds which was divided into 18 load steps. The maximum temperature gradient needed for the structural mechanical integrity assessment
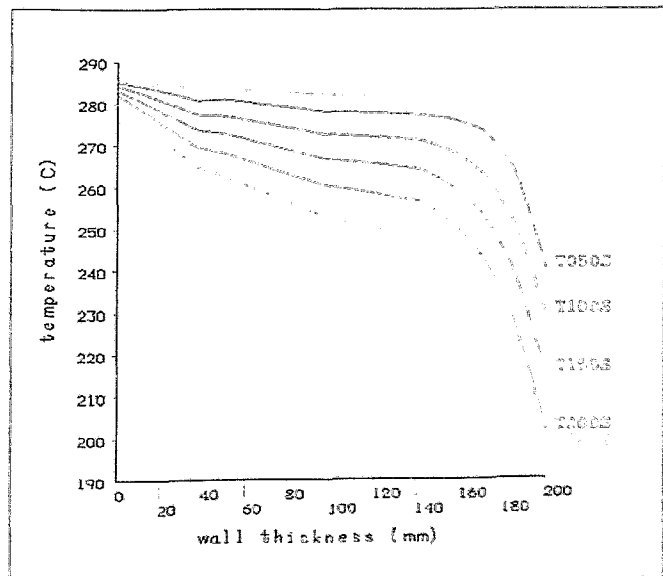
Fig. 1: Transient temperature over the wall thickness in the upper core grid flange of the shroud

87

is reached after some 250 seconds. The maximum temperature difference between the inner and the outer surface of the shroud is about 90 K. Fig. 1 shows the temperature over the wall thickness at the upper core structure flange of the shroud. The different curves represent the increasing time after the start of the cold water injection.

In the second step a static structural mechanical calculation was performed with the maximum temperature gradient over the shroud wall as load input. This calculation provided the structural displacements, the

Fig. 2: Distribution of the von Mises equivalent stress in the core shroud 250 s after the start of the emergency core cooling system.

elastic stresses and strains of the whole structure. For the evaluation of the resulting 3 axial stress tensor the von-Mises equivalent stress was calculated which could be compared to the thresholds fixed in the regulations of the KTA (Kerntechnischer Ausschuß). Fig. 2 shows the stress distribution in the core shroud 250 s after the start of the emergency core cooling system. The stresses in the steam separator pipes were calculated in a similar way.

Though the upper and the lower core structures are not subjected to significant temperature gradients they exhibit significant stresses. This is a consequence of the radial contraction of the core shroud due to the cooling of its outer surface. To obtain the stresses in the upper and lower core structure, which are represented in the model as condensed substructures, these substructures must be expanded by inverting the static condensation. It could be shown that the loads due to a station black-out and emergency core cooling are leading to significant material stresses, but the permissible limits [1] are not exceeded. The mechanical integrity of the internal components is not endangered.

4. Load Case: Break of a Feed Water Line

The break of a feed water line induces a non-axisymmetrical decompression wave in the reactor pressure vessel. Thus the core shroud is loaded by a time dependent asymmetric pressure field.

The dynamic response of the core shroud to this excitation was investigated in a transient structural analysis. The analysis considered a total time interval of 0.05 seconds which was subdivided into 40 loadsteps. As result the displacements, stresses and strains of the core shroud wall for each time step are available. The highest material stresses were observed in the lower region of the core shroud
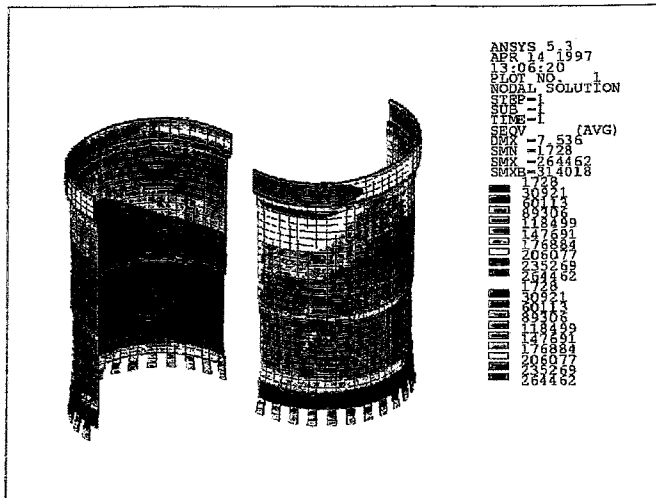
since mainly its first bending mode was excited. Fig. 3 shows the radial displacement of the shroud 12.5 ms after the feed water line break and Fig. 4 the vertical displacement of the lower core structure after 30 ms.

The von-Mises equivalent stresses were compared to the permissible thresholds. It could be shown that the mechanical integrity is maintained.

5. Conclusions

Based on the finite element technique the mechanical stresses in BWR internal components were predicted which might occur during hypothetical accidents. Transient and static mechanical analyses have proven that as well during station blackout and emergency core cooling as during the break of a feedwater line, the integrity of the internals is maintained. The maximum equivalent stresses do not exceed the limits of the related German regulations [1].

Fig. 3: Radial displacement of the core shroud 12.5 ms after a feed water line break.
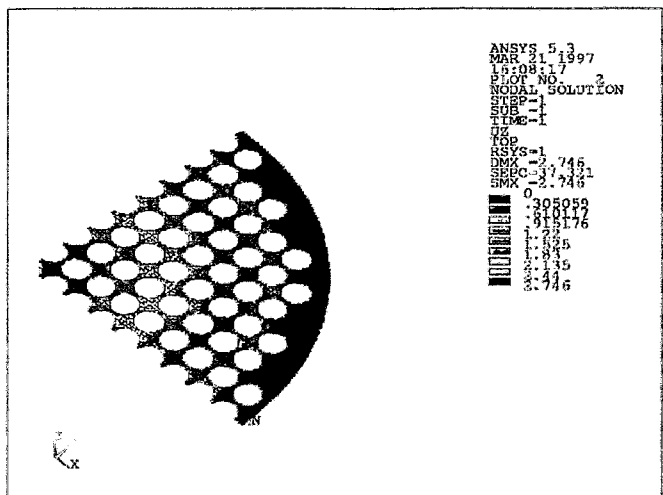
Fig. 4: Vertical displacement of the lower core structure 30 ms after feed water line break.

References

[1] KTA 3204: Sicherheitstechnische Regel des KTA. Reaktordruckbehälter-Einbauten. Fassung 3/84.

COMPARISON OF PRESSURE VESSEL NEUTRON FLUENCES FOR THE BALAKOVO-3 REACTOR WITH MEASUREMENTS AND INVESTIGATION OF THE INFLUENCE OF NEUTRON CROSS SECTIONS AND NUMBER OF GROUPS ON THE RESULTS

H.-U. Barz, B. Boehmer, J. Konheiser, I. Stephan

1. Introduction

The general methodical questions of experimental and theoretical determination of neutron fluences have been described in connection with the measurements and 3-D Monte Carlo calculation for the Rovno-3 reactor [1-7].The same calculation and measurement methods were applied for the Balakovo-3 reactor.

In the first part, the results of the comparison for Balakovo will be given and discussed. However, for this reactor the main attention was focussed on investigations of the accuracy of the calculation. In this connection an important question is the influence of neutron data on the results. With this respect not only the source of the data but also the number of energy groups is important.

Therefore, in the second part the results obtained with different data bases and number of groups are given. ABBN-, ENDF/B-VI- and JEF-2- data were used as data base, the last one with a corrected iron-file, which was contributed by IKE (Stuttgart). Now the ENDF/B-VI data are considered to have the highest standard and therefore for these data additionally the number of groups was changed. Calculations were performed for a simplified model of the Balakovo-reactor with 58, 123 and 246 energy groups within the energy range above 20 keV.

2. Calculated results and comparison with measurements

In Table 1 some integral fluence values at the detector positions within the 60° symmetry sector (see Fig.1) are given. In the second part of the table for the azimuthal angle of 97° the values for the different vertical positions (relative to the midplane of the core) are shown.

Table 1: Fluence values for Balakovo-3, period 5

Degree	Height	Fluence >1.0 MeV	>.5 MeV	>.1 MeV
69.4	-29 cm	2.348e16	7.205e16	1.735e17
92.0	-29 cm	1.078e16	3.573e16	9.682e16
97.0	-29 cm	1.265e16	4.128e16	1.089e17
107.0	-29 cm	2.191e16	6.740e16	1.633e17
115.8	-29 cm	2.434e16	7.522e16	1.817e17

Degree	Height	Fluence >1.0 MeV	>.5 MeV	>.1 MeV
97.0	-91 cm	1.176e16	3.793e16	9.890e16
97.0	-62 cm	1.237e16	3.994e16	1.044e17
97.0	-9 cm	1.271e16	4.117e16	1.083e17
97.0	+14 cm	1.256e16	4.098e16	1.083e17

Table 2 relates the experimental reaction rates to the reaction rates calculated from the group fluxes. h is the distance from the midplane of the core in cm, θ is the azimuthal angle. The calculated values are based on cross section data with 123 groups. It must be mentioned that the Niobium measurements are done for the Balakovo detectors more carefully than for the Rovno reactor, because a new low threshold detector system was available.
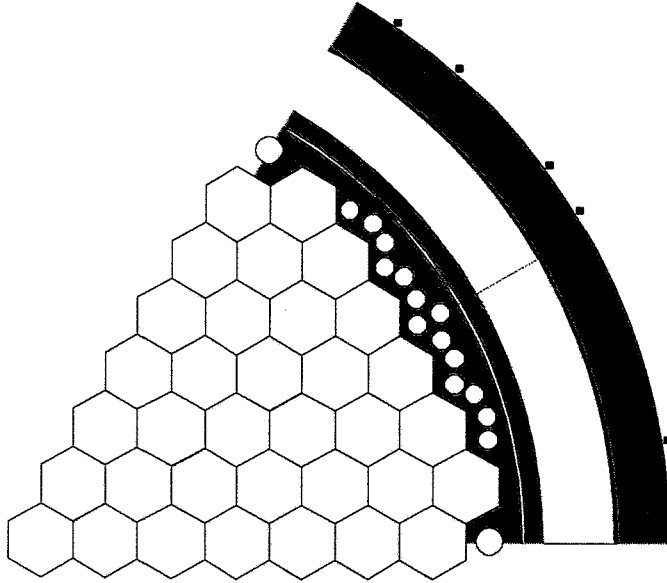
Fig.1: Top view of a simplified symmetry sector and monitor positions of the Balakovo-3 reactor

Table 2: Ratios of calculated and measured detector activities (C/E - values)

Position		Detector Reactions				
h	θ°	^{93}Nb(n,n')^{93m}Nb	^{54}Fe(n,p)^{54}Mn	^{58}Ni(n,p)^{58}Co	^{46}Ti(n,p)^{46}Sc	^{63}Cu(n,α)^{60}Co
-29	69.4	1.010	1.020	1.080	1.000	1.020
-29	92	0.847	0.972	1.010	0.914	0.955
-29	97	0.998	1.010	1.040	0.908	0.969
-29	107	0.992	0.999	1.080	0.987	0.991
-29	115.8	0.958	0.976	1.060	0.973	0.998
+14	97	0.936	1.010	1.010	0.944	0.958
-9	97	0.939	1.010	1.050	0.979	0.949
-62	97	0.971	0.936	1.050	0.915	0.914
-91	97	0.934	0.951	0.993	0.901	0.932

Looking at Table 2 remarkable agreement between measurements and calculations can be observed. As the errors of the measurements are in the order of 5-10% it can be stated, that in general the calculations are within this range of error. Since all known geometrical details are considered and also the pin-wise power history is taken into account for the calculation of the fission source distribution, the sources of errors of the calculation are besides of uncertainties of geometrical dimensions, material densities, and the detailed reactor power history mainly related to the neutron data.

3. Investigation of the influence of neutron data and of the number of energy groups

As the Monte Carlo code TRAMO is coupled with the data preparation code NJOY it is relatively simple to investigate the influence of different data libraries and group numbers. The model for these calculations has been simplified. The pin-wise structure of sources is neglected and only the fission source part of U-235 is treated.

In Table 3 some results of these calculations are presented: the number of reactions/nucleus during the cycle for 3 of the 5 used detector materials for the 123 group ENDF/B-VI basic variant and the relative deviations from that in % for

Table 3: Influence of different neutron data bases on calculated numbers of reactions/nucleus for different angular intervals and three different detectors

Ang. Intervals	$^{93}Nb(n,n')^{93m}Nb$				$^{54}Fe(n,p)^{54}Mn$				$^{63}Cu(n,\alpha)^{60}Co$			
	Reactions /nucleus	Deviation from 123B6 of			Reactions /nucleus	Deviation from 123B6 of			Reactions /nucleus	Deviation from 123B6 of		
	123B6	58B6	246B6	123J	123B6	58B6	246B6	123J	123B6	58B6	246B6	123J
°		%	%	%		%	%	%		%	%	%
0- 6	4.942E-09	-2.5	2.5	-3.5	1.215E-09	-3.1	3.0	-3.9	1.519E-11	-1.2	5.2	-11.2
6-12	4.940E-09	-2.7	2.3	-2.8	1.231E-09	-3.0	1.6	-3.6	1.556E-11	-3.5	1.8	-12.9
12-18	4.025E-09	-3.1	0.9	-3.3	1.008E-09	-4.0	-1.4	-5.0	1.299E-11	-3.8	-0.9	-14.2
18-24	2.923E-09	-3.1	2.5	-3.5	7.120E-10	-4.4	0.3	-7.6	9.440E-12	-4.6	1.4	-15.4
24-30	2.367E-09	-2.6	2.4	-3.2	5.624E-10	-4.1	3.0	-7.2	7.555E-12	-5.2	1.5	-16.3
30-36	2.401E-09	-2.2	2.3	-4.8	5.742E-10	-2.6	3.0	-9.6	7.489E-12	-2.6	5.4	-15.6
36-42	2.997E-09	-2.5	2.4	-4.0	7.366E-10	-3.2	0.9	-6.9	9.725E-12	-3.7	-0.6	-15.3
42-48	4.108E-09	-1.6	3.3	-2.8	1.042E-09	-2.6	2.0	-5.1	1.328E-11	-2.3	1.8	-13.3
48-54	5.049E-09	-1.6	4.7	-3.2	274E-09	-2.5	4.0	-6.0	1.605E-11	-2.9	2.2	-14.4
54-60	5.030E-09	-1.1	4.1	-3.5	1.254E-09	-2.5	2.7	-6.9	1.584E-11	-2.8	2.2	-14.4
0-60	3.878E-09	-2.2	2.9	-3.4	9.604E-10	-3.1	2.0	-5.8	1.231E-11	-3.1	2.1	-14.0
15-45	2.890E-09	-2.6	2.2	-3.6	7.059E-10	-3.7	1.1	-7.1	9.295E-12	-4.0	1.2	-15.4
0-15, 45-60	4.769E-09	-2.0	3.3	-3.2	1.215E-09	-2.7	2.6	-5.1	1.533E-11	-2.6	2.6	-13.2

(Abbreviations: 123B6 for 123 group ENDB/B-VI,   123J for 123 group JEF-2,...)

3 other variants (ENDB/B-VI-58 groups, ENDB/B-VI-246 groups and JEF-2-123 groups). Besides the values for the 6° angular intervals, which have a considera-

ble statistical uncertainty, values averaged over all angular intervals as well as values averaged over the region with the lowest fluences (15°-45°) and values averaged over the region with the largest fluences (0°-15° and 45°-60°) are given. Essential deviations can be found in Table 3 for the high energy detectors with JEF-2 data. Different group numbers for the same data base ENDF/B-VI have only a small effect on the detector reaction rates.
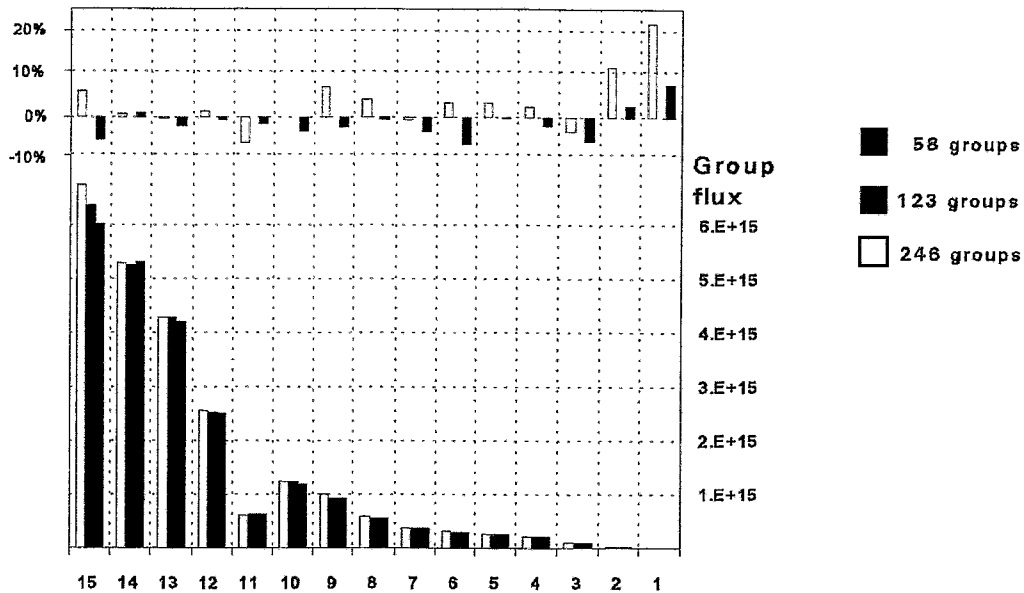
Fig. 2 : Group results and deviations for the outer boundary

Larger differences for single angular intervals especially for ^{63}Cu(n,α)^{60}Co are due to Monte Carlo statistical errors. The given average values show much smaller statistical errors (<1%). The general tendency seems to be: the greater the group number, the greater the reaction values. However, it can be seen that if the 123 and 246 group results for the 0°-60° average values are compared, the highest deviation reaches 2.9% (Niobium). For the other detectors these deviations are approximately equal to 2.0%. Having in mind that the calculation problem is a shielding problem especially sensitive to rather uncertain cross sections, these differences seem to be sufficiently small. In Fig.2 results of calculations for the mean values of the outer boundary with 58, 123 and 246 groups are given in a 29 group representation for the first 15 groups within the energy range above 1 MeV together with the deviations from the basis variant (123 groups)

The deviations of the first 2 groups are because of the very small total contribution generated by the statistical errors. The results in Table 3 and Fig. 2 reflect the fact that for more groups the shielding effect is decreased. This shall be illustrated for a simple example by comparison of a given number of groups and a case, where each group is divided into 2 equal parts. The probability p to overcome a

shielding distance x from the source without further collisions can be expressed for a given group with the total cross section Σ as

$$p = exp(-\Sigma * x).$$

If this group is divided into two equal parts instead p the quantity P reflects the shielding probability

$$P = .5*exp(\Sigma_1/2)*x + .5*exp(\Sigma_2/2)*x.$$

For the comparison the cross section $\Sigma = (\Sigma_1 + \Sigma_2)/2$. If this is introduced into the expression for p it is easy to see (the arithmetic mean value is greater than the geometric mean value) that generally p is smaller than P. The equality is only given for $\Sigma_1 = \Sigma_2 = \Sigma$.

4. Conclusion

The calculation ofpressure vessel fluences for Balakovo-3 using the 3-D-Monte Carlo code TRAMO yields excellent agreement with the measured activities and reaction rates. The influence of group data and of the number of groups have been extensively investigated.

Essential deviations can be found in Table 3 for some detectors for JEF-2 data. Different group numbers for the same data base ENDF/B-VI have only a small impact on the detector reaction rates if the average values are treated, which have a sufficiently small statistical error. This is important especially for the reaction $^{63}Cu(n,\alpha)^{60}Co$. For the other detectors even the single position values only differ from the reference solution in the order of 3%. It is of interest to see the general dependence on the number of groups - the greater the number of groups, the greater the reaction rates. However, it can be seen that if 123 (standard group number) and 246 groups are considered, the greatest difference of the average value is 2.9% (Niobium). For all other detectors these values are about 2.0%. Having in mind that the calculation problem is a shielding problem especially sensitive on the cross sections, these differences are small enough. Nevertheless further calculations with even essentially more groups are planed.

References

[1]   H.-U. Barz, G. Borodkin, B. Boehmer, J. Konheiser, I. Stephan, (1996) "Determination of Pressure Vessel Neutron Fluence Spectra for a Low Leakage Rovno-3 Reactor Core Using Three Dimensional Monte Carlo Neutron Transport Calculations and Ex-vessel Neutron Activation Data", in H.A. Abderrahim, P. D'hondt and B. Osmera (Ed.), *Proceedings of the 9th International Symposium on Reactor Dosimetry*, Prag (pp.58-66)

[2]   H.-U. Barz (1990), *TRAMO - a Flexible Multigroup Neutron Transport Code on the Basis of the Monte Carlo Method for Flux Calculations*, Rossendorf, ZfK- 705

[3]   H.-U. Barz, W. Bertram (1992), Calculation of neutron fluence in the region of the pressure vessel for the history of different reactors by using the Monte-Carlo-method, *Nuclear Engineering and Design* 137, 71

[4]   H.-U. Barz, B. Böhmer, J. Konheiser, I. Stephan (1995), *Ermittlung der Neutronendosis von bestrahlten WWER-Reaktordruckbehältermaterialien*, Rossendorf, FZR-87

[5]   H.-U. Barz (1990), Problems of Weight Determination for the Multigroup Monte Carlo Code TRAMO for Neutron Flux Calculation, *Progress in Nuclear Energy*, 24,69

[6]   G.I. Borodkin, E.B. Brodkin, A.L. Egorov, S.M. Zaritsky (1996), The Neutron Fluence Monitor System for VVER-1000 Vessels and ist Validation, *Proceedings of Radiation protection & shielding topical meeting No. Falmouth*, Massachusetts

[7]   G.I. Borodkin et al. (1993), Pressure Vessel Fluence Monitoring at NPP with VVER: Routine Technique and New Approaches, *Proc. of 8th ASTM-EURATOM Symposium on Reactor Dosimetry*, Vail (Colorado)

TRANSPORT OF REACTING SOLUTES THROUGH THE UNSATURATED ZONE

R. Kuechler, K. Noack

1. Introduction

This contribution presents first tests of a computer code dealing with the flow of water and the transport of several chemical species downwards through a soil (rock) matrix of ten meters thickness. The water motion will be calculated for different soil classes. Transport equations can be derived for chemical species carried with the water. The solute transport system which has been used to simulate this process incorporates the effects of hydrodynamic dispersion, non-linear reaction equations and kinetic chemical interaction between aqueous and solid phases (chemical weathering). At each time step, the Richards equation (water motion) and the transport equations for the chemical species are firstly solved by an implicit difference method. The chemical equilibrium submodel is then used to calculate the distributions of chemical species. These two steps are repeated until the solutions are obtained.

2. Motion of water in the unsaturated zone

The one-dimensional motion of water in porous soil can be described by combining Darcy's Law

$$v = -k(w)\frac{\partial h}{\partial z} \qquad (1)$$

and the continuity equation $\frac{\partial w}{\partial t} + \frac{\partial v}{\partial z} = e(w,z)$. The result is the Richards equation

$$\frac{\partial w}{\partial t} = \frac{\partial}{\partial z} k(w)\frac{\partial h}{\partial z} + e(w,z). \qquad (2)$$

In Eqs. (1) and (2) $w(z,t)$ denotes the volumetric water content of the soil, $v(z,t)$ is the water flow per unit area (m/h), $e(w,z)$ represents existing sources and sinks and $k(w)$ is the hydraulic conductivity (m/h). $h = -\psi + z$ is the total soil water potential (m). $\psi(w)$ is the matrix potential of the soil and z is the distance below the soil surface representing the potential of gravity. The hydraulic conductivity is a function of the volumetric water content: e. g. $k(w)/k_0 = ((w - w_R)/(n_0 - w_R))^{3...4}$, where n_0 is the porosity, w_R the residual water content and k_0 the saturated hydraulic conductivity $(k_0 = k(n_0))$. Choosing $h(z,t)$ as the wanted solution function one gets from Eq. (2) the equation

$$-a(\psi)\frac{\partial h}{\partial t} = \frac{\partial}{\partial z} k(\psi)\frac{\partial h}{\partial z} + e(w,z). \qquad (3)$$

As an example, the soil water capacity $a(\psi) = \partial w / \partial \psi$ and the hydraulic conductivity $k(\psi)$ for sandy soil are depicted in Figure 1. $w(\psi)$ was obtained from a fit to values which are used by the code FEMWATER [1].

The boundary conditions of the differential equation (3) are:

- of Dirichlet's type for the plane $z = z_g$ separating the unsaturated zone from groundwater level: $h(z,t) = z_g$, $(\psi = 0)$;
- of Neumann's type for the surface $z = z_s$:

$$-k\frac{\partial h}{\partial z} = q(t);$$

q(t) describes the time-dependent infiltration (rainfall);
- if $q > k_0$, ponding or surface runoff removing a part of q occur and one has to switch to a first-type boundary condition $(h(z_s,t) \approx 0)$.
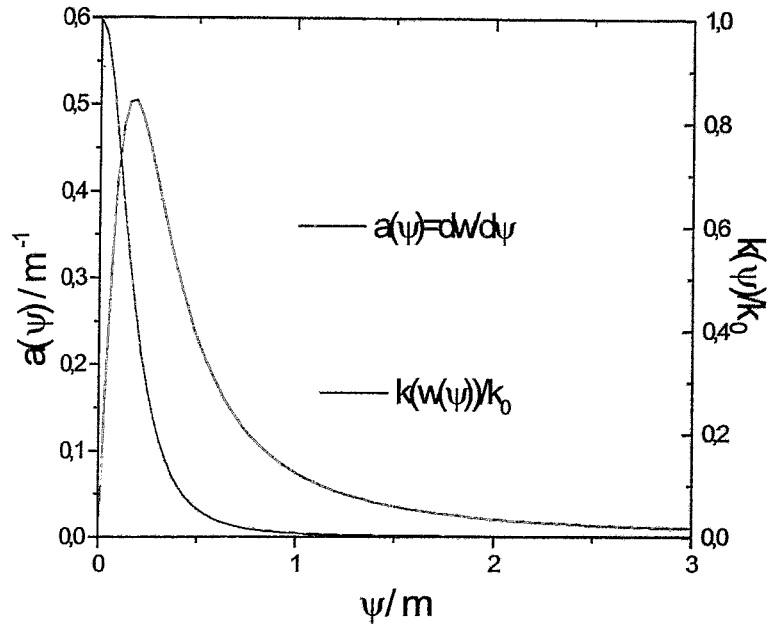
Fig. 1: Coefficients of the Richards equation

Sources and sinks $e(w,z)$ (e.g. evapo-transpiration) will be taken as zero for clarity in the following analysis.

Figure 2 shows the results of the numerical solutions of the Richards equation for a typical annual rainfall (rate 0,68 m/year) and for the five soil classes given in Table 1. The coloured curves represent the water outflows at $z = z_g$.

Table 1: Parameters of soils (according to Dunger [2])

sediment	porosity	k_0 (m/h)	capillary climbing power [3]
1. coarse sand	0,29	1,8	0,2 – 0,5
2. medium sand	0,3	0,36	0,2 – 0,5
3. silty sand	0,33	0,036	0,5 – 1,5
4. sandy silt	0,35	0,0036	0,5 – 1,5
5. clay / silt	0,4	0,000036	0,5 – 3.0
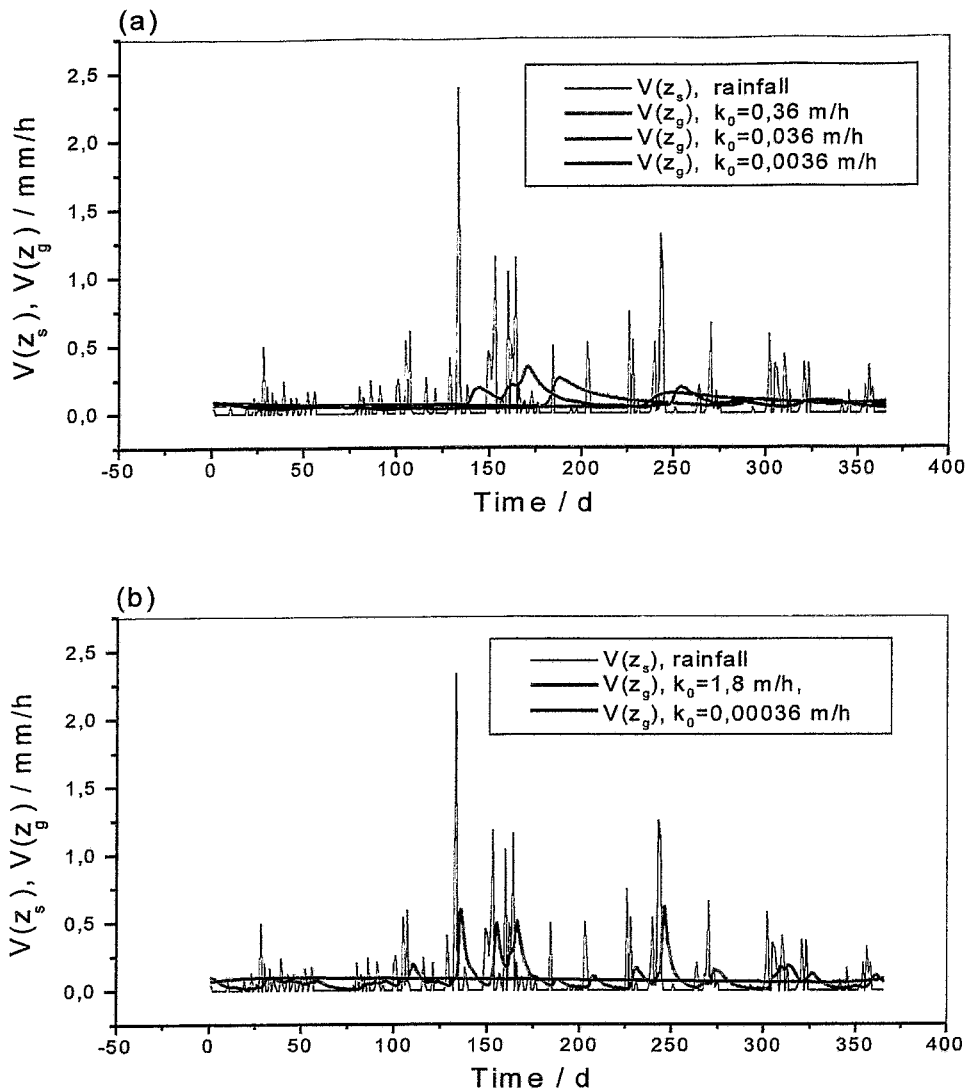
Fig. 2: Infiltration and outflow of water through a 10 m thick soil matrix.
(a) red — medium sand, green — silty sand, blue — sandy silt;
(b) red — coarse sand, blue — clayey silt

3. Transport of reacting solutes

As described above, in order to reach the aquifer, water from precipitation infiltrates through the ground surface and percolates downwards through the unsaturated zone. The same is true for chemical species carried by the water. These species may already be present in the water reaching the ground surface or they may be added and partially removed to the water by dissolution, adsorption and chemical reactions along its flow path from the ground surface to the underlying aquifer. Simplified models for solute transport in the unsaturated zone lump the effects of several processes. This can be illustrated best with the help of the one-dimensional convective-dispersive solute transport equations for species of type $i = 1,...,n$ written as

$$\underbrace{w(z,t)\frac{\partial C_i}{\partial t}}_{storage} = \underbrace{-v(z,t)\frac{\partial C_i}{\partial z} + \frac{\partial}{\partial z}\left(\alpha_L|v(z,t)|\frac{\partial C_i}{\partial z}\right)}_{transport} - \underbrace{\lambda_i C_i}_{decay} +$$

$$\underbrace{q_i(z,t,pH)}_{source} + \underbrace{\sum_{j=1}^{n} S_{ij}(C_1,...,C_n)}_{chemical\ reactions}, \quad i=1,...,n \tag{4}$$

In Eq. (4), $C_i(z,t)$ is the solute concentration (mmol/L). $q(z,t,pH)$ is a production function (mmol/L/h), λ is a first-order decay constant (h^{-1}), and α_L is the dispersivity of the medium (m), i.e. $\alpha_L |v|$ considers the motions of migrants relatively to the convective motion. $\sum S_{ij}$ represents the chemical reactions occuring on the water path. Note that the water content w and the water flow velocity v are computed with the solution of Eq. (3). The boundary conditions are as follows:

- At the ground surface a mixed von-Neuman / Dirichlet boundary condition specifying the solute flux: $v(z_s,t)C_i - \alpha_L |v(z_s,t)| \frac{\partial C_i}{\partial z} = v_0(z_s,t)C_i^{rainfall}$ (e.g. $i = CO_2$).
- The free outflow at the outlet is described by the boundary condition: $\frac{\partial C_i(z \approx 1,2\,z_g)}{\partial z} = 0.$

Table 2: Aqueous reactions and their equilibrium conditions[*]

chemical reaction	reaction equilibrium
$H^+ + HSO_4^- \Leftrightarrow H_2SO$	$\gamma_{H^+} C_{H^+} \gamma_{OH^-} C_{OH^-} = 10^{-7,99}$
$H^+ + SO_4^{2-} \Leftrightarrow HSO_4^-$	$\gamma_{H^+} C_{H^+} \gamma_{HSO_4^-} C_{HSO_4^-} = 10^{6}\, \gamma_{H_2SO_4} C_{H_2SO_4}$
$H^+ + CO_3^{2-} \Leftrightarrow HCO_3^-$	$\gamma_{H^+} C_{H^+}\ \gamma_{SO_4^{2-}} C_{SO_4^{2-}} = 10^{1,02}\ \gamma_{HSO_4^-} C_{HSO_4^-}$
$2H^+ + CO_3^{2-} \Leftrightarrow H_2CO_3$	$\gamma_{H^+} C_{H^+} \gamma_{CO_3^{2-}} C_{CO_3^{2-}} = 10^{-7,33}\ \gamma_{HCO_3^-} C_{HCO_3^-}$
$UO_2^{2+} + SO_4^{2-} \Leftrightarrow UO_2SO_4$	$\gamma_{H^+}^2 C_{H^+}^2 \gamma_{CO_3^{2-}} C_{CO_3^{2-}} = 10^{-8,87}\ \gamma_{H_2CO_3} C_{H_2CO_3}$
$U^{4+} + 2SO_4^{2-} \Leftrightarrow U(SO_4)_2$	$\gamma_{UO^{2+}} C_{UO^{2+}} \gamma_{SO_4^{2-}} C_{SO_4^{2-}} = 10^{-0,15}\ \gamma_{UO_2SO_4} C_{UO_2SO_4}$
$UO_2^{2+} + CO_3^{2-} \Leftrightarrow UO_2CO_3$	$\gamma_{U^{4+}} C_{U^{4+}} \gamma_{SO_4^{2-}}^2 C_{SO_4^{2-}}^2 = 10^{-0,58}\ \gamma_{U(SO_4)_2} C_{U(SO_4)_2}$

[*]All C_i in mmol/L, $i = H^+,...,UO_2CO_3$.

For the test calculations the homogeneous reactions in the aqueous phase listed in Table 2 are taken into consideration. Moreover, it is assumed that the macroscopic flow processes are slowly enough to allow local chemical equilibrium. This assumption makes it possible to solve the transport equation and the set of equilibrium chemistry equations separately, with iterations in between. At each time step the Richards and chemical transport equations are

firstly solved by implicit difference methods described in [4]. The equilibrium chemistry calculations are then carried out to determine the chemical speciations and the reaction mass transfer in each space element. The fix point iteration is applied to solve the set of chemical non-linear algebraic equations $(f_j(C_1,..C_n) = 0 \rightarrow C_i^{new} = g_j(C_1,C_i,...,C_n)$, $i,j = 1,2,...,n)$. For the convergence of this method the determination of the $g_j(C_1,...,C_n)$ is of great importance. In order to eliminate the arbitrary initial conditions of the differential equations the calculation is repeated until the steady state appears. Within this loop the initial condition is replaced by the distribution of the preceding step. The iterations are continued until the errors are less than a prescribed limit. The activity coefficients γ_i which determine the equilibrium between the aqueous species are calculated according to the Davies equation [5].

Chemical reactions take place in heterogeneous systems where different phases are in contact with each other. Thus, solutes often react with the surfaces of the water-conducting channels along which they are transported. The reaction may be, for example, in the form of mineral dissolution (chemical weathering) leading to changes of the reacting solutes. The results of these reactions are the sources of radioactive nuclides and heavy metals.

The dissolution of pyrite involved in the chemical weathering is considered as an example:

$$4FeS_2 \text{ (s)} + 15\ O_2 \text{ (aq)} + 14H_2O \rightarrow 4Fe(OH)_3 \text{ (s)} + 8\ H_2SO_4 \text{ (aq)},$$
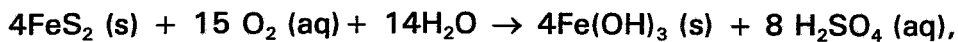
note s = solid, aq = aqueous solution. The source term for H_2SO_4 (aq) by dissolution of pyrite can be expressed as [6]:

$$q_{H_5SO_4}(z,t) = q_0 \sqrt{p_{O_2}(z) / p_{O_2}^{surf}}\, U(pH(z,t)) \qquad \left(\frac{mmol}{L\,h}\right),$$

(5)

$$U(pH) = 1{,}29 /(1 + 10^{2,5-pH} + 10^{pH-4.0}) + 0{,}048.$$

In Eq. (5) is p_{O_2} the partial pressure of oxygen and q_0 is a constant (here $6*10^{-5}\ mmol \cdot L^{-1} \cdot h^{-1}$). It is assumed that the chemical and biological oxygen uptake can be described by a stationary diffusion profile of the partial pressure:

$$p_{O_2}(z) = 0{,}198(1 + z)^{-3} - 0{,}524(1 + z)^{-2} + 0{,}537(1 + z)^{-1} .$$

$U(pH)$ has the shape of a Gaussian distribution with the peak at $pH = 3{,}2$.

For the annual motion of water through the soils 3 and 4 of Table 1 the above reactive transport system was solved numerically. Figure 3 shows the computed profiles of the products of pyrite dissolution and the distribution of the *pH*-value in the middle of the year. In the figures (a) and (b) the solid curves represent the

case $q_{H_2SO_4} = q_0 =$ constant. They show the strong dependence of the concentrations on the water content. With constant values of w and v these curves would be straight lines. Furthermore, the figures show the influence of the pH-value (dotted curves) and of the partial pressure of oxygen (dashed curves) on the distributions of various species. Of more significance than the distributions of species is the integral $I_i = \int (vC_i - \alpha_L \mid v \mid \frac{\partial C_i}{\partial z}) \, dt \Big|_{z=z_0}$, which determines the mass transfer per unit area into the groundwater. Results of these integrals are listed in Table 3. These values show much better the effect of the individual contributions of the source term given by Eq. (5). In the case of a non-reactive tracer emitted by a constant source q_0 the integral $I_{Tracer}(q_0)$ must take the value $I_{Tracer}(q_0) = q_0 * 10 \, m * 8760 \, h \, (1 \, year) = 52{,}56 \, mol/m^2$ in the quasi steady state independently on w $(w{\neq}0)$ and v. This is correctly, as without sinks the number of particles per volume and time unit produced by the constant source is always identically. So, the deviation from this value is the numerical error which is 2,2% for sandy silt and 2,5% for silty sand, respectively.

The comparison of both calculations shows no significant differences. That means that the unsaturated flow through sandy silt or silty sand has no significant effect on the transport results. This behaviour is plausible, because the pH-value only weakly depends on the parameters w, v. Also, a change of the dispersivity $(\alpha_L = 0{,}1 ... 1)$ does not show a significant influence on the results.

Table 3: Annual release rate I_i in mol/m^2

solid class	source term (5)	I_{Tracer}	I_{H^+}	$I_{HSO_4^-}$	$I_{SO_4^{2-}}$
sandy silt	$q_0 = 6 * 10^{-5}$	53,74	85,25	22,23	31,51
	$q_0 U(pH)$	33,97	56,50	11,43	22,54
	$q_0 U(pH)\sqrt{p_{O_2}}$	24,30	41,73	6,88	17,42
	$q_0 U(pH)\sqrt{p_{O_2}}$ *	23,26	38,41	8,11	15,16
silty sand	q_0	53,86	85,25	22,48	31,38
	$q_0 U(pH)$	33,80	56,14	11,45	22,34
	$q_0 U(pH)\sqrt{p_{O_2}}$	24,15	41,41	6,89	17,26
	$q_0 U(pH)\sqrt{p_{O_2}}$ *	23,12	38,12	8,12	15,00

* Activity coefficients $\gamma_i = 1$.

The successful application of reaction transport algorithms for the calculation of the chemical evolution of natural systems requires accurate models of the mineral/fluid surface reaction dynamics. Therefore, the further work aims at the modelling of the main geochemical processes causing the release of pollutants with the help of kinetic rate equations. An example is the chemical interaction of

the weathering products of pyrite and calcite. Pyrite causes the strong generation of acid and in this way the pyrite oxidation is accompanied by a congruent dissolution of calcite and other minerals. The calcite dissolution on its part decreases the *pH*-value and, consequently, constrains the pyrite oxidation.
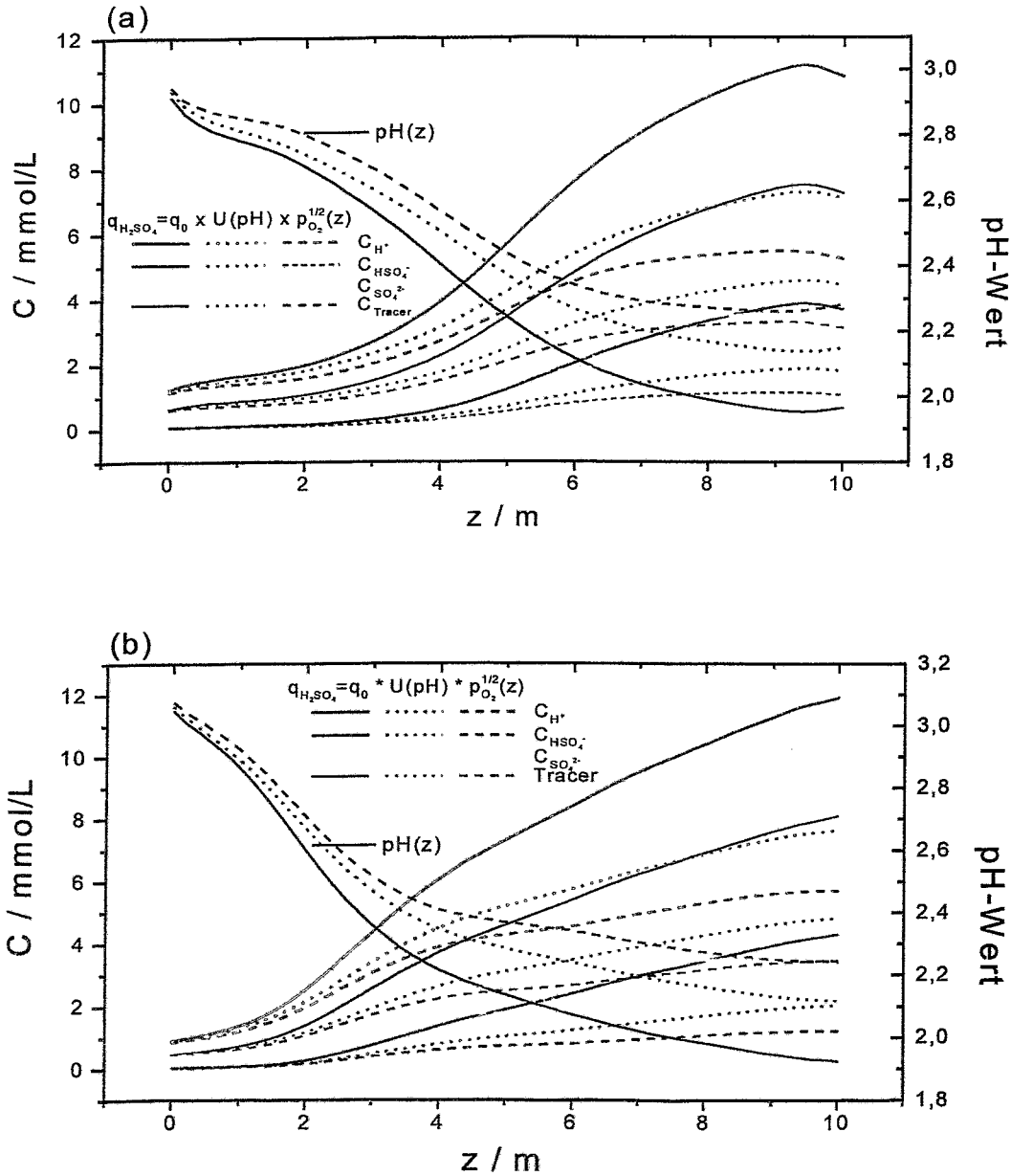
Fig. 3: Concentrations of the products of pyrite dissolution and *pH*-distributions for sandy silt (a) and silty sand (b) in the middle of the year.

Source terms: $q_{H_2SO_4} = q_0$ - solid curves, $q_{H_2SO_4} = q_0 U(pH)$ - dotted curves, $q_{H_2SO_4} = q_0 U(pH) p_{o_2}^{1/2}$ - dashed curves.

References

[1]   T. M. Sullivan, C. J. Suen, *FEMWATER-Manual* , Division of Engineering, Office of Nuclear Regulatory Research, U.S. Nuclear Regulatory Commission, Washington, D.C. 20555, NRG FIN A3276

[2]   V. Dunger, *Dokumentation des Modells BOWAHALD 2 zur Simulation von wasserungesättigten Bergehalden einschließlich Haldenabdeckschichten für tägliche Zeitintervalle,* TU Bergakademie Freiberg, Institut für Geologie, 1995

[3]   H. Prinz, *Abriß der Ingenieurgeologie*, Enke-Verlag, Stuttgart, 1991

[4]   R. Kuechler, K. Noack, *Migration of pollutants in mining dumps,* Forschungszentrum Rossendorf, Institute for Safety Research, Annual Report 1996, pp. 69

[5]   S. Pfeiffer, K. Pecher, *Experimentelle aquatische Chemie,* Heidelberg, Berlin, Oxford, Spektrum, Akad. Verl., 1997

[6]   R. Münze, B. Ullrich, *Beschreibung und Bewertung geochemischer Zustände, die eine Verringerung der Niederschlagsinfiltration in Halden erfordern*, Vortrag zum Workshop Sanierung der Hinterlassenschaften des Uranbergbaus, 10 April 1997

RECRITICALITY CALCULATIONS FOR URANIUMDIOXIDE-WATER SYSTEMS WITH MCNP

H. Kumpf

1. Introduction

Investigations of severe accidents in power reactors will hardly produce data on the geometry, composition and density distributions of fuel mixtures in such detail as demanded for criticality calculations. In view of this rather sloppy formulation of the task one might consider as an objective the search for the 'worst case', i.e. the composition and structure of arrangements with maximum multiplication. The fuel geometry with maximum k_∞ is a hexagonal close package of spheres with a certain radius, immersed in water. But this arrangement is mechanically unstable. Furthermore, the collapsed hexagonal close package with touching spheres is by no means optimal with respect to k_∞. Thus mechanical stability is a necessary additional condition in the search for the worst case. The main part of the report [1] deals with the determination of such a structure. In view of the complexity of the task rigorous mathematical demonstration is not expected to be successful. Instead one adheres to heuristic reasoning.

2. UO$_2$-water structures of increasing disorder

In the report [1] the multiplication factor k_∞ of a series of structures with spherical boundaries between fuel and water have been calculated by means of MCNP. The following systems enumerated in increasing disorder have been investigated: hexagonal close packing of fuel spheres with water in the intermediate space, heaps of fuel spheres immersed in water, including the case of a heap of touching spheres, interpenetrating fuel spheres, randomly distributed in space, with water in between.

Furthermore, calculations have been done for the inverse systems with the water in the spheres and the fuel in the intermediate space, too.

All the above structures are characterized by two parameters: The radius of the spheres making up the structure and the dimensionless fuel/moderator volume ratio. The latter one depends on the average distance of the spheres in the system.

Of course, one feels the urgent need to classify the obtained extensive results. To this end the notion of chord length S, well known in the so called form-independent approximation of reactor theory, has been used. Its definition is:

$$S_{.} = \frac{4V}{O}$$

where V,O are volume and surface area of the fuel. Expressions for S in dependence on the sphere radii and fuel/water ratios have been derived for the six kinds of structures cited above.

If the results for k_∞ are plotted in dependence on the chord length and fuel/water ratio it shows up, that they are roughly independent on the kind of structure i.e. it does not matter whether the structure consists of touching or interpenetrating fuel spheres with water in between nor if it consists of touching or inter-penetrating water droplets with fuel in between. Certainly, neither have all imaginable structures been investigated, nor is the independence on the kind of structure quite rigorous. Nevertheless one can conjecture with confidence, that fuel-water mixtures are sufficiently characterized by their fuel chord-length (or the ratio fuel volume/fuel interior surface) and their fuel/water volume ratio. As a representative system for demonstration purposes one may use e.g. the model of interpenetrating fuel spheres.
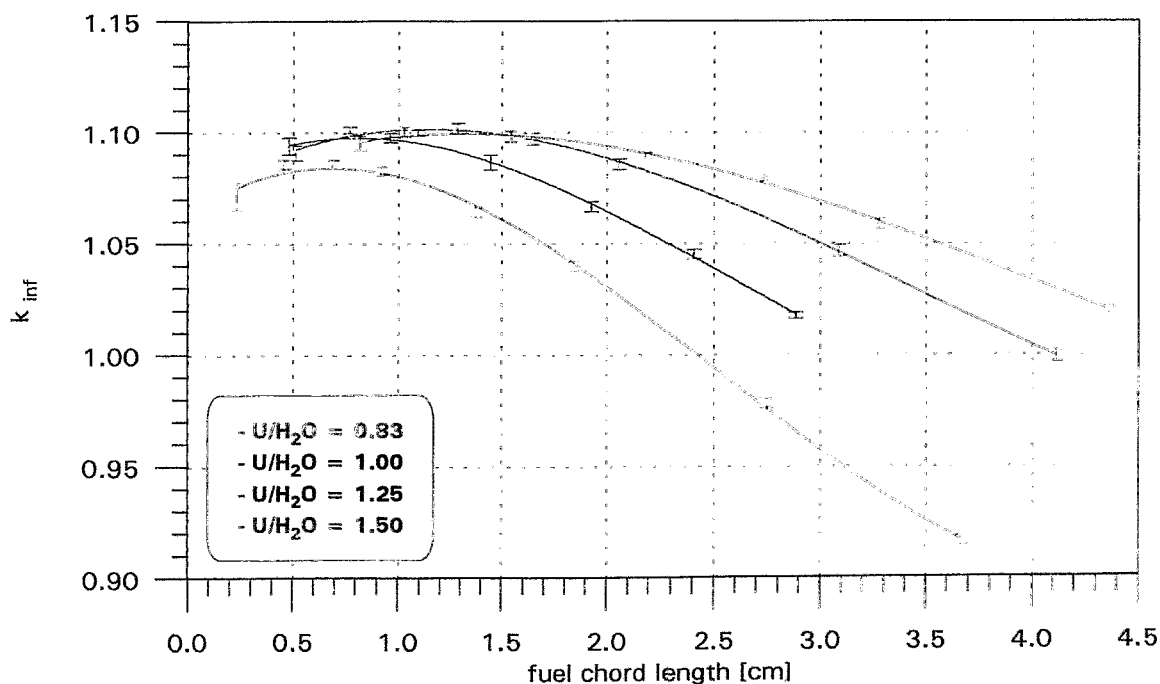
Fig.1: Results of k_{inf} calculations (vertical axis) in dependence on the fuel chord length S_U with the model of overlapping UO_2-spheres enriched to 2.5% and moderated by slightly borated water (220 ppm).

Fig.1 shows calculated results for the multiplication of a structure of 2.5% enriched UO_2 interspersed with slightly borated H_2O in the model of overlapping

105

fuel spheres. Obviously the worst case is determined by fuel chord length $S = 1.1$cm and volume ratio $U/H_2O = 1.25$.
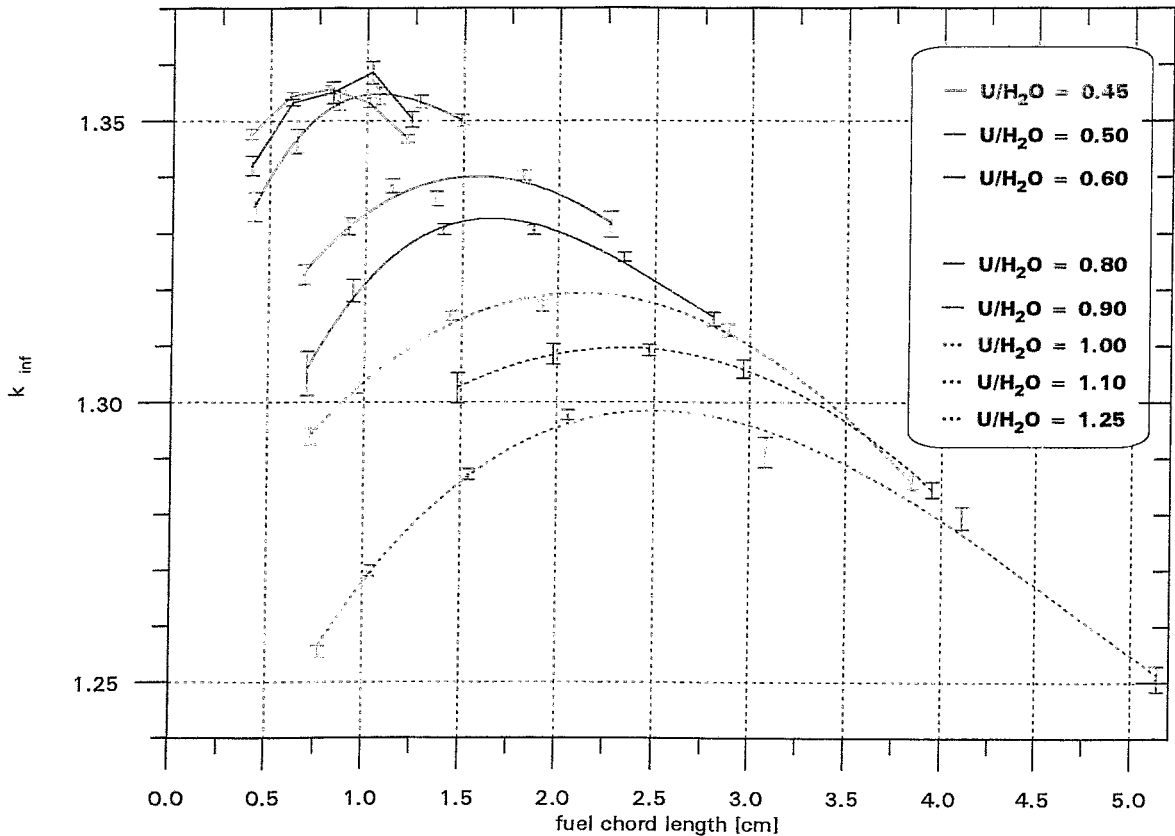
Fig 2.: Results of k_{inf} calculations (vertical axis) for 2.5% enrichment of ^{235}U in dependence on the fuel chord length S_U for UO_2 - pure H_2O mixtures in the model of overlapping fuel spheres. Parameter of the family of curves is the U/H_2O volume ratio.

The next fig.2 contains the corresponding plot for unborated water. Here the worst case with maximum k_∞ appears to be characterized by an almost unchanged $S = 1.0$ cm but much less $U/H_2O = 0.45$. But this volume ratio is so small, that the structure is certainly not stable. Within the model of heaps of touching fuel spheres the only stable configuration exhibits $U/H_2O = 0.83$. Now, the question down to which value for U/H_2O stable stochastic structures are likely to be created by core melt accidents can certainly not be solved rigorously. In the frame of the cited models numerous structures have been generated and regarded by means of visualization procedures like MCNPPLOT or SABRINA. They create the impression that the value of U/H_2O for the stable heap is probably a practical lower limit for the volume ratio. This limiting value may be safely adopted for the

worst case, once the gain in k_∞ by decreasing the volume ratio further from 0.83 to the true worst but unstable 0.45 is not too important (from 1.33 to 1.35).

From fig.2 we extract the value of S = 1.3 cm corresponding to U/H$_2$O = 0.83. Thus, the worst case for stable stochastic structures of UO$_2$ - H$_2$O mixtures is characterized by fuel chord length S = 1.3 cm and fuel/moderator volume ratio = 0.83.

References

[1]   H. Kumpf (1997), *Recriticality Calculations for Uraniumdioxide-Water Systems with MCNP*, Rossendorf, Report FZR-183

[2]   *MCNP4A Monte Carlo N-Particle Transport Code System,* Los Alamos National Laboratory (1993), RSIC Code Package CCC-200

IDENTIFYING DANGEROUS OPERATING STATES IN CHEMICAL PLANTS USING NEURAL NETWORKS

G. Hessel, W. Schmitt, N. Tefera, K. van der Vorst, F.-P. Weiß, J. Neumann [1]

1. Introduction

Accident analyses have shown that human errors are one main cause of incidents with danger potential in chemical plants. According to the "Major Accident Reporting System" of the European Research Centre at Ispra (Italy), the vast majority of accidents could have been prevented by properly implementing the experience of the experts regarding the behaviour of the chemical plant on the one hand, and the sequence of the incidents during similar situations on the other hand [1]. The reasons for human errors under critical situations have mainly been the large amount of data which is generated in complex plants and the overstraining of personnel due to an excessive presentation of information. Consequently, even experienced operators have difficulties to distinguish normal from abnormal operational conditions or to identify the cause of process trends. To diminish the load and stress on operators and to support the operator in decision making, the possibilities for using sophisticated pattern recognition methods should be studied in the framework of a joint project which was financed by the Bundesministerium für Bildung, Wissenschaft, Forschung und Technologie and which was carried out in cooperation with the Fraunhofer Institut für Umwelt-, Sicherheits- und Energietechnik at Oberhausen. In particular, the objective was to test the usefulness of neural networks to identify dangerous operating states of a strongly exothermic reference reaction. This report summarizes the results obtained using neural networks which could be well-suited to support the personnel under critical situations and without individual operator errors even in production processes. The neural networks have first been applied to laboratory size reactor.

2. Classification task and data

The detection of a beginning incident is an essential requirement for preventing accidents in chemical plants. Only if the causes of potentially dangerous situations are recognized by the personnel in due time, it is possible to take the necessary counter measures to avoid a thermal explosion which might result in the release of the reaction mixture or even in the destruction of the plant.

Since a short response time of the personnel, particularly, during transient operating conditions is of crucial importance, the efficiency of an additional supervision method based on pattern recognition and especially on neural networks should be

---

[1] Fraunhofer Institut für Umwelt-, Sicherheits- und Energietechnik UMSICHT, Oberhausen

proven in a exothermic chemical reaction. As a reference process, the catalytic esterification between acetic anhydride and methanol was chosen. This strongly exothermic reaction can be controlled within a certain temperature range. Howe-
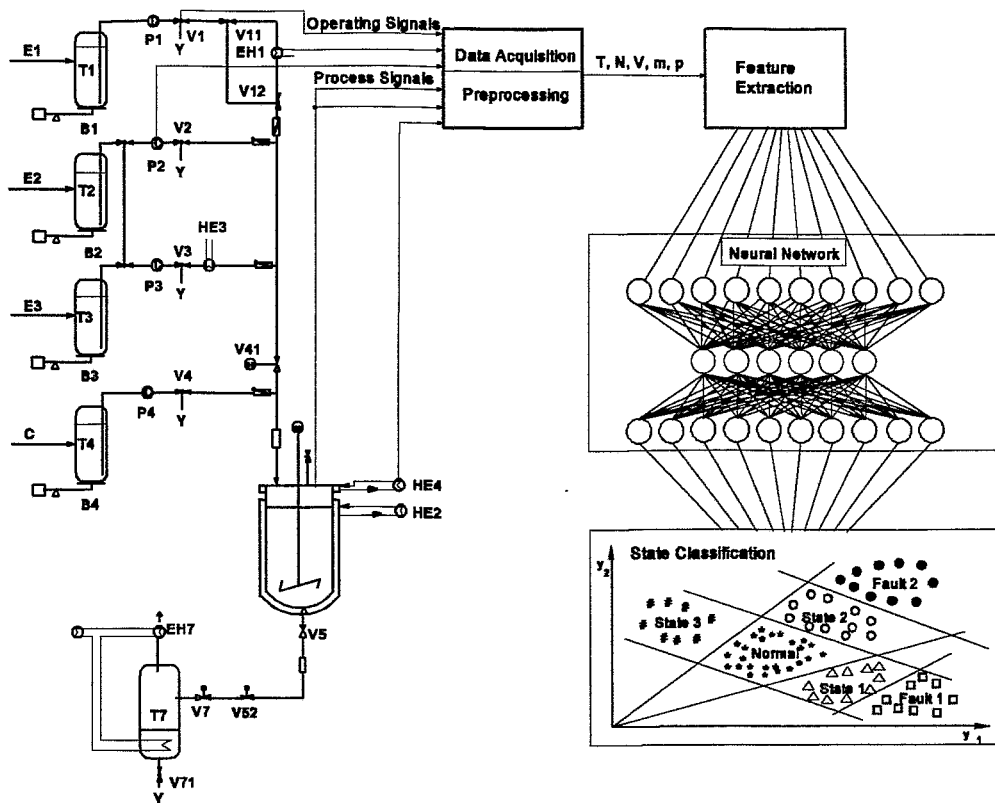
Fig. 1: Identification of dangerous operating states in a chemical plant

ver, it has also enough self-reinforcing potential for heat production to investigate runaway phenomena in dependence on the temperature and on the concentration of the catalyst (sulphuric acid).

Before being applied to the qualitative classification of operating states, such a supervision method first has to be trained with process data from normal operating conditions and different faulty states as well. The scheme in Fig. 1 displays important components of the laboratory reactor used at UMSICHT Oberhausen and shows the working principle of a supervision method based on a neural network.

The main part of the laboratory reactor is a computer-aided reaction calorimeter with a stirred 2 l steel vessel and a jacket heat exchanger (HE 2). Its peripheral units, such as feed tanks (T), balances (B), pumps (P) and valves (V), were used for a dosing-controlled process operation to diminish the rate of a simulated runaway reaction [2]. To investigate different abnormal states, typical faults were simulated in the laboratory reactor, e.g. loss of cooling, stirrer failure, inappropriate feed rate of reactants, inappropriate concentration of catalyst, different reaction temperatures, etc. However, dangerous process states first were simulated numerically with a process simulator developed at Oberhausen to assess the

danger potential of faulty states.

Data sets delivered by the process simulator and by measurements in the laboratory reactor were used for training and testing the state classifiers. In the training phase, the neural network is simultaneously confronted with pairs of feature vectors and target vectors at the input and output layer, respectively. To achieve a good classification ability, the input vectors have to consist of significant features characterizing the respective fault state, while the output vectors contain the experts classification of the specific fault. The feature extraction for the input vector is based on both process signals (filling height, feed rates, stirrer speed, pressure, temperatures of reactor, jacket and of the coolant, etc.) and on calculated values from the measuring/controlling-computer of the laboratory reactor (e.g. thermal capacity and volume of the reaction mass, heat of reaction and reactor temperature gradient).

To avoid multipe neural networks each for a special set-point of temperature or pressure, all features are normalized by relating the different features to the normal process state. For example, temperatures were normalized as a relative deviation from their normal set-point. Furthermore, all features of the input vector were normalized into the range from 0 to 1. Beside extracting suitable features it is also important to choose the appropriate type and the optimum topology of the neural network. In addition to neural networks, fuzzy logic and tensor-based pattern classification are available for comparison. Also, these classifiers first have to be trained with reference feature vectors as described above for neural networks [3].

3. Classification of operating states

Since operating errors in the start-up phase and in other transient conditions of batch and semibatch processes are frequent causes of accidents, it is important to supervise the operating states to recognize human operating errors in an early stage. To investigate the classification of operating states, data of a semibatch process in the laboratory reactor were used representing several state classes like tempering, heating, calibration, cooling, dosing/reaction, danger of runaway and sligth decrease of temperature [4].

Figure 2 illustrates the state classification of a three-layer perceptron network (19/15/7). Its seven output neurons correspond to the several operating state classes characterized by different colours, while the thickness of the coloured layer corresponds to the class membership in percent. At the bottom of Fig. 2, the experts classification of the process states which was used for training is depicted in a reduced diagram. Initially, one reactant and the catalyst were charged into the reactor vessel, then the ingredients were heated, calibrated, and tempered to maintain the temperature set-point at 50°C.

At time t = 106 min, a runaway reaction was initiated by dosing the second reactant over one hour. Due to the large heat production of the catalytic esterification, the temperature of the reaction mixture increases very fast. This is classi-

fied by the neural network as the red-coloured state "danger of runaway" where the red colour hints at the potential danger. By more intensively cooling the reactor jacket, a thermal explosion was avoided. This is shown by the yellow-coloured state "slight decrease of temperature" which indicates that the self-
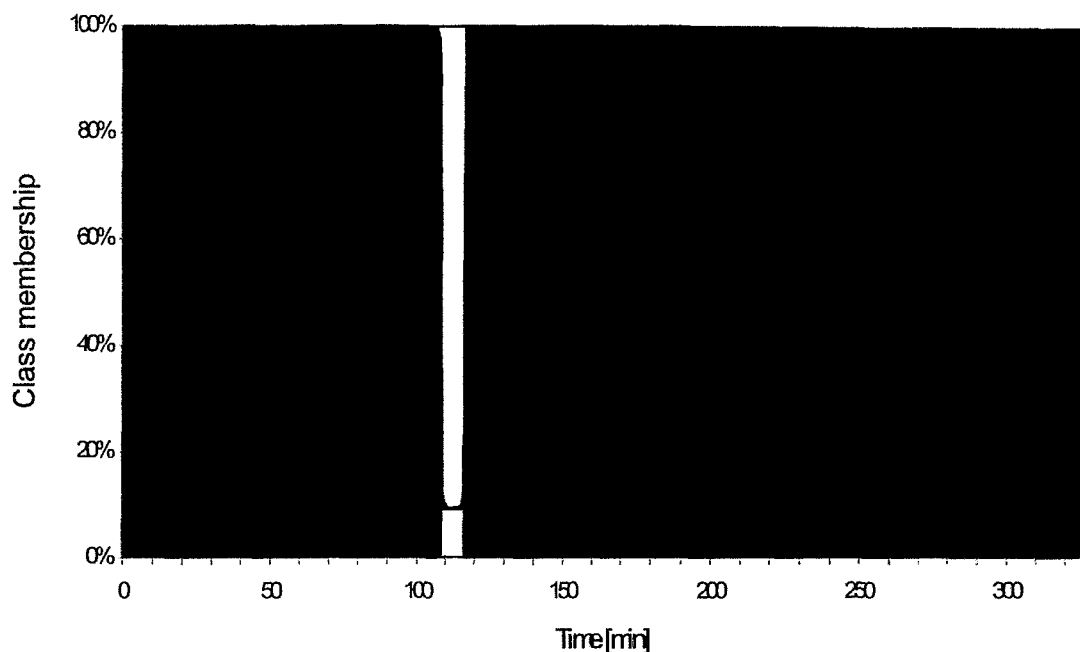
Fig. 2: State classification of a process sequence in the laboratory reactor using the perceptron network (19/15/7)
State classes: tempering, heating, calibration, cooling, dosing/reaction, danger of runaway,

acceleration of the rate of reaction was suppressed by the available reserve of the cooling system. Finally, also a normal operation was ensured as shown by the green-marked state "dosing/reaction". Contrary to the experts classification, the neural network already assigns the dark blue-coloured state "cooling" and the light blue-coloured state "tempering" before the end of dosing (t = 155 min). The reason for this is that the reactant of the hold-up is completely consumed. Therefore, there is no heat production but there are still heat losses. Otherwise, there exist no important differences between the experts decision and the network classification (Fig. 2).

To classify even simultaneously occurring operating states and/or faulty states, the neural network had to be modified regarding the defined class membership and the display of the classification results [5]. For this purpose, a summed class membership was introduced.

In Fig. 3, an untrained sequence of an isoperibolic semibatch process (jacket temperature set-point 28°C) with a stirrer failure was classified by a perceptron network (24/4/18) which was trained with a similar isoperibolic experiment (set-point 40°C).

111

Due to the used normalization of the temperature features, the perceptron network is also capable of classifying an unknown process sequence with a different
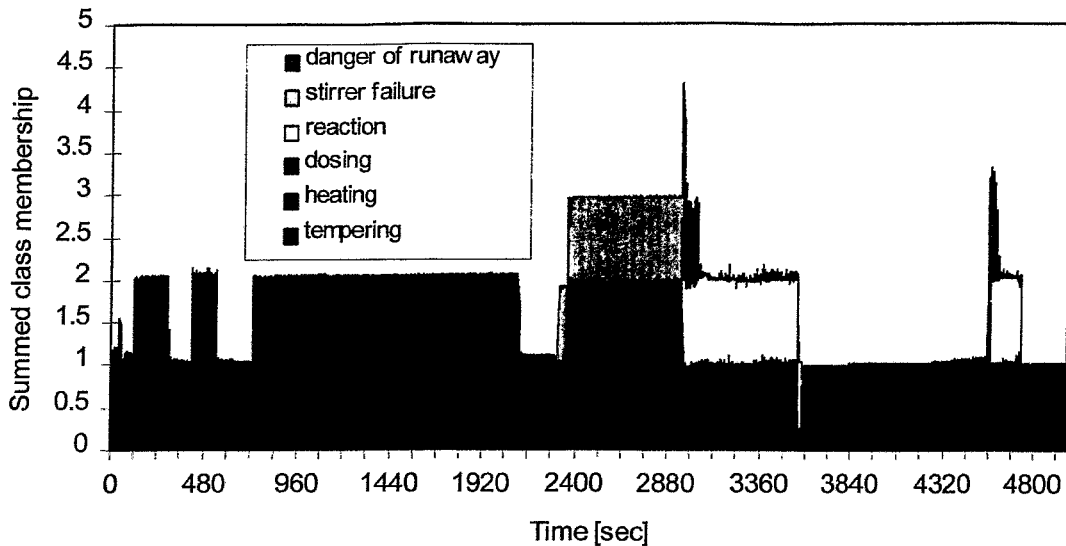
Fig. 3: State classification of an untrained process sequence (set-point 28°C) using a perceptron network (24/4/18) trained by a different process sequence (set point 40°C)

temperature set-point. Even, the critical situation during the stirrer failure, further reactant dosing and stirrer restart (2300-3000 s), where there is a danger of runaway, is classified correctly.

4. Danger classification and fault isolation

A neural network trained for classification of operating states is capable of correctly classifying normal states and several faulty states, but it cannot provide information on the potential danger of the different faults. Since the assessment of the danger and the early warning of the personnel are important for taking suitable counter measures in dangerous states, a new supervision conception was realized. For this purpose, separate neural networks are used for classifying the danger and the faults, respectively.

As it can be seen in Fig. 4 and 5, five warning stages were chosen: normal (green), pre-alarm (yellow), alarm (orange), extreme danger (red) and decreasing danger (blue). To get a good generalization capability, the training data were composed of feature vectors from state changes of the defined warning stages which were chosen by the expert from all the available fault simulation experiments. For improving the sensitivity regarding beginning dangerous faults, the features were mainly extracted from dosing rates, values of the pressure and the reactor temperature and their derivates, the second derivate of the reactor temperature, the temperature difference between reactor and jacket and its rate, the relative deviation of the reactor temperature from the temperature set-point and several values of temperature differences of the cooling system which were

112

normalized relative to the temperature set-point. In total, there are 15 elements in the feature vector.
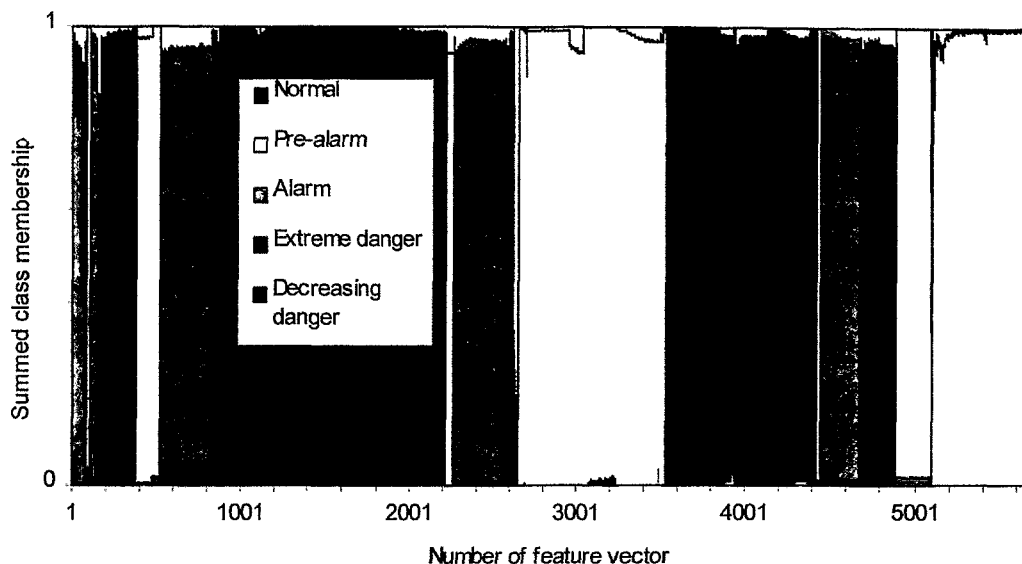
Fig. 4: Reclassification of data used to train the perceptron network (15/4/5) for danger classification

Figure 4 shows the reclassification results of the perceptron network (15/4/5) trained for danger classification. Although a summed class membership was used, more than 99% of the 5686 reference vectors were unambiguously assigned in agreement with the desired warning stages. In Fig. 4, only the feature vectors between number 2610 and 2647 which belong to an alarm stage were not recognized with high class membership, while the normal vectors between 3923 and 3940 were assigned to the pre-alarm stage. However, the results can be accepted because these reference vectors characterize beginning of dosing during a normal operating state.

After having detected a deviation from the approved process control, a second neural network for fault isolation is used. The following six typical fault classes were trained: stirrer failure, loss of cooling, low and high dosing rate, extraneaous substance in the reaction mixture (mischarging) and false temperature level (temperature fault).The training data are based on the same simulation experiments as used for danger classification, but the data ranges for the fault reference vectors were newly chosen. Also, the reference vectors consist of the same features.

The perceptron network (15/3/6) trained for fault isolation can reclassify these training data very well. Even untrained data of two simultaneously occurring faults are unambiguously classified as shown at the bottom of Fig. 5. The unknown data come from a semibatch process where there are a high dosing rate and a stirrer-failure simultaneously.

At the upper part of Fig. 5, the profiles of some process and plant variables are
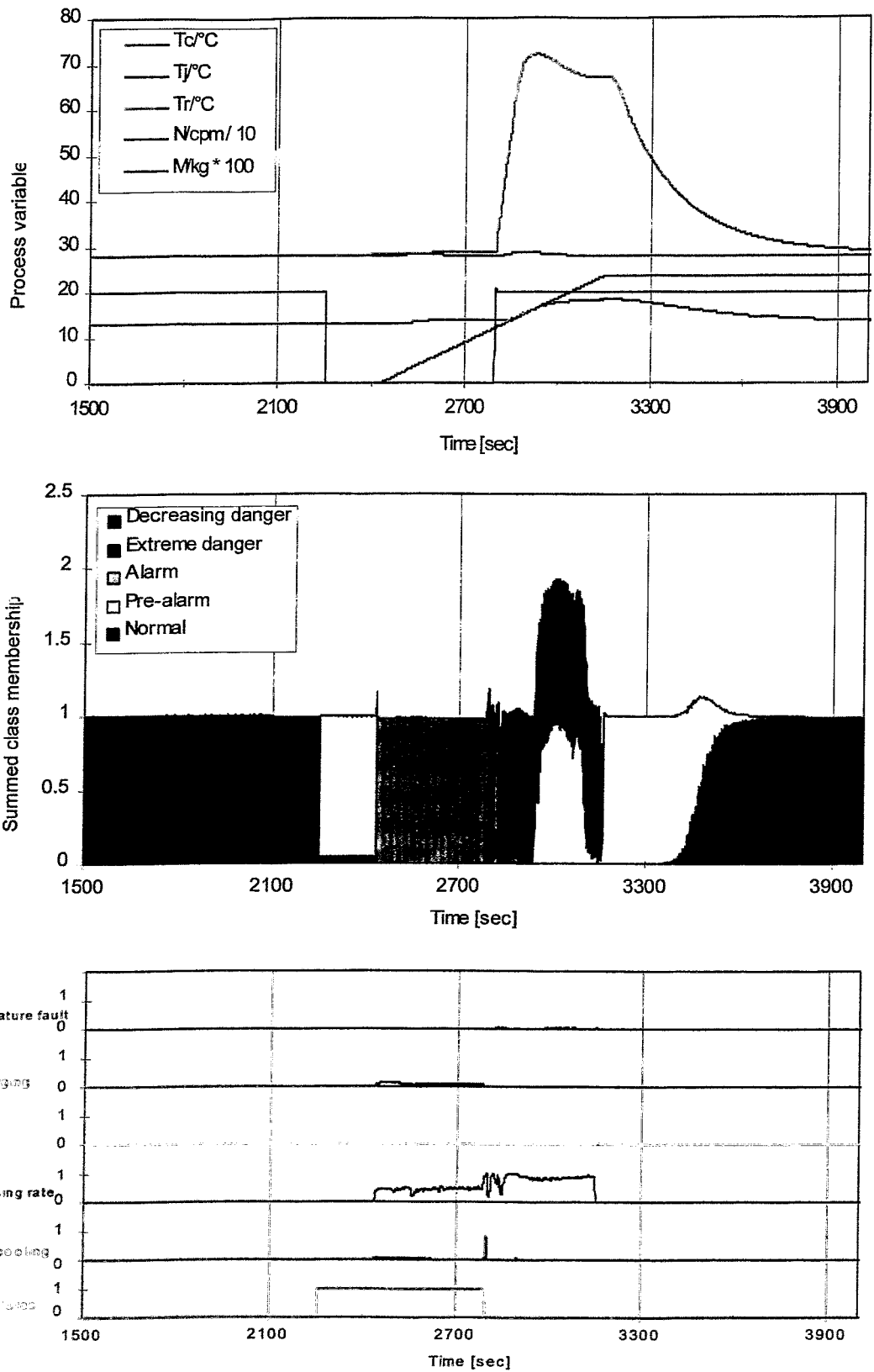
Fig. 5: Profiles of process variables and results of perceptron networks for danger classification and fault isolation during an incident scenario with stirrer failure and high dosing rate

represented, such as the reactor temperature Tr, the jacket temperature Tj, the temperature of the coolant reservoir Tc, the stirrer speed N, and the mass of the second reactant M added to the reaction mixture. In the middle part, the results of the danger classification are depicted for comparison. The fault network recognizes the stirrer failure and the high dosing rate where the maximum class membership of the high dosing rate during the stirrer failure is not reached (see at the bottom of Fig. 5). Obviously, this neural network takes into consideration that the heat production due to the loss of mixing is lower than during normal operation. After restarting the stirrer, the rate of reaction increases exponentially due to the accumulated mass of reactants and due to the insufficient cooling. This is indicated by the short occurrene of the fault - loss of cooling. After that only the fault "high dosing rate" is classified because the exothermic reaction is restabilized by more intensivly cooling of the jacket.

Also, the danger classifier provides reasonable information on the danger potential in this incident scenario. After the stirrer failure, first the neural network indicates a pre-alarm because of the missing dosing rate of the reactant. Then there is an alarm due to dosing of the second reactant. After restarting the stirrer, this extreme danger is correctly classfied because, due to the reactant accumulation, a runaway reaction begins. However, the runaway reaction is stopped by an increased power of cooling. This is shown by the classes "decreasing danger" and "pre-alarm" in the following time. It can be stated that the untrained incident scenario is assigned and assessed by both perceptron networks correctly.

5. Conclusions

The efficiency of the neural-network approach to identify dangerous operating states could be proven by data sets of a strongly exothermic reference process which were delivered by fault simulations in a laboratory reactor. Results show that the multi-layer perceptron network is capable of correctly classifying normal operating states and faults of the investigated process sequences. Even untrained process sequences and simultaneously occurring faults are classified.

However, a neural network trained for classification of operating states cannot assess the potential danger of different faults. Therefore, separate perceptron networks were used for danger assessment and for fault isolation. Early warning and isolating the fault causes should provide sufficient time for the personnel to correct the deviation from safe operation. Future projects are planned to develop this supervision method up to pilot scale and then to large scale production plants.

References

[1]   A. Benuzzi and J. M. Zaldivar (eds.) (1991), *Safety of Chemical Batch Reactors and Storage Tanks*, Dordrecht, Kluwer Academic Publishers

[2]   J. Neumann, G. Deerberg, S. Schlüter, P.-M. Weinspach (1997), *Anwendungsmöglichkeiten neuartiger EDV-gestützter Erkennungsmethoden zur*

Identifizierung gefährlicher Betriebszustände in Chemieanlagen (II), Oberhausen, Abschlußbericht 01RG9424/8

[3]   K. van der Vorst, G. Hessel, D. Hoppe, W. Schmitt, N. Tefera, F.-P. Weiß (1998), *Anwendungsmöglichkeiten neuartiger EDV-gestützter Erkennungsmethoden zur Identifizierung gefährlicher Betriebszustände in Chemieanlagen (I) Abschlußbericht 01RG9424/5*, Rossendorf, Report FZR-223

[4]   J. Neumann, S. Schlüter, P.-M. Weinspach, G. Hessel, W. Schmitt, K. van der Vorst, F.-P. Weiß (1998), Früherkennung sicherheitsrelevanter Betriebszustände in Chemieanlagen mit neuronalen Netzen, *at-Automatisierungstechnik,* 46,2, S.104-110

[5]   G. Hessel, W. Schmitt, K. van der Vorst, F.-P. Weiß, J. Neumann, S. Schlüter (1997), "Identification of Dangerous States in Chemical Batch Reactors Using Neural Networks" , *Proc. of IFAC Symposium on Fault Detection, Supervision and Safety for Technical Processes - SAFEPROCESS'97,*(pp. 926-931), Hull, United Kingdom

A TECHNICAL SYSTEM TO IMPROVE THE OPERATIONAL MONITORING OF THE ZAPOROZHÝE NUCLEAR POWER PLANT

M. Beyer, H. Carl, K. Nowak[1], P. Schumann, A. Seidel, F.-P. Weiß, J. Zschau

1. Introduction

As part of the programme implemented by the German Ministry of Environment, Nature Conservation and Reactor Safety to cooperate with the Central and Eastern European States (CEES) and the Commonwealth of Independent States (CIS) in the area of nuclear safety, a technical system to improve operational monitoring has been designed, specified and established since 1992 as a pilot project in the Zaporozhýe/ Ukraine nuclear power plant by Forschungszentrum Rossendorf and Technischer Überwachungsverein Rheinland with a significant contribution from the State Scientific and Technical Centre of the Ukrainian supervisory authority. The technical system complements existing operational checking and monitoring facilities by including modern means of information technology. It enables a continuous monitoring of the state of unit 5 in normal operation and in cases of anomalies or incidents so that when recognisable deviations from the regular plant operation occur, the Ukrainian supervisory authority can immediately inquire and if necessary impose conditions on the operator. The radiological and meteorological parameters at the nuclear power plant location are monitored to the extent necessary to assess the current radiation situation and to implement efficient emergency management measures.

2. Selection of parameters for monitoring

The parameters to be monitored (fig. 1) were selected on the basis of German and international experience using the criterion of being able to observe and evaluate the adherence to the following four protection aims:

- P1 Assurance of reactor shutdown
- P2 Assurance of core cooling
- P3 Assurance of heat removal from the primary circuit and assurance of its integrity
- P4 Assurance of the integrity of the containment

in connection with nine monitoring tasks which refer to certain parts of the plant, media, processes and plant conditions.

---

[1]Technischer Überwachungsverein Rheinland, Institute for Nuclear Engineering and Radiation Protection, POB 91 09 501, D-51101 Köln
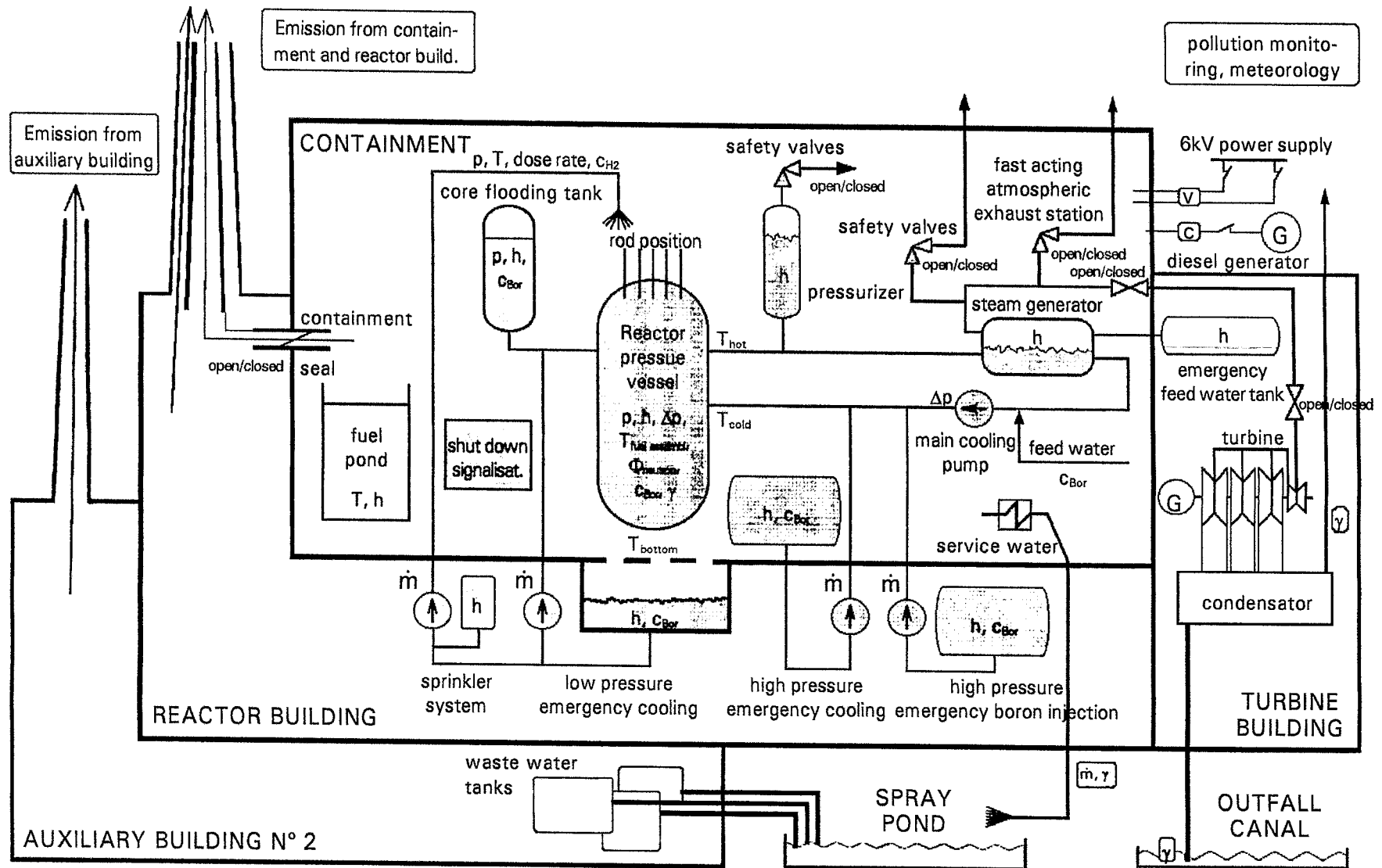
Fig. 1 Parameters selected for the operational monitoring and their assignment to systems and components

On the basis of the protection aims and monitoring tasks concept 49 different safety related operational parameters of the core and unit,18 radiological parameters of the unit and the plant site and 6 meteorological parameters are permanently and automatically recorded, monitored and evaluated.

3. Automatic evaluation at the NPP site

The technical system set up in the Zaporozhýe nuclear power plant is hierarchically structured (fig. 2). The system is realised by a site-wide local area network connecting all six reactor units, two auxiliary buildings, the laboratory building and the so-called Zaporozhýe Centre which is a sheltered room. The on-site radiological and meteorological parameters are collected in the operational computer of the auxiliary building 2. From there these parameters are down-loaded by the Transfer Computer Auxiliary Building 2 and the operational parameters of the monitored unit 5 are down-loaded by the Transfer Computer Unit 5 every four seconds. There they are checked and condensed individually or in monitoring-specific links to representative logical data channels and transferred as data packages at time intervals of one minute to the Server and to the On-site Computer in the laboratory building. In the On-site Computer the process and plant status is finally evaluated by comparing the current data with monitoring-specific limit values and by combining the limit value violation of different parameters. The monitoring-specific limit values generally lie above the operational tolerance values to prevent any restrictions of the operator's room for manoeuvre but necessarily lie below the approved limit values set by the authorities and below the load limit values specified by the manufacturers, respectively. If no violation of the protection aims is found, the users receive a data file every 10 minutes, only. Excess of threshold values causes a report to be sent to the users in the Zaporozhýe Centre (authority) and in the administration building (On-site-inspector and operator). In view of the importance and possible effects of excess, there are three different information levels:

- A Notice ▭ is sent to the authority and the operator in case of a failure in redundant measuring lines or safety systems if it reduces safety margins. The report consists of a short verbal communication on display and logging printer, the indication of the failed measuring channel or system and the repair deadline which must be complied with. The notice is automatically cancelled when the cause has been eliminated.
- A Warning ☎ is conveyed to the users in the event of a violation of at least one protection aim. It consists of verbal communication and announcement on the display, entry in a warning journal and the output of actual values and limit values of the monitored parameters which can be linked to the protection aim violation. This information should give the trained specialist an overview of the process and plant status which emerged. The receipt of warning must be acknowledged by the users. A state of warning may only be cancelled when the authority gives its consent and no further protection aim violation has occurred for a fairly long period.

ADMINISTRATION BUILDING

X-TERMINAL

TRANSCEIVER

LABORATORY BUILDING

ON-SITE-COMPUTER

SERVER

NIU

ZAPOROGE CENTRE

TERMINAL COMPUTER

NIU

SM-2M - OPERATIONAL COMPUTER
TC - TRANSFER COMPUTER
NIU - NETWORK INTERFACE UNIT
COMPUTER NETWORK

AUXILIARY BUILDING 1

2 x SM-2M

NIU

AUXILIARY BUILDING 2

COMPLEMENTARY MEASURING DEVICES

2 x SM-2M

TC

NIU

NIU

6 x SM-2M

UNIT 1

NIU

6 x SM-2M

UNIT 2

NIU

6 x SM-2M

UNIT 3

NIU

6 x SM-2M

UNIT 4

NIU

TC

6 x SM-2M

COMPLEMENTARY MEASURING DEVICES

UNIT 5

NIU

6 x SM-2M

UNIT 6

120

Fig. 2: The structure of the technical system at Zaporoshye NPP site to improve the operational monitoring

– An Alarm ⚠ in the technical system is triggered if in case of a protection aim violation a process or plant status is reached which for safety reasons requires intensified monitoring. This is always necessary when incidents or accidents occur such as in the International Nuclear Event Scale INES for significant events in nuclear engineering installations. Whereas in all states from normal operation to warning the operational information is transmitted to the users at time intervals of ten minutes and the radiological-meteorological data of sixty minutes, in the state of Alarm the intervals between two consecutive transmissions are shortened to one and ten minutes, respectively. Moreover, the conditions of the Warning state are valid, too.

4. State of the system

Test operation of the technical system to improve operational monitoring was commenced at the end of 1995. Since then, the on-site supervisory authority and operator have been able to fulfil their monitoring duties more efficiently than before, based on the automatic evaluation and on presentations of actual parameters. After the completion of the user software by the State Scientific and Technical Centre of the Ukrainian supervisory authority and the operator, which the German partners assisted by consulting, and after having proven the reliability of the system under nuclear power plant conditions the industrial testing phase of the system has been started in the middle of 1996.

In 1997 the technical system has been connected to the Kiev Centre of the Ukrainian supervisory authority. The most essential technical means - first level of realisation - for the data transfer and for monitoring purposes of this centre (fig. 3) were jointly specified, procured in Germany, tested, consigned to the Ukraine and free left to the partner at the place of action. It was proved during testing the information transfer from the Zaporozh'ye NPP to the Kiev Centre that the rented line fulfils the necessary demands. Within a functional test at the end of 1997 on-line date from the on-site system at Zaporozh'ye NPP were correctly transferred to Kiev.

The described technical system is unique in the CEES and in the CIS in terms of its effective monitoring of nuclear power plants with VVER-1000 reactors. The modular and open structure of the system makes it possible to extend the monitoring to all six units at the Zaporozhýe NPP and to connect more users. This project has been founded by the German Federal Ministry for Environmental, Nature Conversation and Reactor Safety.

Fig. 3: Structure of the Kiev Centre

DRAG REDUCTION IN LOW-CONDUCTING LIQUIDS
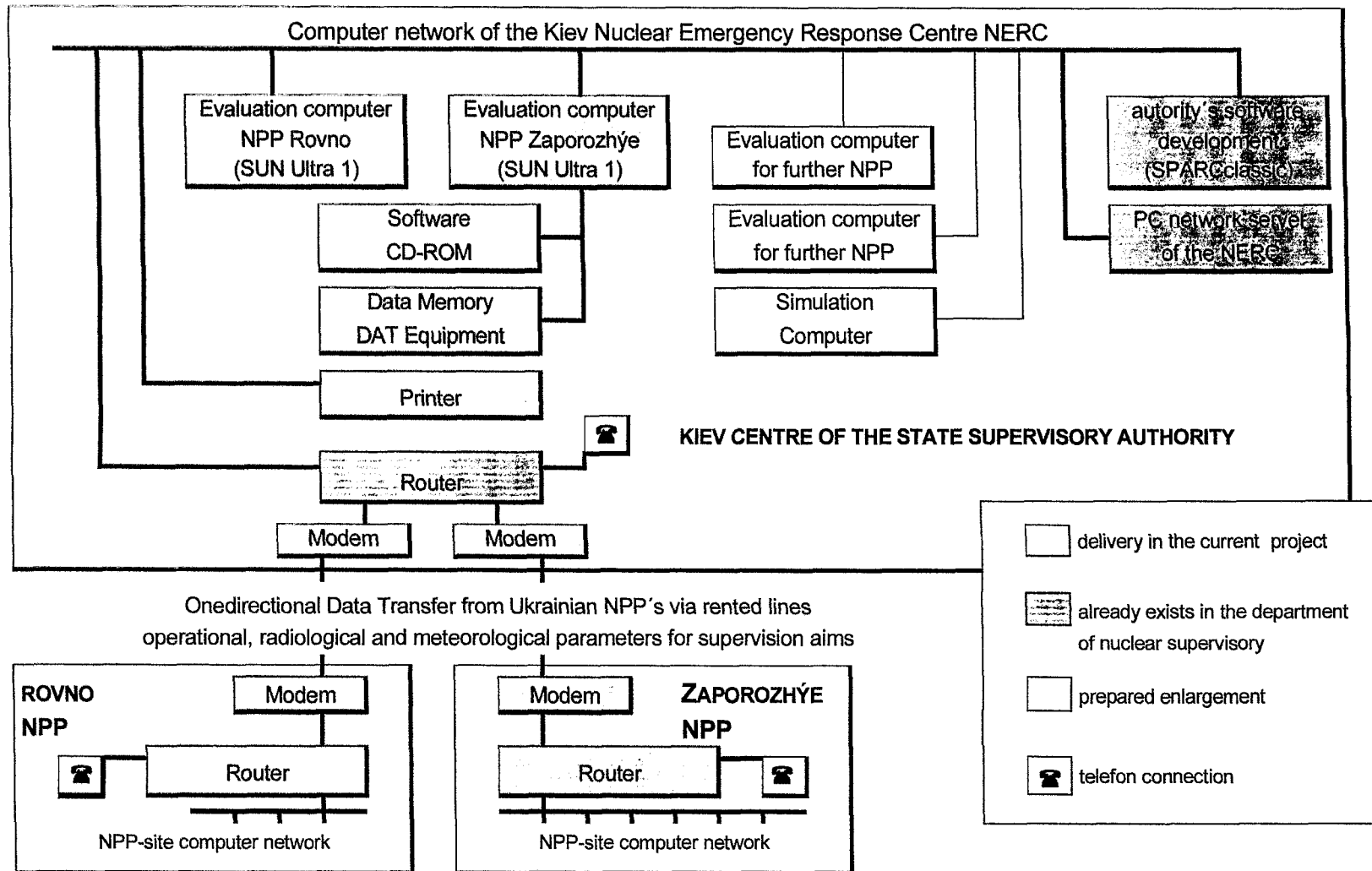
T. Weier, G. Mutschke, G. Gerbeth

1. Introduction

Drag reduction is a main design issue in engineering because drag estimates to a large amount the running costs of transport of or in fluids. If the fluid is electrically conducting, like seawater, apart from conventional methods there is an additional possibility of control by electromagnetic body forces, i.e. Lorentz forces. In low-conducting liquids, these forces may be generated by the application of suitably chosen magnetic and electric fields. This idea was first published by Gailitis and Lielausis in 1961 [1]. The main advantage of the Lorentz force is that it acts on a volume of the flow and is not confined to the edges of the fluid stream. Therefore, electromagnetic flow control has recently attracted the attention of several research groups [2,3]. Main issues are control of turbulent boundary layers by different strategies, transition delay as proposed in [1], separation control and manoeuvrability.

1.1 Turbulent Boundary Layer Control

Most flows relevant for practical applications are turbulent, simply due to the large length-scales involved. Turbulent skin friction is one of the main sources for drag on airplanes and ships. However, the mechanism leading to the orders of magnitude higher skin friction of turbulent compared to laminar boundary layers, is still largely unrevealed. The kinematics of turbulent boundary layers has been intensively studied in the past (e.g. Klebanoff [4]). The region of highest turbulence production is the buffer layer near the wall. This region controls the magnitude of the wall shear stress. Typical flow structures of the buffer layer are low- and high-speed streaks, i.e. spanwise modulations of the streamwise velocity, and streamwise vortices. There is general belief that controlling these structures would lead to considerable reduction of skin friction.

Wall-normal Lorentz forces (see right part of Fig. 1) were applied by Nosenchuck and co-workers [5] in two different configurations. First, a gradient of the conductivity σ produced by injecting an extra electrolyte together with uniform current density and magnetic field was used to suppress lift-off of near wall vortices and therefore Reynolds-stresses. Experiments in a turbulent boundary layer showed a reduction of the friction drag of about 90%.

In a second series of experiments, Nosenchuck and co-workers designed special arrangements of single actuators ("Tiles") to checkerboard patterns These tiles where driven in a certain way to obtain a global modification of the near wall flow characteristics, i.e. a travelling wave structure was generated in the boundary layer, hereby completely replacing the natural flow. Skin friction
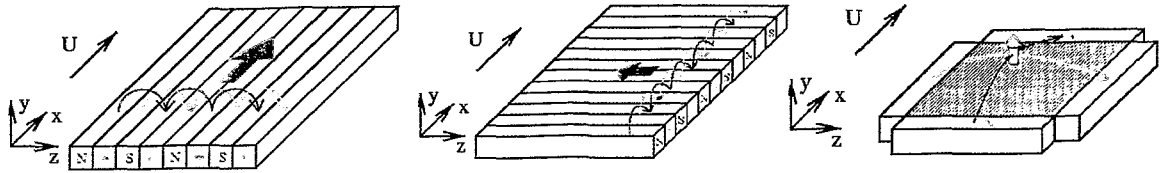
Fig. 1: Electrode/magnet configurations to generate Lorentz forces in stream-
wise (left), spanwise (center) and wall-normal direction (right)

reduction by 55% was measured. Presumably, the reason is a restructuring of
the near wall flow with a changed vorticity distribution.

A first experiment to control a turbulent boundary layer by streamwise forcing
was performed by Henoch and Stace [6]. The Lorentz force is generated by the
simple strip-like geometry (hereafter referred to as SSG, see left part of Fig. 1)
of alternating electric and magnetic poles [1]. At moderate interaction parame-
ters ($0.3 \leq N \leq 1.0$), the fluctuating shear stress and the fluctuating streamwise
velocity components where reduced by approximately 30%, while the mean
quantities left unchanged. Henoch and Stace explain this effect by the pumping
action of the Lorentz force. By the acceleration of the near-wall fluid, the lift-up
of shear-generated wall vortices is disrupted. The inner layer is stabilized by the
addition of high momentum fluid, thereby the process of turbulence production
and dissipation is disrupted. However, in the case of strong interaction parame-
ter, distinct wall jets at the boundaries of electrode and permanent magnet
stripes occur due to a spatially inhomogeneous Lorentz force.

It is widely accepted, that streamwise vortices are the main reason for the high
turbulent wall drag. A weakening of these vortices should therefore also reduce
turbulent skin friction. Several successful attempts have been done to shear the
streamwise vortices with oscillating walls. Kim [7] undertook a direct numerical
simulation of a channel flow and found a skin friction drag reduction of 30% by
imposing oscillating Lorentz forces in spanwise direction (middle part of Fig. 1).

1.2 Transition Delay

The optimum way of controlling turbulence is to prevent its arising because
laminar skin friction is orders of magnitude smaller than turbulent one. There-
fore, the idea is to achieve transition delay which might be of practical impor-
tance at least for flows around smaller objects (e.g. hydrofoils).

The first paper on electromagnetic boundary layer control [1] dealt with transi-
tion delay by introducing an appropriate electromagnetic force to the boundary
layer. The motivation was to create a spanwise-homogeneous and in wall-
normal direction exponentially-decreasing Lorentz force [8] which, under certain
conditions, asymptotically leads to an exponential velocity distribution in the
boundary layer. The key point is that such exponential velocity profiles are
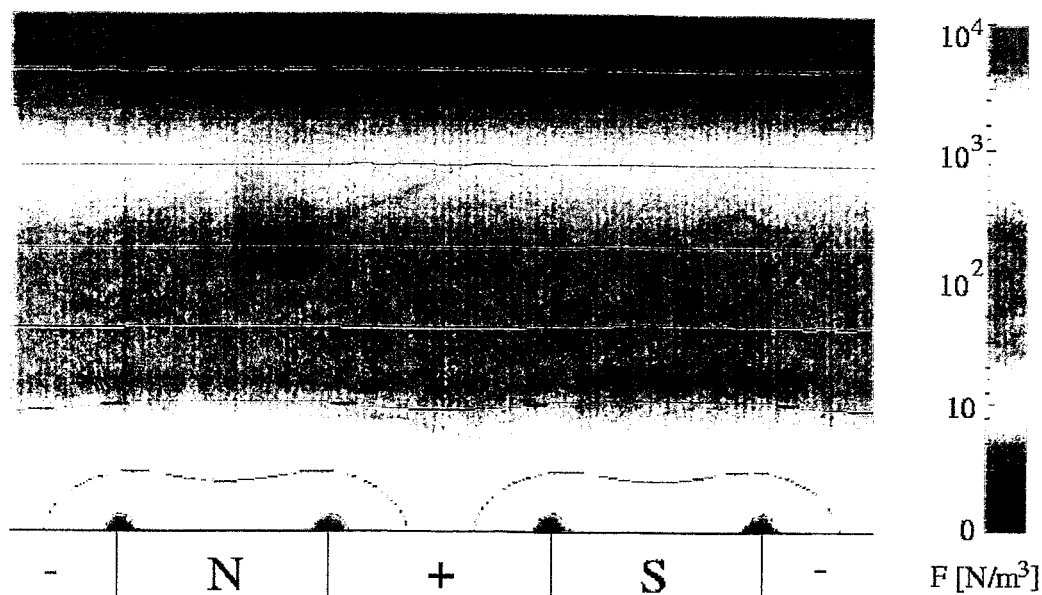
Fig. 2: Typical distribution of the streamwise Lorentz force above the SSG

proven to have much better stability properties than ordinary Blasius profiles as it was intensively investigated in suction experiments in the past.

To benefit from the better stability properties of an exponential velocity profile, one has to find an appropriate setup of electrodes and magnets in order to create that body force. The SSG guaranties a force distribution with streamwise components only. However, already Grinberg [9] showed by an analytical modelling of the field distribution that the resulting force is strongly inhomogeneous in spanwise direction, especially in regions close to the surface. The mathematical reasons behind are simply singularities of the electric and magnetic field at the corners of the electrode planes and the rectangular magnets, respectively. This leads to periodic maxima of the Lorentz force at those places (see Fig. 2).

Any variation of the Lorentz force in spanwise direction is likely to cause 3-D instabilites in the boundary layer which certainly will diminish or might even completely destroy the desired stabilizing influence of the streamwise forcing. Although this has not yet been checked quantitatively, one goal is certainly to design a geometry of electrodes and magnets which creates a perfectly homogeneous force. This is the subject of the current work.

1.3 Separation Prevention and Manoeuvrability

Separation prevention reduces form drag and allows higher lift at larger angles of attack. This might be of importance for flows around hydrofoils and rudders where the energetic balance is not the main goal.
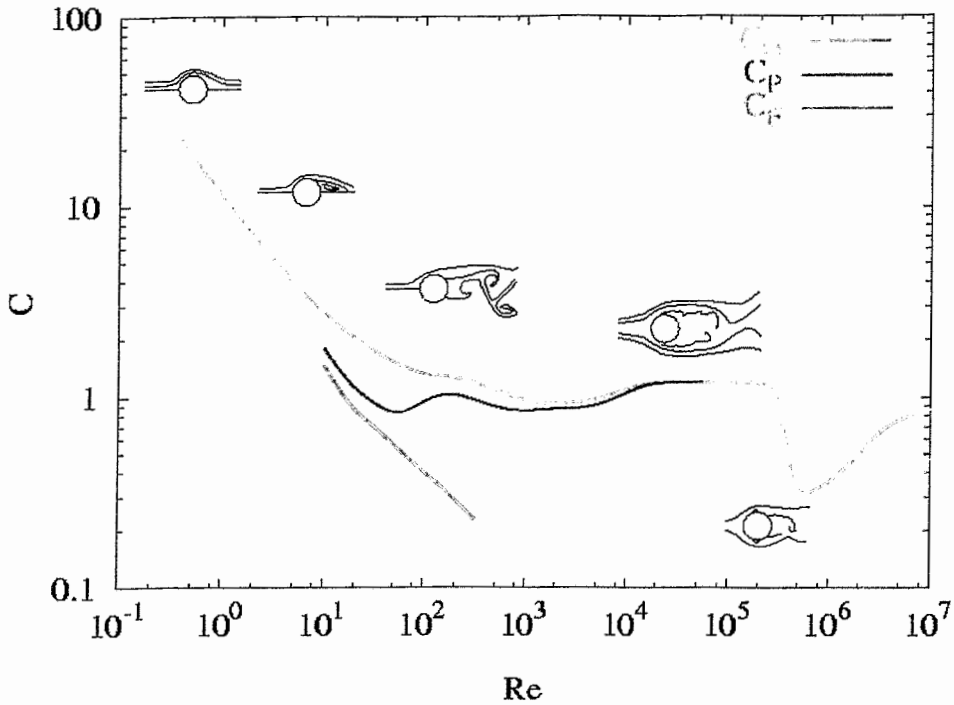
Fig. 3: Different drag components ($c_d = c_p + c_f$) for flow around a circular cylinder versus Reynolds number

2. Model Experiments on Bluff Bodies

First experiments in a simple rotating annular tank (details are described in [10]) were performed to validate the force effects and to visualize flow regimes in order to get qualitative results on the spectrum of possible phenomena. A cylindrical test body covered with electrodes and magnets to create a wall-parallel Lorentz force was assembled. The main focus in these experiments was not on turbulent boundary layers, but on separation control, drag reduction and modification of the wake structure. The range of Reynolds numbers covered in the experiments is $500 < Re < 2000$. Static forcing as well as sinusoidal time-periodic forcing was investigated in detail. The results were obtained by flow visualization with colour-streaks and particles.

To extend these mainly qualitative results and to investigate certain phenomena in detail, new facilities were built and new measurement equipment was installed. An open electrolytic channel was designed to perform low-speed mid-scale experiments. To cover larger velocities and to allow for "real-size" experiments, a closed electrolytic tunnel is currently being assembled.

126
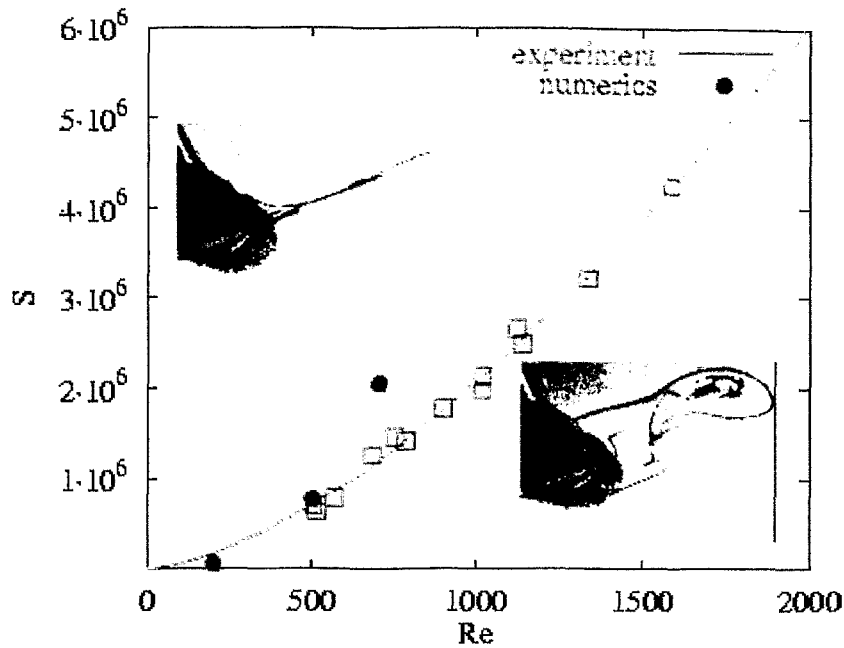
Fig. 4: Stability diagram for steady forcing

3. Results

The flow around bluff bodies includes phenomena, which can not be found in the canonical case of flat plate boundary layer under constant pressure. A main feature here is the occurrence of separation, resulting in an complete restructuring of the flow field. Although the boundary layer remains laminar in the cases considered here, the wake of the body is turbulent even for small Reynolds numbers.

With increasing Reynolds number (see Fig. 3), the flow changes from a creeping flow at Re < 1 to an asymmetric flow for Re < 5, this flow separates for larger Re and the wake becomes unstable at Re$\approx$45. Further increase of the Reynolds number leads to evolving three-dimensional structures at Re$\approx$180 and a transition of the wake flow into turbulence. From Re$\approx$1000 on the separating shear layers are subjected to Kelvin-Helmholtz instabilities, The flow picture doesn't change very much up to Re$\approx$2$\cdot$10^5, where transition of the boundary layer occurs. The now turbulent boundary layer intensifies the momentum transport between boundary layer and the outer flow. Thereby high momentum fluid from the outer flow increases the energy of the boundary layer, and boundary layer separation is shifted towards the rear stagnation point.

Corresponding to these changes in the flow pattern, the total drag c_d on the cylinder changes with the Reynolds number. The friction drag c_f could be obtained from integration of the wall shear stress along the cylinder surface, the pressure drag c_p results from the separated flow at the rear side of the cylinder.

127

Due to this separation, pressure at the rear stagnation point is lower than at the front stagnation point. The friction drag dominates for low Reynolds numbers, while for $Re > 100$ the pressure drag alone determines the total drag.

Separation occurs downstream a critical point where the normal derivative of the streamwise velocity vanishes (2-D, steady flow). Applying a streamwise Lorentz force adds momentum to the near-wall flow and therefore leads in general to a delay of separation. Sufficiently strong forces might be able to suppress it completely in certain flow configurations.

The straightforward application of the SSG to the circular cylinder is to direct the Lorentz force parallel to the cylinder surface. (One could imagine two plates as shown in the left part of Fig. 1 each wrapped around a half cylinder, so that the Lorentz forces on both sides of the cylinder have the same direction. For separation suppression they should of cause point downstream.) The stability diagram of the flow, obtained from flow visualization, is shown in Fig. 4. The Reynolds number Re is defined with the cylinder diameter D as the characteristic length. As the interaction parameter $N = (j_0 B_0 D)/(\rho U_0^2)$ is defined with the imposed magnetic field B_0 and the current density j_0, beside the fluid density ρ the square of the freestream velocity U_0 appears in the denominator. Therefore, a parameter $S = N \cdot Re^2$ is introduced as a nondimensional measure of the applied force which is independent of the flow velocity. Above the drawn critical curve in Fig. 4, vortex-shedding is suppressed. The two inserts show flow snapshots at $Re = 760$. No Lorentz force is acting in the right insert, whereas on the left side the flow was stabilized due to a Lorentz force of $S = 1.47 \cdot 10^6$.

A strong enough downstream forcing results in a jet originating at the rear stagnation point. This jet exerts a net force on the cylinder in upstream direction, and obviously, the total drag becomes negative. On the other hand, a force directed upstream shifts the separation towards the front stagnation point, and a vortex street with larger vortices than in the unforced case forms. In this situation, an increased drag has to be expected. These experimental observations are in line with numerical simulations of the flow.

4. Outlook

The Rossendorf EBLC (electromagnetic boundary layer control) programme is aimed to take benefit of the main property of electromagnetic boundary layer control: its flexibility with respect to the geometrical arrangement of magnets/electrodes and the electrical feeding system. For the future we see the following most interesting scientific questions and applications of EBLC:

- Up to which Re can a flow stabilization be reached with DC-currents by an optimized magnet/electrode configuration?
- Will the use of suitable AC currents really lead to an energetic break-even in the turbulent region at higher Re, as the studies on oscillating cylinders imply?

- Which energetic optimization is possible by means of some reactive concept based on some feedback control strategy?
- What is the practical interest in terms of simple and cost-effective realizations of EBLC-actions for flow manoeuvrability or lift production?

References

[1] A. Gailitis and O. Lielausis (1961), *On a possibility to reduce the hydrodynamical resistance of a plate in an electrolyte,* Applied Magnetohydrodynamics. Reports of the Physics Institute 12, (Prikladnaya Magnitogidrodinamika. Trudy Instituta Fiziki, 12), Riga, 143 (in Russian)

[2] G. Gerbeth (Ed.), *Proceedings of the International Workshop on Electromagnetic Boundary Layer Control (EBLC) for Saltwater Flows,* Dresden, July 7-8, 1997

[3] J.C.S. Meng (1994), Seawater Electromagnetics: A new Frontier, *Magnetohydrodynamics,* 30, 401

[4] P.S. Klebanoff (1954), *Characteristics of turbulence in a boundary layer with zero pressure gradient,* National Advisory Committee for Aeronautics, NACA-Report 1247

[5] D.M. Nosenchuck and G.L. Brown (1993), "Discrete Spatial Control of Wall Shear Stress in a Turbulent Boundary Layer", in: R.M.C. So, C.G. Speziale and B.E. Launder (Eds.) *Near-Wall Turbulent Flows,* (pp. 689-698), Elsevier

[6] C. Henoch and J. Stace (1995), Experimental investigation of a salt water turbulent boundary layer modified by an applied streamwise magnetohydrodynamic body force, *Phys. Fluids,* 7, 1371

[7] J. Kim (1997), "Boundary Layer Control for Drag Reduction: Taming Turbulence", in G. Gerbeth (Ed.), *Proceedings of the International Workshop on Electromagnetic Boundary Layer Control (EBLC) for Saltwater Flows,* Dresden, July 7-8, 1997

[8] A.. Tsinober and A.G. Shtern (1967), On the possibility to increase the stability of the flow in the boundary layer by means of crossed electric and magnetic fields, *Magnitnaya Gidrodinamica,* 2, 152 (in Russian)

[9] E. Grinberg (1961*), On determination of properties of some potential fields,* Applied Magnetohydrodynamics. Reports of the Physics Institute vol. 12, (Prikladnaya Magnitogidrodinamika. Trudy Instituta Fiziki, 12), Riga, 147 (in Russian)

[10] T. Weier, G. Gerbeth, G. Mutschke, O. Lielausis, E. Platacis (1997), Experiments on cylinder wake stabilization in an electrolyte solution by means of electromagnetic forces localized on the cylinder surface, to appear in *Experimental Thermal and Fluid Science*

MEASUREMENT TECHNIQUES TO DETERMINE LOCAL QUANTITIES IN LIQUID METAL FLOWS

S. Eckert, W. Witke, G. Gerbeth

1. Introduction

In the last few decades magnetohydrodynamic (MHD) effects have attracted growing interest because of its potential impact on numerous industrial technologies, such as metallurgy, crystal growth, electron or laser beam melting/evaporation of surfaces, etc.. In processes involving electrically conducting liquids, the application of an external magnetic field offers efficient opportunities for a contactless flow control and fluid handling.

However, for a well-aimed optimisation of the flow structure local information about flow quantities like velocity, pressure, temperature, concentration or void fraction are necessary. In case of liquid metals the choice of a suitable measuring technique is a crucial problem, because the user is confronted with the nature of opaque fluids, high temperatures as well as a strong chemical reactivity of the fluid against a number of materials. Therefore, measuring techniques well-known from ordinary hydrodynamics generally fail for liquid metal applications. As a consequence, no commercial measuring systems are available. In the last years local sensors have been developed, tested and applied to measure the liquid velocity and the void fraction in liquid metal two-phase flows by the MHD department of the Institute of Safety Research:

- liquid velocity: potential probe, mechanic-optical probe
- void fraction, bubble velocity: single- and double-wire resistance probe

Moreover, we have started a collaboration with the Paul Scherrer Institute (Switzerland) aimed for the adaptation of an existing ultrasonic Doppler system for the measurement of velocity profiles in liquid metal flows at higher temperatures. The availability of a non-intrusive method for local velocity measurements in combination with the application of local sensors at special positions inside the flow would be very attractive for a number of applications.

The potential probe and the resistance probes can already be considered as standard techniques in MHD experiments (see Branover [1]) and ordinary two-phase hydrodynamics (see Jones & Delhaye [2]), respectively. The problem to be solved here was the development of special sensors being capable of working reliably in liquid sodium. A new type of mechanic-optical sensor allowing to measure liquid velocities locally has been developed to overcome some drawbacks of the potential probe (limitations to the MHD case, unknown influence of electric noise or temperature gradients,...).

2. Potential Probe

The function of the potential-difference probe (sometimes also called conductance anemometer) is governed by the Ohm's law in moving fluids characterised by the material properties density ρ, kinematic viscosity ν and the electric conductivity σ:

$$\frac{\vec{j}}{\sigma} = \vec{E} + \vec{v} \times \vec{B} \tag{1}$$

Here $\vec{j}$ denotes the electric current density, $\vec{B}$ the external magnetic field and $\vec{E}$ the electric field. Considering MHD channel flows at the limit of high Hartmann numbers $Ha = |\vec{B}| L \sqrt{\dfrac{\rho\sigma}{\nu}}$ (L - characteristic length scale) the induced current $\vec{j}$ depends strongly on the wall conductance ratio $c_w = \dfrac{\sigma_w \delta_w}{\sigma L}$ (σ_w - electric conductivity of the channel wall, δ_w - wall thickness) according the term $\dfrac{c_w}{c_w + 1}$.

Therefore, the magnitude of the current density can be neglected compared to the induction term, if the wall conductance ratio is small enough:

$$|\vec{j}| \ll \sigma |\vec{v} \times \vec{B}|, \qquad \left(\frac{1}{Ha} \ll c_w \ll 1 \right) \tag{2}$$

A detailed discussion about the reliability of this measuring technique is given by Eckert [3]. As a consequence, the measured electric potential drop $\Delta\varphi$ between the electrodes, spatially separated by the distance l_e, has the following simple dependence on the fluid velocity (see also Figure 1),

$$\Delta\varphi = |\vec{B}| \cdot l_e \cdot u \tag{3}$$

where u is the velocity component orthogonal to the applied magnetic field as well as the electrode distance.
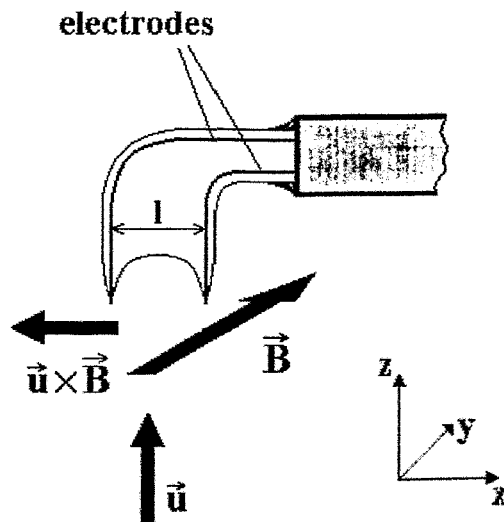
Fig. 1: Principle of the potential probe

The following advantages promote the use of such kind of probes:

- The geometry of the probe is very simple (two isolated electrodes). Therefore, a good minimisation of the sensor size is possible to reduce the flow disturbances caused by the probe itself.
- The sensor is reliable and robust in liquid sodium at temperatures up to 320°C.
- The relation between the voltage signal and the fluid velocity is linear for a broad parameter range.
- The sensor responds promptly and guarantees the suitability to measure the turbulent velocity fluctuations.

Potential probes have been employed to characterise the local, turbulent properties of liquid sodium channel flows by the determination of the turbulence intensities and the power spectra [3]. Some interesting effects have been revealed, for instance, the increase of the turbulence intensity with increasing Stuart number $N = \dfrac{\sigma B^2 L}{\rho u}$ (see Figure 2) or the steeper slope of the spectral energy in the inertial range with increasing Stuart number starting from a $k^{-5/3}$-behaviour for $N \leq 1$ and reaching a k^{-4}-scaling at $N \approx 100$, which becomes obvious in Figure 3 displaying the values of the spectral exponents versus N extracted from the experimental data.
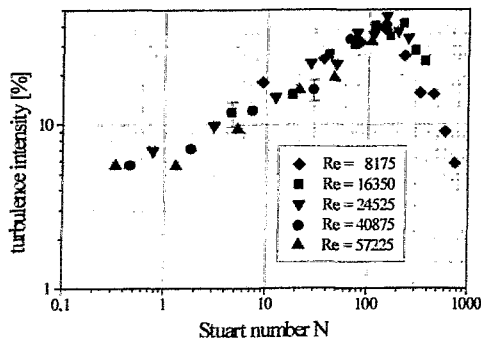
Fig. 2: Turbulence intensity as a function of Stuart number N
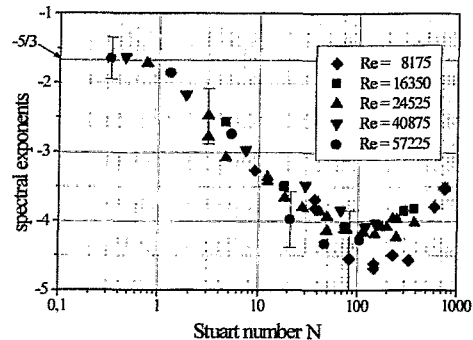
Fig. 3: Slope of the spectral energy versus Stuart number N

However, the use of the potential probe is combined with some serious limitations and difficulties. The measuring principle requires the application of a steady magnetic field, whereas the velocity component parallel to magnetic field lines cannot be determined. To measure the velocity fluctuations one has to deal with very small signals (some µV), which can be disturbed by a significant level of electric noise arising from components of the experimental facility (electromagnetic pump, heating elements). Moreover, equation (2) containing the condition for the linear relation between output signal and velocity is not

valid in channel flows bounded by highly conducting walls, influenced by time-dependant magnetic fields and in regions, where considerable changes of the cross sectional area or the wall conductance ratio appear. Therefore, a simpler measuring principle was searched for another new type of probe.

3. Mechanic-optical probe

Starting two years ago a new measuring system based on a mechanic-optical principle has been developed to determine local velocities in liquid flows. Our intention was to meet the following requirements:

- The sensor should be able to work in non-transparent fluids at high temperatures.
- The resolution should be sufficient to measure also velocities below 0.1 m/s.
- The system should be characterised by good spatial resolution.
- Flow disturbances caused by the sensor should be negligible.
- An influence of external electromagnetic fields or electric noise on the signal should be avoided.

The measuring equipment consists of a mechanical sensor, an endoscope as optical „beam line", a CCD-array and a PC. The sensor, which is made from a borosilicate glass tube ($\varnothing$ 2.5 mm) with a molten tip connected with a very thin rod ($\varnothing$ < 0.05 mm) concentrically fixed only in the front point, can be seen in Figure 4. The interaction with the moving fluid causes a deformation of the sensor tip resulting in a displacement of the upper end of the glass rod, which is observed by the CCD-array sensor being connected via a frame grabber card with the computer. A special software has been implemented allowing the evaluation of the digitised pictures.
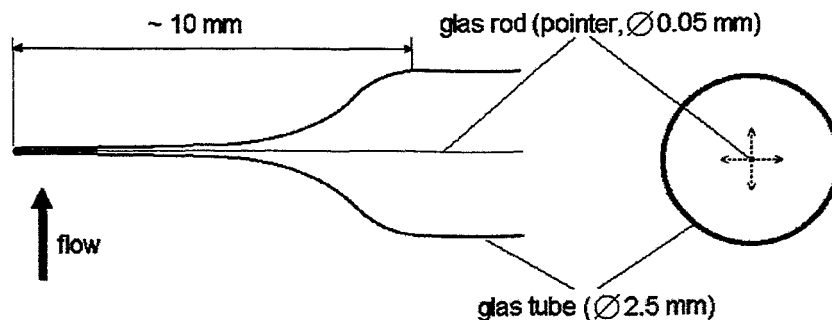
Fig. 4: Schematic drawing of the mechanic-optical sensor

The drag force acting on the sensor in the fluid was modelled by Witke et al. [4]. From those estimates the rod displacement shows a parabolic dependence on the flow velocity. Such a qualitative behaviour has been confirmed by first experimental investigations, where the sensors have been calibrated in a circular rotating channel.

The sensors have been tested in water and InGaSn at room temperature as well as in SnPb at temperatures up to 300 °C (see as an example Figure 5). The suitability of the sensor in this temperature range was demonstrated. A further increase of the temperature can be questionable, because the elastic module of the borosilicate glass becomes then a function of the temperature. The transformation temperature of this type of glass is approximately 650 °C. To use the measuring system at higher temperatures, for instance in aluminium at about 700 °C, the probe tip has to be manufactured from different material. A possible alternative is quartz glass with a transformation temperature above 1200 °C. The adaptation of the existing technology for the sensor production to quartz glass is a subject of further investigation.
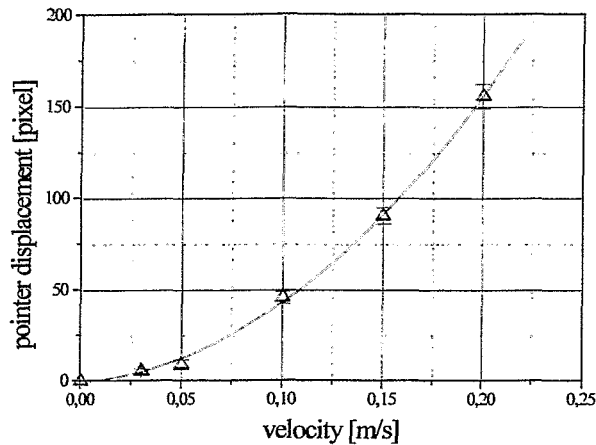
Fig. 5: Calibration curve obtained in SnPb at 206 °C

The installation of spheres at the sensor tip has been considered to enhance the drag resistance and thus the resolution of the system in the range of low velocities. Figure 6 shows a comparison between calibration curves obtained from a sensor before and after the installation of such a sphere at the probe tip demonstrating clearly the increase of sensitivity with an installed sphere.
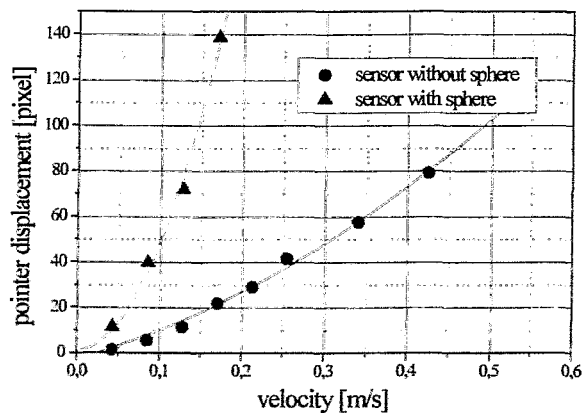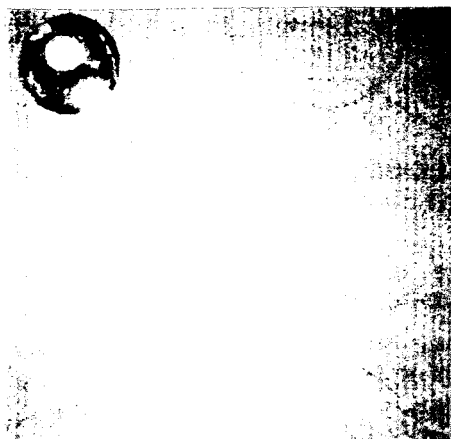
Fig. 6:   Sensor tip with sphere, comparison of calibration curves obtained with and without sphere, respectively

134

As a next step the measuring system shall be used to investigate the local flow structures in real experimental flows. Presently, two experiments are in preparation in our lab:

- Swirling Flow of InGaSn alloy in a circular box created by the application of time-variable (travelling and/or rotating) magnetic fields:
  The interest is focussed on geometry and parameters relevant for crystal growth technologies.
- Channel Flow of liquid sodium at the experimental sodium loop of FZR:
  It is planned to measure the velocity profiles in the channel cross section with and without transverse magnetic field. The obtained results shall be compared with the existing data of the potential probe.

Moreover, there exist some contacts to other institutes and companies (Institute of Physics Riga, University Manchester, Fa. Danieli Italy) to organise measurements at experiments existing there.

4. Measurement of velocity profiles by the Ultrasound-Doppler method

The instantaneous velocity profile is one of the most fundamental quantities in fluid flow phenomena. To realise such measurements an ultrasound velocity profile monitor (UVP) has been developed at the Paul Scherrer Institute (Switzerland) [5]. The principle of this method is to utilise the pulsed echo technique of ultrasound and to detect the Doppler shift of the ultrasound wave reflected from moving particles suspended in the fluid. The position information is derived from the time delay between the start of a pulse burst and the reception time. The velocity information is obtained from the Doppler-shift frequency.

First tests with the UVP have already been performed at the sodium facility of FZR showing that until now this measuring method can not be considered as a standard technique for liquid metal applications at higher temperatures. At the present status the following main problems have been revealed:

- Limitation of the temperature range of the ultrasonic transducer:
  The transducer can be used up to a maximum working temperature of 150°C. Moreover, the efficiency at lower temperatures close to this maximum is low.
- Coupling of the ultrasound into the fluid:
  Due to the high temperatures and the chemical properties of liquid sodium the transducer was installed at the outer channel wall. Therefore, an excellent wetting of the liquid metal at the inner surface of the wall is required to get a small acoustic impedance at the interface steel - liquid metal.
- Availability of tracers in the flow:
  The sensitivity and accuracy of the method depends on the occurrence of flow tracers being able to reflect the ultrasonic beam. If the amount of

naturally existing impurities is not high enough, additional scattering particles have to be added to the flow.

The measuring programme with the UVP system will be continued at FZR.

5. Resistance probes

The single-wire resistance probes are local sensors to measure the local void fraction. There is an electrically conducting tip (Cr/Ni wire, $\varnothing$ 0.1 mm) in direct contact with the liquid metal. The probe is supplied with an alternating current (1-10 kHz), which results in an electric current flowing from the probe tip to the cladding pipe acting as the other electrode. The gas contact at the sensitive wire is detected by an interruption of the current. Due to the huge differences in the electrical conductivity between the gas and the liquid metal we obtain very sharp signals easy to evaluate by a threshold method.

Figure 7 shows some representative isoplots of the void fraction distribution in the cross sectional area of a MHD channel flow obtained at different Reynolds numbers and different values of the magnetic field by Eckert et al. [6]. In the case of a transverse field direction an anisotropic distribution is observed indicating the existence of quasi-two-dimensional vortices as typical for turbulent MHD flows.
To measure gas velocity and bubble size a sensor with two wires close together in flow direction has been used. Then, the contact with the bubble will be recorded by these two sensor tips with a distinct time delay Δt. The bubble velocity v_b and the bubble chord length s_b can be calculated as follows:

$$v_b = \frac{l_s}{\Delta t}, \qquad s_b = v_b \cdot t_b \qquad (4)$$

Here t_b denotes the bubble contact time and l_s the distance between the wire tips, which was determined by means of a light microscope.

An extensive survey about a number of two-phase flow measurements carried out by several kinds of local sensors characterised by different tip sizes and probe shapes is provided by Cartellier & Achard [7]. For example, Serizawa et al. [8] have detected bubble chords of about 1.5 mm with a wire diameter of 100 μm. Similarly, Herringe & Davis [9] have captured bubbles as small as 100 μm with a tip of 8 μm at mean velocities of 5 m/s. As a rough estimation it may be generalised, that bubbles with a minimal size being about 10 times higher as compared to the probe wire can be detected by the sensor. In our experiments single-wire conductance probes with wire diameters of 25 μm and 100 μm have been used.

In order to measure the bubble size the use of double-wire probes is required. But, to arrange two wires in a defined distance would seriously enhance the tip size of the probe. In fact, reliable measurements of bubble diameters less than 1 mm by means of local conductance probes have to be considered as doubtful. Despite of measuring errors of bubble velocities and chord lengths up to about

136
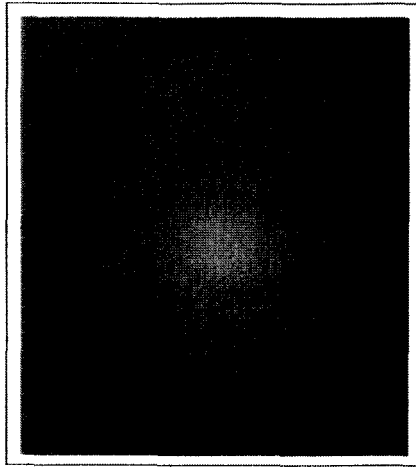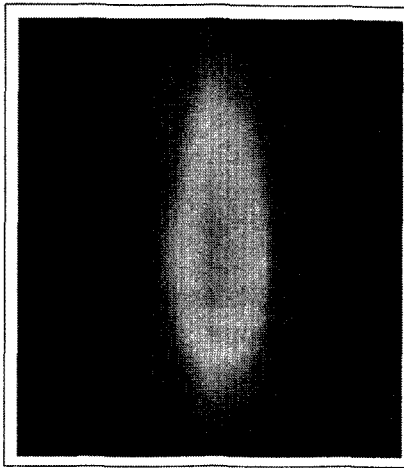
a) Ha = 300, N = 10   b) Ha = 845, N = 77
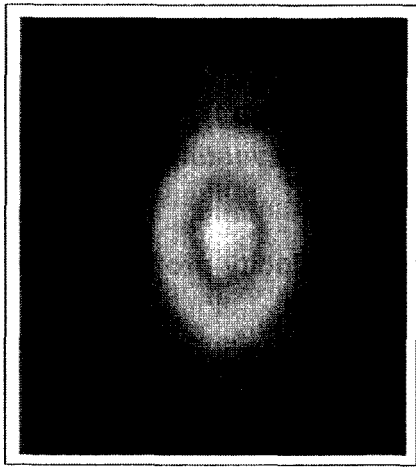
c) Ha = 1505, N = 244   d) Ha = 2410, N = 625
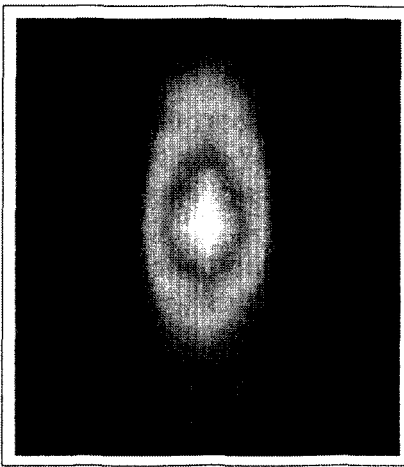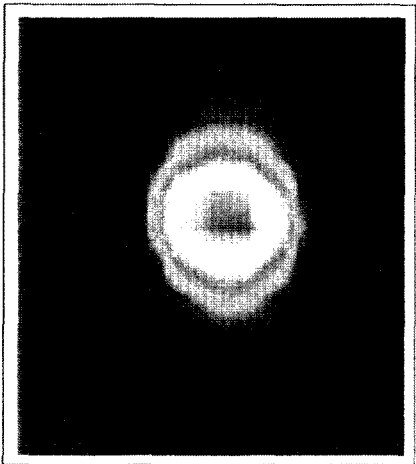
→   B-field direction   →

e) Ha = 2710, N = 790

Fig. 7:   Local distributions of the void fraction α [%] in a turbulent sodium channel flow exposed to a transverse magnetic field (Re = 9300)

20 % for bubble diameters of a few mm also measurements by means of double-wire probes provides us with useful information about the structure of the two-phase flow.

References

[1] H. Branover (1978), *Magnetohydrodynamic Flow in Ducts*, New York, Toronto, John Wiley & Sons

[2] O. C. Jones, J.-M. Delhaye (1976), Transient and statistical measurement techniques for two-phase flows: A critical review, *J. Fluid Mech.*, 147, 89

[3] S. Eckert (1998), *Experimentelle Untersuchung turbulenter Flüssigmetall- und Flüssigmetall-Gas-Strömungen in einem äußeren Magnetfeld*, Rossendorf, Report FZR-219

[4] W. Witke, H. Langenbrunner, G. Gerbeth, S. Eckert (1997), *1. Zwischenbericht zum Teilprojekt B3 des Innovationskollegs „Magnetofluiddynamik elektrisch leitfähiger Flüssigkeiten"*, Rossendorf

[5] Y. Takeda (1991), Development of an ultrasound velocity profile monitor, *Nuclear Engineering and Design*, 126, 277

[6] S. Eckert, G. Gerbeth, O. Lielausis (1997), The behaviour of gas bubbles in a turbulent liquid metal MHD flow - Part I: Dispersion in quasi-two-dimensional MHD turbulence, submitted to: *Int. J. Multiphase Flow*

[7] A. Cartellier, J. L. Achard (1991), Local phase detection probes in fluid/fluid two-phase flows, *Rev. Sci. Instrum.*, 62, 279

[8] A. Serizawa, K. Tsuda, I, Michiyoshi (1983), "Measuring techniques in gas-liquid two-phase flows" in J.-M. Delhaye and G. Cognet (Ed.), *IUTAM Symposium Nancy*

[9] R. A. Herringe, M. R. Davis (1976), Structural development of gas-liquid mixture flows, *J. Fluid Mech.*, 73, 97

Short Contributions

Thermalhydraulic and neutron-kinetic computer codes for accident analyses

U. Grundmann,
S. Mittag,
U. Rohde

as guest
scientists:
F. Hollstein,
E. Laggiard

Development, Validation and Application of the Code DYN3D

For further improvement of the 3D reactor dynamics code DYN3D, a decay heat model was included to simulate the heat release after reactor shut down and during transients. A model for the simulation of xenon/samarium dynamics was implemented. The coolant mixing model for VVER-440 reactors was improved for describing perturbations with changing mass flow rates in the different coolant loops. Validation activities were continued for both VVER and Western type pressurized water reactors.

A benchmark task for a boron dilution transient in a VVER-440 type reactor was calculated with the DYN3D code. A high influence of numerical diffusion on the of boron transport was found. Therefore, a special numerical boron transport model based on a particle-in-cell (PIC) method was developed. This method was also applied for the analysis of boron dilution scenario for a German PWR. DYN3D results for the NEA-NSC benchmarks on uncontrolled withdrawal of control rods in a standard Western PWR showed good agreement with the reference solutions.

In the framework of an European concerted action, first steady state calculations for the investigation of instabilities in the Dodewaard boiling water reactor were carried out demonstrating the applicability of DYN3D for those reactor type.

Activities on the support of Nuclear Regulatory Authorities and related organizations in East European countries were continued and extended. Training courses on the use of the code DYN3D were organized for experts from Bulgaria, Russia and Slovakia. DYN3D was transfered to research and engineering organizations in these countries.

U. Grundmann,
S. Mittag,
S. Kliem,
U. Rohde,
A. Seidel,
T. Scholz

The Coupled Neutron Kinetics/Thermohydraulic Code Complex DYN3D-ATHLET

The code DYN3D has been coupled to the thermo-hydraulic system code ATHLET developed by Gesellschaft für Anlagen- und Reaktorsicherheit. By the help of DYN3D-ATHLET, complex hypothetical accident scenarious can be analyzed.

The 5th AER dynamic benchmark considering the break of the main steam header of a VVER-440 type reactor being

the first international benchmark task for coupled 3D neutronics- thermohydraulics code systems was defined by FZR.

A European PHARE project entitled "Improvement of the verification of coupled thermal-hydraulics/neutron kinetics codes" was started under the leadership of the RC Rossendorf with participants from 3 EC member states and 5 East European countries. The experimental transient data measured in different VVER-440 and VVER-1000 reactors were assessed regarding their qualification for code validation of coupled codes.

By the help of the coupled code system DYN3D-ATHLET, an accident with delayed scram after coastdown of a main coolant pump which occured at NPP Greifswald (VVER-440) in 1989 was analyzed.

The comparison of calculations and measurements for real accidents is very useful for the code validation, but requires a very careful analysis of measurement data.

supported by BMBF and EC

E. Krepper, F. Schäfer

Validation of thermo-hydraulic system codes

The activities were focused on the validation of the thermalhydraulic code ATHLET developed by Gesellschaft für Anlagen- und Reaktorsicherheit by the analysis of experiments performed at thermo-hydraulic integral test facilities.

ATHLET calculations were done for two experiments with pressurizer surge line breaks at the PMK-2 test facility in Budapest. During both experiments, a periodical filling and clearing of the hot leg loop seal was observed. This kind of natural circulation instability is a specific effect of VVER-440 type reactors.

In the framework of the external validation group for ATHLET Mod 1.1 Cycle D, post test analyses calculations of two experiments were carried out, which were performed at the french integral test facility BETHSY for the investigation of the efficiency of accident management measures.

The ATHLET calculations confirmed the experimental results, that in case of the complete loss of steam generator feedwater as well as a steam generator U-tube rupture the safe cooling of the core can be assured by accident management measures.

supported by BMBF

E. Krepper,
U. Rohde

Assessment and application of the Computational Fluid Dynamics Code CFX-4 for the simulation of processes relevant for plant safety

Using the CFD-code CFX-4.1, different analyses concerning experiments with heated liquid pools were performed. Modelling the single phase natural circulation, the heating up process of fluid in a side wall heated tank was investigated. Different constructive measures to avoid undesirable temperature stratification were considered. A benchmark problem with mixed forced and natural convection flow was analyzed. First calculations concerning the operation of an emergency condenser for future BWRs were done considering only single phase laminar flow.

Calculations of natural convection of a liquid-gaseous bubbly flow with a spreading tracer were carried out with CFX-4 for selected experiments on two-phase turbulent dispersion. The dispersion of the radioactive tracer was measured by applying Positron Emission Tomography (PET). The measured dispersion coefficents were compared to those obtained from the CFD calculations. A nearly linear correlation between gas superficial velocity and the dispersion coefficient was found in accordance with other authors.

T. Höhne

Coolant mixing in PWRs (CFD calculations)

For the analysis of boron dilution transients and main steam line break scenarios the modelling of the coolant mixing inside the reactor vessel is important. An input data set for CFX-4 was developed, which describes the downcomer and the lower plenum of a KONVOI type PWR. Various steady state calculations were conducted to obtain the velocity field, temperature and boron distributions in case of different temperature and boron concentration at the inlet nozzles. Experimental results from an air-operated model of the KONVOI and a water-operated model of a Westinghouse reactor were used for comparison with the calculations.

D. Lucas

Modeling of thermo- and fluid-dynamic processes during depressurization of chemical reactors with consideration of foam generation

A new one-dimensional model for reacting multiphase flow in a vessel was developed. A special goal of the code BRICK is the transient simulation of emergency relief from chemical reactors with consideration of foam. An interface, which enables the modelling of generation and

141

decay of foam at the mixture level is included. The model bases on a special particle method and is free of numerical diffusion. The code has an open structure, which makes possible to test the influence of different models for several phenomena as e.g. drift of the phases, phase transfer, bubble generation, coalescence and foam behaviour. The model distinguishes between continuous and disperse phases, which may change with the height. Any of the phases can consist of several components. Chemical reactions are included by a formal kinetic approximation. The code was validated for numerous depressurization experiments.

Separate Phenomena in Two-Phase Flows

A. Böttger,
H.-M. Prasser,
P. Schütz,
J. Zschau

Development and calibration of two-phase flow measurement techniques

Special probes for a diversified level indication in boiling water reactors were developed. Prototypes have been tested for more than 1 year in a test facility of the Gundremmingen NPP. A qualification project for application in NPPs is in preparation.

The mesh sensor for the visualisation of the two-phase flow in pipelines was extensively used for water hammer experiments. The cavitation phenomena behind and in front of fast acting valves of different type were studied. The experiments included the variation of the pipeline geometry, the initial flow velocity, the pipeline diameter. Further, the influence of the injection of non-condensable gases and of the valve closing time was studied. The evalution and the sudden collapse of the cavitation bubble could clearly be detected. The pressure maxima occur when the backflowing water plug reaches the valve.

An extended comparison between different two-phase flow instrumentation was carried out at the test loop of the institute. In a vertical test channel, a wire-mesh sensor, needle shaped conductivity probes, a capacitance tomography system, ultrasonic through-transmission transducers, a radar sensor and an optical observation window with a video system were simultaneously operated in an air-water flow. On the basis of the obtained data, a flow pattern map was constructed. Although the agreement with existing flow maps is satisfying in general, several new effects and deviation were found.

D. Lucas,
T. Kern,
H.-M. Prasser

Basic studies of two-phase flows with foam production

Depressurization experiments of a batch reactor were carried out with foaming fluids. In a small scaled pressure vessel of 2 l weak solutions of different alcohols (Methanol, Ethanol, Buthanol etc.) were heated and depressurized under variation of the initial conditions. The expelled mass shows a strong dependence from the kind of alcohol and its concentration. The tests were modelled by an 1D computer model developed earlier. The foam model is still based on parameters that must be fitted to the experiments. Further work is directed to a prediction of the foaming behaviour on the basis of a simple standard test.

A. Grahn

Thermoconvection and instabilities at the boundary layer of two non-miscible liquid reacting components

Different kinds of thermoconvection at the boundary layer between two non-miscible liquids were visualised in a capillary gap. Main attention was given to the theoretical modelling. A two-dimensional model of the flow in two coupled rectangular regions with a liquid-liquid boundary was developed. The calculations show a good qualitative agreement to the visualisation results in the capillary gap.

C. Schneider

Fluid Mechanics of Electrolytic Cells

In membrane alkaline-chlorine electrolysis cells, the fluid sometimes tends to foam because of the high concentration of electrolytes. This has several negative effects on the cell performance: (1) reduction of the anolyte density, and, as a consequence, local undersupply of the anode and the membrane, causing a decrease of the life time of the membrane and a growth of the cell voltage, (2) stagnation of natural circulation of the fluid inside the anode space, leading to a bad mixing of the fresh sodium chloride solution and (3) bad transient behaviour during load changes. Different measures were tested regarding their capability to prevent foaming and to reduce the gas fraction in the electrolytes without disturbing the mixing inside the sodium chloride solution. The found solution moreover, allows to reduce cell voltage.

H.-W. Viehrig
J. Böhmert

Radioisotope laboratory for material testing

After the construction of the laboratory had been finished and before starting up the regular operation, handling, testing methods and operation of the testing facilities had to be examined under the condition of remote mani-pulation at non-radioactive specimens. The work was focussed on

- measurement of the Charpy-V notch impact energy and additional characteristic energy levels as well as dynamic strength parameters by an instru-mented Charpy pendulum impact tester within the temperature range of -150° to +300°C
- measurement of crack resistance curves of precracked Charpy-V specimens or CT specimens at a servohydraulic test machine by means of the partial unloading compliance method within the temperature range of -150° to 250°C.

In the last case, for ensuring high measuring accuracy, the displacement of the specimen is measured directly via the crack opening with a clip gauge positioned at knife edges near the Charpy-V notch, what is difficult under condition of remote handling.

The test phase with non-radioactive materials is almost finished. As the result of that, conventional and fracture mechanical parameters can be determined for radioactive structural materials with methods and with an accuracy according to the regular standards like DIN 14556, ISO/DIS 14556 or ASTM E13-89. The license for radioactive operation is expected for March 1998.

M. Große
J. Böhmert

Microstructural analysis of irradiated reactor pressure vessel steels by small angle scattering

The investigation of the microstructure of VVER-440-type reactor pressure vessel steels was continued. As the small angle neutron scattering (SANS) experiments were always performed at two different probe-detector-distances, the scattering vector could be measured over a wide measuring range. This allows a more sophisti-cated and reliable evaluation of the scattering pattern. It was recognized that the scattering intensity results from two contributions: the true small angle scattering, depending on the scattering angle, due to small, nano-dispersed structure defects and a constant, that means

independent on the scattering angle, contribution due to inelastic scattering, which is caused by Laue scattering of solved point defects or by the different iron isotopes. Usually, the constant contribution is not considered what yields distorted results. Considering this contribution it is clearly to be seen that the micro-structure due to neutron irradiation is the result of two competing processes: re-dissolving of precipitates already formed by the process of fabrication and formation of nanoscale precipitates or defect clusters from the heavily neutron-damaged matrix containing a high supersatura-tion of point defects.

H. Richter
J. Böhmert

Verification of the acoustic emission method for the detection of crack initiation during an impact bending load
A generally accepted single specimen technique to measure dynamic fracture mechanical parameters has not get been existing. A potential candidate could be the measurement of the acoustic emission (AE). Previous investigations showed that characteristic AE signals appears in the vicinity of crack initiation for the first time. With a specially developed measuring arrangement the method should be verified by simultaneously measuring additional physical parameters at specimens of strongly different levels of toughness and strength. Furthermore the results were compared with the results of multiple specimens technique. To realize the idea the inverted impact pendulum developed and installed at VTT Espoo/ Finland was modified with an AE transducer and a magnetic emission (ME) probe. Thus, at the same specimen crack opening displacement (COD), AE, and ME could be measured. Neither of the three methods can directly detect crack initiation. For steel with not too high toughness, COD indicates crack initiation after a small but not neglectable amount of macroscopic stable crack growth. AE, however, provides weak correlation to the crack initiation although it is very sensitive against material processes which occur in the vicinity of crack initiation. ME does not reflect stable crack initiation and growth. Nevertheless, the fracture mechanical parameter `crack initiation toughness´ can better be estimated by measuring both COD and SE than by other recently applied methods.

Behaviour of LWR components

E. Altstadt,
F.-P. Weiß,
M. Werner,
H.-G. Willschütz

Finite Element (FE) Analysis of Boiling Water Reactor Internals Exposed to Accident Loads

During a hypothetical accident the reactor pressure vessel internals of boiling water reactors can be exposed to considerable loads resulting from temperature gradients and pressure waves. Three dimensional FE models were developed for the core shroud, the upper and the lower core support structure, the steam separator pipes and the feed water distributor. The models of core shroud, upper core support structure and lower core support structure were coupled by means of the substructure technique. All FE models can be used for thermal and for structurel mechanical analyses. As an example the FE analysis for the case of a station black-out scenario (loss of power supply for the main circulating pumps) with subsequent emergency core cooling is demonstrated. The transient temperature distributions within the core shroud and within the steam dryer pipes were calculated based on the fluid temperatures and the heat transfer coefficients provided by thermo-hydraulic codes. At the maximum temperature gradients in the core shroud, the mechanical stress distribution was computed in a static analysis with the actual temperature field being the load. It could be shown that the maximum resulting material stresses do not exceed the permissible thresholds fixed in the appropriate regulations. Another scenario which was investigated is the break of a feed water line leading to a non-symmetric subpressure wave within the reactor pressure vessel. The dynamic structural response of the core shroud was assessed in a tranisient analysis. Even for this load case the maximum resulting stresses remain within the allowed limits at any time.

Simulation of particle and radiation transport

H.-U. Barz,
B. Böhmer,
J. Konheiser

Neutron Dosimetry of Reactor Pressure Vessels

The work aimed at the theoretical and experimental determination of the neutron exposure of the VVER-1000 reactor pressur vessel of Balakovo-3. All calculations and the evaluation of the activation detector results are finished. The calculations took into account the 3-dimensional pin-wise source distribution and a very detailed geometrical model. Further, a 3-D correction was performed to estimate the effect of

decay of some detectors. This allows a better comparison with the activation measurements. The calculated end of irradiation activities were compared with those measured. The agreement was very satisfying. The influence of different cross section data files and of different numbers of energy groups were found to be smaller than expected from uncertainty considerations. The measurements and the reference calculations shall be used to formulation an international benchmark on neutron fluence calculation.

H.-U. Barz,
B. Böhmer

Transport of High Energy Ions and of Fragmentation Products

The Monte Carlo code **IONTRA** for the simulation of the high-energetic ion transport through human tissue has been improved and generalized concerning two issues.

Firstly, now it is possible to calculate the energy deposition and transmission of particles depending on the distance from the axis of initial direction of the ions current. Secondly, the consideration of the fragmentation process was extended with a cascade-model founded on theoretical nuclear physics. This theoretical model is based on Monte-Carlo technique and was made available by the Moscow Institute of Nuclear Physics. The flight direction of fragments can even be inverse to the initial direction. Further, using different control parameters a high flexibility is achieved. Not only different fragmentation models but also different corrections can be optionally used.

R. Küchler,
K. Noack

Transport of Reacting Solutes in Unsaturated Porous Zones

Unsaturated water flow within subsurface regions of mining dumps controls hydrological and geochemical processes which cause the mobilisation and migration of radionuclides. The development of a code system which enables the calculation of the migration of various radioactive nuclides has been continued. Chemical modules describing the pyrite dissolution and the interaction of important chemical species have been developed and incorporated in the transport code. By means of calculations the space-dependent dynamics of the reactive nuclide transport in an one-dimensional model dump has been studied. It turned out that the averaged annual release rates into the groundwater only weakly depend on the water flow parameters of the

147

medium but much stronger depend on the dissolution model used in the calculations.

H. Kumpf

Recriticality Calculations for Uraniumdioxide-Water Systems with MCNP

Some fundamental aspects of the criticality of water-uraniumdioxide mixtures were elucidated. Stochastic geometric arrangements of fuel and water were generated in the frames of several models and their neutron multiplication determined by Monte Carlo code MCNP. It turned out, that they can be characterized globally by two parameters, the fuel chord length and the fuel/moderator volume ratio. The worst case with respect to criticality, still exhibiting mechanical stability, has been identified (see contribution to the present report).

Process monitoring

G. Hessel,
D. Hoppe,
W. Schmitt,
N. Tefera,
K. van der Vorst,
F.-P. Weiß

Identification of Undesired Operational States in Chemical Plants Using Neural Networks

The project contributed to operator-independent assessing of the process and plant states of chemical reactions, particularly to identifying undesired operational states in discontinuous and continuous operations of exothermic reactions. The suitability of pattern recognition for process diagnosis was investigated in a laboratory reactor in which a strongly exothermic chemical reference process, the acid-catalysed esterification between acetic anhydride and methanol, was carried out.

Before being applied to state classification, the pattern recognition-based classifiers first have to be trained using process data of normal and faulty sequences of reaction and with the aid of expert know-how to establish a nonlinear decision model between plant parameters and state classification. Afterwards, the trained classifiers can be used for process diagnosis.

Best results for state classification in semibatch reactions were reached with three-layer perceptron networks. They were also capable of classifying multiple faults and untrained sequences of reaction. For assessing the danger potential of faulty operational states, separate perceptron networks for danger classification and for fault isolation were used. Their

efficiency could experimentally be proven both in semibatch reactions and in continuous operations.

It is planned to test this technique in a pilot plant and then in a chemical production plant. In particular, the objective is to develop a prototype of a supervision system based on neural networks for two-phase hydrogenation processes and to test it in an industrial plant in the long term.

G. Hessel,
K. Richter,
W. Schmitt,
N. Tefera,
F.-P. Weiß

Chemical process lab

To investigate undesired process and plant states of strongly exothermic reactions, an automatically controlled laboratory reactor with changeable stirred tanks (1-10 l), a separator tank and with a relief tank for emergency measures was put into operation. In this miniplant multiphase processes (e.g. hydrogenation) can also be carried out by using gas feeders and liquid feeders.

The chemical process laboratory was completed with a reaction calorimeter (RC1) for measurements of thermo-kinetic parameters. These reaction parameters are needed, for example, for the verification of dynamic process simulation programs and for process optimization.

Applying numerical simulation a multiphase catalytic hydrogeneration reaction as it is running in pharmaceutic chemistry could satisfying be described adjusting e. g. the reaction enthalpy to values measured in a production plant.

M. Beyer,
H. Carl,
K. Nowak*,
P. Schumann,
A. Seidel

Support of the Ukrainian State Supervisory Authority in the realisation of a technical system to improve the operational monitoring of the Zaporozh'ye Nuclear Power Plant (Unit 5) - Fourth level of realisation

The system to improve the operational monitoring which was put into operation in the Zaporozh'ye NPP two years ago has been connected with the Kiev Centre of the Ukrainian Supervisory Authority. The most essential technical means for the data transfer and for monitoring purposes of this centre were jointly specified, procured in Germany, tested consigned to the Ukraine and free leaved to the partner at their place of action. It was proved during testing the information transfer from the Zaporozh'ye NPP to the Kiev Centre that the rented telephone line fulfils the technical demands. Within func

* Technischer
Überwachungs-
verein Rheinland

tional tests on-line data from the above mentioned on-site system at Zaporozh'ye NPP were correctly trans-ferred to Kiev. Furthermore, the same technical means for the connection of the Rovno NPP with the Kiev Centre were handed over to the Ukrainian partners.

Magnetho-hydrodynamics of conductive fluids

W. Witke,
S. Eckert,
G. Gerbeth

Liquid Metal Magnetohydrodynamics
Measuring techniques for liquid metal flows Liquid metals are non-transparent, typically hot and aggressive. There is almost no commercial measuring technique available for a determination of local velocities or pressure. A mechano-optical velocity probe was deve-loped which is able to measure two components of local velocities. It is calibrated and tested in different melts like InGaSn, SnPb or SnBi. The measuring principle consists in the velocity induced elongation of a glass rod which is encapsulated in a glass capillary. This elon-gation is measured by optical means using an endoscope and a camera. Due to its measuring principle the probe is independent of any electromagnetic fields. It should

principally work up to temperatures of about 700°C.

G. Mutschke,
V. Shatrov,
G. Gerbeth

Numerical simulation of the MHD flow around a cylinder
The 3d stability analysis was developed and imple-mented numerically with a new spectral code. The results reveal the complicated mixture of magnetic field influences on the basic 2D flow and the 3d instabilities. The Karman vortex street behind the cylinder can strongly be influenced by the magnetic field. For the first time, a non-expected destabilizing influence of the steady magnetic field was found. At interaction parameters larger than one new 3d-instabilities occur on

the before, i.e. at lower magnetic field strength, completely stabilized flow.

V. Galindo,
G. Gerbeth,
R. Mößner

Numerical simulations for crystal growth problems
Numerical codes have been developed and used for melt flow and heat transport calculations of crystal growth problems. For the industrial interesting Czochralski growth of silicon commercial codes were used in order to simulate the melt control by means of different magnetic fields.

The calculations were compared with model experiments and real growth experiments of silicon single crystals. Parameter regions have been identified where the growth process and the grown crystal show clear improvements. For simulations of transport phenomena and magnetic field influences on growth processes in ampulla an own spectral code was developed. These results are compared with InAs growth experiments performed at Bergakademie Freiberg where a rotating magnetic field is installed in order to enhance the convective transport inside the melt.

Investigations at free liquid metal surfaces

The experiments with free gallium surfaces have been finished. They showed unusual Marangoni flows being in the opposite direction to the expected one at lower temperatures. The quality of the free metal surface was analysed by means of a laser light scattering technique. There were clear indications that such a liquid metal surface is far from a standard Newtonian liquid surface, but reveals elastic properties as well as indications of adsorbed layers. The measured surface flows were theoretically explained only if besides the thermo-capillary driven flows also a surface-active contamination of the surface is taken into account. The theoretical analysis of magnetic field control of Marangoni flows has been finished.

Participation at the Riga Dynamo experiment

The experimental verification of a magnetic field selfexci-tation at the partner institute in Riga was supported by several numerical investigations. The measured water experiment profiles have been checked with respect to their critical magnetic Reynolds numbers. In an iterative procedure between the pump designers and the Riga water experiments the profiles have finally been organized in such a way that selfexcitation should be possible to detect in the forthcoming sodium experiment.

Resulting from the magnetic field calculations additional pre- and post-propeller blades were installed at the Riga facility in order to improve the velocity profiles.

supportet by DFG and industry

*V. Kolevzon,
J. Priede,
A. Cramer,
G. Gerbeth*

supported by German Space Agency and German-Israeli Foundation

*F. Stefani,
A. Gailitis,
G. Gerbeth*

supported by DFG

A. Cramer,
G. Gerbeth,
Yu. Gelfgat,
A. Bojarevics

Melt extraction of metallic fibres

In cooperation with the Fraunhofer institute IFAM-Dresden the stabilization of an inductively stirred melt surface by means of an external magnetic field was studied. A solenoid was installed at the semi-industrial facility of the Fraunhofer institute under hazardous boundary conditions: vacuum, strong induction heater and a crucible with hot melts (up to 1800°C) close to the solenoid. The magnetic field lead to a seriuos stabilization of the melt surface which improved the process significantly. Unfortunately, the diameter distribution of the produced fibres was almost not influenced by the magnetic field since its action on the meniscus directly at the wheel is not sufficient.

T. Weier,
G. Mutschke,
U. Fey,
G. Gerbeth

Electromagnetic boundary layer control for saltwater

The flow of saltwater around bodies can strongly be controlled by electromagnetic forces localized directly on the surface of the body even though the elctromagnetic forces penetrate only slightly into the low-conducting fluid. With suitable arrangements of electrodes and permanent magnets Lorentz forces can be produced which for instance accelerate the fluid motion parallel to the body surface. This results in a stabilized flow, drag reduction of the body, and prevention of flow separation. A new facility working with NaOH has been installed in order to study those effects. A cooperation with ship builders has been started guiding the investigations to problems of ship builders relevance.

Hazard ranking and risk management for waste deposits

A. Polte,
W. Ferse

Application of a decision criteria system to a lifecycle analyses problem

In 1997 the investigations concerning the application of decision analyses to the assessment of safety relevant industrial problems were continued. In close co-operation with the Technical University of Dresden and the ETH Zürich an actual decision problem, the analyses of a set of alternatives for the transport of a hazardous substance across different regions in Switzerland, was accompanied. Different scenarios for the normal operation and accident cases were developed. The system of decision criteria which has been developed at the Research Centre Rossendorf was adapted to the

problem in a way which allows to compare and to weight the consequences of these scenarios.

W. Ferse,
T. Reitz

Development of a graphical knowledge acquisition module for the risk assessment system XUMA/GEFA

XUMA/GEFA is a knowledge based program system for the uniform evaluation of environmental hazards due to contaminated sites. XUMA/GEFA which has been developed in co-operation with the Research Centre Karlsruhe and the Technical University of Dresden has been in use countrywide since 1995. In 1997 the knowledge acquisition module of XUMA/GEFA was redesigned, because the users were not able to handle the former acquisition module which was oriented at the syntactical structure the knowledge base without the help of the program developers.

The new knowledge acquisition which was designed in close co-operation with the users presents the knowledge in a graphical flow chart. The structure of the chart is derived from the direction of view of the environmental experts. First applications of the modul have shown that the users are now able to work independently with this interactivly by editable knowledge flow chart.

Publications

Publications in scientific and technical journals
and in conference proceedings

Altstadt, E., M. Scheffler, F.-P. Weiß, J. Runkel, U. Südmersen
Numerische und experimentelle Untersuchungen zum Schwingungsverhalten
eines Siedewasserreaktors
Jahrestagung Kerntechnik '97
Aachen, 13. –15. Mai 1997, Tagungsbericht S. 437

Aszodi, A., P. Liewers, E. Krepper, H.-M. Prasser
Untersuchung der Erwärmungsprozesse in Lagertanks mit gefährdenden Flüssig-
keiten bei äußerer Brandeinwirkung
Technische Überwachung 38(1997)4, 22-25

Bagryansky, P. A., K. Noack, St. Krahl, S. Collatz
Effect of Wall Conditioning on Neutral Gas Transport in the Gas-Dynamic Con-
finement System
Plasma Physics Report, Vol. 23, No. 11, 1997, pp. 903 - 910
Translated from: Fizika Plasmy, Vol. 23, No. 11, 1997, pp. 979-987

Barz, H.-U., B. Böhmer, J. Konheiser, K. Noack, I. Stephan
Monte Carlo Fluence Calculations and Spectrum Adjustment for the Pressure
Vessel of the VVER-1000 Balakovo-3 (Invited Paper)
1997 ANS Winter Meeting, Albuquerque, New Mexico, November 16-20
Trans. Am. Nucl. Soc., Vol. 77, 1997, pp. 343-344

Barz, R.-U., G. Gerbeth, Yu. Gelfgat, E. Buhrig, U. Wunderwald
Modelling of the melt flow due to rotating magnetic fields in crystal growth
Journal of Crystal Growth, Vol.180, 1997, pp. 410-421

Barz, H.-U., B. Böhmer, I. Stephan
Eine Methodik zur Bestimmung der Neutronenbelastung von Reaktordruckbe-
hältern und deren Anwendung auf WWER
Jahrestagung Kerntechnik 97
Aachen, 13.-15. Mai 1997, Tagungsbericht S. 37-40

Becker, H., K. Kiefer, U. Rindelhardt, G. Heilscher
5 Years of Operational Experience in the German 1000-Roof-PV-Programme Re-
sults of Monitoring and Inspektion
in H.A. Ossenbrink, P. Helm, H. Ehmann (Ed.) Proc. of the 14th European Pho-
tovoltaic Solar Energy Conference and Exhibition, Barcelona (Spain), 30 June -
4 July 1997, Vol. II,1677

Beyer, M., H. Carl, K. Nowak, P. Schumann, A. Seidel, F.-P. Weiß, J. Zschau
A Technical System to improve the Operational and Radiological Monitoring of
the Zaporozh'ye Nuclear Power Plant
Radiation Protection Dosimetry, Vol. 73, pp. 151-154 (1997)

Beyer, M., H. Carl, K. Nowak, P. Schumann, A. Seidel, F.-P. Weiß, J. Zschau
A Technical System to improve the Operational Monitoring of the Zaporozh'ye Nuclear Power Plant
Proc. of the International Topical Meeting on VVER Instrumentation and Control
Prague, Czech Republic, April 21 - 24, 1997, p. 105

Böhmert, J., M. Große
Nachweis verformungsbedingter Strukturschädigung in Rißnähe durch Röntgenkleinwinkelstreuung
29. Tagung des DVM-Arbeitskreises Bruchvorgänge, Febr. 1997
Stuttgart, DVM-Bericht 229, 299-306

Böhmert, J., M. Große, P. Nitzsche
SANS investigations of the irradiation-caused structural damages in VVER 440-type reactor pressure vessel steels
Physica B 234-236 (1997) 997-998

Brünig, D., U. Rindelhardt
Solare Warmwasserbereitung und Fernwärmeversorgung
Sonnenenergie und Wärmetechnik, Heft 1/1997, S. 14

Dudlik, A., S. Schlüter, H.-M. Prasser
Transiente Strömungsvorgänge in Rohrleitungen, Messung und Berechnung von Druckstößen und Kavitationsschlägen
Tagung Monitoring und Diagnostik in energietechnischen Anlagen
Braunschweig 8.-9.10.1997, VDI-Bericht Nr. 1359, S. 353-367

Dudlik, A., S. Schlüter, H.-M. Prasser
Visualisierung und Berechnung von Kavitation in Rohrleitungssystemen hinter schnellschließenden Regelklappen
Workshop „Meßtechnik für stationäre und transiente Mehrphasenströmungen"
Rossendorf 6. - 7. November 1997, Report FZR-204, S. 39-50

Ezsöl, G., A. Guba, L. Perneczky, E. Krepper, H.-M. Prasser, F. Schäfer
Simulation of a small cold leg break experiment on PMK-2 test facility using the codes RELAP5 and ATHLET
Nuclear Technology 118(1997) No. 2, 162-174

Fiorini, G. L., E. Friesen, T.v.d. Hagen, J. Lopez Jimenez, P. Meloni, U. Rindelhardt
BWR Physics and Thermohydraulics Complementary Actions to the BWR R & D Cluster
Proc. of the FISA-97 Symposium on EU Research on Severe Accidents
Luxembourg, 17 to 19 November, 1997

Große, M., J. Böhmert, R. Gehrke
ASAXS-Investigations of the Influence of the Irradiation Temperature on the Formation of Defects in Nuclear Pressure Vessel Steel A-533-B1
Hamburger Synchrotronstrahlungslabor HASYLAB, Jahresbericht 1996, Hamburg, 1997, S. 255

Hadek J., U. Grundmann
Neutron Flux Reconstruction in a Hexagonal Cassette - Theory and Implementation into the Code DYN3D/H1.1
Nucleon No. 3 (1997), pp. 8-14

Hadek J., U. Grundmann
Reconstruction of Pointwise Neutron Flux Distribution in a Hexagonal Cassette - Theoretical Background and Implementation into the Code DYN3D/H1.1
Proc. of the 7th Symposium of Atomic Energy Research, p.469
Hörnitz, 23. - 26.09.1997

Heilscher, G., M. Schneider, R. Pfatischer, M. Feneberg, H. Becker, U. Rindelhardt
Technische Überprüfung von Photovoltaik-Systemen
12. Symp. Photovoltaische Solarenergie
Staffelstein, 26.-28.2. 1997, Tagungsband S. 140

Hensel, F.
Studies of Liquid-Gaseous Two-Phase Systems by Positron Emitting Radiotracers
Applied Radiation and Isotopes, Vol. 48 (1997) p. 1485-1492

Hensel, F., H.-M. Prasser
Studies of Bubbly Flows by Positron Emitting Radiotracers
Proceedings of the Conference Frontiers in Industrial Process Tomography II
Delft, The Netherlands, April 9-12, 1997, pp. 47 - 51

Hessel, G., W. Schmitt, K. van der Vorst, F.-P. Weiß, J. Neumann, S. Schlüter
Identification of dangerous states in chemical batch reactors using neural networks
Proc. of the IFAC Symposium on Fault detection, supervision and safety for technical processes SAFEPROCESS 97 (Ed.: R.J. Patton)
Hull, UK, August 26-28, 1997, pp. 926-931

Hessel, G., W. Schmitt, K. van der Vorst, F.-P. Weiß, J. Neumann, S. Schlüter
Fault Diagnosis in Chemical Semibatch Reactors Using Neural Networks
Proc. of the 5th European Congress on Intelligent Techniques and Soft Computing EUFIT 97
Aachen, Germany, September 8-11, 1997, pp. 1704-1708

157

Hirsch, W., U. Rindelhardt, D. Brünig
Windpotentiale in Sachsen
Hrg.: Sächsisches Staatsministerium für Umwelt und Landesentwicklung
Reihe: Materialien zum Klimaschutz, Heft I/1997, 70 Seiten

Hirsch, W., U. Rindelhardt
Windenergiepotential in Sachsen
DEWI-Magazin Nr. 11, August 1997, S. 44-49

Kliem, S.
Definition of the fifth Dynamic AER Benchmark Problem - a Benchmark for Coupled Thermohydraulic System/ Three-Dimensional Hexagonal Neutron Kinetic Codes
Proc. of the 7th Symposium of Atomic Energy Research, 429
Hörnitz, 23. - 26.09.1997

Kliem, S.
Analysis and Calculation of an Accident with Delayed Scram on NPP Greifswald using the Coupled Code DYN3D/ATHLET
Proc. of the 7th Symposium of Atomic Energy Research, 457
Hörnitz, 23. - 26.09.1997

Kliem, S., U. Grundmann, U. Rohde
The Coupled Code Complex DYN3D/ATHLET - Application to Main Steam Line Break Analysis
Proc. of the Joint International Conference on Mathematical Methods and Supercomputing for Nuclear Applications, 1358
Saratoga Springs, New York, USA, October 5-10, 1997

Kolevzon, V.,
Light scattering study of viscoelastic properties of a gallium surface
Journal of Chemical Physics, Vol. 106, 1997, pp. 5816-5823

Kolevzon, V., G.Pozdniakov
Temperature-dependent behaviour of capillary waves at Hg-vapour and Hg-HgO interfaces
Journal of Physics: Condensed Matter, Vol. 9, 1997, pp. 6815-6826

Kolevzon, V.
Relaxations of temperature and charges at a liquid metal surface
Physics Letters A 230, 1997, pp. 358-362

Kolevzon, V., G.Gerbeth, G.Pozdniakov
Light scattering study of the mercury liquid/vapor interface
Physical Review E, Vol.55, No.3, 1997, pp. 3134-3142

Krepper, E.
Post test calculations to 11% break LOCA experiments at the integral test facility ISB-VVER using the thermalhydraulic code ATHLET
Nuclear Engineering and Design 170 (1997) 3-7

Krepper, E.
Natural circulation experiments at the ISB-VVER integral test facility and calculations using the code ATHLET
Jahrestagung Kerntechnik '97
Aachen, 13. –15. Mai 1997, Tagungsbericht S. 85

Mutschke, G., G.Gerbeth, V.Shatrov, A.Tomboulides
2-D and 3-D Instabilities of the Cylinder Wake in an Aligned Magnetic Field
Physics of Fluids, Vol.9, 1997, pp. 3114-3116

Prasser, H.-M., A. Böttger, J. Zschau
A New Wire-Mesh Tomograph for Gas-Liquid Flows
Proceedings of the Conference Frontiers in Industrial Process Tomography II
Delft, The Netherlands, April 9-12, 1997, pp. 109-112

Prasser, H.-M.
Leitfähigkeitssensoren für die Bestimmung von Parametern einer Zweiphasenströmung
Workshop "Meßtechnik für stationäre und transiente Mehrphasenströmungen"
Rossendorf, 06.-07. Nov. 1997, Report FZR-204, S. 64-71

Priede, J., G. Gerbeth
Dynamic instabilities in electromagnetic levitation
Proc. of 3rd Int. Conference on Transfer Phenomena in Magnetohydrodynamic & Electroconducting Flows,
Aussois, France, Sept.22-26, 1997, Vol.2, pp. 377-384

Priede, J., G. Gerbeth
Hydrothermal wave instability of thermocapillary driven convection in a coplanar magnetic field
Journal of Fluid Mechanics, Vol.347, 1997, pp. 141-169

Priede, J., G. Gerbeth
Influence of thermal boundary conditions on the stability of thermocapillary driven low-Prandtl-number convection
Physics of Fluids, Vol. 9, 1997, pp. 1621-1634

Priede, J., G. Gerbeth
On some instabilities of electromagnetically levitated spherical bodies
Proc. of Int. Congress "Electromagnetic Processing of Materials"
Paris, May 27-29, 1997, Vol.2, pp. 419-424

Priede, J., G. Gerbeth
Convective, absolute and global instabilities of thermocapillary-buoyancy con-
vection in extended layers
Physical Review E, Vol. 56, 1997, pp. 4187-4199

Richter, H., J. Böhmert, M. Valo, H.-W. Viehrig
Ermittlung bruchmechanischer Kennwerte im instrumentierten Kerbschlag-
biegeversuch- Vergleichsuntersuchungen zur Rißdetektion mit Schallemission
und dem Laserstreulichtverfahren
Deutscher Verband für Materialforschung und -prüfung e.V., Tagung Werk-
stoffprüfung '97
Bad Nauheim, Dez. 1997, Vortragsband S. 217-227

Richter, H.
Untersuchungen zum Rißeinleitungsverhalten von Stahl unter schlagartiger Be-
lastung mittels Schallemission
Deutsche Gesellschaft für Zerstörungsfreie Prüfung e.V., Statusberichte zur
Entwicklung und Anwendung der Schallemissionsanalyse, 11. Kolloquium
Schallemission
Jena, 6.-7.3.1997, Berichtsband 58, S. 77 ff

Rindelhardt, U., W. Hirsch
Das sächsische Windenergiepotential und seine Wirtschaftlichkeit
Energie und Umwelt '97,
Chemnitz, 19./20.3. 1997, Tagungsband S. 159

Rindelhardt, U.
Stand und Wirtschaftlichkeit der Windenergienutzung in den neuen Bun-
desländern
IDEE Informationsdienst Erneuerbare Energien, Nr.25 (1997), 10

Rindelhardt, U., G. Teichmann, B. Decker, J. Grochowski
Revised Performance Data of Small Grid Connected PV Systems Based on in
situ Measurements
in H.A. Ossenbrink, P. Helm, H. Ehmann (Ed.) Proc. of the 14th Eurepean Pho-
tovoltaic Solar Energy Conference and Exhibition, Barcelona (Spain), 30 June -
4 July 1997, Vol. II, 2652

Rindelhardt, U.
Perspektiven der Windenergienutzung in den neuen Bundesländern
Tagungband Windenergienutzung im Binnenland, S. 168-178
Kassel, 8./9. Oktober 1997

Rohde, U.
Zur Physik und Sicherheit von WWER-Reaktoren
Atomwirtschaft-Atomtechnik 42 (1997) 792

Rohde, U., I. Elkin, V. Kalinenko
Analysis of a boron dilution accident for WWER-440 combining the use of the codes DYN3D and SiTAP
Nucl. Eng. Design 170 (1997) pp. 95-99

Rohde, U., Lucas, D.
Solution of the 4th Dynamic Benchmark by Use of the Code DYN3D with a Particle-In-Cell Method for the Description of Boron Transport
Proc. of the 7th Symposium of Atomic Energy Research, p. 387
Hörnitz, 23. - 26.09.1997

Schaffrath, A., H.-M. Prasser, E. F. Hicken, H. Jaegers: Der passive Notkondensator des SWR-1000, Test und Berechnung
Atomwirtschaft-Atomtechnik 42 (1997), S. 697-700.

Schurig, C., U. Fiedler, J. Böhmert
Nondestructive Characterization of Reactor Pressure Vessel Materials Using Neural Networks
Proc. of EUROMAT '97, p. 347
Maastricht, April 1997

Shatrov, V., G. Mutschke, G. Gerbeth
A numerical three-dimensional stability analysis of the MHD cylinder wake flow
Proc. of 3rd Int. Conference on Transfer Phenomena in Magnetohydrodynamic & Electroconducting Flows
Aussois, France, Sept. 22-26, 1997, Vol.2, pp. 323-328

Stefani, F., G. Gerbeth, A. Gailitis
Velocity profile optimization for the Riga dynamo experiment
Proc. of 3rd, Int. Conference on Transfer Phenomena in Magnetohydrodynamic & Electroconducting Flows
Aussois, France, Sept. 22-26, 1997, Vol.1, pp. 27-32

Viehrig, H.-W., J. Böhmert
Specimen Reconstitution Technique and Verification Testing for Charpy Size SENB Specimens
Symposium on Small Specimen Test Techniques, Eds. W.R. Corwin, S.T. Rosinski, E. van Walle, ASTM STP 1329
New Orleans, January 1997

Weiß, F.-P., G. Hessel, W. Schmitt, N. Tefera, K. van der Vorst, J. Neumann, S. Schlüter
Untersuchung von Störungen in einem Semibatch-Versuchsreaktor
Preprints der 3. Merseburger Fachtagung: Automatisierung, Meßmethoden und Experimente in der chemischen Reaktionstechnik
Merseburg, 6./7. November 1997, S. 109-116

Oral Conference Contributions

Altstadt, E., F.-P. Weiss, M. Werner
Mechanical Response of a BWR to Loads Imposed by External Events
27-th Informal Meeting on Reactor Noise (IMORN-27)
Valencia, November 18-20, 1997

Anikeev, A. V., K. Noack, G. Otto
High Power Neutral Beam Heating Experiments in the Gas Dynamic Trap
24th EPS Conference on Controlled Fusion and Plasma Physics
Berchtesgaden, Germany, June 9-13, 1997, Posterbeitrag

Aszodi, A., E. Krepper
Verhalten von Lagertanks bei externem Feuer
ACHEMA 97, 25. Internationales Treffen für Chemische Technik, Umweltschutz
und Biotechnologie, Frankfurt am Main, June 9 – 14, 1997

Barz, H.-U., J. Konheiser
Rossendorf Monte Carlo Calculations for the Balakovo-3 Experiment and Compa-
rison to Experimental Results
International Workshop on the Balakovo-3 Interlaboratory Pressure Vessel Dosi-
metry Experiment, Rossendorf, 2.-5. September 1997

Bergner, F., U. Bergmann
Anwendung eines Ultraschallverfahrens zur Rißfortschrittsmessung in Bruch-
mechanikversuchen
Institutsseminar, Otto-von-Guericke-Universität Magdeburg, Institut für Werk-
stofftechnik und Werkstoffprüfung, 27. Mai 1997

Böhmer, B.
Spectrum Adjustment for the Balakovo-3 Experiment
WGRD VVER - EWGRD Workshop on RPV Neutron Dosimetry
Sandanski, Bulgaria, 29 September - 5 October 1997

Böhmer, B.
Rossendorf Spectrum Adjustment for the Balakovo-3 Experiment
International Workshop on the Balakovo-3 Interlaboratory Pressure Vessel Dosi-
metry Experiment
Rossendorf, 2.-5. September 1997

Böhmer, B.
Summary of the International Workshop on the Balakovo-3 Interlaboratory Expe-
riment
WGRD VVER - EWGRD Workshop on RPV Neutron Dosimetry
Sandanski, Bulgaria, 29 September - 5 October 1997

Böhmert, J., M. Große
Effect of Irradiation and Annealing on the Microstructure of VVER-440-Type Reactor Pressure Vessel Steel
Conference PLIM+PLEX 97, Prag, 8-10 Dec. 1997, Posterbeitrag

Böhmert, J., W. Reimche
Zerstörungsfreier Nachweis der Strahlenversprödung von Reaktordruckbehälterstählen
3. Sitzung des VGB-Fachausschusses "Werkstoffe und Beanspruchungen"
Mannheim, 02.09.1997

Böhmert, J., M. Große
Charakterisierung der Strahlenschäden in Reaktordruckbehälterstählen
Materialwissenschaftliche Tagung WBL
Berlin, Oktober 1997

Bojarevics, J., Yu. Gelfgat, G. Gerbeth
An experimental technique to investigate thermocapillary convection and solid-liquid phase transition in thin metal layer with free surface
Symposium on Physical Sciences in Microgravity
St.Petersburg, June 1997

Cramer, A.
Magnetic field stabilization of melt extraction processes
Int. Workshop "The use of magnetic fields in metallurgy and metals processing"
Frankfurt/Main, Oct.1-2, 1997

Cramer, A., Bojarevics, Y. Gelfgat, G. Gerbeth
Experimental results on Marangoni flows at a gallium surface
Int. Workshop on Hydrodynamic Aspects of Electron Beam Technologies
Dresden, March 16-18, 1997

Ferse, W.
Erweiterung des GEFA-Wissenserwerbs für Rüstungsaltlasten
Seminar der Rüstungsaltlastenvertreter der neuen Bundesländer
Umweltbundesamt Berlin, Januar 1997

Ferse, W., Th. Reitz
Die Anwendung wissensbasierter Methoden bei der Bewertung von Altlasten
XPS'97
4. Deutsche Jahrestagung Wissensbasierter Systeme
Bad Honnef, März 1997

Ferse, W., W. Geiger, M. Reißfelder, Th. Reitz, U. Schneider, R. Weidemann
Das wissensbasierte System XUMA-GEFA für Altlasten: Vom Prototyp zum Produktionssystem
11. Internationales Symposium der Gesellschaft für Informatik
Straßburg, 10.-12. September 1997

Ferse, W.
Möglichkeiten und Grenzen der Entscheidungsanalyse bei der Unterstützung von öffentlichen Entscheidungen
Workshop "Nachhaltigkeit - Leitbild für die Wirtschaft", Zentrum für Interdisziplinäre Technikforschung der Technischen Universität Dresden
Dresden, 24.-26. September 1997

Gerbeth, G., S. Eckert, G. Mutschke
Destabilizing actions of steady magnetic fields on electrically conducting flows
3rd European Fluid Mechanics Conference EUROMECH
Göttingen, Sept. 15-18, 1997

Gerbeth, G.
The Dresden Innovationskolleg on Magnetofluiddynamics
Int. Workshop "The use of magnetic fields in metallurgy and metals processing"
Frankfurt/Main, Oct.1-2, 1997

Gerbeth, G.
Destabilizing actions of steady magnetic fields
3rd Int. Conference on Transfer Phenomena in Magnetohydrodynamic & Electroconducting Flows
Aussois, France, Sept. 22-26, 1997

Große, M., V. Denner, J. Böhmert, M.-H. Mathon
SANS Investigations of the Irradiation-induced Microstructural Changes in Surveillance Specimens of VVER-440-Type Reactor Pressure Vessel Steel 15Kh2MFA and Weld Metal Sv-1OMFT
Table Ronde LLB Saclay, November 1997, Posterbeitrag

Große, M.
Kleinwinkelstreuexperimente mit Neutronen- und Synchrotronstrahlung zur Untersuchung der strukturellen Mechanismen der Neutronenversprödung
Paul Scherrer Institut Villingen, 21.10.1997

Große, M., J. Böhmert, R. Gilles
SANS Investigation of the Microstructure of WWER-440-Type RPV Steels after Low Temperature Irradiation
Annual User's Meeting, Hahn-Meitner-Institut
Berlin, November 1997, Posterbeitrag

Hensel, F.
Dichtemessung mit Positronenstrahlung
ACHEMA 97, 25. Internationales Treffen für Chemische Technik, Umweltschutz und Biotechnologie, Frankfurt am Main, June 9 - 14, 1997

Höhne, T.
CFD-Anwendungen zur Kühlmittelvermischung in Druckwasserreaktoren
CFX-Anwendertreffen
Bad Dürkheim, 16./17. September 1997

Kliem, S.
Proposal on Dynamic Benchmark Problem for Coupled Thermohydraulic/3D
Hexagonal Neutron Kinetic Codes
AER Working Group D Meeting
Budapest, 05-07 May, 1997

Kliem, S.
Development of an ATHLET Input Data Deck for the Dodewaard Reactor
Status Report BWRCA-Meeting
Rossendorf, 27/28 October, 1997

Kliem, S.
Eine Frischdampfleitungsleckanalyse für den WWER-440 mit dem gekoppelten
Programmkomplex DYN3D/ATHLET
4th ATHLET-User Group Meeting
Garching, 11/12 June, 1997

Kolevzon, V., G. Gerbeth
Light scattering study of the mercury liquid/vapor interface
Int. Workshop on Hydrodynamic Aspects of Electron Beam Technologies
Dresden, March 16-18, 1997

Krepper, E.
Simulation von Erwärmungsprozessen in großen Behältern mit dem Code CFX
CFX-Anwendertreffen
Bad Dürkheim, 16./17. September 1997

Kyrki-Rajamäki, R.,S. Mittag et al.
Guidelines for the collection of NPP measurement data to be used in transient
code validation
1st Meeting on the CEC PHARE project SRR1-95
Rossendorf, September 1997

Laggiard, E., U. Grundmann, U. Rohde, F.-P. Weiß, J. Runkel, D. Stegemann
Noise Analysis Measurements and Numerical Evaluations of the Moderator
Temperature Coefficients in PWRs
27th Informal Meeting on Reactor Noise (IMORN-27)
Valencia, November 18-20, 1997

Lucas D., H.-M. Prasser
Pulsationen bei der Druckentlastung von Reaktoren
ACHEMA 97, 25. Internationales Treffen für Chemische Technik, Umweltschutz und Biotechnologie
Frankfurt am Main, June 9 – 14,1997

Manturov, G., B. Böhmer
Covariance Matrices for the Calculated Spectra at the VVER-1000 Cavity
International Workshop on the Balakovo-3 Interlaboratory Pressure Vessel Dosimetry Experiment
Rossendorf, 2.-5. September 1997

Neumann, J., S. Schlüter, W. Schmitt, K. van der Vorst
Zustandserkennung in Chemieanlagen mit neuronalen Netzen
DECHEMA-Fachausschuß "Sicherheitsgerechtes Auslegen von Chemieapparaten"
Oberhausen, 26./27. November, 1997

Priede, J., G. Gerbeth
Magnetic stabilization of thermocapillary driven convection
Int. Workshop on Hydrodynamic Aspects of Electron Beam Technologies
Dresden, March 16-18, 1997

Rindelhardt, U., G. Teichmann
Leistungsmessungen an netzgekoppelten PV-Anlagen und Bestimmung des Performance Ratio
1000-Dächer-Workshop TÜV Rheinland
Köln, 16./17.9. 1997

Schäfer, F.
Investigations of Natural Circulation Instabilities in VVER-type Reactors at LOCA Conditions
27-th Informal Meeting on Reactor Noise (IMORN-27)
Valencia, November 18-20, 1997

Schneider, C.
Untersuchungen zur Fluiddynamik von Schaum
GVC-Fachausschuß Mehrphasenströmungen, Würzburg, 25. - 28. Februar 1997

Schäfer, F.
ATHLET Calculations of Selected Experiments at PMK-2
GRS-Project Meeting PHARE 4.2.6b
Berlin, 15.06.1997

Stephan, I.
Rossendorf Activation Measurements for the Balakovo-3 Experiment
International Workshop on the Balakovo-3 Interlaboratory Pressure Vessel Dosimetry Experiment
Rossendorf, 02.-05.09.1997

Viehrig, H.-W., J. Böhmert
Report on Contribution of the Forschungszentrum Rossendorf e.V. to the Project Reconstitution Techniques Qualification & Evaluation to Study Aging Phenomena of Nuclear Pressure Vessel Materials (RESQUE)
Project: No. PL960344, European Atomic Energy Community, Nuclear Fission Safety (1994 - 1998), 1st Progress Meeting
Erlangen, Germany, October 14-15,1997

Viehrig, H.-W.
Anwendung des Master-Curve-Konzeptes
Vortrag auf der Sitzung der DVM Arbeitsgruppe "Instrumentierter Kerbschlagbiegeversuch"
Staatliche Materialprüfungsanstalt MPA der Universität Stuttgart,
26. September 1997

Viehrig, H.-W., H.-U. Barz, J. Boehmert, B. Boehmer
Consideration of Neutron Flux Gradients for Sophisticated Evaluation of Irradiation Experiments
IAEA Specialist's Meeting on Irradiation Effects and Mitigation
Vladimir, Russia, 15-19 September 1997

Viehrig, H.-W., J. Böhmert
Report on Contribution of the Forschungszentrum Rossendorf e.V. to IAEA Co-ordinated Research Programme "Assuring Structural Integrity of Reactor Pressure Vessel - CRP Phase IV
IAEA Coordinated Research Programme Meeting
Vienna, Austria, October 8-10, 1997

Weier, T., G.Gerbeth, G.Mutschke, O.Lielausis, E.Platacis
Cylinder wake control by means of electromagnetic forces
Int. Workshop on Electromagnetic Boundary Layer Control for Saltwater Flows
Dresden, July 7-8, 1997

FZR-Reports and other publications

Altstadt, E.,G. Grunwald, M. Scheffler, F.-P. Weiß
Analytische Modellierung mechanischer Schwingungen von Primärkreiskomponenten des Druckwasserreaktors WWER-440 mit finiten Elementen
Abschlußbericht zum BMBF Projekt 1500916
Report FZR-172, April 1997

Altstadt, E., F.-P. Weiß, M. Werner, V. Bulavin, D. Gutsev, V. Pavelko, G. Anikin, A. Usanov und V. Dodonov
Entwicklung von theoretischen Schwingungsmodellen für WWER-Reaktoren auf der Grundlage der Finite-Elemente-Methode und Justierung dieser Modelle mit Schwingungsmessungen von Originalanlagen
Abschlußbericht zum BMBF-TRANFORM Projekt 1500999
Report FZR-196, Oktober 1997

Bergmann, U., F. Bergner
Mathematisch-numerische Modellierung der Ultraschallstreuung an oberflächenverbundenen Rissen mit dem EFIT-Code
Report FZR-177, 1997

Beyer, M., H. Carl, P. Schumann, A. Seidel, J. Zschau
Aufbau eines behördlichen Fernüberwachungssystems zur betrieblichen Überwachung des KKW Saporoshje (Block 5) - 3. Realisierungsstufe -
Report FZR-174, März 1997

Beyer, M., H. Carl, K. Nowak, P. Schumann, A. Seidel, F.-P. Weiß, J. Zschau
Ein Technisches System zur verbesserten betrieblichen Überwachung des Kernkraftwerkes Saporoshje/Ukraine
Report FZR-171, März 1997

Erbacher, F.J., H. Schmidt, P. Saey, R. Häusler, L. Wetzel, J. Böhmert, L. Lübke
Temperaturtransiente Kriechberstversuche an Zirconium-Niob1-Hüllrohen in Vergleich zu Zircaloy-4-Hüllrohren
Wissenschaftliche Berichte Forschungszentrum Karlsruhe, FZKAST-26 (August 1997)

Grundmann, U., U. Rohde
Verification of the Code DYN3D/R with the Help of International Benchmarks
FZR-195, Rossendorf, October 1997

Grundmann, U., S. Mittag, U. Rohde
Dodewaard Core – Capabilities of the Coupled Code DYN3D-ATHLET. Definition of the necessary steps for input data set development
BWRCA Report 4.1.6 – 1, May 1997

Grunwald, G.
Theoretische Untersuchungen zur Fluid-Struktur-Wechselwirkung in zweiphasig durchströmten Schwingungsmodellen
Report FZR-178, April 1997

Hackstein, G., J. Riedel, U. Rindelhardt, M. Schwanitz
Elektroenergieerzeugung aus erneuerbaren Energien in Sachsen
Report FZR-193, August 1997

Höhne, T.
Vergleich von Kühlmittelströmung- und Vermischung in einem 1:5 skalierten Modell des DWR Konvoi mit den Vorgängen im Originalreaktor
Report FZR-210, September 1997

Horche, W., E. Krepper, F. Schäfer, I. Trosztel
Summary Technical Report of PMK-2 Test No. 2: Pressuriser Surge Line Break Verification Report
Gesellschaft für Anlagen- und Reaktorsicherheit mbH, Garching, Nov. 1997

Kolevzon, V.
Quasi-elastic light scattering from capillary waves at the liquid metal surface
Dissertation, TU Berlin, Juli 1997

Kruber, St.
Anwendung der Entscheidungsanalyse bei der Sanierung von Altlasten
Report FZR-201, Dissertation, TU Dresden, November 1997

Kumpf, H.
Recriticality Calculations for Uraniumdioxide-Water Systems with MCNP
Report FZR-183, June 1997

Mittag, S.
Dodewaard core - Reactor physical modelling and neutron kinetic computer simulations. Progress report on the application of the coupled code DYN3D-ATHLET
BWRCA report 4.1.6-2, August 1997

Mittag, S., U. Grundmann, U. Rohde, S. Kliem, T. Scholz
Dodewaard core - Reactor physical modelling and neutron kinetic computer simulations. Final report on the application of the coupled code DYN3D-ATHLET
BWRCA report 4.1.6-3, December 1997

Prasser, H.-M., A. Böttger, A. Schaffrath
Strömungsformen bei Kondensationsvorgängen im Notkondensator-Versuchsstand
Report FZR-186, Juli 1997

Prasser, H.-M. (Herausgeber)
"Workshop Meßtechnik für stationäre und transiente Mehrphasenströmungen"
06.-07. Nov. 1997 in Rossendorf
Tagungsband FZR-204, Dez. 1997

Prasser, H.-M., P. Schütz, N. Kossok
Berührungslose Detektion der Struktur und Messung ausgewählter Parameter
von Zweiphasenströmungen durch Mustererkennungsverfahren unter Verwendung von Ultraschall als Meßsonde
Abschlußbericht zum BMBF-Vorhaben 1500967
Report FZR-203, November 1997

Richter, H.
Verifizierungsuntersuchungen zur Detektion von Rißinitiierung bei duktilem Materialverhalten unter schlagartiger Belastung
Abschlußbericht zum Forschungsaufenthalt am VTT Espoo (Finland) an die
Deutsche Akademie der Naturforscher Leopoldina, Juli 1997

Meetings and Workshops

Meetings and Workshops

International Workshop on Electromagnetic Boundary Layer Control (EBLC) for Saltwater Flows
Dresden, 7.-8. Juli 1997

Internationales Arbeitstreffen zum BMU-Vorhaben:
„Fernüberwachung KKW Saporoshje, Block 5"
Rossendorf, 18. - 29. August 1997
Teilnehmer (nat./internat.) 10/2

International Workshop on the Balakovo-3 Interlaboratory Pressure Vessel Dosimetry Experiment, Rossendorf, 2.- 5. September 1997
Offizielle Teilnehmer : 17 (11 ausländische und 6 deutsche)

7th AER Symposium on VVER Reactor Physics and Reactor Safety
Hörnitz (Zittau), 23.-26. September 1997

4th Project Meeting of the BWR Concerted Action
Rossendorf, 27.-28. Oktober 1997

Workshop "Meßtechnik für stationäre und transiente Mehrphasenströmungen"
Rossendorf, 6.-7. November 1997

German-Russian Workshop on Vibration Modelling of VVER Type Reactors
Rossendorf, 02-04 December 1997

Patents

Patents

1. J. Priede, G. Gerbeth, J. Gelfgat
    Verfahren und Vorrichtung zur Herstellung von Einkristallen in Ampullen
    unter Magnetfeldeinfluß
    Patent DE 197 04 075
    Anmeldung 04.02.1997

2. W. Witke, G. Gerbeth, S. Eckert
    Einrichtung zur Messung lokaler Strömungsgeschwindigkeiten in Gasen und
    Flüssigkeiten
    Patent DE 197 04 449
    Anmeldung 06.02.1997

3. H.-M. Prasser, J. Zschau, A. Böttger
    Anordnung zur Messung der lokalen elektrischen Leitfähigkeit in Fluiden
    Patent DE 197 04 609
    Anmeldung 07.02.1997

4. H.-M. Prasser, J. Zschau, A. Böttger
    Anordnung zur Messung der lokalen elektrischen Leitfähigkeit mittels
    Sonden sowie zur Sonden-Funktionskontrolle
    Patent DE 197 04 494
    Anmeldung 07.02.1997

5. H.-M. Prasser, C. Schneider
    Anordnung zur hydrostatischen Füllstandsmessung in einem Druckbehälter
    Patent DE 197 14 168
    Anmeldung 07.04.1997

Institute Seminars

SEMINARS 1997

1. Dr. H. Kumpf
   Rechnungen zur Rekritikalität mit MCNP
   16.01.97

2. T. Weier
   Experimente zur MHD-Strömungskontrolle in Elektrolyten
   30.01.97

3. Dr. W. Hansen (TU Dresden)
   Der Ausbildungsreaktor AKR der TU Dresden und seine Bestrahlungsmöglichkeiten
   06.02.97

4. Dr. G. Grunwald
   Untersuchungen zur Fluid-Struktur-Wechselwirkung in zweiphasig durchströmten Schwingungsmodellen
   12.02.97

5. Dr. A. Polte
   Ein Kriteriensystem zur Bewertung von Industrieansiedlungen in urbanen Gebieten
   13.02.97

6. Dr. Pollmer (GEOCONTROL Gera)
   Chemie in Uranbergbauhalden
   20.02.97

7. Dr. U. Grundmann, Dr. F. Hollstein
   Applikation des Codes DYN3DH zur Berechnung des Neutronenflußrauschens in WWER-Reaktoren bei strömungsinduzierten BE-Schwingungen
   27.02.97

8. Dr. A. Krüssenberg (Ruhr-Universität Bochum)
   Experimentelle und analytische Untersuchungen zur Sicherheit von Fusionsreaktoren
   06.03.97

9. C. Schneider
   Hydrodynamik einer seitlich begasten Blasensäule
   13.03.97

10. G. Hessel
Fehlerdiagnose mit dezentraler Signalverarbeitung in Chemieanlagen
10.04.97

11. Prof. Dr. S. Collatz
Rekritikalität bei Kernschmelzstörfällen an Druckwasserreaktoren
17.04.97

12. Dr. H.-W. Viehrig
Probenrekonstruktion - Eine Methode zur Erweiterung von RDB-Versprö-
dungsüberwachungsprogrammen
24.04.97

13. U. Hampel (TU Dresden, Fakultät Elektrotechnik, Institut für Biomedizi-
nische Technik)
Optische Tomographie
22.05.97

14. Dr. E. Krepper, Dr.U. Rohde
Strömungssimulation mit CFX4 (FLOW3D)
29.05.97

15. Dr. E. Altstadt, Dr. M. Werner, H.-G. Willschütz
Mechanische Beanspruchung von SWR-Komponenten in Störfallsituationen
15.05.97

16. J. Konheiser
Bestimmung der Neutronenfluenzbelastung in WWER-1000 Reaktordruck-
behältern
12.06.97

17. S. Kliem
Verfikation des Programmkomplexes DYN3D-ATHLET anhand von KKW-
Transienten
26.06.97

18. F. Hensel, J. Schmidt
Stand der Arbeiten zur Qualitätssicherung
21.08.97

19. Dr. F. Dittes (FWKS)
Neue Monte-Carlo-Verfahren zur Optimierung komplexer Systeme
01.09.97

20. Dr. E. Zienicke (Observatoire de Nice, France)
    Wird Chaos durch ein wachsendes Magnetfeld unterdrückt?
    09.09.97

21. Dr. M. Umbreit (TU Dresden)
    Theoretische Untersuchungen zur Containmentbelastung von KKW infolge
    turbulenter Wasserstoffverbrennung während schwerer Störfälle
    18.09.97

22. Dr. V. Kolevzon
    Quasielastische Lichtstreuung von kapillaren Wellen auf einer Flüssigmetall-
    oberfläche
    02.10.97

23. Dr. E. Gelfort (Bundesamt für Strahlenschutz Berlin)
    Die Entwicklung der Kernkraftwerke - Sicherheitsauslegung der zukünftigen
    3. Generation
    23.10.97

24. A. Hennion (Universität Lille / Frankreich)
    Thermal and irradiation embrittlement of VVER-440 pressure vessel steels
    24.10.97

25. Dr. D. Lucas
    Das Programm BRICK - ein Simulationstool für Druckentlastungsprozesse
    auf der Basis einer Partikelmethode
    13.11.97

26. Dr. D. Hoppe
    Anwendung des tensororientierten Mustererkennungsverfahrens zur Identi-
    fikation gefährlicher Betriebszustände in Chemieanlagen
    20.11.97

27. M. Beyer, Dr. H. Carl, Dr. P. Schumann
    Automatisierte Fernüberwachung des KKW Saporoshe / Ukraine
    11.12.97

28. Dr. H.-W. Viehrig
    Das Radioisotoplabor für Werkstoffuntersuchungen
    18.12.97

Doktorandenseminar am 1. Dezember 1997

Ute Bergmann
Ultraschall-Rißfortschrittsmessung an Biegeproben

Tom Weier
Experimentelle Arbeiten zur elektromagnetischen Strömungskontrolle

Thomas Repp
Fluid-Struktur-Wechselwirkung bei Druckschlägen in Rohrleitungen

Carsten Beckert
3-dimensionale integrale Neutronentransportrechnungen

Alexander Grahn
Konvektionsströmungen an Grenzflächen reagierender nichtmischbarer Flüssig-
keiten

Tommy Kern
Einfluß von Schaum auf Druckentlastungsvorgänge

Carola Schneider
Strömungsvorgänge im Anodenraum von Alkalielektrolysezellen

Frank Hensel
Strömungsmessungen mit Positronenemittern

Frank Schäfer
Thermohydraulische Instabilitäten im Primärkreis von Druckwasserreaktoren

Lecture Courses

Lectures

1. U. Rindelhardt
   Erneuerbare Energien I und II
   Universität Leipzig, Fakultät für Physik und Geowissenschaften
   SS 97 und WS 97

2. F.-P. Weiß
   Zuverlässigkeit und Sicherheit technischer Systeme
   TU Dresden, Fakultät für Maschinenwesen
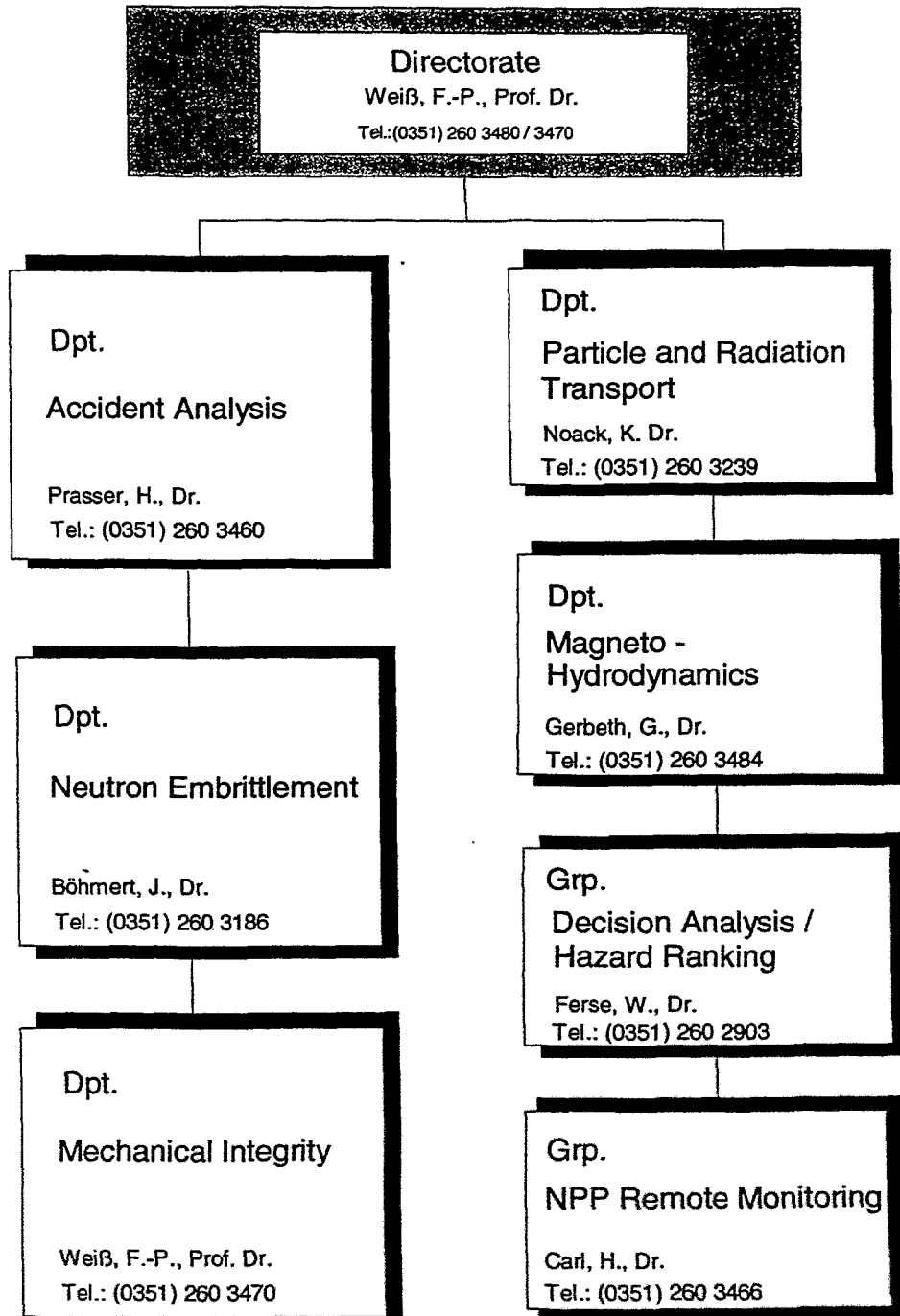   SS 97 und WS 97

Practical Training

1. U. Rindelhardt, G. Teichmann
   Photovoltaik
   TU Dresden, Fakultät für Maschinenwesen

Departments of the Institute

Research Center Rossendorf, Inc.

Institute for Safety Research
01314 Dresden, PF 510119

Directorate
Weiß, F.-P., Prof. Dr.
Tel.:(0351) 260 3480 / 3470

Dpt.
Accident Analysis
Prasser, H., Dr.
Tel.: (0351) 260 3460

Dpt.
Particle and Radiation Transport
Noack, K. Dr.
Tel.: (0351) 260 3239

Dpt.
Neutron Embrittlement
Böhmert, J., Dr.
Tel.: (0351) 260 3186

Dpt.
Magneto - Hydrodynamics
Gerbeth, G., Dr.
Tel.: (0351) 260 3484

Dpt.
Mechanical Integrity
Weiß, F.-P., Prof. Dr.
Tel.: (0351) 260 3470

Grp.
Decision Analysis / Hazard Ranking
Ferse, W., Dr.
Tel.: (0351) 260 2903

Grp.
NPP Remote Monitoring
Carl, H., Dr.
Tel.: (0351) 260 3466

Personnel

Director: Prof. Dr. F.-P. Weiß

Scientific Staff
Altstadt, Eberhard Dr.
Barz, Hansulrich Dr.
Bergmann, Ute
Beyer, Matthias
Brünig, Dietlinde Dr.
Böhmer, Bertram
Böhmert, Jürgen Dr.
Böttger, Arnd
Carl, Helmar Dr.
Cramer, Andreas Dr.
Erlebach, Stephan
Ferse, Wolfgang Dr.
Fietz, Jürgen Dr.
Galindo, Vladimir Dr.
Gerbeth, Günter Dr.
Große, Mirco
Grundmann, Ulrich Dr.
Grunwald, Gerhard Dr.
Hessel, Günter
Hirsch, Werner Dr.
Hollstein, Frank Dr.
Hoppe, Dietrich Dr.
Hüller, Jürgen Dr.
Kliem, Sören
Koch, Reinhard Dr.
Kolevzon, Vladimir Dr.
Konheiser, Jörg
Krepper, Eckhard Dr.
Kruber, Stefan Dr.
Krüssenberg, Anne-Kathrin Dr.
Kumpf, Hermann Dr.
Küchler, Roland Dr.
Laggiard, Eduardo Dr.
Lucas, Dirk Dr.
Mittag, Siegfried Dr.
Mößner, Ralph, Dr.
Mutschke, Gerd
Noack, Klaus Dr.
Polte, Annette Dr.
Prasser, Hans-Michael Dr.
Priede, Janis Dr.
Reitz, Thomas
Rindelhardt, Udo PD Dr.
Rohde, Ulrich Dr.
Schaffrath, Andreas Dr.
Schmitt, Wilfried Dr.
Scholz, Thomas
Schütz, Peter
Schumann, Peter Dr.
Seidel, Andre
Stephan, Ingrid Dr.
Stephani, Frank Dr.
Teichmann, Günther
Tefera, Nurelegne Dr.
van der Vorst, Klaus
Viehrig, Hans-Werner Dr.

Werner, Matthias Dr.
Willschütz, Hans-Georg
Witke, Willy
Zschau, Jochen Dr.
Zippe, Winfried Dr.
Zippe, Cornelius Dr.

PhD Students
Beckert, Carsten
Bergmann, Ute
Eckert, Sven
Grahn, Alexander
Hensel, Frank
Höhne, Thomas
Kern, Tommy
Ramisch, Kai
Repp, Thomas
Richter, Holger
Schäfer, Frank
Schneider, Carola
Ulbricht, Andreas
Weier, Tom
Zoller, Jürgen

Technical Staff
Baldauf, Dieter
Behrens, Sieglinde
Blumentritt, Thea
Bombis, Doris
Borchardt, Steffen
Eichhorn, Christine
Forker, Klaus
Futterschneider, Hein
Heinze, Gerda
Kaule, Christian
Kunadt, Heiko
Leonhardt, Wolf-Dietrich
Leuner, Bernd
Losinski, Claudia
Lotzmann, Roland
Otto, Gerlind
Pietzsch, Jens
Richter, Annett
Richter, Henry
Richter, Joachim
Richter, Karl-Heinz
Richter, Petra
Rott, Sonja
Russig, Heiko
Schleßiger, Heike
Seidler, Christa
Skorupa, Ulrich
Tamme, Marko
Tamme, Günter
Webersinke, Wolfgang
Weichelt, Steffen
Weiß, Rainer
Zimmermann, Wilfried